

INFORMATION TO USERS

This manuscript has been reproduced from the microfilm master. UMI films the text directly from the original or copy submitted. Thus, some thesis and dissertation copies are in typewriter face, while others may be from any type of computer printer.

The quality of this reproduction is dependent upon the quality of the copy submitted. Broken or indistinct print, colored or poor quality illustrations and photographs, print bleedthrough, substandard margins, and improper alignment can adversely affect reproduction.

In the unlikely event that the author did not send UMI a complete manuscript and there are missing pages, these will be noted. Also, if unauthorized copyright material had to be removed, a note will indicate the deletion.

Oversize materials (e.g., maps, drawings, charts) are reproduced by sectioning the original, beginning at the upper left-hand corner and continuing from left to right in equal sections with small overlaps. Each original is also photographed in one exposure and is included in reduced form at the back of the book.

Photographs included in the original manuscript have been reproduced xerographically in this copy. Higher quality 6" x 9" black and white photographic prints are available for any photographs or illustrations appearing in this copy for an additional charge. Contact UMI directly to order.

UMI

**A Bell & Howell Information Company
300 North Zeeb Road, Ann Arbor, MI 48106-1346 USA
313/761-4700 800/521-0600**



Order Number 9518390

**The structure and properties of anhydrous, alkali ultra-phosphate
glasses**

Hudgens, James Jay, Ph.D.

Iowa State University, 1994

U·M·I
300 N. Zeeb Rd.
Ann Arbor, MI 48106



The structure and properties of anhydrous, alkali ultra-phosphate glasses

by

James Jay Hudgens

**A Dissertation Submitted to the
Graduate Faculty in Partial Fulfillment of the
Requirements for the Degree of
DOCTOR OF PHILOSOPHY**

**Department: Materials Science and Engineering
Major: Ceramic Engineering**

Approved:

Signature was redacted for privacy.

In Charge of Major Work

Signature was redacted for privacy.

For the Major Department

Signature was redacted for privacy.

For the Graduate College

**Iowa State University
Ames, Iowa**

1994

**Dedicated to my family and
especially my wife, Suzi,
for their love and support during my education.**

TABLE OF CONTENTS

TABLE OF CONTENTS	iii
LIST OF TABLES	vi
LIST OF FIGURES	viii
1. INTRODUCTION	1
1.1 Technological Importance of Phosphate Glasses	1
1.2 Problems in Phosphate Glass Research	2
1.3 Objectives of the Research	3
1.4 General Outline for the Thesis	3
2. LITERATURE REVIEW	5
2.1 The Structures and Properties of Crystalline Phosphates	5
2.1.1 Introduction	5
2.1.2 Crystalline P_4O_{10}	5
2.1.3 Reorganization Theory	8
2.1.4 Ultra-Phosphate Crystals	15
2.1.5 Metaphosphate Crystals	17
2.1.6 Poly-, Pyro- and Orthophosphate Crystals	19
2.1.7 Summary	20
2.2 The Structures and Properties of Phosphate Glasses	20
2.2.1 Vitreous P_2O_5	20
2.2.2 Ultra-Phosphate Glasses	24
2.2.3 Metaphosphate Glasses	27
2.2.4 Polyphosphate Glasses	28
2.2.5 Summary	29
2.3 The Glass Transition and Enthalpy Relaxation	30
2.4 Melt Processing Dependence of Properties	35
2.4.1 Introduction	35
2.4.2 Examples of Melt Processing Dependence	36
3. EXPERIMENTAL PROCEDURES	40
3.1 Introduction	40
3.2 Preparation of the Glass	40
3.2.1 Dry Samples Preparation Facility	40
3.2.2 Starting Materials for Glass Compositions	41
3.2.3 Tube Sealing Procedures	41
3.2.4 Drying Procedures	43
3.2.5 Melting and Quenching	43

3.2.6 Annealing.....	44
3.2.7 Water Content.....	44
3.3 Measurement of Physical Properties.....	45
3.3.1 Introduction.....	45
3.3.2 T_g Determinations	46
3.3.3 Heat Capacity Measurements	46
3.3.4 Density Measurements	48
3.4 Structure Determination.....	50
3.4.1 Infrared Spectroscopy	50
3.4.2 Raman Spectroscopy.....	50
3.4.3 ^{31}P MAS-NMR Spectroscopy.....	51
3.5 Enthalpy Relaxation.....	52
3.5.1 Introduction.....	52
3.5.2 Normalizing Heat Capacity Data	52
3.5.3 Activation Enthalpies	53
3.5.4 Fitting the heat capacity data	53
4. RESULTS	55
4.1 Glass Formation.....	55
4.1.1 $\nu\text{-P}_2\text{O}_5$	55
4.1.2 The $\text{Li}_2\text{O}+\text{P}_2\text{O}_5$ System	55
4.1.3 The $\text{Na}_2\text{O}+\text{P}_2\text{O}_5$ System	56
4.2 Physical Properties of the Glasses	57
4.2.1 Water Content.....	57
4.2.2 Glass Transition Temperatures	59
4.2.3 Enthalpy Relaxation	64
4.2.4 Density Measurements	71
4.3 Structural Determination.....	74
4.3.1 Infrared Spectroscopy.....	74
4.3.2 Raman Spectroscopy.....	84
4.3.3 ^{31}P MAS-NMR Spectroscopy.....	102
5. DISCUSSION	115
5.1 Vitreous P_2O_5	115
5.1.1 ^{31}P MAS-NMR	115
5.1.2 Vibrational Spectra	117
5.1.3 Physical Properties.....	118
5.2 Alkali Ultra-Phosphate Glasses	120
5.2.1 Site Distributions.....	120
5.2.2 Oxygen Bonding	124
5.2.3 Glass Transition Temperatures	143
5.2.4 Density.....	146
5.2.5 Heat Capacity and Structural Relaxation	151

5.3 The Melt Processing Dependence of Properties.....	157
6. CONCLUSIONS	115
LIST OF REFERENCES.....	174
ACKNOWLEDGMENTS.....	182
APPENDIX A: THE HEAT CAPACITIES OF SODIUM ULTRA- PHOSPHATE GLASSES.....	183
APPENDIX B: THE INFRA-RED SPECTRA OF SODIUM AND LITHIUM ULTRA-PHOSPHATE GLASSES.....	199
APPENDIX C: THE RAMAN SPECTRA OF SODIUM AND LITHIUM ULTRA-PHOSPHATE GLASSES.....	218
APPENDIX D: THE ^{31}P MAS-NMR SPECTRA OF SODIUM AND LITHIUM ULTRA-PHOSPHATE GLASSES.....	235
APPENDIX E: THE COMPUTER PROGRAM 'TN'	252

LIST OF TABLES

Table 2.1	Interatomic distances and bond angles for the different polymorphs of c- P_4O_{10}	7
Table 2.2	The bond lengths in Mg, Zn and Ca ultra-phosphate crystals	16
Table 2.3	The bond lengths and bond angles in long chain and cyclic metaphosphate crystals.	18
Table 2.4	The average number of π bonds per σ bond for BO and BO's for the different PO_4 units.	20
Table 2.5	The glass transition temperatures and $C_p(l)/C_p(s)$ ratios for several 'strong', 'intermediate', and 'fragile' glass-forming liquids.	23
Table 2.6	The bond lengths and bond angles in several meta-phosphate glasses [76].	28
Table 2.7	Comparisons of glass transition temperatures for several metaphosphate glasses [105].	29
Table 4.1	Analyzed glass compositions of several sodium ultra-phosphate glasses.	56
Table 4.2	The six regions where P-O-H groups cause absorbtions in vibrational spectra [111].	57
Table 4.3	The water contents of several sodium ultra-phosphate glasses.	59
Table 4.4	The glass transition temperatures ($\pm 3^\circ C$) of lithium ultra-phosphate glasses.	60
Table 4.5	The glass transition temperatures of sodium ultra-phosphate glasses ($\pm 3^\circ C$).	62
Table 4.6	Heat capacities at T_g for serveral sodium ultra-phosphate glasses	65
Table 4.7	Heating rate data for several sodium ultra-phosphate glasses.	68
Table 4.8	Activation enthalpies for structural relaxation of several sodium ultra- phosphate glasses.	68
Table 4.9	The best fit parameters used to fit the normalized heat capacity of several sodium ultra-phosphate glasses.	70
Table 4.10	The densities of lithium ultra-phosphate glasses.	71
Table 4.11	The densities of sodium ultra-phosphate glasses.	71

Table 4.12	Absorbance regions for the P-NBO, P-BO, and P=O modes of Q ² and Q ³ units.	77
Table 4.13	The wavenumbers of the centers of the different absorbance bands in the MIR spectra of lithium ultra-phosphate glasses and the vibrational modes assigned to those bands.	83
Table 4.14	The wavenumbers of the centers of the different absorbance bands in the MIR spectra of sodium ultra-phosphate glasses.	86
Table 4.15	The wavenumbers of the centers of the different Raman scattering modes in lithium ultra-phosphate glasses. The 50 mole% data is from reference [].	93
Table 4.16	The wavenumbers of the centers of the different Raman scattering modes in sodium ultra-phosphate glasses. The values in parenthesis are the depolarization ratios.	97
Table 4.17	The approximate chemical shift ranges for different types of phosphate tetrahedra in phosphate materials.	103
Table 4.18	The Q ³ and Q ² site distributions in the system x Li ₂ O + (1-x) P ₂ O ₅ calculated from the ³¹ P MAS-NMR spectra.	108
Table 4.19	The isotropic chemical shift and diagonal chemical shift tensor elements of glasses in the system x Li ₂ O + (1-x) P ₂ O ₅	109
Table 4.20	The anisotropy (δ) and asymmetry parameters (η) for lithium ultra-phosphate glasses.	109
Table 4.21	The Q ³ and Q ² site distributions in the system x Na ₂ O + (1-x) P ₂ O ₅ calculated from the ³¹ P MAS-NMR spectra.	112
Table 4.22	The chemical shift anisotropies of glasses in the system x Na ₂ O + (1-x) P ₂ O ₅	113
Table 4.23	The anisotropy (δ) and asymmetry parameters (η) for for Q ³ and Q ² species in sodium ultra-phosphate glasses.	113
Table 5.1	The ³¹ P chemical shielding parameters of the polymorphs of c-P ₄ O ₁₀ and glassy P ₂ O ₅	116
Table 5.2	The glass transition temperatures and Cp(l)/Cp(s) ratios for the glass forming liquids in Figure 5.2	122
Table 5.3	The T _g , fragility and non-exponentiality parameter of representative glass forming liquids [147].	158

LIST OF FIGURES

Figure 2.1	The structure of PO_4 tetrahedra found in the polymorphs of $\text{c-P}_4\text{O}_{10}$	8
Figure 2.2	The meta-, pyro-, and orthophosphate groups found in simple alkali phosphate materials.	8
Figure 2.3	The compositional dependence of the different Q^n species in phosphate glasses assuming totally ionic O-M bonds.	11
Figure 2.4	The experimental and calculated compositional dependence of the fraction of PO_4 structural units present in a series of zinc phosphate glasses. The theoretical fractions of structural units were calculated using $K_1=10^{-3}$ and $K_2=0.025$ [20].	13
Figure 2.5	General model of structural transition in the ultra-phosphate region.	14
Figure 2.6	A projection of the crystal structure of $\text{ZnP}_4\text{O}_{11}$ onto the b, c axis plane. The structures of $\text{ZnP}_4\text{O}_{11}$ and $\text{MgP}_4\text{O}_{11}$ are isomorphous [15].....	16
Figure 2.7	A reduced T_g plot of the glass forming liquids P_2O_5 , SiO_2 , GeO_2 , a sodium disilicate liquid, and sodium metaphosphate	22
Figure 2.8	The water contents of sodium ultra-phosphate glasses increases dramatically for compositions with >55 mole% P_2O_5 . The solid line represents anhydrous glasses. Brow et al. [72] (diamonds) and Gray et al. [4] (circles).	25
Figure 3.1	Assembly used to evacuate and seal vitreous silica tubes and dry the raw materials.	42
Figure 3.2	The dotted construction lines show how glass transition temperatures were calculated from temperature dependent heat flow traces.	47
Figure 3.3	DSC scans of a glass sample, sapphire, and blank pan. The arrows y and y' indicate the how the values $\left(\frac{dH}{dt}\right)_{\text{sample-baseline}}$ and $\left(\frac{dH}{dt}\right)_{\text{sapphire-baseline}}$ were calculated, respectively.	49
Figure 4.1	The MIR spectra of $\text{v-P}_2\text{O}_5$ with the absorbance regions arising from P-OH stretching vibrations highlighted. The inset expands the region where the strongest P-OH absorbances occur.....	58

Figure 4.2	The glass transition temperatures of glasses in the system $x \text{Li}_2\text{O} + (1-x) \text{P}_2\text{O}_5$ obtained at $q_c = q_h = 20^\circ\text{C}/\text{min}$. The reproducibility of the transition temperatures is $\pm 3 \text{ K}$	61
Figure 4.3	The glass transition temperatures of glasses in the system $x \text{Na}_2\text{O} + (1-x) \text{P}_2\text{O}_5$. For sodium metaphosphate, the T_g of the glass prepared in a sealed tube (\blacklozenge) is significantly less than the T_g of the same glass prepared in an open crucible (\bullet). The reproducibility of the transition temperatures is $\pm 4 \text{ K}$	62
Figure 4.4	The temperature dependent heat flow traces for $v\text{-NaPO}_3$ prepared in an open silica crucible and prepared in a sealed silica tube. T_g , crystallization temperature, T_x , and melting temperature, T_m , are larger for the glass prepared in an open silica crucible.	63
Figure 4.5	Heat capacity curve for the glass composition $35 \text{Na}_2\text{O} + 65 \text{P}_2\text{O}_5$. The dashed construction lines show how $C_p(l)$ and $C_p(s)$ were calculated.	65
Figure 4.6	DSC scans of $45 \text{Na}_2\text{O} + 55 \text{P}_2\text{O}_5$ glass at $q_h = q_c$ of 5, 10, 20, 30, and 40 K/min . The lines represent the construction used to calculate onset T_g . The scans have been offset to improve comparison.	66
Figure 4.7	T_g for 45 mole% sodium ultra-phosphate glass measured at different heat/cool rates plotted in the Arrhenius form to yield enthalpy relaxation activation energies.	67
Figure 4.8	The activation enthalpies for structural relaxation of glasses in the $x \text{Na}_2\text{O} + (1-x) \text{P}_2\text{O}_5$ system.....	69
Figure 4.9	The best fit of the normalized heat capacity data to a model based on the Tool-Narayanaswamy (T-N) equation.....	70
Figure 4.10	The densities of $x \text{Li}_2\text{O} + (1-x) \text{P}_2\text{O}_5$ glasses.	72
Figure 4.11	The densities of glasses in the $x \text{Na}_2\text{O} + (1-x) \text{P}_2\text{O}_5$ system.....	73
Figure 4.12	The MIR spectra of crystalline and glassy $\text{Ca}_2\text{P}_4\text{O}_{11}$ [15] illustrating the band complexes found in the MIR spectra of amorphous materials as opposed to the sharp peaks in crystalline materials.	76
Figure 4.13	The MIR spectra of the $0.35 \text{Na}_2\text{O} + 0.65 \text{P}_2\text{O}_5$ glass showing absorbance due to uncombined H_2O in the KBr, a doublet caused by residual CO_2 in the dry air within the spectrometer bench, H_2O rotational spectra due to residual H_2O in the dry air, and baseline curvature due to difference in thicknesses between the background KBr pellet and the sample pellet.....	78

Figure 4.14	The MIR spectrum of the H form of crystalline P_4O_{10} .	80
Figure 4.15	The MIR spectra of $v\text{-}P_2O_5$ indicating absorbances due to the symmetric and asymmetric stretches of Q^3 units.	81
Figure 4.16	The MIR spectra of lithium ultra-phosphate glasses. The spectra can be divided into four band complexes. Complex I, centered near 1350cm^{-1} , consists of $\nu(P=O)$ and $\nu(PO_2)_a$ stretching vibrations. Complex II, centered near 1000cm^{-1} , consists of the $\nu(POP)_a$ and $\nu(PO_2)_s$ stretching vibrations. Complex III, centered near 750cm^{-1} , contains the $\nu(POP)_s$ stretching vibrations and complex IV contains the deformation modes. The spectra have been offset to improve comparison.	82
Figure 4.17	The infra-red spectra of sodium ultra-phosphate glasses. The spectra can be divided into four band complexes. Complex I, centered near 1350cm^{-1} , consists of $\nu(P=O)$ and $\nu(PO_2)_a$ stretching vibrations. Complex II, centered near 1000cm^{-1} , consists of the $\nu(POP)_a$ and $\nu(PO_2)_s$ stretching vibrations. Complex III, centered near 750cm^{-1} , contains the $\nu(POP)_s$ stretching vibrations and complex IV contains the deformation modes. The spectra have been offset to improve comparison.	85
Figure 4.18	The raman spectra of $c\text{-}NaPO_3$ and MIR spectra of $c\text{-}Ca(PO_3)_2$, showing the differences between the two techniques.	88
Figure 4.19	The unpolarized, HV polarized, and HH polarized Raman spectra of $v\text{-}P_2O_5$. The spectra have been offset to improve comparison.	89
Figure 4.20	The raman spectra of lithium ultra-phosphate glasses from 0 to 20 mole% Li_2O . the spectra have been offset to improve comparison.	91
Figure 4.21	The raman spectra of lithium ultra-phosphate glasses from 0 to 20 mole% Li_2O . the spectra have been offset to improve comparison. The 50 mole% data is from reference [].	92
Figure 4.22	The Raman spectra of glasses in the system $x Na_2O + (1-x) P_2O_5$, where $0 \leq x \leq 0.25$. The spectra have been offset to improve comparison.	95
Figure 4.23	The Raman spectra of glasses in the system $x Na_2O + (1-x) P_2O_5$, where $0.30 \leq x \leq 0.45$. The spectra have been offset to improve comparison. The 50 mole% spectra is from ref. [74].	96
Figure 4.24	The Raman spectra of the glass $0.40 Na_2O + 0.60 P_2O_5$ heated from room temperature to 650°C .	99

Figure 4.25	The Raman spectra of the glass $0.40 \text{ Na}_2\text{O} + 0.60 \text{ P}_2\text{O}_5$ cooled from 900°C to 450°C	100
Figure 4.26	The Raman spectra of the glass $0.40 \text{ Na}_2\text{O} + 0.60 \text{ P}_2\text{O}_5$ cooled from 400°C to room temperature. The spectra have been offset to improve comparison.	101
Figure 4.27	The ^{31}P MAS-NMR spectrum of $\nu\text{-P}_2\text{O}_5$. The peak labeled Q^3 is the resonance due to a Q^3 unit, the remaining peaks are spinning sidebands.....	105
Figure 4.28	The ^{31}P MAS-NMR spectra of lithium ultra-phosphate glasses. The peaks marked with the (+) are spinning sidebands. The spectra have been offset to improve comparison.....	106
Figure 4.29	The ^{31}P MAS-NMR spectra of lithium ultra-phosphate glasses. The peaks marked with the (+) are spinning sidebands. The spectra have been offset to improve comparison.....	107
Figure 4.30	The ^{31}P MAS-NMR spectra of sodium ultra-phosphate glasses. The peaks marked with the (+) are spinning sidebands. The spectra have been offset to improve comparison.....	110
Figure 4.31	The ^{31}P MAS-NMR spectra of lithium ultra-phosphate glasses. The peaks marked with the (+) are spinning sidebands. The spectra have been offset to improve comparison.....	111
Figure 5.1	The MIR and Raman spectra of $\nu\text{-P}_2\text{O}_5$. The frequencies of non-degenerate A_1 vibrational modes are indicated [54].	118
Figure 5.2	The dependence of viscosity on reduced T_g [46, 60]. Network liquids (SiO_2 and GeO_2) show Arrhenius behavior, but can be converted into non-Arrhenius liquids by decreasing the number of covalent interconnections. Although P_2O_5 contains no modifier, there are only three covalent interconnections whereas there are four in GeO_2 and SiO_2 . Therefore, P_2O_5 is not the archetypal Arrhenius liquid.	121
Figure 5.3	Q^3 , Q^2 , and Q^1 site distributions measured from the ^{31}P MAS-NMR spectra as compared to those predicted from the glass compositions using Equation (38).	123
Figure 5.4	As the number of non-bridging oxygens per PO_4 tetrahedra increases, the P-NBO bond lengths decrease and P-BO bond lengths increase due to π -bond delocalization. Therefore, the vibrational frequencies of the NBO peaks decrease while those of the BO peaks increase. The largest	

- amount of shift is seen on going from Q^3 to Q^2 species. The crystal spectra were taken from ref. [74]. 126
- Figure 5.5 The peak frequencies of the vibrational modes of Q^2 and Q^3 species in sodium and lithium ultra-phosphate glasses as determined from Raman (open symbols) and MIR (filled symbols) spectroscopies. $\nu(P=O)$, (\blacktriangle) is the stretching mode of a terminal oxygen on a Q^3 , $\nu(PO_2)$, (\blacktriangle) and $\nu(PO_2)_{as}$ (\blacklozenge) are the symmetric and asymmetric stretching modes of $P-O^-M^+$ terminal oxygens and $\nu(POP)$, (\bullet) and $\nu(POP)_{as}$ (\blacksquare) are the symmetric and asymmetric stretching modes of bridging oxygens. The compositional dependence of these peak frequencies can be divided into three regions. 127
- Figure 5.6 The creation of Q^2 species results in resonance structures where the counteraction charge balances both terminal oxygens. The terminal oxygen lengths on Q^2 species are identical but are longer than the terminal oxygen bond length on Q^3 species. 129
- Figure 5.7 As the second Q^2 species is added to each Q^3 species (>20 mole% modifier), anionic repulsions between terminal oxygens results in an increase in $P(Q^2)-O-P(Q^3)$ bond angles, shortening of Q^3-Q^2 P-O bond lengths, lengthening of the P-O terminal oxygen bond length and conversion of the $P=O$ terminal oxygens on Q^3 species into $P-O^-M^+$ terminal oxygens. 130
- Figure 5.8 The shapes of the MIR spectra are similar in three distinct composition regions. Comparison of representative spectra from these regions with the MIR spectra of ultra-phosphate crystals [15] suggest the topologies of the glassy network are also different between these regions. 131
- Figure 5.9 The relationship between Q-species and isotropic chemical shift [130]. 132
- Figure 5.10 The ^{31}P isotropic chemical shifts of Q^3 (circles) and Q^2 (triangles) species in sodium and lithium ultra-phosphate glasses. 134
- Figure 5.11 The relationship between the full width at half-maximum (FWHM) of the ^{31}P isotropic chemical shifts (± 0.5 ppm) of Q^2 (triangles) and Q^3 (diamonds) species in sodium (solid symbols) and lithium (open symbols) ultra-phosphate glasses and alkali content. The lines represent linear least-squares best fits for the data. 136
- Figure 5.12 The relationship between ^{31}P FWHM and covalent interconnection of the network. The line represents the linear least-squares best fit for the data. The data for the Q^1 and Q^0 ^{31}P FWHM are from refs. [130, 61]. 137

- Figure 5.13 The asymmetry parameters of the ^{31}P chemical shift of Q^2 (triangles) and Q^3 (circles) species in lithium (filled symbols) and sodium (open symbols) ultra-phosphate glasses. The error for all measurements is estimated as ± 0.5 138
- Figure 5.14 The ^{31}P chemical shift anisotropy ($\Delta\delta$) of Q^2 (triangles) and Q^3 (circles) species of sodium (filled symbols) and lithium (open symbols) ultra-phosphate glasses. The lines represent linear least squares fits of the sodium ultra-phosphate data. 140
- Figure 5.15 The relationship between type of phosphate group and the difference between upfield (σ_{33}) and intermediate (σ_{22}) chemical shielding tensors for crystalline phosphates [70, 71]. Also shown are the $\sigma_{33}-\sigma_{22}$ values for Q^3 (— — —, \blacktriangle) and Q^2 (- - - -, \blacklozenge) species in sodium ultra-phosphate glasses. 142
- Figure 5.16 The glass transition temperatures of anhydrous lithium (\blacktriangle) and sodium (\oplus) as compared to hydrated lithium (Δ) [7] and sodium (\circ) [105] ultra-phosphate glasses. 144
- Figure 5.17 The densities of several crystalline ultra-phosphates. Densities have been calculated from lattice parameters [15]. 146
- Figure 5.18 The densities of both lithium (\blacklozenge) and sodium (\bullet) ultra-phosphate glasses show a minimum at 20 mole% alkali. The data cannot be accurately modeled using a simple additive model (----). 147
- Figure 5.19 The molar volumes of lithium (\blacktriangle) and sodium (\bullet) ultra-phosphate glasses. The network expands at a significantly faster rate at low alkali concentrations. 149
- Figure 5.20 The crystal structure of an ultra-phosphate showing the large amount of free volume [15]. The square represents the projection of a unit cell in the b-c plane. 151
- Figure 5.21 The $C_p(l)/C_p(s)$ at T_g increases with increasing depolymerization, while %3Rn goes through a minimum. The error bars are applicable to all measurements. 154
- Figure 5.22 The activation enthalpies, ΔH^* , of several sodium ultra-phosphate glasses. 155
- Figure 5.23 The glass transition temperatures ($\pm 3^\circ\text{C}$) of sodium ultra-phosphate glasses held at 900°C for 0.25hrs (\blacktriangle , — - —), 3hrs. (\blacklozenge , ———), and 24hrs. (\bullet , - - - -). At the metaphosphate composition, T_g was

	independent of melt annealing time for all sealed tube preparations. The higher T_g resulted from preparing sodium metaphosphate in an open silica crucible.	161
Figure 5.24	The MIR spectra of sodium metaphosphate glasses prepared in a sealed crucible and open crucible. There is virtually no difference in the spectra.	163
Figure 5.25	The glass transition temperatures of the 40 mole% Na_2O glass as a function of hold time at 900°C . All glasses were quenched at identical rates.	164
Figure 5.26	The densities of sodium ultra-phosphate glasses after melt annealing for 3 hrs. (●, —) and 24 hrs. (▲, - - -).	165
Figure 5.27	The MIR spectra of a 40mole% Na_2O ultra-phosphate glass after holding for 1 and 22 hrs at 900°C . The MIR spectrum of the 40mole% Na_2O glass held at 900°C for 1hr. resembles the MIR spectra of ring-dominated calcium ultra-phosphate crystals [15]. Alternatively, the MIR spectrum of the 40mole% Na_2O glass held at 900°C for 15hr. resembles the MIR spectra of the chain-dominated calcium metaphosphate crystal [15].	167
Figure 5.28	The Raman spectra of a 40mole% sodium ultra-phosphate glasses on heating from room temperature to 900°C	170
Figure 5.29	The Raman spectra of a 40mole% sodium ultra-phosphate glasses on heating from room temperature to 900°C	171

1. INTRODUCTION

Phosphorus pentoxide (P_2O_5) was one of Zachariason's [1] four glass formers, along with B_2O_3 , GeO_2 and SiO_2 . Binary alkali borate, germanate and silicate glass-forming systems have been extensively studied. Likewise, alkali phosphate glasses with an alkali oxide fraction ≥ 0.5 are among the easiest of all glasses to prepare and have received enormous attention in literature [2]. Alternatively, the hygroscopic nature and volatility [3- 5] of vitreous P_2O_5 have prevented a thorough examination of binary alkali phosphate materials with less than 50 mole% alkali, the ultra-phosphates. Therefore, nearly two-thirds of the simplest phosphate glass forming systems have not been examined.

To better understand the significance of a study of the structures and properties of anhydrous, alkali ultra-phosphate glasses, it is necessary to address the technological importance of such materials. Moreover, to realize the uniqueness of the research presented in this thesis, it is prerequisite to describe the preparation difficulties which, prior to the present study, have not been overcome to prepare anhydrous, alkali ultra-phosphate glasses.

1.1 Technological Importance of Phosphate Glasses

Alkali phosphate glasses are often the basis for more complicated, technologically useful glass compositions. Binary alkali phosphate based glass compositions are used in glass seals, such glasses generally have higher thermal expansion coefficients and lower transition temperatures than silicate or borate glasses. In this way, glass to metal seals can be made with high expansion steels, such as stainless steel. Phosphate glasses are also unique among glass forming systems in that some compositions are bio-compatible. Dental ceramics, bone replacement ceramics and other materials used for biological applications are often formed from recrystallized phosphate glasses. Phosphate glasses are not only suited for biological applications because of their bio-compatibility, but also because of their low durabilities. The poor aqueous durabilities of phosphate glasses allows them to be used to temporarily replace bone enabling the bone to slowly replace the phosphate material.

Beyond their uses as bio-materials and glass sealing materials, phosphate based glasses are also being developed as solid state ionic materials, dosimeters, and for many other such technologically important applications. Understanding how the structures and properties of the simplest phosphate glasses evolve with composition is critical in being able to design glasses with specific properties. Therefore, research of the structures and properties of ν - P_2O_5 and the simplest binary ultra-phosphate glass systems will be valuable archival data for researchers in many fields.

1.2 Problems in Phosphate Glass Research

Solid state, inorganic phosphate glass research is limited by the hygroscopic and volatile nature of pure phosphoric pentoxide. The commercially available form of crystalline P_4O_{10} has a vapor pressure that becomes appreciable just above 200°C and reaches atmospheric pressure at 359°C [3]. Since most inorganic phosphate materials are formed at temperatures $>500^\circ\text{C}$, P_2O_5 loss using conventional open crucible melting techniques is a critical problem. This problem is compounded at ultra-phosphate compositions because of the small number of known ultra-phosphate crystals. As is true for polyphosphate crystals, ultra-phosphate crystals would undoubtedly have lower vapor pressures at the temperatures used to prepare phosphate materials. The second problem confronting phosphate glass research is the hygroscopic nature of most ultra-phosphate materials.

Traditionally, phosphate glasses have been prepared with ammonium salts such as $(\text{NH}_3)\text{H}_2\text{PO}_4$. Use of such starting materials can result in as much as 30 mole% H_2O being retained in ultra-phosphate glasses [4]. The incorporation of water into phosphate glasses is not in the form of H_2O molecules trapped within the interstices of the structure, but the water depolymerizes the glassy network through the conversion of P-O-P bridging oxygens to P-OH terminal oxygens. Such depolymerization causes dramatic changes in the properties and structures of ultra-phosphate glasses [6]. The use of anhydrous starting materials, such as P_4O_{10} , and traditional open crucible preparation techniques also results in H_2O contamination. When put in contact with water, the commercially available form of P_4O_{10} dissolves with a

hissing sound accompanied by spattering, and in the form of a fine powder it reacts with explosive violence [3]. Even when exposed to atmospheric moisture, P_4O_{10} crystal disappears within 24 hours leaving behind a pool of phosphoric acid. The hygroscopic and volatile nature of $c\text{-}P_4O_{10}$ and ultra-phosphate materials has prohibited the study of even the most basic binary alkali ultra-phosphate glass systems.

1.3 Objectives of the Research

The goal of this research was to prepare and characterize anhydrous, binary alkali glasses in the compositional series $xM_2O + (1-x) P_2O_5$, where $M = \text{Li and Na}$ and $0 \leq x \leq 0.5$. Glass transition temperatures, densities, and heat capacities were measured to determine their compositional dependence. Likewise, the compositional dependencies of bridging, non-bridging, and doubly-bonded oxygen fractions were determined. In this way, a structure/composition map was developed for ultra-phosphate glasses.

It has been proposed that the structures of lithium ultra-phosphate glasses can be 'switched' through variations in melt processing [7]. Therefore, the extent and form of melt-processing dependence of the alkali ultra-phosphate glasses was characterized. Research also focused on the structural relaxation dynamics of these glasses. The viscosity of $v\text{-}P_2O_5$ has been shown to have an Arrhenius temperature dependence over several orders of magnitude [46], therefore, according to the Adam's and Gibb's theory of liquids, $v\text{-}P_2O_5$ should have single relaxation time kinetics [8]. Mathematical models were used to simulate the heat capacity of anhydrous, $v\text{-}P_2O_5$ to determine if it does, indeed, have single relaxation time kinetics. Similarly, since the addition of alkali to $v\text{-}P_2O_5$ will alter the temperature dependence of the viscosity, heat capacities of the ultra-phosphate glasses were modeled to investigate the dependence of the spectrum of relaxation times on glass composition.

1.4 General Outline for the Thesis

The thesis is divided into five chapters. Chapter 1 provides a brief overview of the structures and properties of alkali phosphate glasses and polycrystals and gives concise

descriptions of the phenomenology of the glass transition and enthalpy relaxation in glassy materials. Chapter 3 outlines the experimental procedures and modeling methods used to characterize the alkali ultra-phosphate glasses. Chapter 4 presents the results of experiments described in Chapter 3. Chapter 5 discusses the short-range order (SRO), properties, melt-processing dependence of properties, and enthalpy relaxation of alkali ultra-phosphate glasses. Finally, Chapter 6 summarizes the results of the research with emphasis on those goals outlined in the introduction to the thesis. Appendices are included at the end of the dissertation which contain spectroscopic data, a comprehensive listing of the properties of anhydrous, alkali ultra-phosphate glasses and a listing of the code used to mathematically model the glass transition.

2. LITERATURE REVIEW

2.1 The Structures and Properties of Crystalline Phosphates

2.1.1 Introduction

Although there exists sparse literature concerning the structure and properties of ultra-phosphate materials, the crystal structures of the different polymorphs of crystalline P_4O_{10} and a few crystalline ultra-phosphates have been determined. Conversely, much is known concerning the high-alkali crystalline phases of meta-, poly-, pyro-, and ortho-phosphate materials.

The following sections will concentrate on the structures of the different polymorphs of crystalline P_4O_{10} (c- P_4O_{10}), ultra-, and meta- phosphate crystals. Structural reviews will emphasize the nature of the PO_4 tetrahedra and the role of oxygen bonding. Brief sections will also cover the structures of poly-, pyro- and ortho- phosphate crystals.

2.1.2 Crystalline P_4O_{10}

In most inorganic phosphate materials, centrally bonded phosphorus atoms exhibit sp^3 σ -bonding with four oxygens and one $d_{\pi}-p_{\pi}$ bond to balance the +5 charge of phosphorus. In this way, all polymorphs of c- P_4O_{10} are built from PO_4 tetrahedra, as shown in Figure 2.1. The three polymorphs of P_4O_{10} are: a metastable rhombohedral polymorph of the hexagonal system (H form) where the PO_4 tetrahedra exist as discrete molecules of four phosphate tetrahedra [9- 11], a metastable orthorhombic polymorph (O form) of the hexagonal system where the PO_4 tetrahedra form corrugated sheets of interconnected rings and a tetragonal polymorph (T form) where the PO_4 tetrahedra are three-dimensionally branching [12,13]. The H form is the phase that is sold commercially, however, it is metastable with respect to the O form which is, in turn, metastable with respect to the T form.

The vapor pressure of the H form reaches atmospheric pressure at 359°C while O and T forms have triple points at much higher temperatures, 562°C and 580°C, respectively. Therefore, the H form will sublime before transforming into the other polymorphs. The T form has the highest melting temperature ($580\pm5^\circ\text{C}$), the O form has an intermediate melting temperature ($558\pm6^\circ\text{C}$), and the H form has the lowest melting temperature ($422\pm6^\circ\text{C}$). Density is highest for the branching T form ($\sim 2.9\text{ g/cc}$), lowest for the molecular H form (2.3 g/cc) with the sheet O form having an intermediate density ($\sim 2.72\text{ g/cc}$) [3].

The molecular H form is the least resistant to water attack while the O form is most resistant; however, all polymorphs react vigorously with water. In response to observations of the durabilities of phosphate materials the anti-branching rule was developed [14]. The anti-branching rule states: "In any environment in which reactions involving the degradation of condensed phosphates are possible, it is to be expected that assemblies in which three of the four oxygens of a PO_4 tetrahedron are shared with other PO_4 tetrahedra will be exceedingly unstable and will degrade much more rapidly as compared to those in which one or two oxygens are shared." This rule is a manifestation of the unbalance in π bonding on phosphate tetrahedra.

Table 2.1 shows that the terminal oxygen (P-O_t) and bridging oxygen (P-O_b) bond lengths and P-O-P bond angles for the O form differ considerably from those of the H and T polymorphs of $\text{c-P}_4\text{O}_{10}$. The structure of the O form is characterized by corrugated sheets of linked rings of six PO_4 tetrahedra with two equivalent sites for PO_4 tetrahedra, where there is only one in the other polymorphs of $\text{c-P}_4\text{O}_{10}$ [15, 16]. Between the sheets there are non-bonded $\text{O}_t\text{-O}_b$ contacts. The increase in P-O-P bond angle allows such contacts to be separated by $\sim 3\text{\AA}$, typical for Van der Waal's contact between sheets, larger P-O-P bond angles would decrease this distance, increasing repulsion [10]. The increase in length of the P-O_t and decrease of P-O_b bond length are directly related to the changes in P-O-P bond angle. For larger P-O-P bond angles the bridging oxygen p-orbitals can take part in π bonding with the d_π orbitals of the phosphorus atom. Owing to the sharing of π character, the P-O_t bonds are lengthened while the added π character shortens the P-O_b bond lengths.

Table 2.1 Interatomic distances and bond angles for the different polymorphs of c-P₄O₁₀.

Structure	Composition	P-O _t (Å)	P-O _b (Å)	P-O-P (°)	O _t -P-O _b (°)	O _b -P-O _b (°)	Ref.
Hexagonal							
Gaseous	P ₄ O ₁₀	1.429	1.604	123.5	116.5	101.6	[9]
Solid	P ₄ O ₁₀	1.40	1.60	124	116	102	[10]
Orthorhombic	P ₂ O ₅	1.49	1.56	145	116	103	[17]
Tetragonal	P ₂ O ₅	1.40	1.65	124	117	96	[10]

Quadruply connected crystalline phosphorus compounds contain a significant amount of π bonding, as indicated by their 20-30% shorter P-O_t bond lengths and higher enthalpies than calculations would suggest [18]. Unlike silicate materials where π -bonding is divided evenly between oxygens, the π -bonding in c-P₄O₁₀ is localized on the non-bridging oxygen (NBO). π -bonding is facilitated because four connected phosphorus compounds can utilize d orbitals in bonding. In a tetrahedral ligand field the $d_{x^2-y^2}$ and d_{z^2} orbitals of the central phosphorus atom are lowered in energy as compared to the remaining d orbitals. The lower energy d _{π} orbitals from the phosphorus atom can bond with p _{π} orbitals from an oxygen atom. In this way, bonding in phosphates averages approximately one π bond and four σ bonds per phosphorus atom [19]. The π -bond may be localized on a single bond or distributed among different P-O bonds. Because the length of the bonds is inversely proportional to the π/σ bonding ratios, the P-O bond lengths can be used as a measure of π -bond delocalization. In the H and T forms of P₄O₁₀, the π -bond is localized on the P-O_t bond. In the O form, the P-O_t bond length is longer and P-O_b bond lengths shorter than in the H and T forms, indicating π -bond character has been delocalized away from the P-O_t.

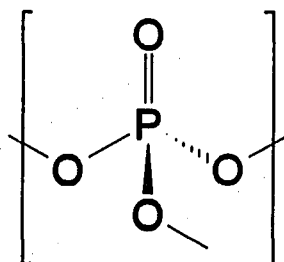


Figure 2.1 The structure of PO_4 tetrahedra found in the polymorphs of $\text{c-P}_4\text{O}_{10}$.

2.1.3 Reorganization Theory

Inorganic phosphate materials built from phosphate tetrahedra have a discrete number of building blocks from which structures can be built. PO_4 units with three bridging oxygens (BO's) are Q^3 units (here the superscript denotes the number of bridging oxygens per phosphate tetrahedra). A PO_4 group with two BO species is the metaphosphate or Q^2 unit. A PO_4 group with one BO is the pyrophosphate or Q^1 unit. A PO_4 group with no bridging oxygens is the orthophosphate or Q^0 unit. The Q^3 unit is shown in Figure 2.1, while the remaining phosphate groups are shown in Figure 2.2. In addition to the PO_4 groups shown in Figure 2.2, a four-way branching unit may exist when electron-pair-acceptor atoms are present. Examples of such materials are phosphate-borates and phosphate-aluminates.

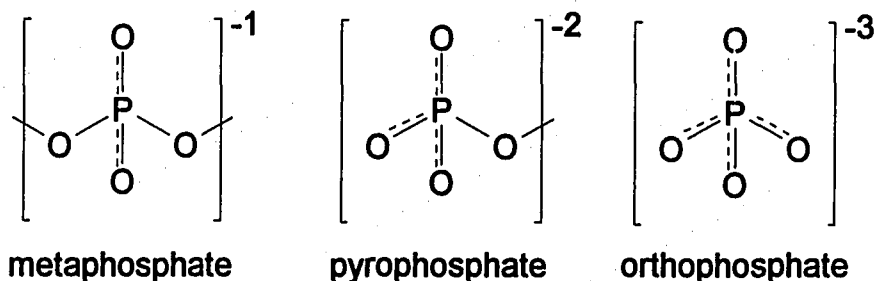


Figure 2.2 The meta-, pyro-, and orthophosphate groups found in simple alkali phosphate materials.

In the liquid state, single phase phosphates undergo reorganization of the aforementioned structural units. Van Wazer established a theory for the compositional dependence of the structural units based on liquid chromatography of meta-, poly- and pyrophosphate crystals and glasses [14]. Van Wazer assumed: (i) the different structural groups are interchanging through the making and breaking of P-O-P linkages, (ii) phosphorus atoms are surrounded by four oxygens at all times during reorganization, and (iii) the BO to NBO ratio remains constant. The exchange between structural units in the liquid can then be completely described by Equations 2.1-2.3 and combinations of the same.



Because Equations 2.1-2.3 represent equilibria, the corresponding equilibrium constants, Equations 2.4-2.6 can be derived.

$$K_1 = \frac{[Q^3][Q^1]}{[Q^2]^2} \quad (2.4)$$

$$K_2 = \frac{[Q^2][Q^0]}{[Q^1]^2} \quad (2.5)$$

$$K_3 = \frac{[Q^1]^2[M_2O]}{[Q^0]^2} \quad (2.6)$$

While in some phosphate systems there exists unreacted material, i.e. the $P_2O_5 + H_2O$ system, at ultra-phosphate and compositions up to the orthophosphate composition, Equations 2.3 and 2.6 need not be considered.

The modifier to phosphorus ratio, $R = M_2O/P_2O_5$, can be expressed in terms of structural units:

$$R = \frac{(3[Q^0] + 2[Q^1] + [Q^2])}{([Q^0] + [Q^1] + [Q^2] + [Q^3])} \quad (2.7)$$

Also, the total fraction of structural units is normalized according to Equation 8.

$$[Q^3] + [Q^2] + [Q^1] + [Q^0] = 1 \quad (2.8)$$

Using the four Equations (4,5,7 and 8) the compositional dependence of the fractions of the different structural units can be determined. The values of the equilibrium constants depend on the ionization potential of the modifying cation. For completely ionized modifying cations, such as alkali cations, all equilibrium constants should be zero. When equilibrium constants are non-zero, regions of higher and lower concentrations of modifying cations must exist, an unlikely situation for highly mobile ionized cations. As the M-O bond becomes slightly covalent and the cations become less mobile, both K_1 and K_2 become non-zero.

At ultra-phosphate compositions, the electronic structure of Q^3 units are unbalanced due to the unbalance in π -bonding. Therefore, the formation of a Q^2 unit from a Q^3 unit will decrease the energy of the system over the disproportionation of two Q^2 units into a Q^3 and Q^1 unit. Therefore, the equilibrium constant K_1 will always be near zero. Figure 2.3 shows the compositional dependence of the different Q^n units assuming completely ionized modifying cations, $K_1 = K_2 = 0$. For the values $R = 0, 1, 2$, and 3 , only one type of structural unit exists; Q^3, Q^2, Q^1 , and Q^0 , respectively. For the region $0 < R < 1$, only Q^3 and Q^2 units are found. For the region $1 < R < 2$, only Q^2 and Q^1 units are found. For the region

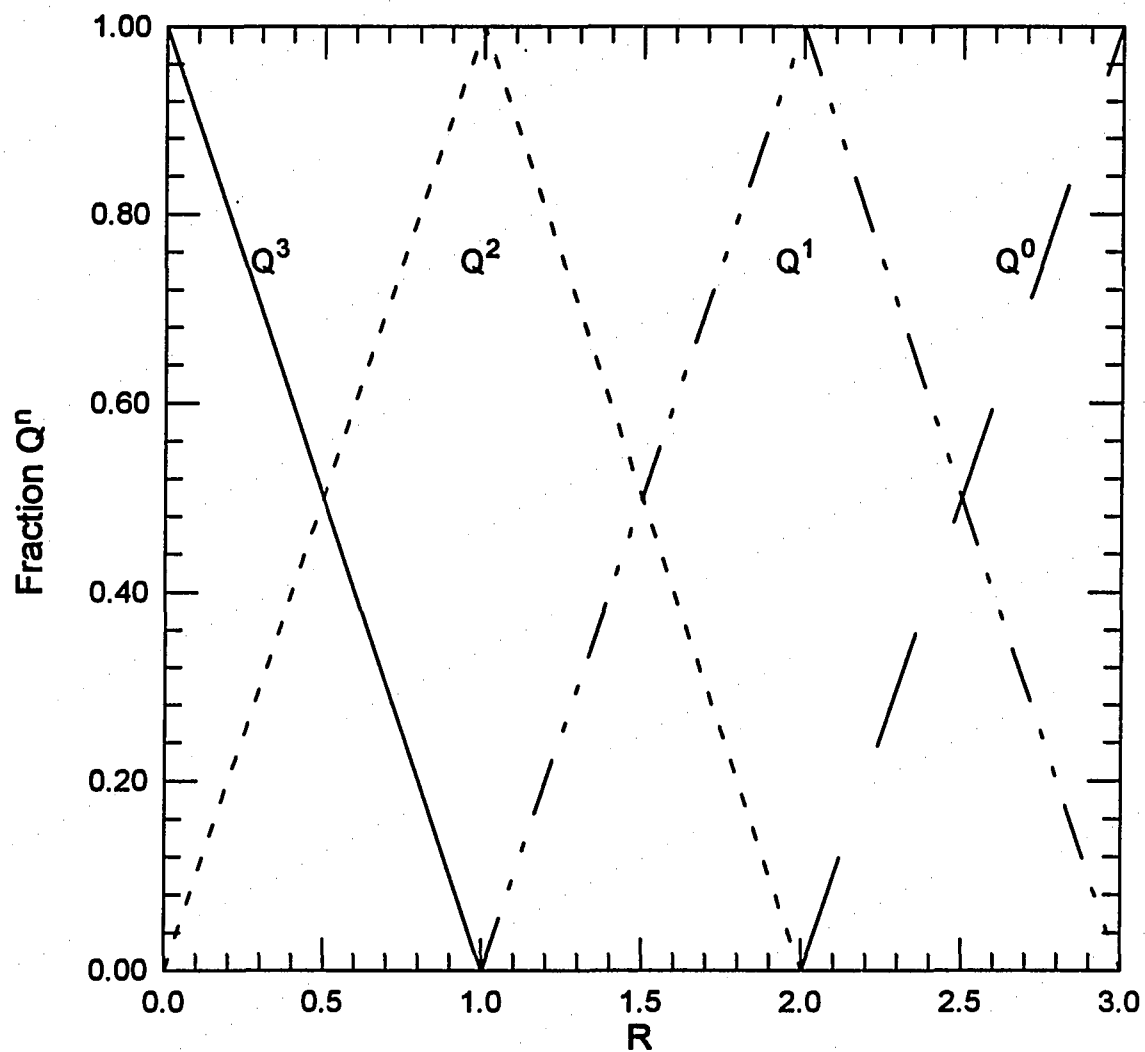


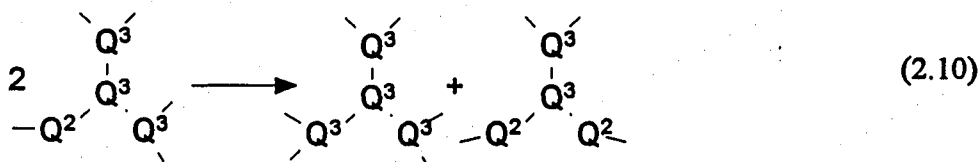
Figure 2.3 The compositional dependence of the different Q^n species in phosphate glasses assuming totally ionic O-M bonds.

$2 < R < 3$, only Q^1 and Q^0 units are found. Additionally, at $R > 3$ all the PO_4 groups are Q^0 structural units and additional modifier will be unreacted. Such chemically simple depolymerization of the phosphate network can also be described by the pseudo-reaction:



where M is the modifying counteraction. When there is partial covalent character to the O-M bond, as is the case in zinc phosphate glasses, more than two structural units can occur at a given composition. Figure 2.4 shows the experimental fraction of structural units in zinc phosphate glasses as determined from ^{31}P MAS-NMR [20]. K_2 was estimated as 0.025 using Equation 2.5 and the experimental data. The lines represent the fractions of Q^n units calculated using $K_2 = 0.025$. In this case, disproportionation results in greater structural complexity than found for the completely ionic case.

Stachel and Reiss have used Van Wazer's reorganization theory to develop a model of the linkages of structural units in the ultra-phosphate region [53]. Assuming $K_1 = K_2 = 0$, at $Q^3:Q^2$ ratios of 3:1, 2:1, 1:1, 1:2, and 1:3, ultra-phosphate crystalline compounds can be built where the simple building unit is a combination of Q^3 and Q^2 units in the respective ratios. The compositional dependence of the fraction of such simple building units can, in turn, be calculated. Such a structure/composition map is shown in Figure 2.5. For example, at 0 mole% M_2O , every Q^3 unit is connected to three other Q^3 units. As the amount of M_2O increases, some Q^3 units are connected to two Q^3 units and one Q^2 . At 20 mole% M_2O , every Q^3 will be connected to one Q^2 and two Q^3 units, and no 'disproportionation', as given in Equation 2.10, will occur.



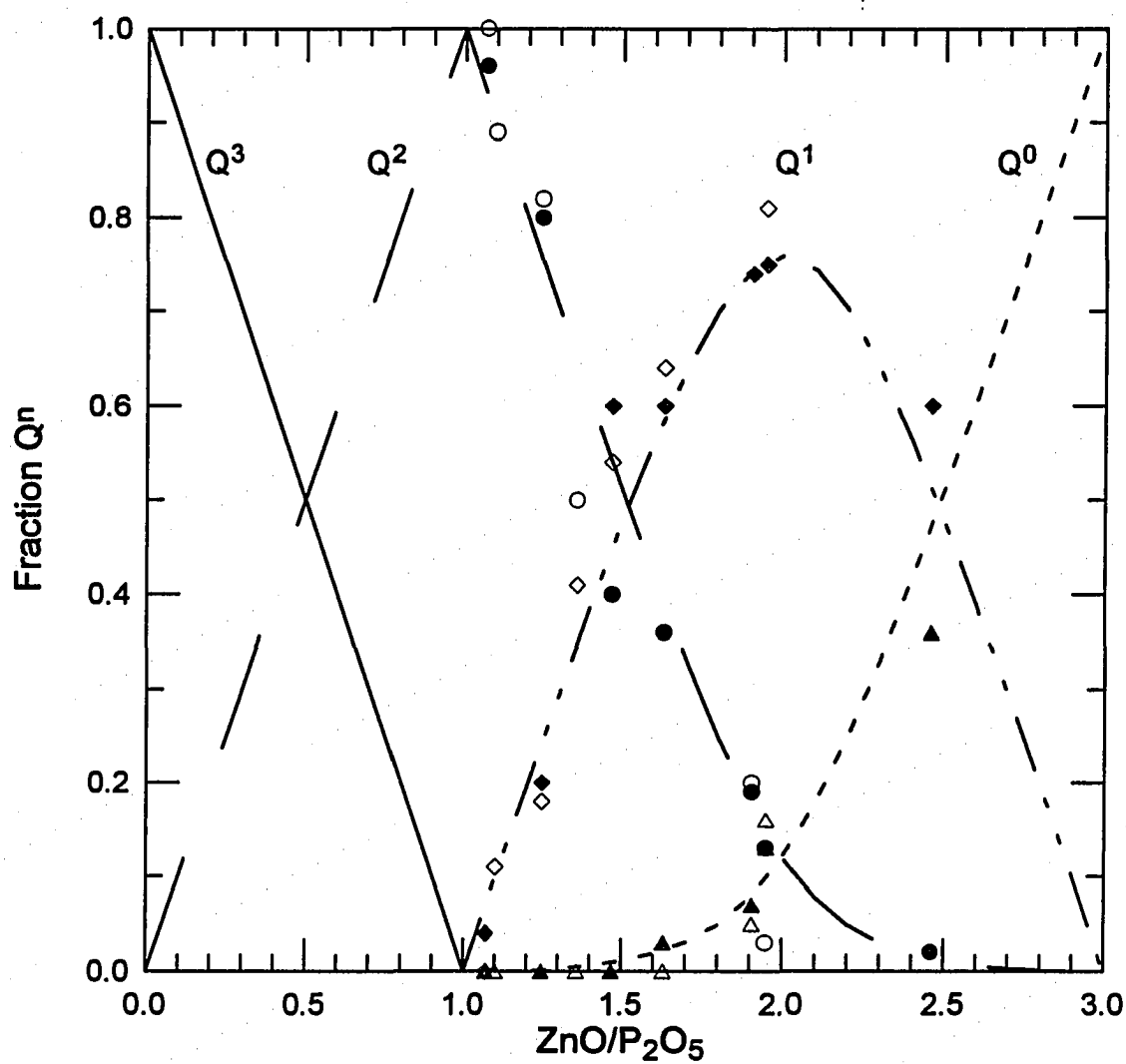


Figure 2.4 The experimental and calculated compositional dependence of the fraction of PO_4 structural units present in a series of zinc phosphate glasses. The theoretical fractions of structural units were calculated using $K_1=10^{-3}$ and $K_2=0.025$ [20].

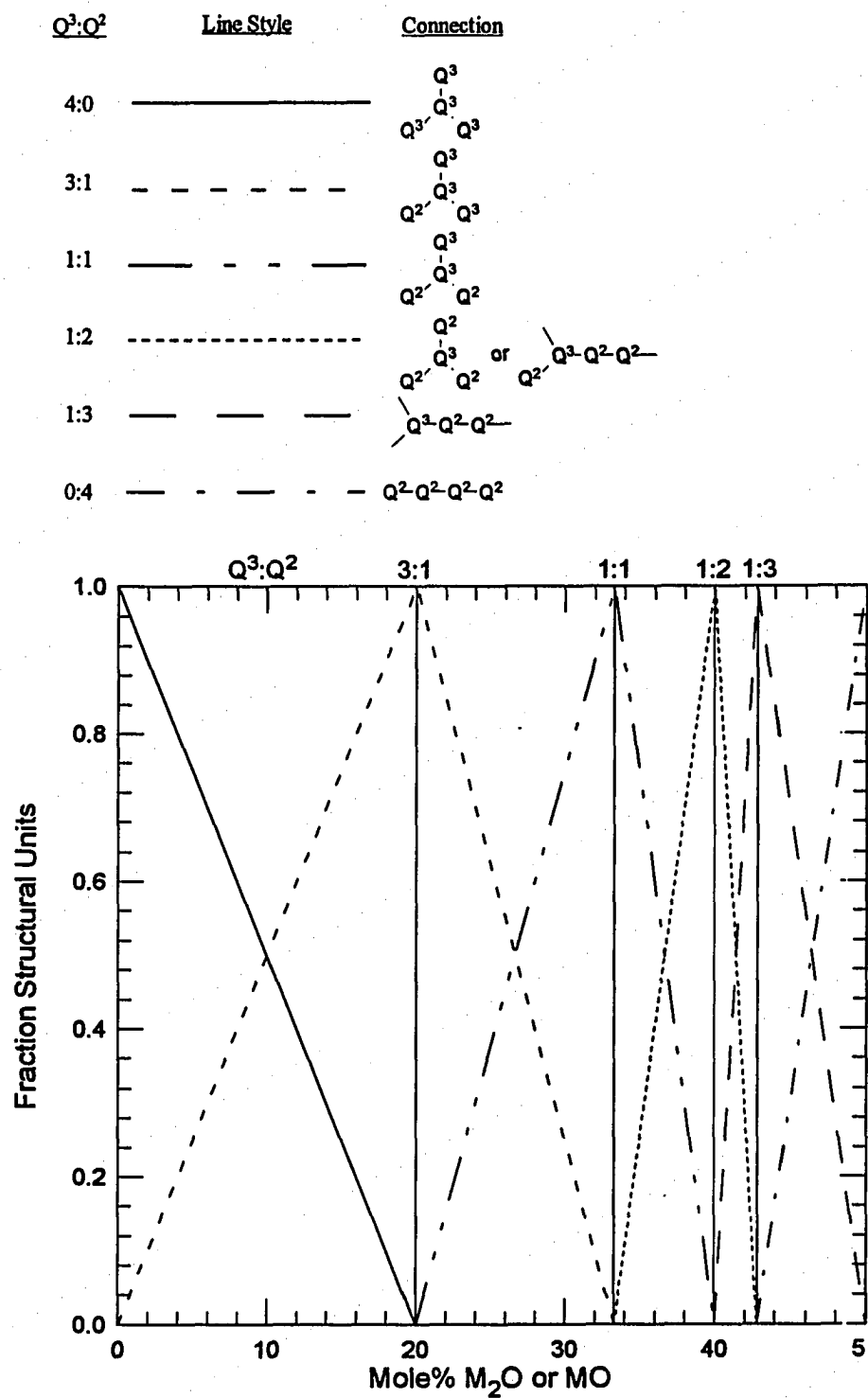


Figure 2.5 General model of structural transition in the ultra-phosphate region.

2.1.4 Ultra-Phosphate Crystals

From the observations outlined in Section 2.1.3, Van Wazer [21] derived a general structure formula for all phosphates:

$$M_{nR}P_nO_{n(5+R)/2} \quad (2.11)$$

where $R=M_2O/P_2O_5$ and n is an integer. To form crystalline compounds, the subscripts nR , n and $n(5+R)/2$ must all be whole numbers. When $R<1$, Equation 2.11 describes ultra-phosphate crystals. Following the constraints of Equation 2.11 two different families of ultra-phosphate crystals are hypothesized. One family consists of repeating units of rings directly attached to each other forming long chains of interconnected rings. The other family contains repeating units of rings alternating with chains forming chain-like structures. All known ultra-phosphate crystals consist of sheets of interconnected rings.

The structures of ultra-phosphate crystals have been refined for the compositions $2CaO \cdot 3P_2O_5$ [22-26], $MgO \cdot 2P_2O_5$ [23, 24], $ZnO \cdot 2P_2O_5$ [25], and $CaO \cdot 2P_2O_5$ [26, 27]. The $MgO \cdot 2P_2O_5$ and $ZnO \cdot 2P_2O_5$ crystal structures are isomorphous and are characterized by layers of sixteen-membered rings of PO_4 tetrahedra interconnected with four-membered PO_4 rings, as shown in Figure 2.6. The structure of $Ca_2P_4O_{11}$ is characterized by corrugated sheets of linked rings of eight and twelve PO_4 tetrahedra and the structure of $Ca_2P_6O_{17}$ is characterized by corrugated sheets of linked ring of fourteen PO_4 tetrahedra. It is interesting to note the similarity in the structures of these compounds, all having rings connected together to form sheet structures, not branching structures.

Table 2.2 shows that as the electronegativity of the countercation increases, both $P-O_t$ and $P-O_b$ bonds lengthen. All of the ultra-phosphate crystals have longer terminal oxygens on Q^3 units and shorter $P-O$ Q^3 bond lengths than in any of the polymorphs of $c-P_4O_{10}$. Therefore, as in the O form of $c-P_4O_{10}$, π -bonding is not localized on the $P-O_t$ in ultra-phosphate crystals. Also, the $P-O$ BO's on Q^3 units bridging to Q^2 units are shorter than the

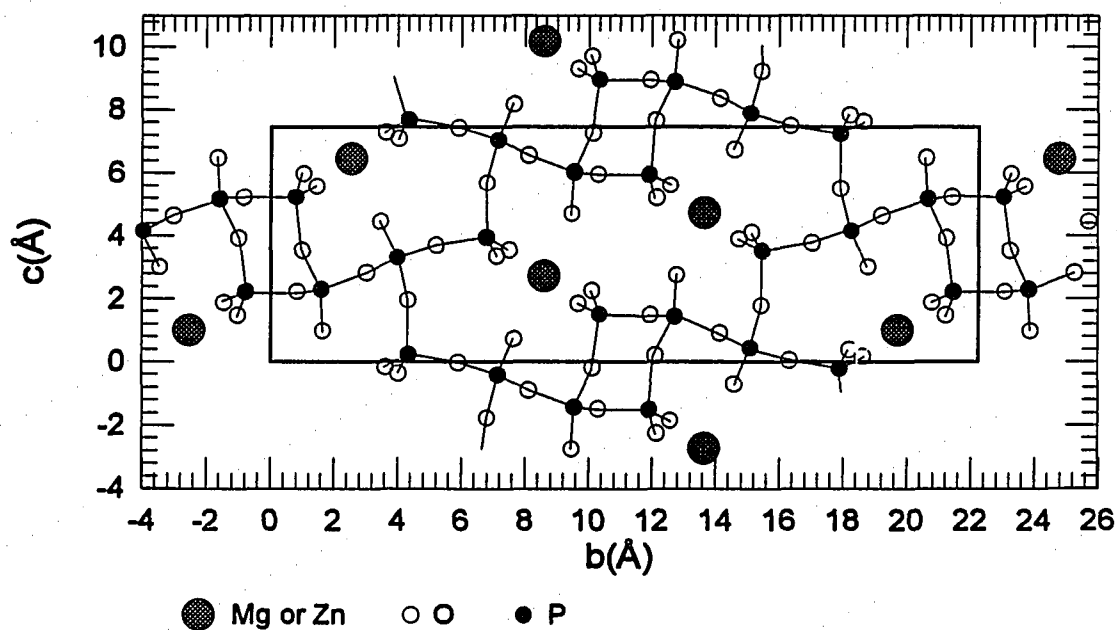


Figure 2.6 A projection of the crystal structure of $\text{ZnP}_4\text{O}_{11}$ onto the b, c axis plane. The structures of $\text{ZnP}_4\text{O}_{11}$ and $\text{MgP}_4\text{O}_{11}$ are isomorphous [15].

Table 2.2 The bond lengths in Mg, Zn and Ca ultra-phosphate crystals.

Composition	$\text{P}(\text{Q}^3)\text{-O}_t$ (Å)	$\text{P}(\text{Q}^3)\text{-O}_b$ (Å)	$\text{P}(\text{Q}^2)\text{-O}_t$ (Å)	$\text{P}(\text{Q}^2)\text{-O}_b$ (Å)	Ref.
P_2O_5	1.40	1.65			[17]
$\text{MgO} \cdot 2 \text{P}_2\text{O}_5$	1.450	1.564	1.464	1.624	[15]
$\text{ZnO} \cdot 2 \text{P}_2\text{O}_5$	1.450	1.561	1.460	1.620	[15]
$\text{CaO} \cdot 2 \text{P}_2\text{O}_5$	1.442	1.566	1.460	1.618	[15]
$2\text{CaO} \cdot 3\text{P}_2\text{O}_5$	1.457	1.561	1.451	1.618	[15]

P-O bridging between Q^3 units, indicating more of the π -bonding is localized on P-O bonds bridging from Q^3 to Q^2 units. The P-O_t bond lengths on Q^2 units are longer than those on Q^3 units at 33 mole% modifier, but are shorter at 40 mole% modifier. This indicates the gradual conversion of P=O type NBO's on Q^3 units to P-OM⁺ type NBO's as on Q^2 units. Also, there are non-equivalent sites for Q^3 and Q^2 units, as can be seen by the splitting of peaks in the IR spectra of these compounds [15].

2.1.5 Metaphosphate Crystals

As mentioned in Section 2.1.2, hydrolysis of ultra-phosphate materials occurs at branching points. Therefore, as the number of branching points decreases, durabilities increase [4]. Hence, metaphosphate crystals, which contain no branching points, have been studied extensively.

Metaphosphate crystals are built from Q^2 tetrahedra arranged in chains, and in three-, four-, or six-membered rings. Table 2.3 shows the bond lengths and P-O-P bond angles of several chain and cyclic metaphosphates. The average P-O_t bond length is longer, P-O-P bond angle is larger, and P-O_b bond length shorter in metaphosphate crystals than in the H and T forms of $c\text{-P}_4\text{O}_{10}$ and the ultra-phosphate crystals, suggesting a large amount of π -bond delocalization. Note there has been no differentiation between the terminal oxygens in the metaphosphate crystals. Both are P-O⁻ type terminal oxygens. The transformation of the P=O to P-O⁻ type NBO is due to the large amount of π -bond delocalization.

On average, bond lengths do not change between the chain and ring metaphosphates indicating the π -bond character remains the same. However, the P-O-P bond angle between tetrahedra and O-P-O angle within tetrahedra do change. Three and six-membered rings require smaller angles between tetrahedra and terminal oxygens as compared to long chain, or four-membered ring metaphosphates. Substituting divalent for monovalent cations increases the P-O_t, decreases P-O_b bond lengths and increases the P-O-P bond angle between tetrahedra. The larger electronegativity of divalent cations pulls electron density from the terminal oxygens decreasing the covalent character of the P-O_t, shortening the P-O_t bond

Table 2.3 The bond lengths and bond angles in long chain and cyclic metaphosphate crystals.

Structure	Composition	Z/r	P-O _t (Å)	P-O _b (Å)	P-O-P (°)	O _t -P-O _t (°)	O _t -P-O _b (°)	O _b -P-O _b (°)	Ref.
Chain	α -(NaPO ₃) _∞	1.03	1.479	1.610	130.5	117.6	109.6	99.2	[28]
	(KPO ₃) _∞	0.752	1.47	1.60	131	118	110	98	[29]
	(RbPO ₃) _∞	0.681	1.488	1.616	128.97	120.05	107.97	103.08	[30]
	(AgPO ₃) _∞	0.793	1.45	1.59	130	118	109	102	[31]
	[Mg ₂ (PO ₃) ₄] _∞	3.03	1.48	1.59	136.5				[32]
	[Ca ₂ (PO ₃) ₄] _∞	2.02	1.483	1.582	138.8	117	109.4	101.4	[32]
	[Zn ₂ (PO ₃) ₄] _∞	2.702	1.488	1.591	135.5	118.8	108.6	102.53	[33]
	[Pb ₂ (PO ₃) ₄] _∞	1.66	1.48	1.56	142	116	107	109	[34]
	Average	-	1.477	1.592	134.15	117.92	108.79	102.17	
Ring (3)	Na ₃ P ₃ O ₉	-	1.484	1.614	126.9	120.2	108.4	101.3	[35]
	Na ₃ P ₃ O ₉ ·H ₂ O	-	1.48	1.62	124.1	121.0	108.1	102.0	[32]
	Ag ₃ P ₃ O ₉ ·H ₂ O	-	1.488	1.612	127.1	119.7	108.7	100.8	[36]
	LiK ₂ P ₃ O ₉ ·H ₂ O	-	1.480	1.611	128.9	121.2	108.3	100.3	[37]
	Ba ₂ Zn(P ₃ O ₉) ₂ ·10H ₂ O	-	1.483	1.620	126.6	119.2	108.3	103.1	[38]
	Average	-	1.483	1.615	126.72	120.26	108.36	101.5	
Ring (4) monoclinic triclinic	Na ₂ H ₂ P ₄ O ₁₂	-	1.49	1.60	132.9	119.3	107.6	106.1	[39]
	Na ₄ P ₄ O ₁₂ ·4H ₂ O	-	1.486	1.609	128.9	121	108.5	99.9	[40]
	Na ₄ P ₄ O ₁₂ ·4H ₂ O	-	1.471	1.601	133.8	120.6	108.3	101.2	[41]
	(NH ₄) ₄ P ₄ O ₁₂	-	1.49	1.62	130.6	121.8	108.0	104.5	[42]
	Tl ₄ P ₄ O ₁₂	0.680	1.48	1.62	133.3	120.0	108.6	100.5	[43]
	Cu ₂ P ₄ O ₁₂	2.77	1.486	1.590	137	117.6	108.8	102.8	[44]
	Average	-	1.483	1.607	132.75	120.05	108.3	102.5	
Ring (6)	Na ₆ P ₆ O ₁₈ ·6H ₂ O	-	1.49	1.61	128.4	118.8	109.8	98.8	[45]

length and decreasing the $O_t\text{-P-O}_t$ bond angle. The smaller $O_t\text{-P-O}_t$ bond angle allows the P-O-P bond angle to become larger decreasing the spatial extent of the P d_π -orbitals increasing $d_\pi\text{-p}_\pi$ back bonding and decreasing the length of the P-O bonds.

2.1.6 Poly-, Pyro- and Orthophosphate Crystals

Crystalline phosphate compounds containing a mixture of Q^1 and Q^2 tetrahedral units are polyphosphates. Polyphosphates consist of chains of Q^2 units terminated by Q^1 units. The length of such chains is, therefore, controlled by the Q^1/Q^2 ratio. Sodium tripolyphosphate, $Na_5P_3O_{10}$, is an example of a polyphosphate compound. $Na_5P_3O_{10}$ has a $P\text{-O}_t$ bond length of 1.50Å, $P(Q^2)\text{-O}_b$ bond length of 1.61Å, $P(Q^1)\text{-O}_b$ of 1.68Å, P-O-P bond angle of 121° , $O_b\text{-P-O}_b$ bond angle of 98° and $O_b\text{-P-O}_t$ bond angle of 106° . The limiting polyphosphate composition, no Q^2 fraction, is the pyrophosphate composition.

Crystalline compounds of composition $R^{n+}_{2n}(PO_{3+\frac{1}{2}n})_{2n}$ are pyrophosphates. Such crystals are composed solely of Q^1 units forming dimers. Pyrophosphates have an average P- O_b bond length of 1.540Å and P-O-P bond angle of 149° . Sodium pyrophosphate, $Na_4P_2O_7 \cdot 10H_2O$, has a P-O-P bond angle of 130° , P- O_b bond length of 1.612Å, and P- O_t bond length of 1.523Å.

Q^1 units in both polyphosphate and pyrophosphate glasses have longer P- O_t and shorter P- O_b bond lengths than Q^2 units in chain metaphosphates. Therefore, Q^1 units have a larger degree of π -bond delocalization than do Q^2 units (Table 2.4).

The limiting phosphate composition is the orthophosphate composition. At this composition, the PO_3 tetrahedra contain four NBO's and no BO's. Any addition of modifier to this composition would not result in any further depolymerization of the phosphate network, only in inclusion of unreacted modifier. One example of an orthophosphate is $Na_3PO_4 \cdot (NaOH)_{0.25} \cdot 12H_2O$. All four P- O_t bond lengths are 1.526Å, indicating π -bonding is distributed equally over the entire PO_3 tetrahedra.

Table 2.4 The average number of π bonds per σ bond for BO and BO's for the different PO_4 units.

PO_4 unit	BO	NBO
	π bonds per σ bond	π bonds per σ bond
Branching	0.1-0.2	1.4-1.9
Middle	0.1-0.3	0.7-0.8
End	0.3-0.4	0.5-0.6
Ortho-		0.3-0.4

2.1.7 Summary

With the addition of ionic modifiers to $\text{c-P}_4\text{O}_{10}$, the fraction and types of structural units created are consistent with the ionic model of Van Wazer's reorganization theory and Stachel's model of structural transition in the ultra-phosphate region. Moreover, in the ultra-phosphate region, crystals are characterized by sheets of interconnected rings of PO_4 tetrahedra.

Generally, as the number of NBO's per phosphate tetrahedra increases, P-O_i bond lengths become longer, P-O_b bond lengths become shorter and P-O-P bond angles are larger. Also, the fraction of Q^2 units increases in the ultra-phosphate region, the nature of π -bonding on Q^3 units changes dramatically. On all structural units stabilizing resonance structures are created where there are no discernible P=O present on PO_4 tetrahedra for meta- pyro- or orthophosphate compositions.

2.2 The Structures and Properties of Phosphate Glasses

2.2.1 Vitreous P_2O_5

The T_g [46], expansion coefficient [47,48], density [49- 51], infrared spectra [52, 53], ^{31}P MAS-NMR spectra [69], elevated temperature Raman spectrum [54], XPS [56], and neutron diffraction study [55] have been reported for $\text{v-P}_2\text{O}_5$. The high temperature Raman spectra of pure vitreous P_2O_5 ($\text{v-P}_2\text{O}_5$) is not similar to the bipyramidal molecule PF_5 , but to

the four-coordinated molecule POF_3 [54]. The Raman spectra of both $\nu\text{-P}_2\text{O}_5$ and POF_3 have a symmetric stretching mode at $\approx 1400\text{ cm}^{-1}$. In the POF_3 molecule, this stretch is attributed to a $\text{P}=\text{O}$ suggesting the existence of a $\text{P}=\text{O}$ in $\nu\text{-P}_2\text{O}_5$. A neutron diffraction study of $\nu\text{-P}_2\text{O}_5$ shows [55] that the IRO in $\nu\text{-P}_2\text{O}_5$ closely resembles that of GeO_2 and SiO_2 , consisting of a 3-D network of tetrahedral PO_4 units, while the network topology more resembles the three-connected As_2O_3 . XPS [56], ^{31}P MAS-NMR spectra [69], and MIR spectra also suggest that $\nu\text{-P}_2\text{O}_5$ is built from phosphate tetrahedra, each having three bridging oxygens and one NBO. Two P-O bond lengths, $1.426 \pm 0.004\text{ \AA}$ and $1.576 \pm 0.002\text{ \AA}$, have been reported for $\nu\text{-P}_2\text{O}_5$ [55]. These distances are similar to the P-O_i and P-O_b bond lengths found in the O form of $\text{c-P}_2\text{O}_5$. The similarity of these bond lengths indicates some π -bond delocalization in $\nu\text{-P}_2\text{O}_5$.

The density of $\nu\text{-P}_2\text{O}_5$ ($\sim 0.7\%\text{H}_2\text{O}$) is 2.52 g/cc [57], a value intermediate to the densities of the H and O forms of $\text{c-P}_2\text{O}_5$. Because the density of $\nu\text{-P}_2\text{O}_5$ is higher than the molecular H form of $\text{c-P}_2\text{O}_5$ and because of the requirements of 3-D bonding for glass formers, it is likely that $\nu\text{-P}_2\text{O}_5$ is formed from the stable T form of $\text{c-P}_2\text{O}_5$, maintaining a similar 3-D branching structure.

The first value for the T_g of $\nu\text{-P}_2\text{O}_5$ found in literature [58] is 252°C and was based on the Arrhenius law extrapolation of the viscosity data reported by Cormia et al. [59]. Martin and Angell [46] were the first to experimentally determine the value of T_g for P_2O_5 . The DSC-determined T_g of P_2O_5 was found to be $317 \pm 2^\circ\text{C}$ at a heating rate of $\approx 10\text{ K/min}$. Because their experimental value was in good agreement with the extrapolated liquid viscosity data [58], Martin and Angell suggested P_2O_5 behaves in a strictly Arrhenius fashion with respect to the temperature dependence of viscosity. Figure 2.7 shows the $\nu\text{-P}_2\text{O}_5$ viscosity data as compared with other representative liquids. Those liquids with three dimensionally extensive covalent bonding scheme, such as SiO_2 and GeO_2 , show a nearly Arrhenius viscosity dependence on temperature, such liquids have been termed 'strong' liquids [60]. As covalent bridges are replaced with ionic bonds, configurational degeneracy increases and the temperature dependence of the viscosity becomes increasingly non-Arrhenius, such behavior is

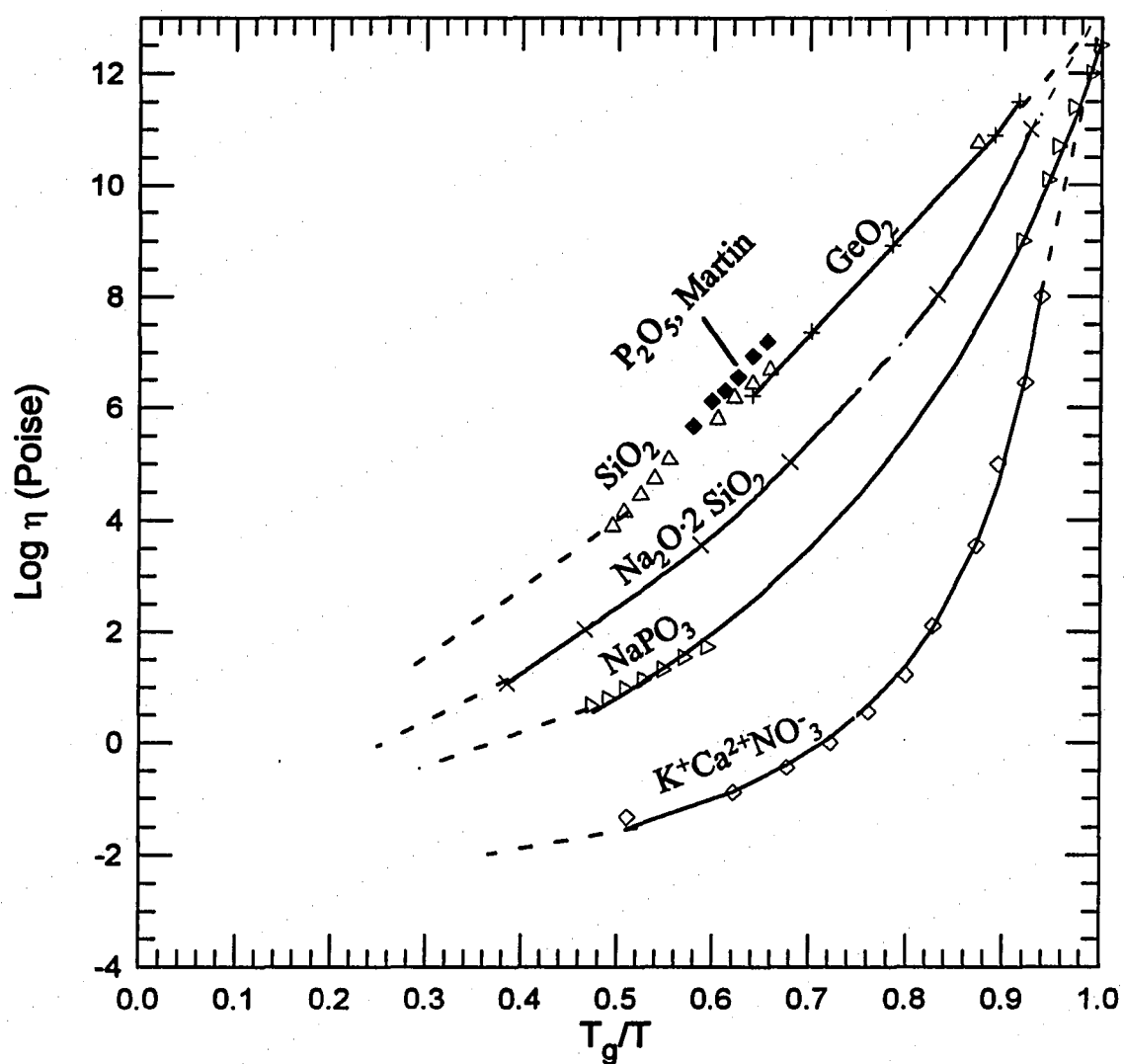


Figure 2.7 A reduced T_g plot of the glass forming liquids P_2O_5 , SiO_2 , GeO_2 , a sodium disilicate liquid, and sodium metaphosphate

often modeled using the Vogel-Tannen-Fulcher equation [147]. Silicates, germanates, and phosphates modified with alkali or alkaline earth oxides are examples of such 'intermediate' liquids. When there exist no covalent bonding scheme, as in the ionic salt $\text{KNO}_3 + \text{Ca}(\text{NO}_3)_2$, the liquid is 'fragile' showing a strong dependence of the viscosity on temperature. As Table 2.5 shows, the strength of glass forming liquids can be roughly determined by T_g and the ratio $C_p(\text{liq.})/C_p(\text{glass})$.

Table 2.5 The glass transition temperatures and $C_p(l)/C_p(s)$ ratios for several 'strong', 'intermediate', and 'fragile' glass-forming liquids.

Liquid	T_g (K)	$C_p(l)/C_p(s)$	Classification
P_2O_5	537.4	1.2	strong
SiO_2	1446	1.0	strong
GeO_2	818	1.10	strong
$\text{Na}_2\text{O} \cdot 2\text{SiO}_2$	713	1.18	intermediate
$\text{Na}_2\text{O} \cdot \text{P}_2\text{O}_5$	555	1.40	intermediate
$\text{K}^+\text{Bi}^{3+}\text{Cl}^-$ (K:Bi = 1:2)	332	1.55	fragile
$\text{K}^+\text{Ca}^{2+}\text{NO}_3^-$ (K:Ca = 3:2)	306	1.50	fragile

The Adams-Gibbs theory of transport processes in glass-forming liquids is given as

$$\eta = \eta_0 \exp\left(\frac{C}{S_c}\right) \quad (2.12)$$

where S_c is the configurational entropy content of the liquid and C is a constant [8]. Differences between the liquid heat capacity, $C_p(l)$, and the solid heat capacity, $C_p(s)$, are the result of a temperature dependence of S_c . Liquids like SiO_2 and GeO_2 , where the self-reinforcing, covalent network bonding opposes changes in short and intermediate range order with increasing temperature have limited configuration degeneracy. The amount of configurational degeneracy is proportional to the amount of energy available to activate the

translational and rotational degrees of freedom. Therefore, 'strong' liquids have small $C_p(l)/C_p(s)$ ratios, as shown in Table 2.5. As bonding becomes more non-directional with the introduction of ionic bonds, the number of possible particle arrangements increases for a given energy input and the $C_p(l)/C_p(s)$ ratio increases. T_g is also dependent on the degree of covalent bonding in the network. In this way, T_g generally decreases on going from a strong to a fragile liquid.

While Figure 2.7 shows P_2O_5 to be the archetypal Arrhenius liquid, Table 2.5 shows the T_g for $v\text{-}P_2O_5$ is much less than those for the other "strong" liquids. Additionally, the $C_p(l)/C_p(s)$ ratio for P_2O_5 (1.2) is smaller than expected for a glass that shows Arrhenius behavior of the viscosity. Given the three connected covalent network topology and the T_g of $v\text{-}P_2O_5$, the temperature dependence of the viscosity should be near that of sodium disilicate, a network liquid with a three-connected topology.

2.2.2 Ultra-Phosphate Glasses

As mentioned in Section 1.2, the volatility of the crystalline polymorphs of P_4O_{10} is a problem when preparing ultra-phosphate glasses. The H form of P_4O_{10} has a vapor pressure that becomes appreciable just above 200°C and reaches atmospheric pressure at 359°C . The molecular H form converts to the glass-forming branching O and T forms at $\sim 260^\circ\text{C}$, well into the regime where volatilization occurs. Therefore, while the O and T forms have triple points near 580°C , it is the extremely volatility of the H form that causes the P_2O_5 losses during glass preparation [3].

Water retention is also a problem in the preparation of ultra-phosphate glasses when using traditional preparation methods. Figure 2.8 shows the water contents of sodium ultra-phosphate glasses prepared in open crucibles dramatically increases below 45mole% alkali [4, 5, 62]. Furthermore, quantitative evaluation of site distributions in hydrated ultra-phosphate glasses shows the fraction of Q^2 and Q^3 tetrahedra are dependent on the $[\text{Na}+\text{H}]/[\text{P}]$. Unlike silicate glasses where water is retained as H_2O trapped within the glassy network, these results imply that water is present as terminal $-\text{OH}$ groups that depolymerize the network.

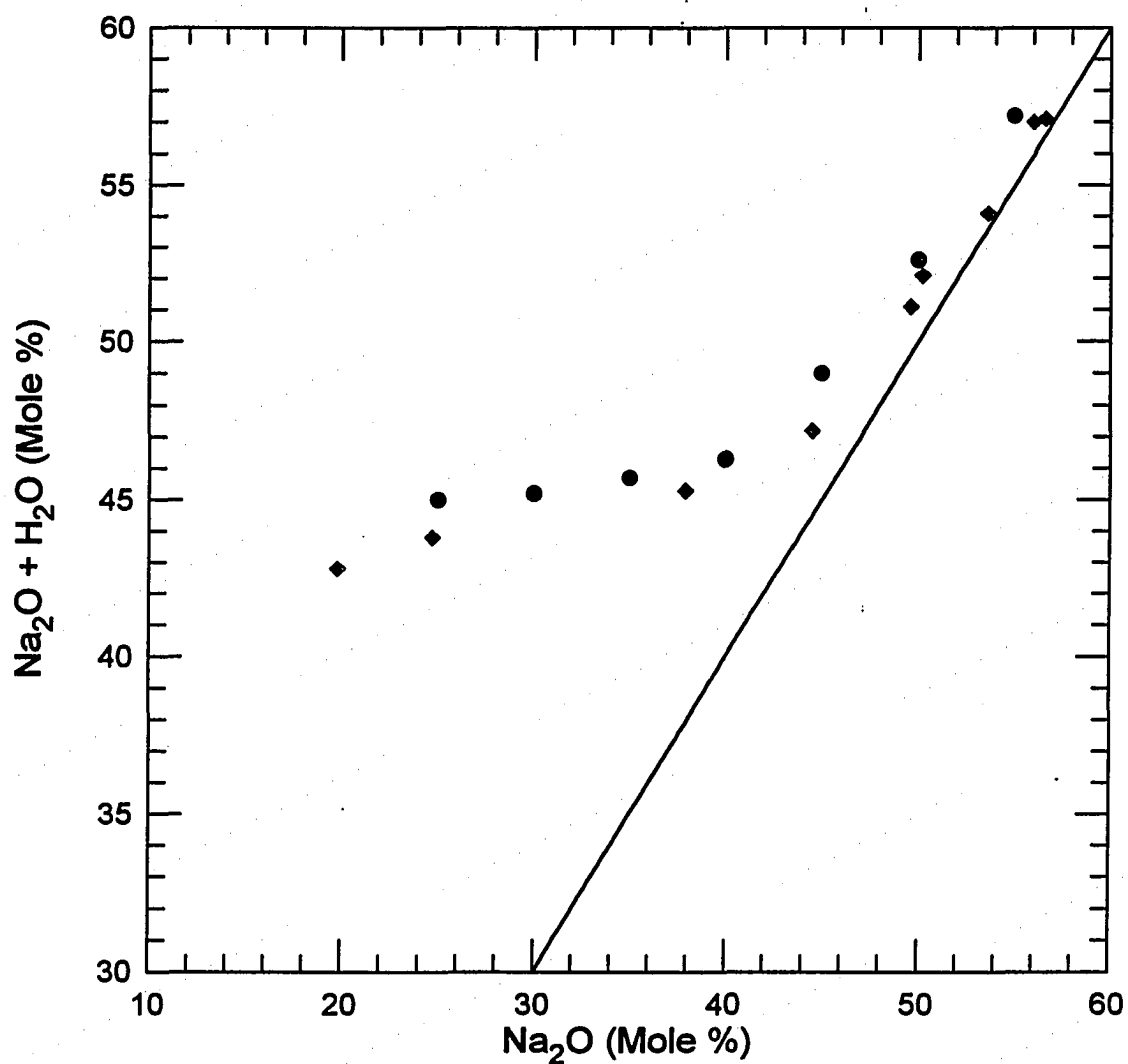


Figure 2.8 The water contents of sodium ultra-phosphate glasses increases dramatically for compositions with >55 mole% P_2O_5 . The solid line represents anhydrous glasses. Brow et al. [72] (diamonds) and Gray et al. [4] (circles).

Additionally, the high polarizing power of H^+ as compared to alkali ions causes an increase in the optical basicity of the ultra-phosphate glasses. Optical basicity is a measure of the ability of the oxygens in an oxide glass to donate electrons to a probe ion such as Pb^{2+} [61]. An increase in optical basicity causes a diminishing of the nephelauxetic effect causing changes in optical and NMR spectra. The smaller size and larger polarizability of H^+ over alkali ions also causes changes in T_g , density and most other physical properties. Therefore, great care must be taken to exclude water when preparing ultra-phosphate materials.

Chemically simple depolymerization of the phosphate network, as theorized by Van Wazer, has not been confirmed in the ultra-phosphate region. Recently, ^{31}P MASS-NMR has been used to examine the structure of phosphate glasses [62-71]. Brow et al. [62] examined hydrated sodium ultra-phosphate glasses ($42.8 \leq [H_2O + Na_2O] \leq 57.1$) and found the predicted relative site populations to be in excellent agreement with the ionic model of Van Wazer's reorganization theory. Similarly, XPS spectra [56] of sodium ultra-phosphate glasses show two separate O1s peaks, one due to terminal oxygens and the other to bridging oxygens. Quantitative analysis of the peaks show the NBO/BO ratios to be in agreement with Van Wazer. While the depolymerization of the phosphate network appears to follow a chemically simple model in the ultra-phosphate region; as in the crystalline phosphates, there are changes in oxygen bonding.

Gresch et al. [56] have examined sodium ultra-phosphate glasses, $0.15 \leq [Na_2O] \leq 0.53$, and found a strong shift of the 722 eV peak at low alkali concentrations is not only due to the formation of the first non-bridging oxygen (NBO), but also to the displacement of the $p\pi-d\pi$ bond of the $P=O$ unit towards the new non-bridging oxygen due to the increased π -bond delocalization. In a more recent XPS study of the low alkali sodium ultra-phosphate glasses, Brow [72] examined the BO- and NBO- full width at half maximum (FWHM) of the O(1s) spectra of sodium ultra-phosphate glasses finding both go through a minimum at the metaphosphate composition. These minima indicate r.o distinct $P=O$ or $P-O-Na^+$ exist on the tetrahedron of $NaPO_3$ supporting the structural hypothesis of a distributed resonance structure. Furthermore, in their ^{31}P MAS-NMR study of hydrated sodium ultra-

phosphate glasses, Brow et al. [72] show the compositional changes in Q^2 chemical shift are related to an increase in average π character of the P-O bonds as the number of NBO's increases, ^{23}Na NMR measurements are also consistent with π bond delocalization. Also, vibrational [74] spectra of $\nu\text{-P}_2\text{O}_5$ and alkali ultra-phosphate glasses show a decrease in the frequency of the P=O mode with increasing NBO content, suggesting a decrease in bond strength of NBO's due to π -bond delocalization. Therefore, as in crystalline ultra-phosphate materials, the nature of oxygen bonding on the Q^3 units is altered with changing modifier content.

Kreidl [73] stated that $\nu\text{-P}_2\text{O}_5$ is the weakest, lowest melting glass in any binary alkali phosphate system and its structure is strengthened by the addition of alkali (RO or R_2O) yielding alkali phosphates with higher melting points than pure $\nu\text{-P}_2\text{O}_5$. Martin [7] reported the glass transitions for glasses in the lithium ultra-phosphate system and found, in contrast to Kreidl's prediction, the addition of alkali causes the T_g to initially decrease, reaching a minimum near 20 mole% alkali, then increases monotonically to the metaphosphate composition. Similarly, other studies of ultra-phosphate glasses have shown T_g increases up to the metaphosphate composition, but show no minimum [105]. However, a T_g minimum must exist, for the T_g of $\nu\text{-P}_2\text{O}_5$ is higher than those reported for any of the ultra-phosphate glasses.

2.2.3 Metaphosphate Glasses

Chromatography [77], ^{31}P MAS-NMR [62], Raman [74], and IR spectroscopies [111] all indicate only Q^2 structural units exist at the metaphosphate composition in glasses modified by an ionic modifier, in agreement with the ionic model of Van Wazer's reorganization theory. Additionally, neutron diffraction [55, 75] and X-ray [76] studies of several metaphosphate glasses show only two bond lengths exist at the metaphosphate composition (Table 2.6) one corresponding to a BO and the other to an NBO. In this way, the cation charge balances both terminal oxygens and no P=O terminal oxygens exist at the metaphosphate composition.

Liquid chromatography [77] of dissolved metaphosphate glasses show they consist of primarily long chains with <10% of the Q^2 units in trimeta- or tetrametaphosphate cyclic units. Table 2.6 shows the bond lengths for the metaphosphate glasses in correspond to those of their corresponding crystalline metaphosphates, supporting a similarity between the structures of glassy and crystalline metaphosphates. Like the crystalline metaphosphates, the $P-O_t$ bond lengths are not correlated with changes in the charge density while the $P-O_b$ lengths decrease with increasing charge density.

Table 2.6 The bond lengths and bond angles in several metaphosphate glasses [76].

Metal Oxide	%P ₂ O ₅ Analyzed	P-O _t (Å)	P-O _b (Å)	P-O-P	Z/r
ZnO	48.3	1.49	1.61	-	2.70
MgO	48.7	1.50	1.61	-	3.03
CaO	48.9	1.50	1.60	-	2.02
SrO	49.2	1.50	1.62	-	1.78
BaO	50.8	1.49	1.63	-	1.49
Na ₂ O	50.0	1.50	1.64	130	1.03

Table 2.7 shows the glass transition temperatures of several metaphosphate glasses. As the electronegativity of the counter cation increases, the ability of the cation to "crosslink" between different phosphate chains increases and T_g increases. It is significant to note that crystal field stabilized transition metal cations, such as Ni^{+2} , show the maximum T_g in this series, as also seen in Table 2.7.

2.2.4 Polyphosphate Glasses

The glass forming limit of most binary phosphate systems, with the exception of systems where the modifier is an electron pair acceptor or is itself glass-forming or where extremely fast quench rates have been used, is on the phosphate-rich side of the pyrophosphate composition. A necessary requirement for glass formation is covalent

bonding, Q^0 structural units have none between tetrahedra; therefore, the quenched melts of liquids containing large numbers of Q^0 units tend to crystallize. This limit, in addition to the hygroscopicity of ultra-phosphate materials, has resulted in most of the studies of such binary phosphate glass systems to be concentrated in the polyphosphate region.

Liquid chromatography of such polyphosphate glasses reveal they consist of primarily long chains, the length of which is dependent on the $Q^2:Q^1$ ratio [77]. In addition to chains, a small percentage of cyclic units have also been found in the dissolved phosphate glasses. T_g is found to decrease with increasing modifier in the polyphosphate region [105]. The decrease in T_g with increasing modifier content is correlated with the decrease in number average length of the phosphate chains.

Table 2.7 Comparisons of glass transition temperatures for several metaphosphate glasses [105].

Glass Composition	T_g (°C)	Glass Composition	T_g (°C)
$Li_2O \cdot P_2O_5$	335	$CaO \cdot P_2O_5$	520
$Na_2O \cdot P_2O_5$	280	$SrO \cdot P_2O_5$	485
$K_2O \cdot P_2O_5$	255	$BaO \cdot P_2O_5$	470
$Rb_2O \cdot P_2O_5$	245	$NiO \cdot P_2O_5$	650
$Cs_2O \cdot P_2O_5$	235	$Al_2O_3 \cdot 3P_2O_5$	750
$MgO \cdot P_2O_5$	550		

2.2.5 Summary.

The structure of $v\text{-P}_2\text{O}_5$ is similar to that of the branching polymorph of $c\text{-P}_4\text{O}_{10}$ consisting of interconnected PO_4 tetrahedra where each tetrahedra contains three bridging oxygens and one terminal oxygen. When ionic modifiers are added to $v\text{-P}_2\text{O}_5$, the network is depolymerized as described by Van Wazer. The topology of the network changes from 3-D branching for $v\text{-P}_2\text{O}_5$ to chain dominated at the metaphosphate composition then, with increasing modifier content, the average length of these chains is decreased. As in their

crystalline analogues, oxygen bonding changes with increasing modifier content as π -bond delocalization occurs. As in the phosphate crystals, terminal oxygens lengths are shorter and bridging oxygen lengths longer with increasing modifier content. P=O terminal oxygens are only found on Q^3 units. On more depolymerized structural units, the P=O terminal oxygens has been converted to P-O⁻ terminal oxygens.

T_g initially decreases as modifier is added to $v\text{-P}_2\text{O}_5$, it then goes through a minimum near 20 mole% alkali and a maximum at the metaphosphate composition. While it is known the decrease in T_g as modifier is added to the metaphosphate composition is due to the depolymerization of the glassy network, the structural origins of the minimum in T_g near 20 mole% modifier are not understood. Also not understood are the extent and compositional dependence of π -bond delocalization.

2.3 The Glass Transition and Enthalpy Relaxation

When a liquid is subjected to a step change in temperature or pressure, properties such as thermal expansion coefficient(α), density (ρ), viscosity (η), enthalpy (H) etc. first show an instantaneous elastic-like change then relax to the equilibrium value of the property described by the new temperature. At temperatures well above glass transition, T_g , the characteristic time, τ_p , for this relaxation is very short, however, as T_g is approached τ_p becomes longer until, at $T < T_g$, τ_p is on the time scale of the experiment. Phenomenologically, predicted equilibrium values for properties are never reached, leaving the liquid in a non-equilibrium state, or, more commonly, the glassy state. Structurally, this departure from equilibrium arises because, whereas the structure can rearrange easily when $T \gg T_g$, as T_g is approached individual atoms cannot be displaced easily because the cooperative motions of the other atoms necessary for the displacement of one atom are sluggish due to the lack of sufficient thermal energy. At $T < T_g$ all atomic rearrangements are kinetically arrested; therefore, any change in measured properties below T_g is independent of structural rearrangements. Thus, the glass transition is a kinetic phenomenon.

It was Tool [78] who first recognized the need to describe the "physiochemical" state of a glass through both the actual temperature and the other temperature where the glass would be in equilibrium. Tool [78] termed this equilibrium temperature the fictive temperature, T_f . The difference between T_f and T_{actual} gives the measure of departure from equilibrium of a measured property.

Using the concept of fictive temperature to describe the physio-chemical state of a glass, heat capacity measurements through the glass transition region can be mathematically modeled. The rate of approach of a non-equilibrium glass to equilibrium, dT_f/dt , is inversely proportional to the viscosity. The temperature dependence viscosity is non-linear for most glass forming liquids, therefore, so is the rate of approach of a non-equilibrium glass to equilibrium. Several authors [79- 82] argue that the "memory" phenomenon is due to the existence of two or more relaxation mechanisms in the glass. Simply put, the memory effect is where a glass initially in a non-equilibrium state remembers this, hence, properties evolve in a fashion different than a glass where its initial structure corresponds to the equilibrium structure at that temperature [83]. Narayanaswamy [79] was the first to develop a model of structural relaxation that took into account both the non-exponential and non-linear experimental observations of the measured properties of glass. Narayanaswamy started with three assumptions that allowed him to treat the non-linearity and non-exponentiality of the glass transition simultaneously. Structural relaxation is postulated to have a spectrum of relaxation mechanisms all with identical activation energies. Glass-forming liquids were assumed to be thermorheologically simple. The shape of the response function is fixed. and the only cause of non-linearity was assumed to be the changing viscosity of glass as the structure changes.

In the manner of Tool, Narayanaswamy [79] accounted for the dependence of the relaxation time, τ_0 , on both the temperature of the material, T , and the temperature which describes the physiochemical state of the glass, T_f , by taking $\tau_0 = \tau(T, T_f)$:

$$\tau_0 = A \exp \left[\frac{x\Delta H}{RT} + \frac{(1-x)\Delta H}{RT_f} \right] \quad (2.13)$$

where A is a constant, ΔH is the activation enthalpy for structural relaxation, x is an empirical parameter accounting for the non-linearity of structural relaxation, and R is the ideal gas constant. Non-exponentiality was included in the model through introducing a normalized distribution of relaxation times, $g(\tau)$, into the relaxation function $\phi(t)$ by:

$$\phi(t) = \int_0^\infty g(\tau) e^{-\left(\frac{t}{\tau}\right)} d\tau \quad (2.14)$$

Where the normalization condition exists:

$$\int_0^\infty g(\tau) d\tau = 1 \quad (2.15)$$

An empirical expression found to fit a variety of relaxations in vitreous systems is the Kaulraush-William-Watts (KWW) equation [84]:

$$\phi(t) = \exp \left[-\left(\frac{t}{\tau_0} \right)^\beta \right] \quad (2.16)$$

Where $0 \leq \beta \leq 1$ and τ_0 is the characteristic relaxation time calculated from Equation (11). Here β directly corresponds to the $g(\tau)$ in Equation 2.15 and is therefore the measure of non-exponentiality. When $\beta=1$ the T-N equation is exponential, otherwise, when $\beta \neq 1$ the equation is non-exponential.

Narayanaswamy [79] also noted that, since the function is linearized, the response to any temperature time history may be evaluated through summing the responses to a series of step functions, the method used was the Maxwell-Boltzmann superposition principle.

$$\begin{aligned} T_f(t) &= T_0 + \Delta T_1[1 - \phi(t_1)] + \Delta T_2[1 - \phi(t_2)] + \dots + \Delta T_m[1 - \phi(t_m)] \\ &= T_0 + \sum_{j=1}^m \Delta T_j[1 - \phi(t_j)] \end{aligned} \quad (2.17)$$

The superposition of T_f allows the evaluation of an isothermal relaxation in response to more than one temperature step. Moynihan et al [85] first adapted the T-N equation to account for rate heating allowing heat capacity data to be modeled. Moynihan adapted the T-N equation by assuming rate heating, or cooling, at rate q as a series of temperature jumps dT followed by isothermal holds, $dt = dT/q$, and accounted for the continuous change in temperature by replacing the summations in Equation 2.17 with integrals carried out over the actual temperature-time path starting at a temperature well above the transition region, T_0 , where the system is in equilibrium:

$$T_f(t) = T_0 + \int_{T_0}^T dT \left\{ 1 - \exp \left[- \left(\int_{T_0}^T \frac{dT'}{q\tau_0} \right)^\beta \right] \right\} \quad (2.18)$$

In order to model physical data, Equation 2.18 must be related to a property.

In general, the temperature coefficient of the fictive temperature at some temp. T' can be described as:

$$\left. \frac{dT_f}{dT} \right|_T = \frac{\left[\frac{dp}{dT} - \left(\frac{\partial p}{\partial T} \right)_g \right]_T}{\left[\left(\frac{\partial p}{\partial T} \right)_e - \left(\frac{\partial p}{\partial T} \right)_g \right]_{T_f}} \quad (2.19)$$

This term is a normalized relaxational temperature of p . For example, take enthalpy as the property and we arrive at:

$$\begin{aligned} \left. \frac{dT_f}{dT} \right|_T &= \frac{\left[\frac{dH}{dT} - \left(\frac{\partial H}{\partial T} \right)_g \right]_T}{\left[\left(\frac{\partial H}{\partial T} \right)_e - \left(\frac{\partial H}{\partial T} \right)_g \right]_{T_f}} \\ &= \frac{C_p - C_{p_g}}{C_{p_e} - C_{p_g}} = C_{p_n} \end{aligned} \quad (2.20)$$

Equation 2.20 provides a link between a physical property, in this case C_p , and the mathematical model of the response of the property with changes in T . The T-N equation contains three fitting parameters x , A and β and two constants ΔH^* and R . ΔH^* may be obtained by setting it equal to the enthalpy of activation for shear viscosity or from the slope of the plot of the logarithm of the cooling rate, q , vs. the reciprocal of the limiting T_f .

$$\frac{d \ln|q|}{d\left(\frac{1}{T_f'}\right)} \approx -\frac{\Delta h^*}{R} \quad (2.21)$$

A complete model has been developed which can be used to calculate heat capacity data by differentiating Equation 2.18 from a temperature, T_0 , above T_g to a temperature far below T_g and reheating to T_0 again. Debolt et al [86] achieved this task by integrating Equation (13) numerically over 1K temperature steps:

$$T_f = T_0 + \sum_{j=1}^m \Delta T_j \left[1 - \exp \left(- \sum_{k=j}^m \frac{\Delta T_k}{q_k \tau_{0,k}} \right)^\beta \right] \quad (2.22)$$

2.4 Melt Processing Dependence of Properties

2.4.1 Introduction

At temperatures well above the glass transition temperature ($T \gg T_g$), a glass forming liquid is assumed to rearrange to an equilibrium state in milliseconds. As the temperature of the glass forming liquid nears T_g , relaxation times increase, frustrating rearrangement of the liquid and the liquid may be in a non-equilibrium state for several seconds or even minutes. When the temperature of the glass forming liquid falls far below T_g rearrangement effectively ceases (relaxation times $> 10^6$ sec.) and a non-equilibrium glass is formed. Therefore, to modify the metastable state of a glass, bring the glass closer to or further from equilibrium, processing must occur near T_g or through T_g . A glass that is quenched very rapidly through T_g will be further from equilibrium than the same glass quenched extremely slowly through T_g . Similarly, if a glass is held at a temperature near T_g , its physiochemical state will move closer to equilibrium. Conversely, it is assumed any processing of a glass forming liquid at $T \gg T_g$, where relaxation times are extremely short, will have no effect on the physiochemical state of the glass. For example, a glass with a T_g of 200°C should be in the same metastable state whether it was melted at 600 or 900°C or held for varying times at the melt temperature, given the same thermal treatments through and near T_g and barring any chemical changes in

the glass forming liquid: volatilization loss, reaction with crucible material etc. caused by the high temperature processing. However, recent experiments have shown the metastable state of a few glass forming systems to be dependent on high temperature melt processing.

2.4.2 Examples of Melt Processing Dependence

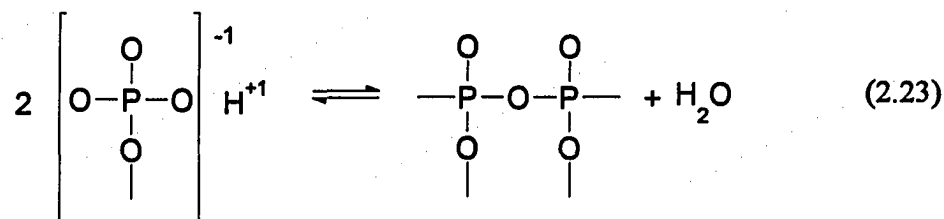
Various studies [87-93] have shown that the properties and structure of GeO_2 are dependent on melt processing. In these studies, the glass forming liquids were equilibrated at different temperatures well above T_g , then quenched at identical rates into the metastable glassy state. It was reported that glass thermoluminescence [89], Raman spectra [88], dc conductivity [90], UV absorption [91], and annealing behavior were affected by changing the initial melt temperature. The slow equilibrium rates at high temperatures for GeO_2 are attributed to diffusion of O_2 , which determines the number of defects, which in turn have an effect on glass properties and structure [92].

Studies have also shown that the properties and structure of sodium borate glasses are dependent on melt processing [93, 94]. Kamitsos and Karakassides [93] have attributed changes in the room temperature Raman spectra of a $0.7 \text{ Na}_2\text{O} + 0.3 \text{ B}_2\text{O}_3$ glass depended on the melting temperature from which the glass was rapidly quenched. Also, Huang et al. [94] have shown the room temperature density, activation for dc conductivity, and IR reflectance/absorption spectra for a sodium triborate glass all change with melt annealing time at 850°C . The changes are attributed to very slow transformation of tetrahedrally coordinated boron units to less compact triangularly coordinated boron units. Unlike GeO_2 where the anomalous property trends were dependent on oxygen diffusion, the anomalous trends in sodium triborate glasses are related to extremely slow rearrangement of structural units. Upon quenching, a 'snapshot' of the metastable state of the melt is captured by the glass.

Phosphate based glasses also show melt processing dependence of their properties. However, most changes in properties due to melt annealing are related to the water content of the glasses. The majority of stable phosphate glasses are formed from liquids which have a network or chain structure. The structure of high alkali phosphates has been shown through

chromatographic determinations of average polymeric chain lengths [77,95,96] to consist of long chains, the length of which is a strong function of the alkali oxide fraction above the metaphosphate composition. These chains are built up of PO_4^{-1} corner-sharing tetrahedra with the alkali ions decorating the edges of the chains at charge compensating non-bridging oxygens. The chain lengths have been shown to decrease from ≈ 1000 for MPO_3 (50 mol%) to 2 for $\text{M}_4\text{P}_2\text{O}_7$ (66.7 mol%) [97,98]. The length of such chains and the degree of cross-linking have a direct effect on T_g .

Cross-linking of chains in phosphate glasses only occurs at ultra-phosphate compositions, at $\text{M}_2\text{O}/\text{P}_2\text{O}_5$ ratios of greater than unity only linear chains exist. The cross-link density in oxide glasses is defined as the average number of bridging oxygen atoms in excess of two per network-forming atom [99]. As discussed in Section 2.2.2, hydroxyl groups can depolymerize the phosphate network. Therefore, the amount of residual water in the sample can also have an effect on T_g . The reversible reaction:



can be driven to the right if the phosphate melt is held at temperatures between 700 and 800°C. At higher temperatures, an azeotrope in the $\text{P}_2\text{O}_5\text{-H}_2\text{O}$ phase diagram causes the reaction to be driven to the left. A study of the effect of melting time on the dehydration of phosphate glasses shows that the evaporation of water proceeds until an equilibrium exist between the water vapor in the atmosphere and the hydroxyl groups in the liquid [100]. Therefore, preparation of ultra-phosphate glasses from anhydrous starting materials and in vacuum or in an inert atmosphere should reduce the T_g dependence on melt processing. For such preparations, however, T_g has been found to be dependent on melt processing.

Martin [7] found that for lower alkali glasses, the T_g 's of glasses made using an open crucible preparation technique fell consistently below those for glasses prepared using a sealed tube preparation scheme. The factor found to influence this difference was a difference in the quench rate. Glasses made in open crucibles (at 1000°C) were splat quenched at a cooling rate of 1000°C/sec while those made using the sealed tube technique were quenched from 1000°C at $\approx 0.1^\circ\text{C}/\text{sec}$. Martin hypothesized the structures of these phosphate liquids are highly temperature dependent. At high temperatures the available thermal energy is on the order of the free-energy difference between the two different structures available to the liquid, therefore, entropy considerations would favor structures where more configurational disorder exists; less connected structures. At lower temperatures the driving force towards a more-connected structure is larger than the available thermal energy, in this case the lower free energy, less-connected structures are preferred. Therefore, at $T \gg T_g$ all phosphate liquids share the same disordered, less-connected, IRO, it is the quench rate that determines the non-equilibrium (glassy state) IRO. A rapid quenching rate (splat quenching) allowed the high temperature, disordered IRO to be "frozen" into the glass, while the polymerization process necessary to produce a more-connected glass was kinetically arrested. However, a slow quench rate (sealed tube preparation) allowed the necessary time for polymerization to take place, creating a more connected structure. To explore this hypothesis Martin [7] proposed an experiment where a melt would be sealed in a closed ampoule and then subjected to isothermal holds for increasing periods of time. At the end of each hold the melt would be rapidly quenched to room temperature in order to freeze in the equilibrium structure of the liquid into the non-equilibrium glass, and the T_g measured.

Here, a glass that was initially cooled at 1000°C/sec was hermetically sealed inside a gold DSC sample pan and then subjected to heat treatments aimed at replicating glass formation using a slow cooling rate, 0.01°C/sec. The sample was first soaked at $T \approx T_g$ (600°C) for increasing periods of time, where T_g was measured after each hold. T_g increased ≈ 150 K after soaking 25 hrs. at 600°C. The sample was then soaked at 900°C for 12 hrs., to simulate a fast cooling rate, and T_g was measured again. T_g decreased ≈ 150 K to a value very

near the same as the "as prepared" value of 450 K. Reproducibility was tested by reheating the sample to 600°C for 48 hrs. and T_g was found to again increase by ≈150 K. Martin hypothesized these phenomena were the result of highly processing dependent IRO structures in the alkali phosphate liquids he studied; however, he did not define the structures present.

3. EXPERIMENTAL PROCEDURES

3.1 Introduction

Due to the hygroscopic nature and high vapor pressure of the H form of $c\text{-P}_4\text{O}_{10}$, as described in section 2.1.2, non-traditional preparation procedures were developed to prepare, handle, and analyze the reactive alkali ultra-phosphate glasses. Many of the procedures have been modified from procedures used to prepare chalcogenide glasses. This chapter describes the procedures used to prepare, handle and characterize anhydrous, alkali ultra-phosphate glasses.

3.2 Preparation of the Glass

3.2.1 Dry Samples Preparation Facility

Because of the hygroscopic nature of glassy and crystalline ultra- and meta-phosphates, it was necessary to batch and store all glasses in a dry box. Built from ¼" stainless steel, the dry box can be evacuated to a pressure of ~100 millitorr to check for leaks and help the removal of surface water on initial pump down. An 18" ante-chamber was attached to the dry box to allow the transfer of materials into and out of the dry box. The ante-chamber was equipped with both a roughing pump (Welch 1320) and a diffusion pump, although the diffusion pump was not used. Pressure in the antechamber and roughing line was monitored with thermocouple vacuum gauges. Nominally, items entering the dry box were evacuated within the antechamber until the pressure inside the antechamber was <100 millitorr, ~20 minutes. To prevent backstreaming of pump oil into the antechamber, a backstream preventer was placed in the roughing line.

The dry box was equipped with a VAC Atmospheres dry train which incorporated reactive copper and a molecular sieve material to getter both oxygen and water. Nitrogen was first run through the dry train then recirculated through the dry box and drytrain by a cyclone blower placed inside the dry box. The blower was equipped with an air filter to prevent fine

powers from entering the dry train and rendering the molecular sieve material useless. The drytrain was regenerated once per month. The level of moisture within the dry box was monitored by exposing the energized element of a 20 Watt lightbulb to the dry box atmosphere. It was estimated that as long as the lightbulb stays lit there existed ppm levels of both H_2O and O_2 within the dry box. Regularly, lightbulbs remained lit for several months. The amount of moisture within the dry box was also monitored by observing a small amount of crystalline $\text{c-P}_4\text{O}_{10}$ left exposed to the dry box atmosphere. When the surface of the P_4O_{10} became hard or gelled it was known a high level of moisture existed within the dry box.

Pressure was controlled in the dry box by the use of a VAC atmospheres pedalrol unit. The pressure inside of the dry box was kept higher than ambient. While handling glasses or starting materials, plastic gloves were worn over the butyl dry box gloves to prevent cross-contamination between samples and/or starting materials. A Denver Instruments electronic balance was placed within the dry box. All lab utensils were first washed then dried in a 110°C drying oven before being introduced into the dry box facility.

3.2.2 Starting Materials for Glass Compositions

Crystalline P_4O_{10} (99.99% Cerac) was first dried, as described below, then used to prepare the alkali ultra-phosphate glasses. Lithium ultra-phosphate glasses were prepared by mixing stoichiometric amounts of the dried crystalline P_4O_{10} with anhydrous, crystalline Li_2O (99.99% Cerac). Because sodium hyperoxide (Na_2O_2) is the only reagent grade sodium oxide available commercially, dried Graham's salt, $(\text{NaPO}_3)_n$, (99.99% Spectrum) was used to prepare the sodium ultra-phosphate glasses.

3.2.3 Tube Sealing Procedures

Due to the low vapor pressure of $\text{c-P}_4\text{O}_{10}$, alkali ultra-phosphate glasses were prepared in sealed, evacuated tubes. Vitreous silica tubes were used because of their high glass transition temperatures ($\sim 1500\text{K}$) in comparison to the anticipated glass melt temperatures ($< 1300\text{K}$) and because v-SiO_2 and $\text{v-P}_2\text{O}_5$ are chemically incompatible and probably mix

endothermically. As an alternative to vitreous silica tubes, high purity copper tubes are often used to prepare phosphorus compounds. These tubes are sealed mechanically, but not evacuated. This technique was examined, however, at the high temperatures required to prepare the phosphate glasses, the phosphate melt reacted with the copper tubing, yielding a ruby colored copper phosphate glass.

The v-SiO₂ tubes were evacuated and sealed using an oxygen torch. With one end of the tube already necked and sealed using the oxygen torch, the valve assembly, with the valve closed, was attached to the silica tube and the whole assembly attached to the liquid nitrogen trap. The liquid nitrogen trap (i) prevented backstreaming of pump oil into the sample tube and (ii) prevented residual water vapor within the v-SiO₂ tube from reaching the pump oil. The rouging line was then evacuated to <100 millitorr, as measured by a thermocouple vacuum gauge. The valve was then opened and the assembly evacuated to <100 millitorr. With the valve still in the open position, the tube was necked and sealed using the oxygen torch. A schematic of the tube sealing assembly and procedure is shown in Figure 3.1.

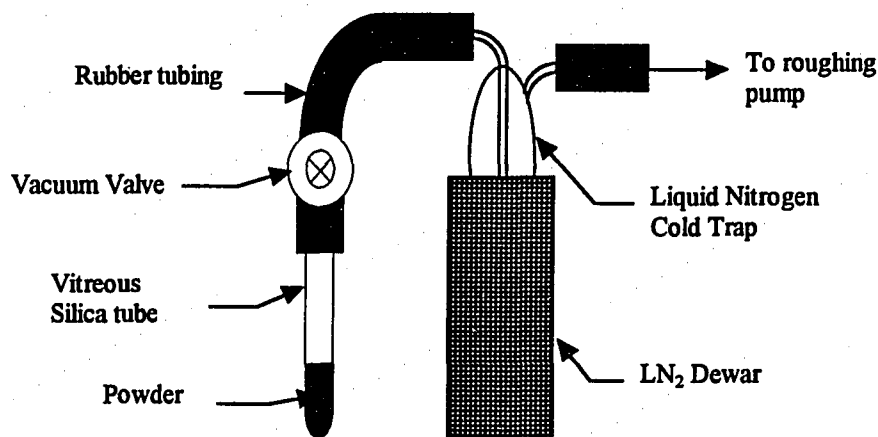


Figure 3.1 Assembly used to evacuate and seal vitreous silica tubes and dry the raw materials.

3.2.4 Drying Procedures

3.2.4.1 Crystalline P_4O_{10}

The silica tube was flame dried under vacuum using the vacuum assembly shown in Figure 3.1. Within the dry box preparation facility, approximately four grams of crystalline P_4O_{10} was loaded into the 12" long 8 mm i.d. x 10mm o.d. flame dried, vitreous silica tube. The procedures described in section 3.2.3 were used to evacuate the silica tube. While still attached to the vacuum/coldtrap assembly, ~6" of the tube was placed into a vertical tube furnace and heated to ~400°C. Glass fiber insulation was placed around the top of the furnace, thereby leaving the upper portion of the tube at room temperature. Due to the extremely low vapor pressure of c- P_4O_{10} , it vaporized in the hot section of the tube and condensed on the upper, cooler, portion of the tube. Since only the anhydrous portion of the P_4O_{10} vaporized, the hydrated material remained at the bottom of the tube, moreover, any moisture was carried out of the tube and into the cold trap. Once a majority of the material sublimed, the tube was removed from the furnace. The upper portion of the tube was then separated from the lower by necking and sealing the bottom portion to isolate the dry from the wet c- P_4O_{10} .

3.2.4.2 Crystalline $(NaPO_3)_n$

Using the procedures described in Sections 3.2.4.1 and 3.2.3, the crystalline sodium metaphosphate was placed in a flame dried silica tube which was attached to a roughing pump. The assembly was then placed in a vertical tube furnace and dried for ~10hrs. at 120°C to drive off any moisture. The dried Graham's salt was stored in the dry box preparation facility.

3.2.5 Melting and Quenching

After batching, sealing and evacuating the vitreous silica tubes, they were fired in a vertical tube furnace. A furnace with a large hot zone was chosen to ensure no thermal gradient across the length of the tube thereby preventing the P_2O_5 from subliming onto the

cooler section of the tube. Except those compositions where the melt temperature/time dependence was probed, glass were fired at 900°C for 3 hrs. The fused silica crucibles were then removed from the furnace and quickly transferred to the antechamber of the dry box, which was then evacuated. This step was necessary because the difference in thermal expansion of the silica tube and alkali phosphate glass would produce enough stress to implode the silica tube on cooling near the T_g of the glass (~350°C). By placing the hot vitreous silica ampoule in the antechamber of the dry box the alkali phosphate glass could not react with moisture in the atmosphere after the tube imploded. By calculating the time from when the tube was removed from the furnace and when it broke in the antechamber and estimating the T_g , the average quench rate was estimated as ~200°C/min..

3.2.6 Annealing

Because the silica tubes used to prepare the alkali ultra-phosphate glasses shattered during quenching, the glasses could not be annealed during preparation. Glasses were not annealed after preparation due to difficulties in annealing the glasses within the dry box. Therefore, all measurements are reported on non-annealed glass samples, unless otherwise indicated.

3.2.7 Water Content

Hydrogen contents of representative glass samples were determined using a PE series II CHNS/O Analyzer (Perkin Elmer Corporation, Norwalk, Ct.). Within a dry box, glass samples were crushed and ground in a sapphire mortar and pestle. Approximately 2.5mg of the glassy powder was placed in tin foil which was pre-weighed on a Perkin Elmer microbalance. Three foils were prepared for each glass composition. The foils were folded several times to enclose the sample then were transferred from the dry box to the hydrogen analyzer within sealed scintillation vials. Immediately prior to loading the samples into the analyzer, they were re-weighed using a Perkin Elmer microbalance.

The analyzer was operated in CHN mode where elemental analysis for carbon, hydrogen and nitrogen were determined simultaneously. In the CHN operating mode the PE 2400 Series II CHNS/O Analyzer uses a combustion method to convert the sample elements to simple gases (CO_2 , H_2O , and N_2). The sample is first oxidized in a pure oxygen environment using classical reagents. Products produced in the combustion zone include CO_2 , H_2O , and N_2 . Elements, such as halogens and sulfur, are removed by scrubbing reagents in the combustion zone. The resulting gases are homogenized and controlled to exact conditions of pressure, temperature, and volume. The homogenized gases are allowed to de-pressurize through a column where they are separated in a stepwise steady-state manner and detected as a function of their thermal conductivities. Once the weight fraction of hydrogen had been determined, the mole% H_2O could be calculated by assuming the composition of the remaining sample to be as batched.

3.3 Measurement of Physical Properties

3.3.1 Introduction

The small size of the samples and their hygroscopic nature limited the number of physical properties which could be measured. Thermal expansion measurements could not be accurately made due to the small size and irregular shape of the samples. Dissolution rate measurements were also impractical because the surface area of the samples could not be accurately determined due to their irregular shape. The samples could not be polished to a uniform shape because the glasses were not annealed and cracked when polishing was attempted within the dry box. Additionally, great care had to be taken in making the density measurements, for the small size of the glass samples required using several samples to obtain accurate density measurements. In addition to density measurements, T_g and heat capacity were also determined for the alkali ultra-phosphate glasses.

3.3.2 T_g Determinations

Glass transition temperature measurements were determined from temperature dependent heat flow traces obtained on a Perkin-Elmer DSC-4 scanning calorimeter (Perkin-Elmer Corporation, Norwalk CT.). Samples of ≈ 20 mg were hermetically sealed in aluminum sample pans within a dry box facility. Glass is in a non-equilibrium, metastable state. The magnitude of the departure from equilibrium, which describes the physio-chemical state of the glass, is determined by the quenching rate at which the glass was prepared, therefore, T_g is sensitive to the quenching rate. Consequently, the DSC head, empty reference pan and glass samples were each given thermal histories of cooling at $20^\circ\text{C}/\text{min.}$ through the glass transition regions to give each glass the same thermal history. Temperature dependent heat flow traces were collected at a heating rate of $20^\circ\text{C}/\text{min.}$ The temperature axis was calibrated for $20^\circ\text{C}/\text{min.}$ using the melting point of In (m.p. 156.61°C), Sn (m.p. 231.96°C), Pb (m.p. 327.5°C) and Zn (419.58°C) metals. The glass transition temperature reported is the onset T_g , calculated as shown in Figure 3.2.

3.3.3 Heat Capacity Measurements

Heat capacities of the alkali ultra-phosphate glasses were measured on both Perkin-Elmer DSC-4 and DSC-10 calorimeters. To calculate heat capacities from temperature dependent heat flow traces, a sample scan, baseline scan and reference (single crystal sapphire) scan were made for each sample and each temperature range [101]. The masses of the glass sample, single crystal sapphire and sample pans were determined using a Perkin-Elmer microbalance ($\pm 0.10\text{mg}$). Sample pans were sealed as described in Section 3.3.2. An empty sample pan was used on the reference side of the calorimeter for all runs. At the beginning and end of each run, isothermal holds determined the isothermal baseline. The isothermal baselines should not change since the isothermal baseline is a function of the power dissipation of the sample holder, not the samples in the pans. Temperature dependent heat flow traces were collected for the sample, empty pan, and single crystal sapphire over identical

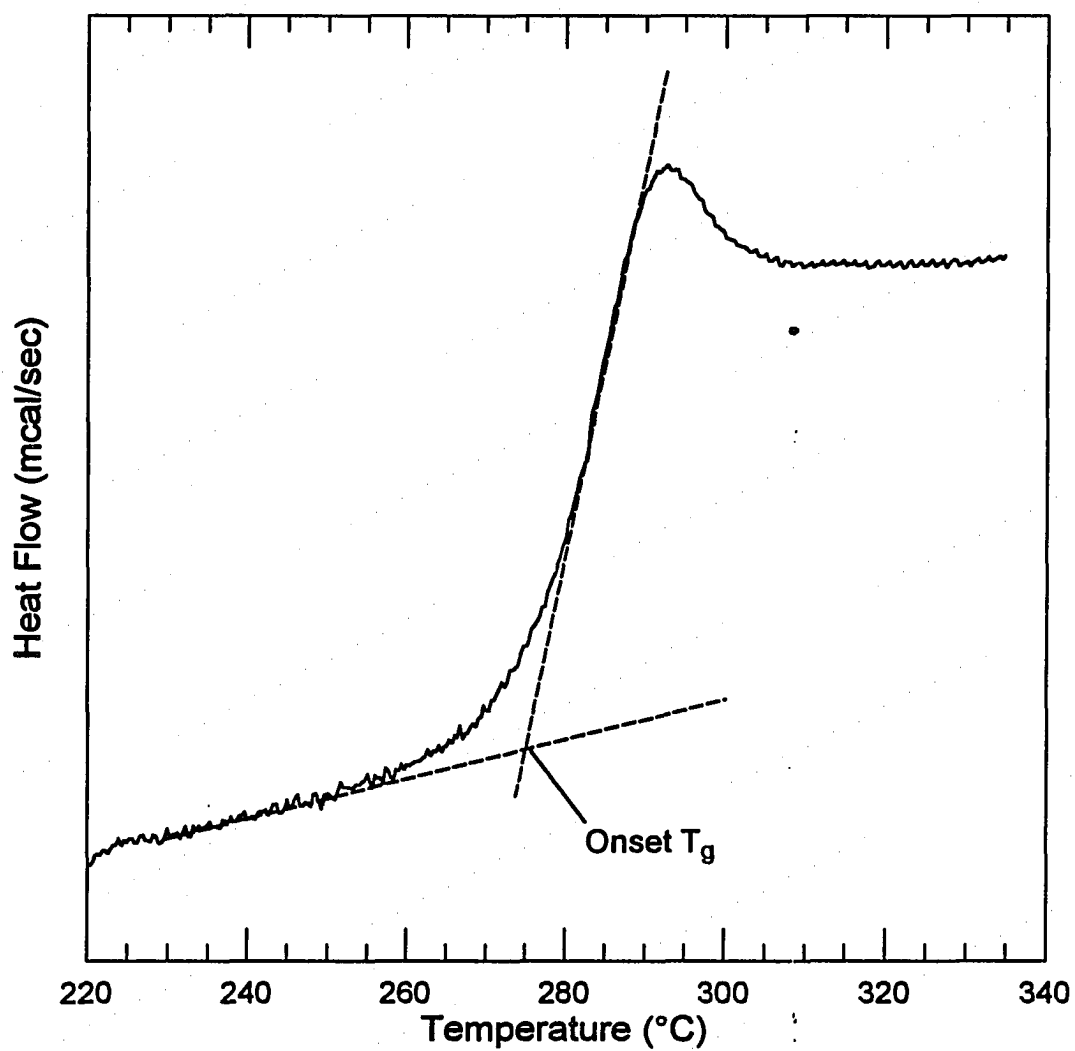


Figure 3.2 The dotted construction lines show how glass transition temperatures were calculated from temperature dependent heat flow traces.

temperature ranges at identical heating rates. The isothermal baselines for each run were then normalized and the heat capacity of the sample was calculated using:

$$C_p(\text{glass}) = C_p(\text{sapphire}) \frac{\left[\left(\frac{dH}{dt} \right)_{\text{glass}} - \left(\frac{dH}{dt} \right)_{\text{blankpan}} \right]}{\left[\left(\frac{dH}{dt} \right)_{\text{sapphire}} - \left(\frac{dH}{dt} \right)_{\text{blankpan}} \right]} \cdot \frac{m_{\text{sapphire}}}{m_{\text{glass}}} \quad (3.1)$$

where $\left(\frac{dH}{dt} \right)_x$ is the heat flow rate into the material in mcal/sec, and $C_p(\text{sapphire})$ is the heat capacity of sapphire (cal/g) [102] at that same temperature. Figure 3.3 shows how such calculations were made. Heat capacity data for sapphire was taken from reference [102].

3.3.4 Density Measurements

Density was measured using the Archimedes method in kerosene, given by:

$$\rho_{\text{glass}} = \frac{\rho_{\text{kerosene}} \cdot m_{\text{dry}}}{(m_{\text{dry}} - m_{\text{suss}})}, \quad (3.2)$$

where m_{dry} is the mass of the dry glass sample and m_{suss} is the mass of the sample suspended in kerosene. Before measuring the density of the glasses, the density of the kerosene was determined using a microsyringe. All weights were measured using a Denver Instruments electronic balance inside the dry box facility. To ensure the kerosene was anhydrous, sodium metal was placed in the kerosene and cut repeatedly until the metal remained shiny, showing no oxidation layer. Suspended weight measurements were made by hanging an aluminum basket under the electronic balance and letting it hang freely in a beaker filled with kerosene. Due to the small size of many of the glass samples, several shards of glass were used to

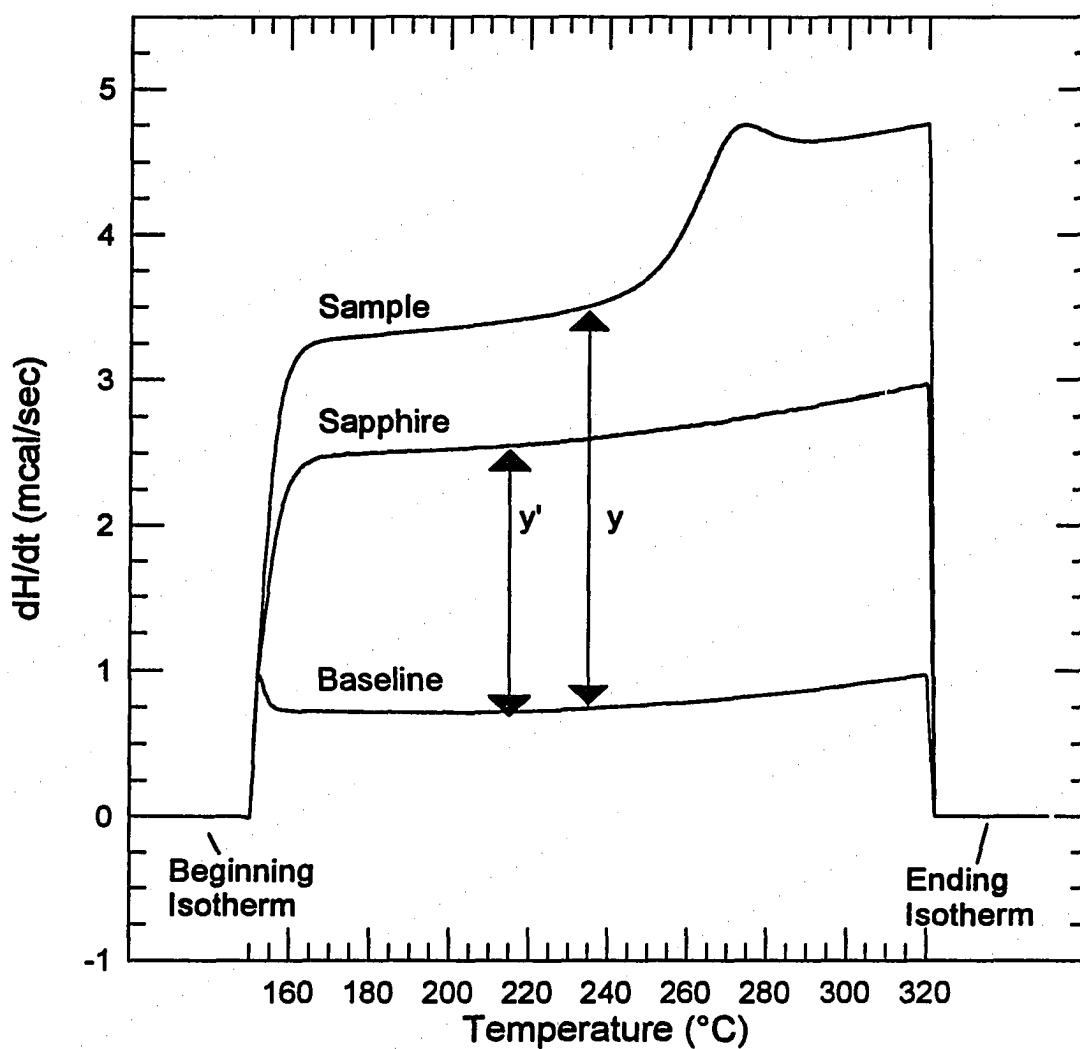


Figure 3.3 DSC scans of a glass sample, sapphire, and blank pan. The arrows y and y' indicate the how the values $\left(\frac{dH}{dt}\right)_{\text{sample-baseline}}$ and $\left(\frac{dH}{dt}\right)_{\text{sapphire-baseline}}$ were calculated, respectively.

determine dry and suspended weights. To determine the reproducibility of the density measurements, each measurement was repeated three times.

3.4 Structure Determination

3.4.1 Infrared Spectroscopy

MIR absorbance spectra were obtained on a BioRad FTS-40 FT-IR spectrometer (BioRad-Digilab, Boston MA.). Due to the high vapor pressure of alkali ultra-phosphate glasses [3], thin films could not be blown, therefore, the KBr briquette method was used [103]. Samples were prepared in the dry box using the appropriate glass ground in an impact mortar and pestle and mixed with KBr (IR grade, Wilmad Glass Co., Buena, NJ) in the ratio KBr to glass 20:1 in an agate mortar and pestle. The KBr was vacuum dried to limit water contamination of the glass samples. A sample ($\approx 200\text{mg}$) of the KBr and glass mixture was pressed in a Wilmad minipress to form a transparent KBr mull. The entire press was transferred to the spectrometer in a sealed container and placed, with the use of a dry bag, into the sample holder of the FT-IR spectrometer. Dried and decarbonated air was passed through the spectrometer bench to prevent contamination of the glassy samples. Spectra were obtained between 4400cm^{-1} and 450cm^{-1} using 64 scans at 2 cm^{-1} resolution and a background spectra of KBr was subtracted from the resulting spectra.

3.4.2 Raman Spectroscopy

Samples were kept in evacuated and sealed SiO_2 tubes during collection of all spectra. Raman spectra were collected using both a scanning double monochromator with a photoncounting photomultiplier tube and a triple spectrograph with a charge-coupled detector (CCD). Both instruments were operated at 6 cm^{-1} resolution. The samples were irradiated with 100mW of 514.5 nm light from an argon ion laser and scattered light was collected at 90° from the incident beam. Unpolarized and HH and HV polarized spectra were obtained for each glass sample.

High temperature (up to 900°C) spectra were collected on several samples. A glass boule was hermetically sealed in a silica ampoule. The ampoule was specially formed with a flat window on the bottom to reduce scattering. The spectra collected in a 90° scatter configuration. The laser beam was directed up the axes of the tube furnace into the suspended sample. Two small ports are located 180° apart halfway up the furnace for alignment and to allow Raman-scattered light to escape for collection and analysis. A K-type thermocouple is positioned next to the silica ampoule to monitor sample temperature during the heating and cooling experiments. Raman spectra were gathered at 10-20°C intervals from room temperature to 900°C. The sample was held at 900°C for two hours, then cooled with Raman spectra being gathered at 10-20°C intervals down to room temperature. To compensate for increased phonon populations at increased temperatures, Bose-Einstein populations were subtracted at each temperature.

3.4.3 ^{31}P MAS-NMR Spectroscopy

Solid state ^{31}P magic angle spinning nuclear magnetic resonance spectra were recorded at 80.8 Mhz on a Chemagnetics console interfaced to a General Electric 1280 data station. Glasses were packed into ceramic rotors in a dry bag and were never exposed to air before or during analyses. First, the t_1 relaxation time was measured for several samples and were found to be approximately six seconds for both Q^2 and Q^3 sites. Therefore, spectra were recorded with delay times ranging from 30 to 40 seconds and the signal was averaged over 64 scans. The samples were spun at 5-6 kHz in a ceramic rotor using nitrogen as the spinning gas. Spectra were obtained at two different spinning speeds for each sample in order to identify spinning sideband peaks. All chemical shifts reported are relative to 85% phosphoric acid (H_3PO_4). More positive chemical shifts correspond to less shielding.

The resonances were decomposed into Gaussian components using the General Electric software. to represent the isotropic peaks and their associated spinning sidebands and the relative total area was used as a measure of the respective site concentrations.

Chemical shift tensors were calculated using the graphical approach of Herzfeld and Berger [104], and the chemical shift asymmetry and anisotropy was calculated from these parameters.

3.5 Enthalpy Relaxation

3.5.1 Introduction

The enthalpy relaxation of glasses is characterized by fitting normalized heat capacity data using an empirical function. The function contains three fitting parameters and one calculated parameter, the activation enthalpy. The following sections describe how the heat capacity data is normalized, the activation enthalpy for each sample is calculated from T_g data, and how the three parameter model is fit to the normalized data.

3.5.2 Normalizing Heat Capacity Data

As described in Section 2.3, the mathematical model used to fit the heat capacity data actually fits normalized heat capacity data. The heat capacity data was normalized by fitting the C_p of the solid ($T < T_g$) to Equation 3.3.

$$C_p(s) = A + B \cdot T + \frac{C}{T^2} \quad (3.3)$$

The liquid heat capacity, $C_p(l)$, is fit using a first degree polynomial. The heat capacity data was then normalized using Equation 3.4.

$$C_p(n) = \frac{C_p(g) - C_p(s)}{C_p(l) - C_p(s)} \quad (3.4)$$

In this way, $C_p(s)$ was normalized to 0 and $C_p(l)$ to 1.

3.5.3 Activation Enthalpies

The activation enthalpy for structural relaxation can be calculated from Equation 3.5 [85].

$$\frac{d\left(\frac{1}{T_g}\right)}{d \ln|q|} = -\frac{R}{\Delta H} \quad (3.5)$$

In Equation 3.5, q is the heating and cooling rate, R the gas constant and ΔH is the activation enthalpy. This equation is valid for $-1.5 \leq -\log_{10}|q| \leq 2.0$. For each glass sample, temperature dependent heat flow traces were taken through the glass transition range by first cooling through the transition range at $q = 5, 10, 20$ or $40^\circ\text{C}/\text{min}$. then heating at the same rate and collecting data. The activation enthalpy is then determined by calculating the slope of a graph of $\ln|q|$ vs. $1/T_g$ for each composition. Following Equation 3.5, the slope of such a graph yields $-\Delta H/R$ from which ΔH can easily be calculated.

3.5.4 Fitting the heat capacity data

The Tool-Narayanaswamy model was fit to the normalized heat capacity data through numerically integrating Equations 3.6 and 3.7 then using a non-linear least squares fitting algorithm to adjust the fitting parameters. In order to numerically integrate the normalized heat capacity data, the data was divided into 1°K increments. In addition to the normalized heat capacity data, heating rate, cooling rate, the activation enthalpy for structural relaxation, and best guesses for the fitting parameters $\ln(A)$, x and β were input to the program. Best guesses to the fitting parameters were found by manually adjusting the fitting parameters using a routine written in Pascal. Fortran code provided by I. Hodge was adapted and transcribed onto the DEC parallel processor system (Project Vincent) at Iowa State University. A full listing of the code is supplied in the Appendix. The Levenberg-Marquardt non-linear least-squares regression algorithm was used to find the best fit of the three fitting parameters to the normalized heat capacity data.

$$T_{f,m} = T_0 + \sum_{j=1}^m \Delta T_j \left[1 - \exp \left(- \sum_{k=j}^m \frac{\Delta T_k}{q_k \tau_{0,k}} \right)^\beta \right] \quad (3.6)$$

$$\tau_{0,k} = A \exp \left[\frac{x \Delta H}{RT_k} + \frac{(1-x) \Delta H}{RT_{f,m-1}} \right] \quad (3.7)$$

4. RESULTS

4.1 Glass Formation

4.1.1 v-P₂O₅

The v-P₂O₅ prepared in this study was a clear glass. The v-P₂O₅ wetted the SiO₂ tubes and, due to the large thermal expansion difference between the two materials, the P₂O₅ glass shattered during cooling (250-350°C) leaving fractured glass shards 2-3mm long. In attempts to prepare larger v-P₂O₅ samples, the 10mm x 12mm silica tubes were replaced with 12mm x 14mm tubes. Using the larger tubes, glass shards ~1cm long could be produced, however, increased partial pressure of P₂O₅ within the tubes resulted in several explosions, therefore, tube sizes were limited to ≤ 10mm x 12mm. X-ray dot-mapping of the v-P₂O₅/silica interface revealed no interaction layer; however, hackle on the inner surface of the v-SiO₂ tube indicated a layer of v-SiO₂ adhered to the surface of the v-P₂O₅ and pulled away when the tubes shattered during quenching. X-ray dot mapping revealed that, on average, the v-SiO₂ layer on the surface of the v-P₂O₅ was < 0.2mm, therefore, glass samples used for analysis were taken from the centers of the preparation tubes.

4.1.2 The Li₂O+P₂O₅ System

Glasses in the system $x \text{ Li}_2\text{O} + (1-x) \text{ P}_2\text{O}_5$ were prepared in 0.05 mole fraction steps where $0 \leq x \leq 0.5$. All compositions were glass-forming; however, at 45 mole% Li₂O metallic lithium precipitated on the surface of the glass melt during quenching. Therefore, the 45 mole% Li₂O glass was not analyzed. The remaining glasses were clear in color showing no signs of phase separation. Glass formation of representative samples was confirmed through X-ray analysis. All lithium ultra-phosphate glasses wetted the vitreous silica tubing and, therefore, shattered during cooling (250-350°C) yielding heavily fractured glass shards 2-3mm in diameter. Glass batch yield ranged from 1 to 2 grams. As with v-P₂O₅, X-ray dot mapping revealed a layer of v-SiO₂ of < 0.2 mm on the lithium ultra-phosphate glasses. Therefore, only

glass samples from the center of the preparation tube were used for analysis. All glasses were stored in the dry box facility ($<2\text{ppm H}_2\text{O}$) to limit water contamination. Quantitative analysis of ^{31}P MAS-NMR spectra, Section 5.2.1, reveal the as-batched composition to be near the glass composition, therefore, as-batched glass compositions are reported.

4.1.3 The $\text{Na}_2\text{O}+\text{P}_2\text{O}_5$ System

Glasses in the system $x \text{Na}_2\text{O} + (1-x) \text{P}_2\text{O}_5$ were prepared in 0.05 mole fraction steps from the end member $v\text{-P}_2\text{O}_5$ to the metaphosphate composition, $v\text{-NaPO}_3$. All glasses were clear in color and glass batch yields ranged between 1 and 3 grams. Glasses with low alkali content (< 35 mole%) wetted and shattered the silica tube during quenching ($250\text{-}350^\circ\text{C}$) yielding heavily fractured glass shards 2-3 mm in diameter. The remaining ultra-phosphate glasses (>35 mole% alkali) did not wet the silica glass tubing and solid cylinders 4-5 cm long and 8mm in diameter were produced. Glass formation of representative glass samples was confirmed through X-ray analysis. As with $v\text{-P}_2\text{O}_5$ and lithium ultra-phosphate glasses, X-ray dot mapping revealed a layer of $v\text{-SiO}_2$ of < 0.2 mm on the surface of the sodium ultra-phosphate glass with < 35 mole% sodium. Therefore, only glass from the center of the preparation tubes was used for analysis. All glasses were stored in the dry box facility ($<2\text{ppm H}_2\text{O}$) to limit water contamination.

The $[\text{Na}]/[\text{P}]$ ratios for several representative samples were determined using inductively coupled plasma atomic emission spectroscopy. Samples were dissolved in acid, spiked with an internal standard and analyzed by ICP-AES against NIST certified solution standards. Samples were prepared in triplicate and analyzed in triplicate to calculate 95% confidence levels. As shown in Table 4.1, batched compositions are in good agreement with analyzed glass compositions.

Table 4.1 Analyzed glass compositions of several sodium ultra-phosphate glasses.

Batched Na ₂ O (Mole%)	Oxides	Oxide Content (wt%)	95% Confidence Limits	Oxide Content (Mole%)
0	P ₂ O ₅	96.8	1.9	100.0
	Na ₂ O	<0.1	-	-
15	P ₂ O ₅	90.7	5.9	83.0
	Na ₂ O	8.1	0.6	17.0
20	P ₂ O ₅	87.0	1.9	78.4
	Na ₂ O	10.5	1.1	21.6
35	P ₂ O ₅	78.5	1.7	62.6
	Na ₂ O	20.5	2.1	37.4
40	P ₂ O ₅	75.4	1.5	58.1
	Na ₂ O	23.8	2.2	41.9
50	P ₂ O ₅	68.0	1.4	48.1
	Na ₂ O	32.1	3.0	51.9

4.2 Physical Properties of the Glasses

4.2.1 Water Content

The amount of hydroxyl in the glass samples was qualitatively determined from MIR spectroscopy. Use of the KBr briquette method to gather the MIR spectra disallowed quantitative estimates of the water content of the alkali ultra-phosphate glasses. Qualitative estimates of hydroxyl content could be made by comparing P-O-H absorptions (Table 4.2) [111] to main vibrations of the phosphate network. Figure 4.1 shows the MIR spectra of ν -P₂O₅, with the regions where absorption bands arising from P-OH groups indicated. The strongest absorptions resulting from P-OH groups in the MIR spectrum of ν -P₂O₅ (Figure 4.1) are located at 2750cm⁻¹, 1900cm⁻¹ and 1750cm⁻¹ corresponding to bands I and III, respectively. These absorbances are ~0.5% of the strongest absorbances in the MIR spectra of most ultra-phosphate glasses; therefore, < 1 mole% H₂O is a reasonable estimate of the

Table 4.2 The six regions where P-O-H groups cause absorptions in vibrational spectra [111].

Band	Wavenumbers (cm^{-1})	Origin
I	3000-2525	(P)-O-H stretching
II	2400-2000	(P)-O-H stretching
III	1900-1600	P-O-H combination modes
IV	1400-1200	(P)-O-H deformation
V	1030-820	P-O-(H) stretching
VI	540-450	P-O-(H) deformation

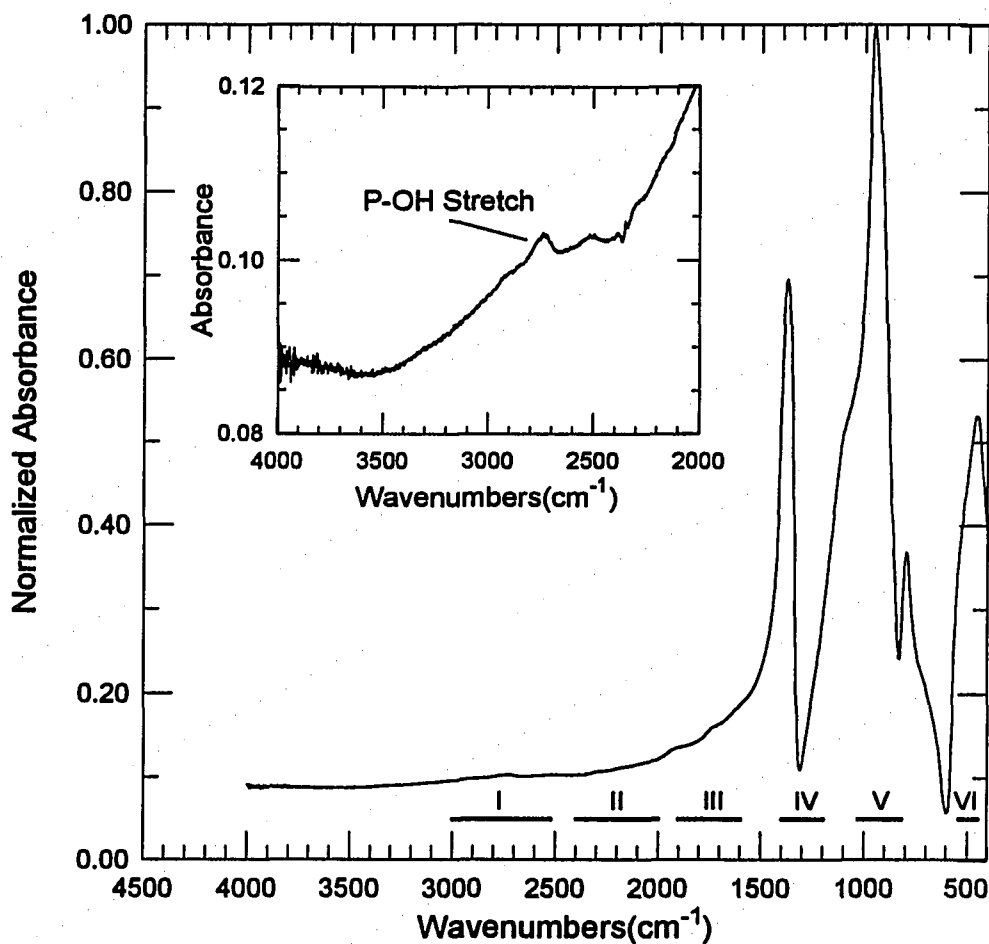


Figure 4.1 The MIR spectra of $v\text{-P}_2\text{O}_5$ with the absorbance regions arising from P-OH stretching vibrations highlighted. The inset expands the region where the strongest P-OH absorptions occur.

water content. Although less sensitive to P-O-H modes, Raman spectra also indicate no P-OH stretching vibrations.

Quantitative measurements of H₂O contents were calculated from measured hydrogen contents of selected sodium ultra-phosphate compositions. Table 4.3 shows the H₂O contents averaged over several runs for representative glass samples. The ν -P₂O₅ sample showed physical signs of water contamination; discoloration and a glutinous surface. Consequently, this sample had the largest average water content, >6 mole%. Glasses showing similar physical signs of water contamination were not used for analysis. For the samples not showing physical signs of hydration, the average water content was 0.75±0.6 mole%.

Table 4.3 The water contents of several sodium ultra-phosphate glasses.

Na ₂ O (Mol%)	Wt. (mg)	[H] (wt%)	[H ₂ O] (mol%)	Wt. (mg)	[H] (wt%)	[H ₂ O] (mol%)	Wt. (mg)	[H] (wt%)	[H ₂ O] (mol%)	<H ₂ O> (mol%)
0	5.440	0.070	4.761	3.370	0.120	7.927	-	-	-	6.344
5	3.541	0.000	0.000	2.919	0.000	0.000	4.309	0.010	0.686	0.229
15	2.392	0.010	0.646	2.918	0.000	0.000	2.636	0.000	0.000	0.215
20	1.824	0.000	0.000	1.890	0.060	3.660	2.728	0.020	1.246	1.635
35	3.147	0.010	0.567	-	-	-	-	-	-	0.567
40	2.282	0.000	0.000	3.886	0.040	2.160	-	-	-	1.080

4.2.2 Glass Transition Temperatures

4.2.2.1 ν -P₂O₅

From this study, the calorimetric T_g obtained at a q_c = q_h = 20°C/min for vacuum sublimed, anhydrous P₂O₅ melted in sealed silica ampules at 900°C for three hours was determined to be 393±4°C. Previously, the T_g for ν -P₂O₅ was reported as 262°C [58], based on an Arrhenius law extrapolation of viscosity data [59] in the temperature range 545-645°C, and 319±2°C [46] as determined calorimetrically at a scanning rate of 10°C/min for P₂O₅ melted in sealed SiO₂ ampules at 1000°C. The T_g of ν -P₂O₅ measured in this study is ~74°C higher than has previously been reported.

4.2.2.2 The $\text{Li}_2\text{O}+\text{P}_2\text{O}_5$ System

The glass transition temperatures for glasses in the $x \text{Li}_2\text{O} + (1-x) \text{P}_2\text{O}_5$ series, where $0 \leq x \leq 0.5$ are given in Table 4.4 and Figure 4.2. Onset glass transition temperatures were calculated from temperature dependent heat flow traces collected at $q_h = q_c = 20^\circ\text{C}/\text{min.}$ Repeated T_g measurements on selected samples resulted in an uncertainty of $\pm 3^\circ\text{C}$. Figure 4.2 shows T_g decreases 150°C with the addition of 20 mole% Li_2O to $v\text{-P}_2\text{O}_5$. T_g then increases $\sim 90^\circ\text{C}$ between 20 and 50 mole% Li_2O . Martin has also found the T_g of lithium ultra-phosphate glasses goes through a minimum near 20 mole% Li_2O [7]. Additionally, as will be shown in section 0, the T_g of sodium ultra-phosphate glasses go through a minimum in T_g at 20 mole% alkali. The T_g measured for lithium metaphosphate compares favorably with literature values (see, for example, ref. [105]), however, previously reported glass transition temperatures [7] for lithium ultra-phosphate glasses fall consistently below those reported in Table 4.4.

Table 4.4 The glass transition temperatures ($\pm 3^\circ\text{C}$) of lithium ultra-phosphate glasses.

Li_2O (Mole%)	T_g ($^\circ\text{C}$)	Li_2O (Mole%)	T_g ($^\circ\text{C}$)
0	392	0.3	283
0.05	297.5	0.35	300
0.1	272	0.4	308
0.15	260	0.45	-
0.2	248.5	0.5	340
0.25	263.5		

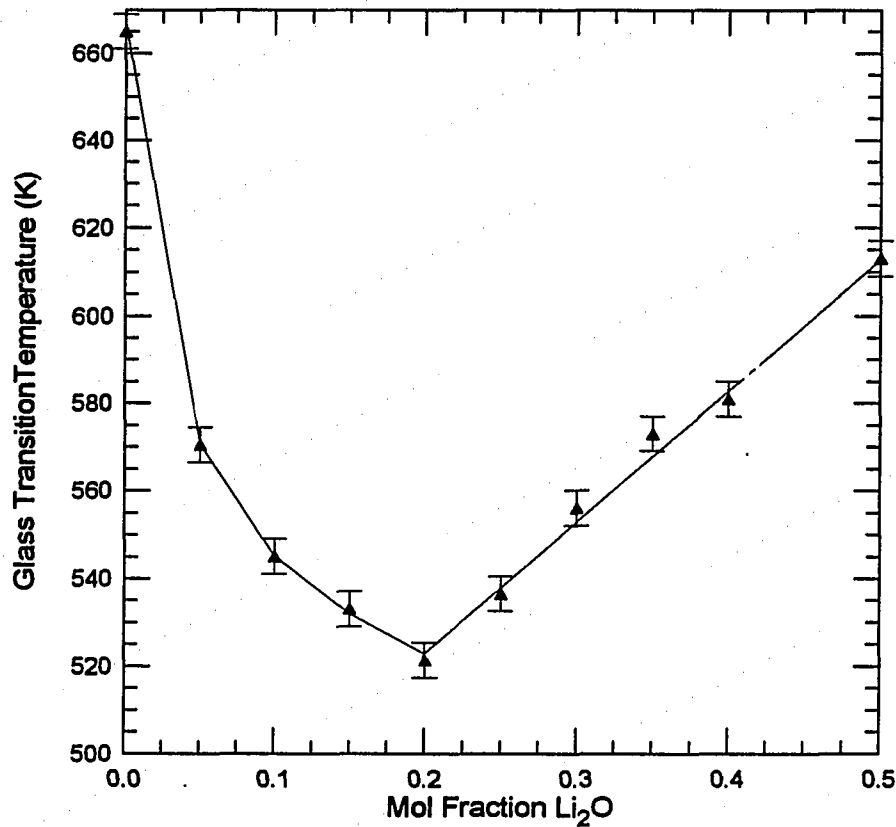


Figure 4.2 The glass transition temperatures of glasses in the system $x \text{Li}_2\text{O} + (1-x) \text{P}_2\text{O}_5$ obtained at $q_c = q_h = 20^\circ\text{C}/\text{min}$. The reproducibility of the transition temperatures is $\pm 3 \text{ K}$.

4.2.2.3 The $\text{Na}_2\text{O} + \text{P}_2\text{O}_5$ System

Table 4.5 lists and Figure 4.3 shows the calorimetric glass transition temperatures of glasses in the $x \text{Na}_2\text{O} + (1-x) \text{P}_2\text{O}_5$ system, where $0 \leq x \leq 0.5$, obtained in the present study. The temperature dependent heat flow traces used to calculate T_g were collected at $q_h = q_c = 20^\circ\text{C}/\text{min}$. Glass transition temperatures were measured at the transition onset. Repeated T_g measurements of selected glass samples gave an uncertainty of $\pm 3^\circ\text{C}$. T_g decreases 170K with the addition of 20 mole% Na_2O to $v\text{-P}_2\text{O}_5$. T_g then increases $\sim 50\text{K}$ between 20 and 45 mole% Na_2O . As Figure 4.3 shows, a similar T_g minimum is found in the lithium ultra-phosphate system, however, a T_g minimum has not previously been reported in the sodium ultra-phosphate glass system.

Table 4.5 The glass transition temperatures of sodium ultra-phosphate glasses ($\pm 3^\circ\text{C}$).

Na ₂ O (Mole%)	T _g (°C)	Na ₂ O (Mole%)	T _g (°C)
0	390	0.3	250.4
0.05	267.05	0.35	255.5
0.1	243.4	0.4	259
0.15	229	0.45	278
0.2	227	0.5 (sealed tube)	258
0.25	233.1	0.5 (open crucible)	290

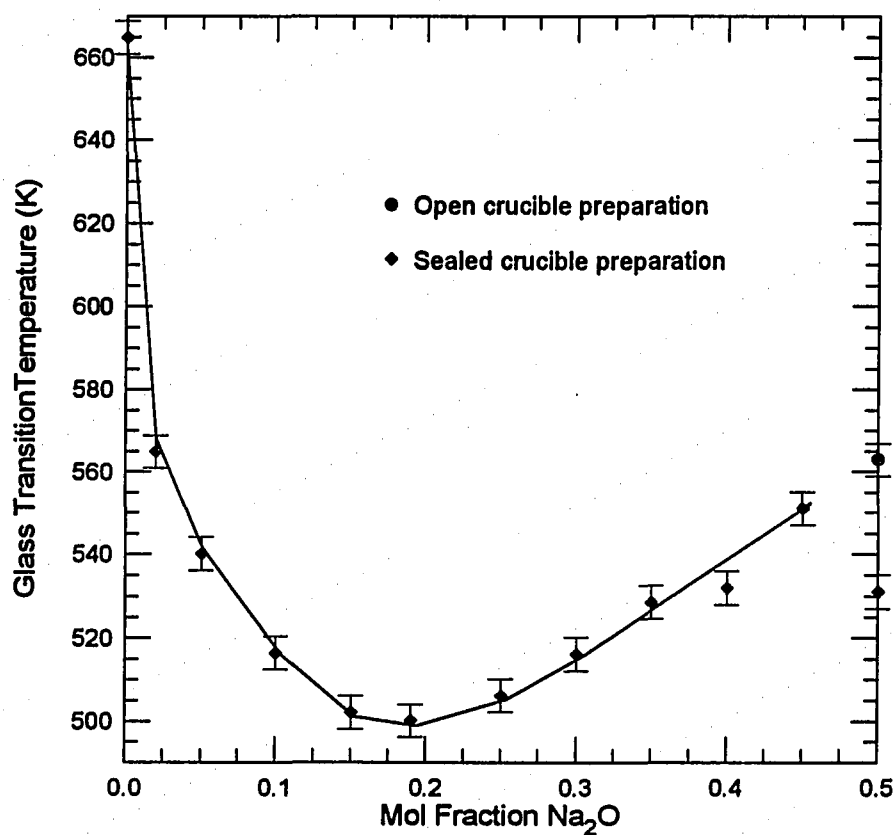


Figure 4.3 The glass transition temperatures of glasses in the system $x \text{Na}_2\text{O} + (1-x) \text{P}_2\text{O}_5$. For sodium metaphosphate, the T_g of the glass prepared in a sealed tube (\diamond) is significantly less than the T_g of the same glass prepared in an open crucible (\bullet). The reproducibility of the transition temperatures is $\pm 4\text{K}$.

The T_g of $v\text{-NaPO}_3$ was found to be dependent on the preparation method. The T_g for $v\text{-NaPO}_3$ prepared in a sealed silica tube is 30K lower than for the same glass prepared in an open silica tube. Additionally, as shown in Figure 4.4, the crystallization and melting temperatures are lower for the $v\text{-NaPO}_3$ prepared in the sealed silica tube. The T_g for sodium metaphosphate prepared in an open silica crucible is consistent with literature values (see, for example, [105]). The glass transition temperatures of hydrated sodium ultra-phosphate glasses [130] fall consistently below those given in Table 4.5.

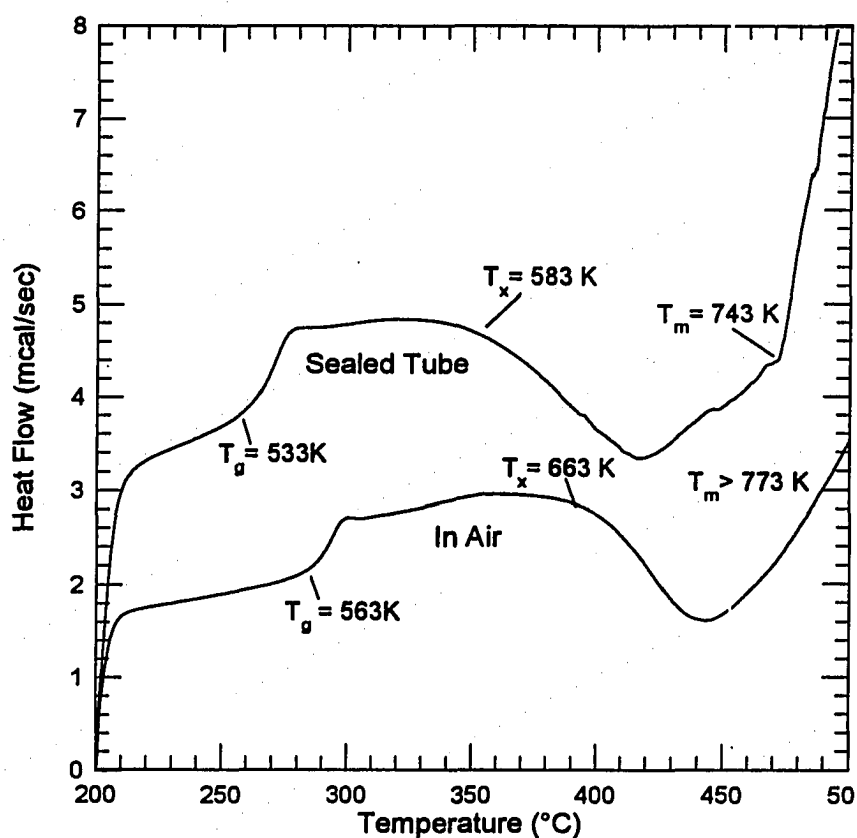


Figure 4.4 The temperature dependent heat flow traces for $v\text{-NaPO}_3$ prepared in an open silica crucible and prepared in a sealed silica tube. T_g , crystallization temperature, T_x , and melting temperature, T_m , are larger for the glass prepared in an open silica crucible.

4.2.3 Enthalpy Relaxation

4.2.3.1 Heat Capacity Measurements

Heat capacities were measured for $v\text{-P}_2\text{O}_5$ and several sodium ultra-phosphate glasses. Figure 4.5 shows a typical heat capacity curve for an ultra-phosphate glass. The dotted lines on Figure 4.5 indicate how $C_p(l)$ and $C_p(s)$ at T_g were calculated. Table 4.6 lists the heat capacity data calculated for several sodium ultra-phosphate glasses, the heat capacity curves are in the Appendix. The glassy state heat capacities increase with temperature and approach, but do not exceed, $3Rn$. The liquid state heat capacities show little dependence on temperature.

For $v\text{-P}_2\text{O}_5$, $C_p(l)/C_p(s)$ at T_g is calculated to be 1.18, less than the value of 1.27 reported by Martin [46]. At T_g , the heat capacity of $v\text{-P}_2\text{O}_5$ reaches ~90% of the classical $3Rn$ (41.7 cal/K·mole) value. Alternatively, Martin reports the heat capacity at T_g for $v\text{-P}_2\text{O}_5$ falls significantly below (~70%) the Dulong-Petit $3Rn$ value [46]. Both $\Delta C_p(T_g)$ and $C_p(l)/C_p(s)$ increase with increasing depolymerization between $v\text{-P}_2\text{O}_5$ and the metaphosphate composition. Additionally, % $3Rn$ goes through a minimum near 20 mole% Na_2O .

4.2.3.2 Activation Enthalpies

Figure 4.6 shows the DSC scans for the 45 Na_2O + 55 P_2O_5 glass collected at $q_c = q_h$ of 40, 30, 20, 10 and 5 °C/min. Similar scans were collected for several sodium ultra-phosphate glasses. The onset T_g at the different heating rates were determined as indicated by the arrows in Figure 4.6. Activation enthalpy for structural relaxation was calculated for each composition by plotting $1/T_g$ vs. $\ln |q_h|$ (shown in Figure 4.7), according to:

$$\ln |q| = \ln A - \Delta H^*/(R \cdot T_g) \quad (4.1)$$

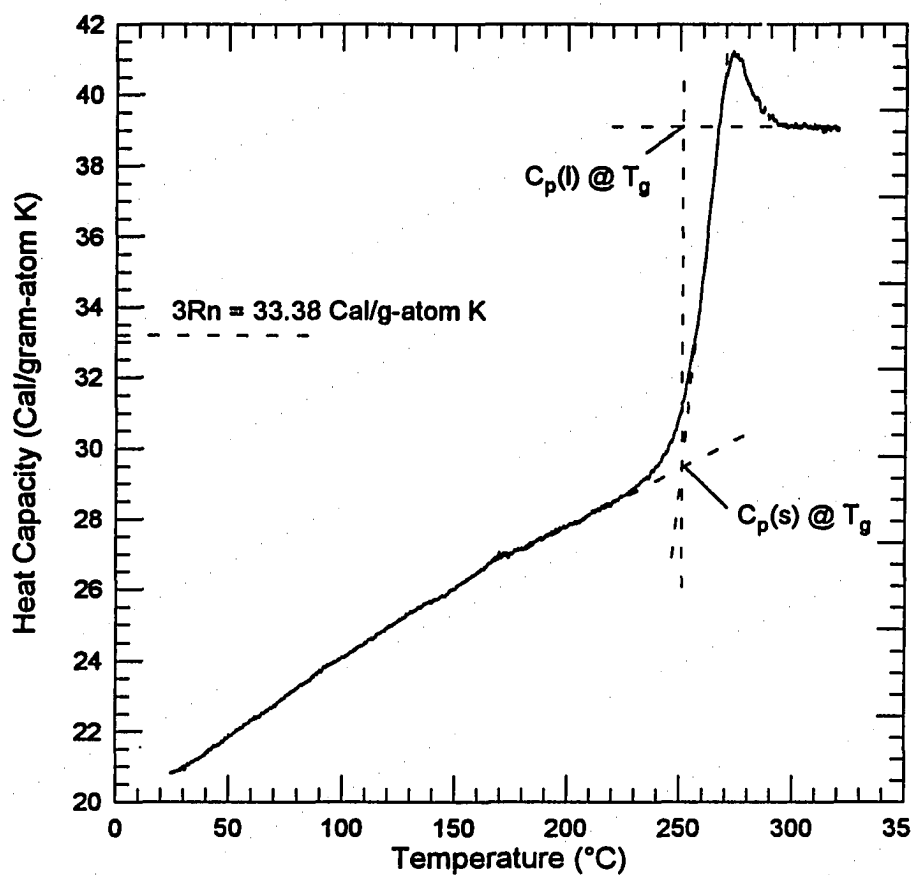


Figure 4.5 Heat capacity curve for the glass composition 35 Na₂O+65 P₂O₅. The dashed construction lines show how $C_p(l)$ and $C_p(s)$ were calculated.

Table 4.6 Heat capacities at T_g for several sodium ultra-phosphate glasses

Na ₂ O (mol%)	3Rn (cal/mole-K)	$C_p(s) @ T_g$ (cal/mole-K)	$C_p(l) @ T_g$ (cal/mole-K)	$C_p(l)/C_p(s)$	$C_p(l) - C_p(s)$ (cal/mole-K)	%3Rn @ T_g
0	41.73	37.12	43.41	1.17	6.29	89
10	39.34	34.71	43.00	1.24	8.29	88
15	38.15	32.18	39.33	1.22	7.15	84
20	36.96	32.21	40.63	1.26	8.42	87
30	34.57	29.76	38.09	1.28	8.33	86
35	33.38	29.50	39.14	1.33	9.64	88
40	32.19	28.81	37.61	1.31	8.80	89
45	30.99	28.50	40.18	1.41	11.68	91
50	29.81	27.50	37.40	1.40	9.90	92

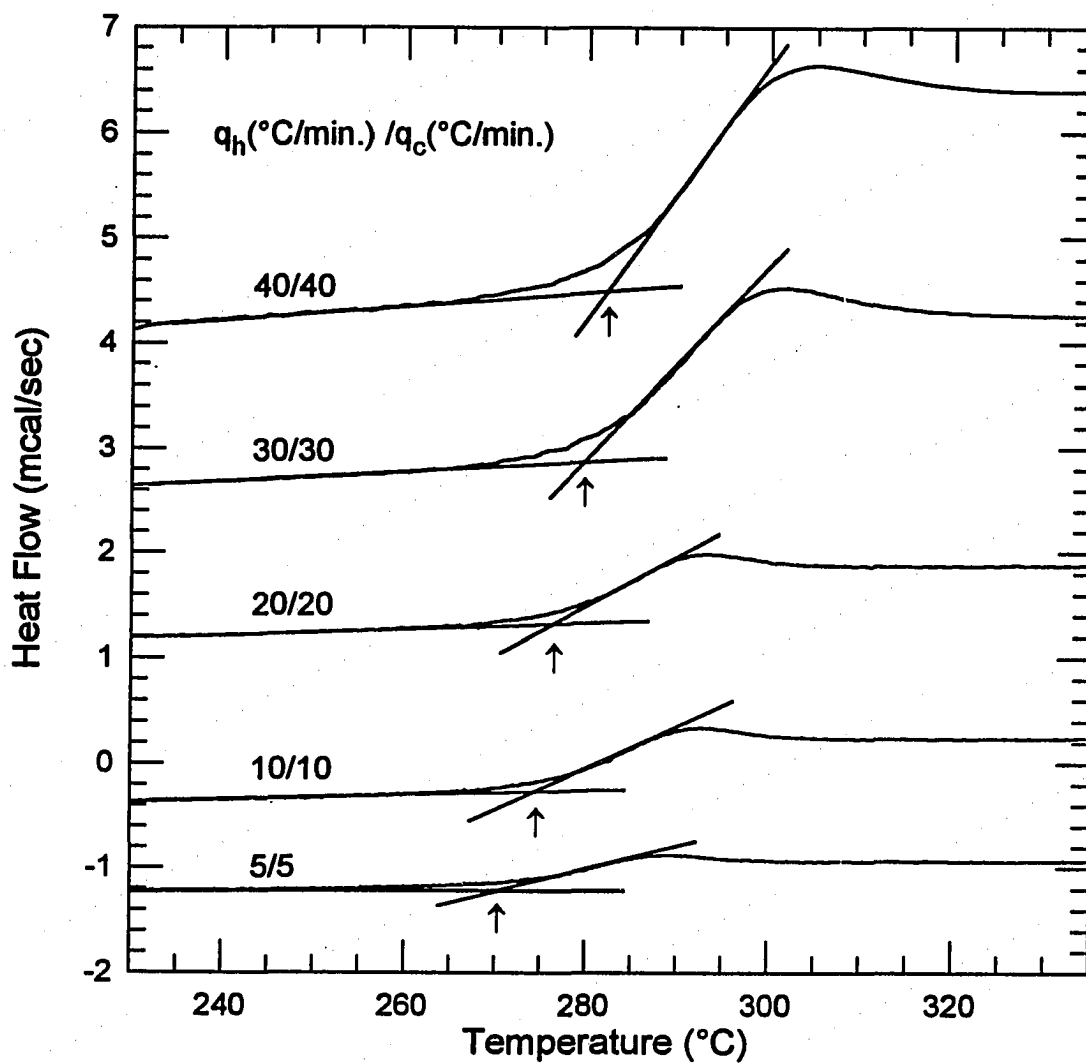


Figure 4.6 DSC scans of 45 Na₂O + 55P₂O₅ glass at $q_h=q_c$ of 5, 10, 20, 30, and 40 K/min. The lines represent the construction used to calculate onset T_g . The scans have been offset to improve comparison.

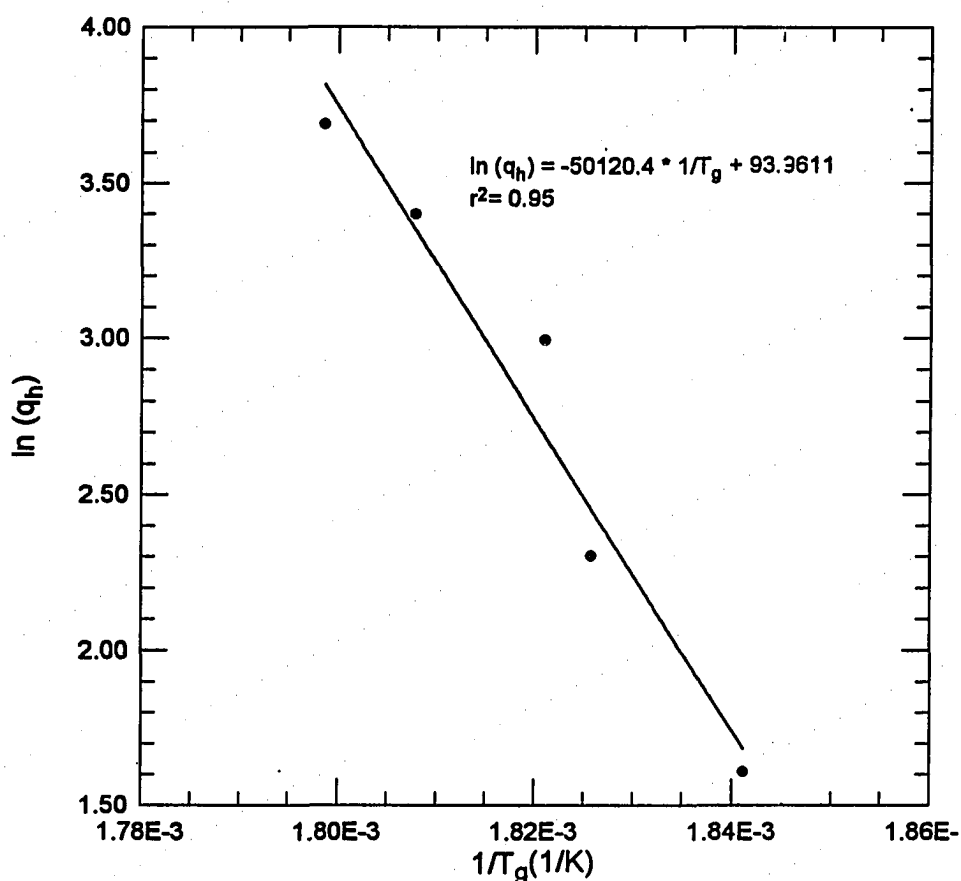


Figure 4.7 T_g for 45 mole% sodium ultra-phosphate glass measured at different heat/cool rates plotted in the Arrhenius form to yield enthalpy relaxation activation energies.

The activation enthalpy for structural relaxation and correlation coefficients of the best fits used to calculate ΔH^* are given in Table 4.8. Figure 4.8 shows ΔH^* decreases from 123 kcal/mol to ~52 kcal/mol at the 20 mole% composition. ΔH^* then increases to 101 kcal/mole at the metaphosphate composition. The value of 123 kcal/mole is significantly larger than the value of 46 kcal/mole reported by Martin [46]. Also, the value of 120 kcal/mole for the activation energy of NaPO_3 is smaller than the value reported by Wasche et al.[106], 215 kcal/mole.

Table 4.7 Heating rate data for several sodium ultra-phosphate glasses.

Composition (Mole% Na ₂ O)	q_h (K/min) $\ln(q_h)$	5	10	20	30	40
0	$T_g(^{\circ}\text{C})$	382.8	387.7	393	395.7	397.8
	$1/T_g(\text{K})$	0.002611	0.002579	0.001502	0.002527	0.002514
10	$T_g(^{\circ}\text{C})$	239.1	240	247.9	249.2	252.5
	$1/T_g(\text{K})$	0.001952	0.001949	0.001919	0.001914	0.001902
15	$T_g(^{\circ}\text{C})$	217.073	221	228.857	232	234.857
	$1/T_g(\text{K})$	0.00204	0.002024	0.001992	0.00198	0.001968
20	$T_g(^{\circ}\text{C})$	212.083	215.835	222.917	227.083	231.25
	$1/T_g(\text{K})$	0.002061	0.002045	0.002016	0.001999	0.001983
30	$T_g(^{\circ}\text{C})$	234.375	248.286	252.286	254.857	257.429
	$1/T_g(\text{K})$	0.00197	0.001918	0.001903	0.001894	0.001885
45	$T_g(^{\circ}\text{C})$	270	274.57	276	280	282.85
	$1/T_g(\text{K})$	0.001841	0.001826	0.001821	0.001808	0.001799
50	$T_g(^{\circ}\text{C})$	274	276.83	280.75		
	$1/T_g(\text{K})$	0.001828	0.001818	0.001805		

Table 4.8 Activation enthalpies for structural relaxation of several sodium ultra-phosphate glasses.

Composition (Mol% Na ₂ O)	Intercept	$\Delta H^*/R$ (1/K)	r^2	ΔH^* (kcal/mol)
0	95.9689	-61917.5	0.994142	123.03
10	74.44959	-37174.6	0.934113	73.865
15	58.64445	-27912.2	0.988599	55.461
20	55.24928	-25956.5	0.980111	51.57
30	83.8112	-42483.3	0.99271	84.41
45	93.96124	-50120.5	0.951199	99.58
50	112.973	-60901.1	0.993714	121.01

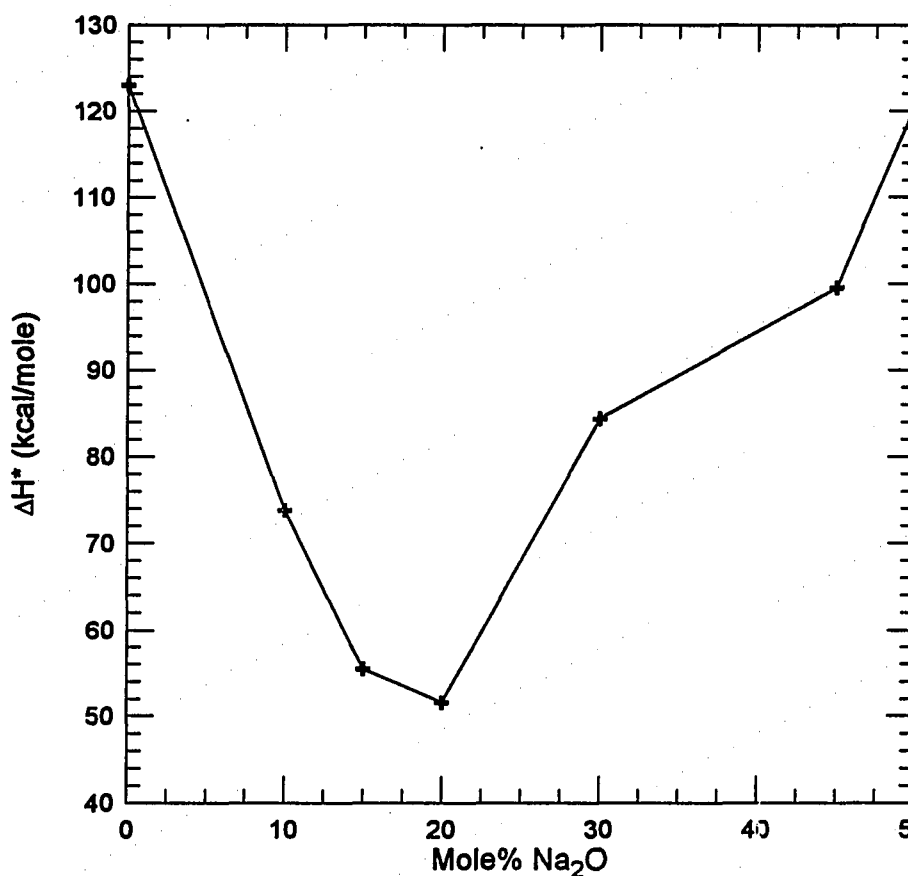


Figure 4.8 The activation enthalpies for structural relaxation of glasses in the $x \text{ Na}_2\text{O} + (1-x) \text{ P}_2\text{O}_5$ system.

4.2.3.3 Structural Relaxation

Normalized heat capacity curves of several sodium ultra-phosphate glasses were fit using the fitting procedures outlined in Section 2.3. An example of such a fit is shown in Figure 4.9. There was a significant amount of noise in the heat capacity curves of glasses with between 0 and 25 mole% Na_2O . These scans contained more noise because the transition region was spread out over a large temperature range and the overshoot was small. This noise was amplified when the data was normalized. Therefore, the fits in this range are poor (Table 4.9). The remaining fits yielded β parameters ranging from 0.6 to 0.8. Generally, β increases with increasing Na_2O content.

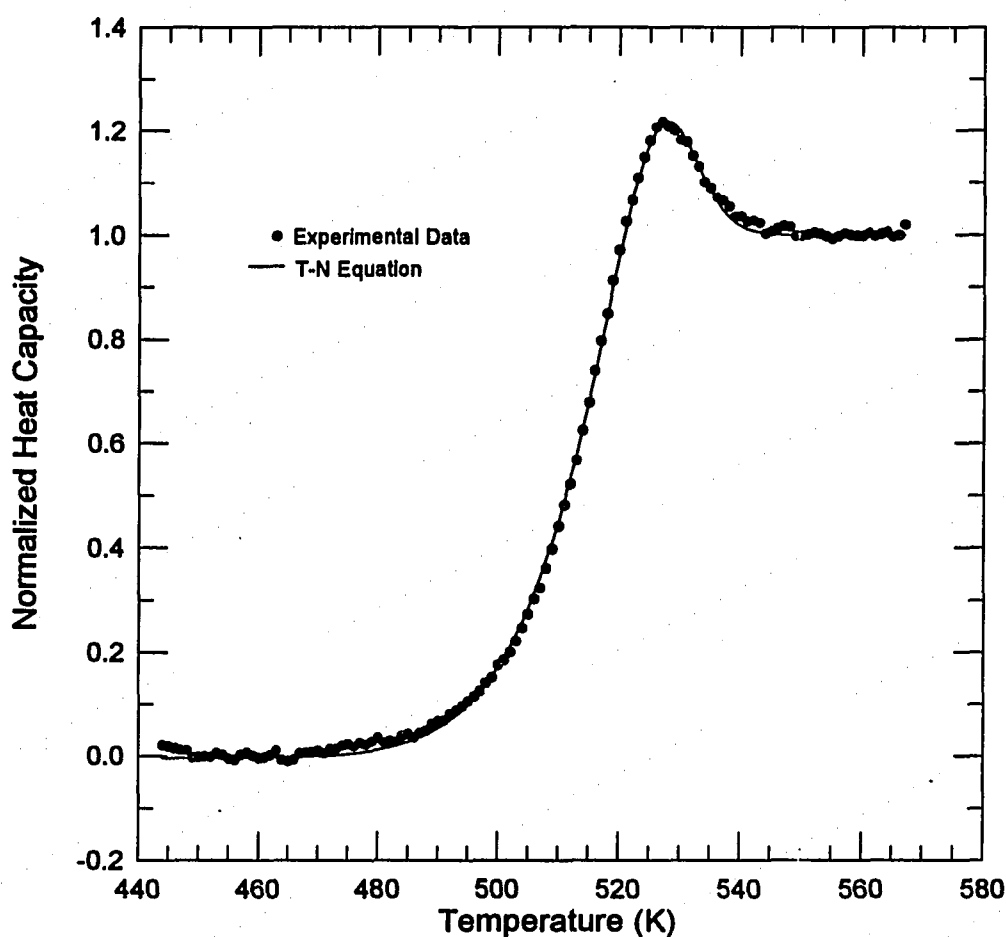


Figure 4.9 The best fit of the normalized heat capacity data to a model based on the Tool-Narayanaswamy (T-N) equation.

Table 4.9 The best fit parameters used to fit the normalized heat capacity of several sodium ultra-phosphate glasses.

Composition (Mole% Na ₂ O)	Beta	ln (A)	x	Residual
0	0.5980	-86.746	0.4190	0.167
10	0.5018	-66.554	1	0.0505
20	0.7654	-48.376	1	0.7654
30	0.6804	-76.186	0.5757	0.107
35	0.5898	-81.532	0.8239	0.383
45	0.6297	-87.354	0.9219	0.09118
50	0.7861	-106.96	0.6327	0.1704

4.2.4 Density Measurements

4.2.4.1 The $\text{Li}_2\text{O}+\text{P}_2\text{O}_5$ System

The densities of glasses in the $x \text{Li}_2\text{O} + (1-x)\text{P}_2\text{O}_5$ system are listed in Table 4.10 and shown in Figure 4.10. Uncertainties were calculated by making three independent density measurements on the glasses. The larger uncertainties at low Li_2O contents is due to the large amount of fracturing at such compositions. Density decreases from 2.47g/cc to 2.32 g /cc between 0 and 20 mole% Li_2O , then increases to 2.35 g/cc at the metaphosphate composition. The density measured for $v\text{-P}_2\text{O}_5$ is less than the value of 2.52g/cc reported by Sales [129]. The density of $v\text{-LiPO}_3$ is consistent with literature values [105]. Previously reported density values for hydrated lithium ultra-phosphates fall consistently below those reported in Table 4.10 and no minimum is observed [105].

Table 4.10 The densities of lithium ultra-phosphate glasses.

Li_2O (Mole%)	Density (g/cc)	Standard Deviation	Li_2O (Mole%)	Density (g/cc)	Standard Deviation
0	2.47	0.005	30	2.346	0.005
5	2.405	0.031	35	2.369	0.01
10	2.393	0.018	40	2.346	0.02
15	2.342	0.011	45	2.353	0.005
20	2.3233	0.011	50	2.35	0.002
25	2.333	0.007			

4.2.4.2 The $\text{Na}_2\text{O}+\text{P}_2\text{O}_5$ System

The densities of glasses in the $x \text{Na}_2\text{O} + (1-x)\text{P}_2\text{O}_5$ system are listed in Table 4.11 and shown in Figure 4.11. Uncertainties were calculated by making three independent density measurements on the glasses. The larger uncertainties at low Na_2O contents is due to the large amount of fracturing of the glass samples at these compositions. Density decreases from 2.47g/cc to 2.385 g /cc between 0 and 20 mole% Na_2O , then increases to 2.508g/cc at the metaphosphate composition. The density of $v\text{-NaPO}_3$ is consistent with literature values

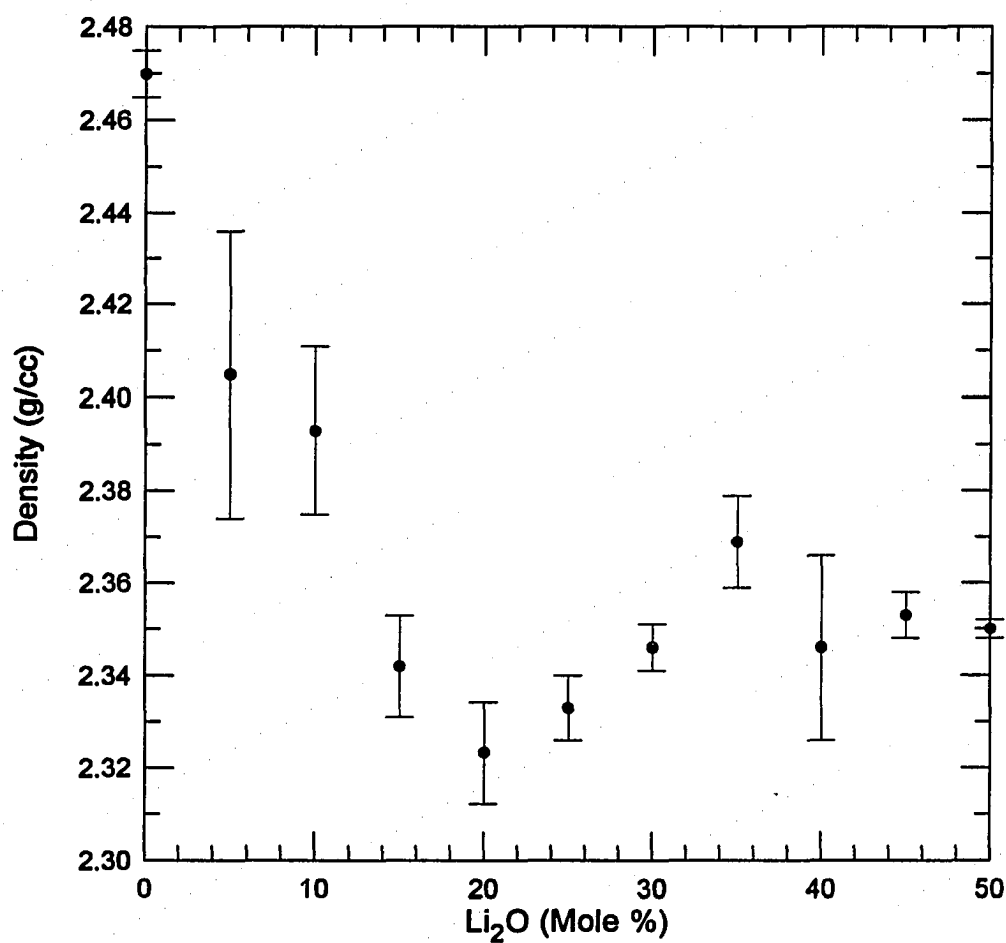


Figure 4.10 The densities of $x \text{Li}_2\text{O} + (1-x) \text{P}_2\text{O}_5$ glasses.

Table 4.11 The densities of sodium ultra-phosphate glasses.

Na ₂ O (mole%)	Density (g/cc)	Standard Deviation	Na ₂ O (mole%)	Density (g/cc)	Standard Deviation
0	2.47	0.005	30	2.418	0.0137
5	2.438	0.0067	35	2.442	0.0137
10	2.432	0.021	40	2.48	0.002
15	2.414	0.0082	45	2.4888	0.0035
20	2.385	0.0099	50	2.508	0.006
25	2.397	0.008			

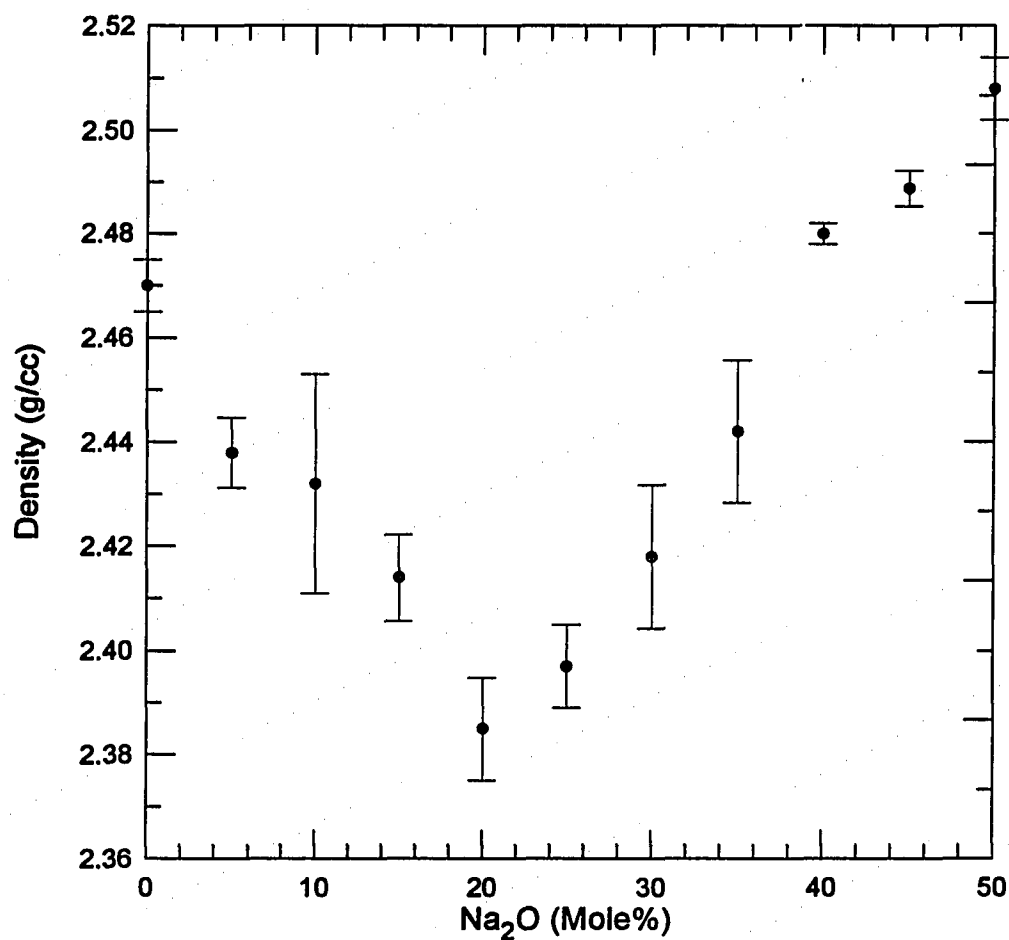


Figure 4.11 The densities of glasses in the $x \text{ Na}_2\text{O} + (1-x) \text{ P}_2\text{O}_5$ system.

[105]. Previously reported density values for hydrated sodium ultra-phosphates fall consistently below those reported in Table 4.11 and no minimum is observed [105].

4.3 Structural Determination

4.3.1 Infrared Spectroscopy

Atoms connected by bonds can be treated as masses connected by springs. In this way, fundamental (normal) modes exist which vibrate at single, well-defined frequencies. To the first order, the frequencies of such vibrations can be calculated as:

$$\omega_0 = \sqrt{\frac{k}{\frac{1}{\left(\frac{1}{m_1} + \frac{1}{m_2}\right)}}} \quad (4.2)$$

where k is the force constant of the bond and m_1 and m_2 are the masses of the two atoms. At higher order, the vibrational modes can accurately be calculated using group theory. However, all such vibrations are not IR-active, only those vibrations that result in a net dipole moment. Such selectivity is present because IR spectra are gathered by coupling polychromatic light at IR wavelengths directly to vibrational modes via the dipole moment created by the vibration.

The infrared spectra of meta- and higher alkali content phosphate glasses have been reported extensively [107-109], while few studies have reported the infrared spectra of ν - P_2O_5 and anhydrous low alkali phosphates [15, 52, 53, and 110]. For interpretation of the vibrational modes of alkali ultra-phosphate glasses it is necessary to identify all possible network vibrations. Theoretically, each Q^3 tetrahedron leads to one terminal oxygen stretching vibration ($\nu(P=O)_s$), and one symmetric and two asymmetric bridging oxygen stretching vibrations ($1\nu(POP)_{as}$, $2\nu(POP)_s$) [15]. Similarly, each Q^2 tetrahedron leads to one symmetric and one asymmetric terminal oxygen stretching vibration ($\nu_{as}(PO_2)$, $\nu_s(PO_2)$), and one symmetric and one asymmetric bridging oxygen stretching vibration ($\nu_{as}(POP)$, $\nu_s(POP)$). However, crystalline ultra- and metaphosphates contain more than one equivalent site for each

type of tetrahedron. With the exception of α - $\text{Ca}_2\text{P}_6\text{O}_{17}$, where there is a single Q^3 site, all ultra-phosphate crystals contain two Q^3 and two Q^2 equivalent sites and chain metaphosphate crystals contain four equivalent sites for Q^2 units. Therefore, the total number of theoretical network vibrations for ultra-phosphate crystals is between 14 and 16. However, the actual number of stretching vibrations may be larger due to in-phase and out-of-phase vibrations in the rings of PO_4 tetrahedra present in all ultra-phosphate crystals. In addition to MIR absorptions due to the stretching vibrations of the network units, there are also absorbances due to deformation modes.

The positions of the MIR absorbances due to network stretching vibrations range between 650 and 1400cm^{-1} , while those due to deformation modes of network units occur at lower wavenumbers. In crystalline materials, where absorbance peaks are narrow and well separated, bond lengths can be used as a qualitative measure of bond strength to assign the different stretching vibrations. However, in amorphous materials, the disorder of the structure leads to broader absorbance peaks which overlap leading to band complexes. The MIR spectrum of glassy $\text{Ca}_2\text{P}_6\text{O}_{17}$ in Figure 4.12 is typical of glassy ultra- and meta-phosphates showing four complexes of bands. As with all ultra-phosphate materials, the absorbance complexes of the glass occur in the same range as the corresponding crystal, in this way, the stretching vibrations causing the absorbance complexes can be identified. Complex I, centered near 1350cm^{-1} , consists of $\nu(\text{P}=\text{O})$ and $\nu_{\text{as}}(\text{POP})$ stretching vibrations. Complex II, centered near 1000cm^{-1} , consists of the $\nu_{\text{s}}(\text{POP})$ and $\nu_{\text{as}}(\text{PO}_2)$ stretching vibrations. Complex III, centered near 750cm^{-1} , contains the $\nu_{\text{s}}(\text{PO}_2)$ stretching vibrations and complex IV contains the deformation modes. However, as given in Equation 4.2, the frequency of the vibrations is directly proportional to the strength of the bonds and inversely proportional to the masses of the atoms. In this way, the vibrational frequencies of normal modes depend on the cationic potential modifying cation. Table 4.12 gives the frequency ranges for the vibrational modes of Q^3 and Q^2 units as compiled from a number of different phosphate crystals and glasses.

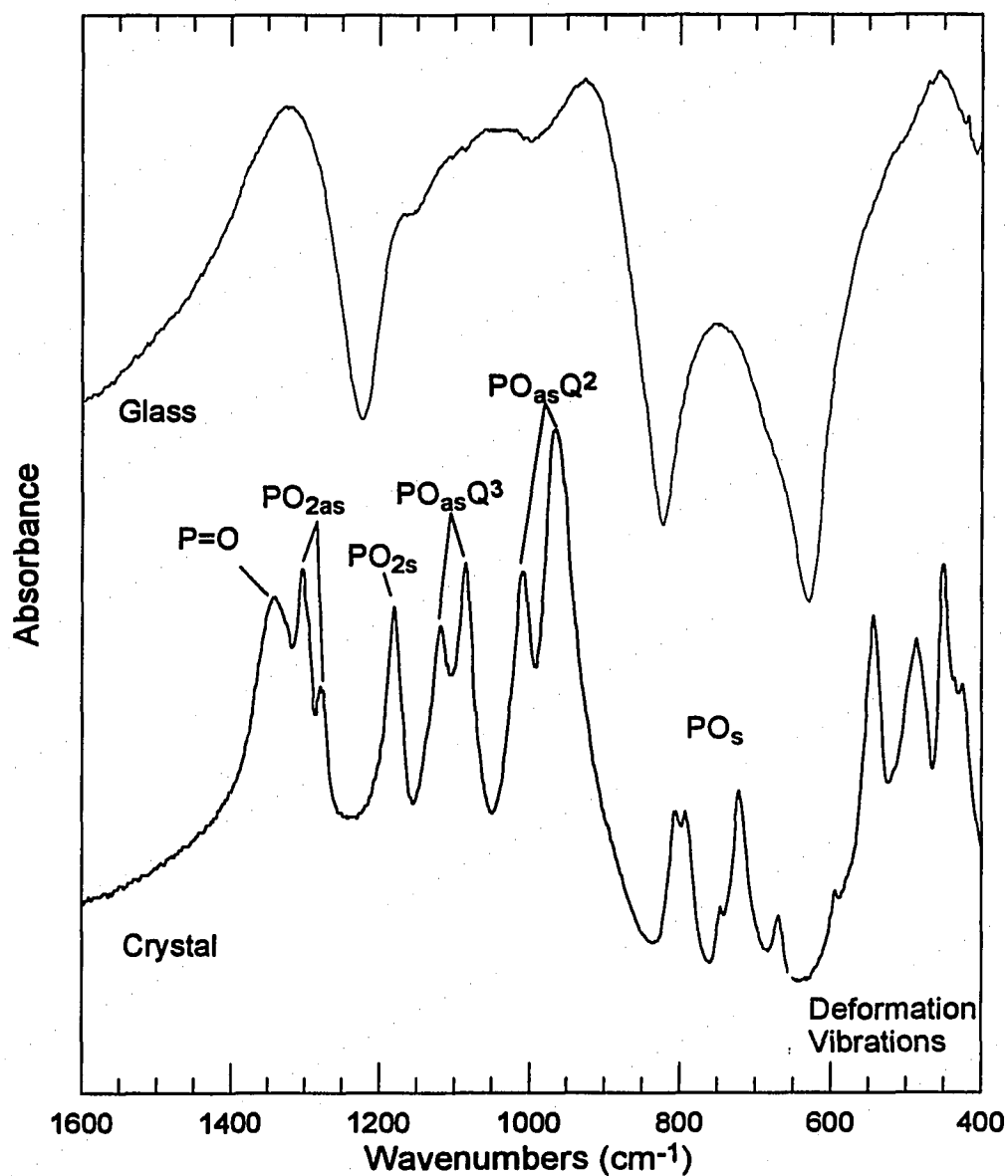


Figure 4.12 The MIR spectra of crystalline and glassy $\text{Ca}_2\text{P}_4\text{O}_{11}$ [15] illustrating the band complexes found in the MIR spectra of amorphous materials as opposed to the sharp peaks in crystalline materials.

Table 4.12 Absorbance regions for the P-NBO, P-BO, and P=O modes of Q^2 and Q^3 units.

Absorbance band (cm^{-1})	Absorbance Mode	Structural Unit
1450-1200	$\nu(\text{P=O})_s$	Q^3
1050-850	$\nu(\text{POP})_{as}$	$Q^2 Q^3$
800-650	$\nu(\text{POP})_s$	$Q^2 Q^3$
530	(POP) bending	$Q^2 Q^3$
1323-1140	$\nu(\text{PO}_2)_{as}$	Q^2
1170-1100	$\nu(\text{PO}_2)_s$	Q^2

MIR spectra were obtained for the polycrystals LiPO_3 , $(\text{NaPO}_3)_n$, and the H form of $c\text{-P}_4\text{O}_{10}$ and for glasses in the systems $x \text{R}_2\text{O} + (1-x) \text{P}_2\text{O}_5$, where $\text{R}=\text{Li}, \text{Na}$ and $0 \leq x \leq 0.5$. Because of the volatility of the glass melts at the temperatures necessary to blow thin films ($>700^\circ\text{C}$), KBr mulls were used to obtain the MIR spectra. The KBr was dried prior to mixing with the glass powder, however, some of the MIR spectra show O-H stretches at $\sim 3600 \text{ cm}^{-1}$ indicating water is present in the KBr. Also, dried and decarbonated air was passed through the MIR spectrometer bench to prevent water reacting with the moisture sensitive glass and to prevent the characteristic CO_2 doublet ($\sim 2350 \text{ cm}^{-1}$) and H_2O rotational spectra from complicating spectra. However, due to intermittent problems with the dry air filtration system, several of the MIR spectra show the CO_2 doublet and rotational spectra. Additionally, difference in thickness between the background KBr pellet and sample pellet resulted in non-linearity in the baseline for some samples. Figure 4.13 shows the spectra of the $0.35 \text{ Na}_2\text{O} + 0.65 \text{ P}_2\text{O}_5$ glass which exhibits all of the experimentally introduced absorbances.

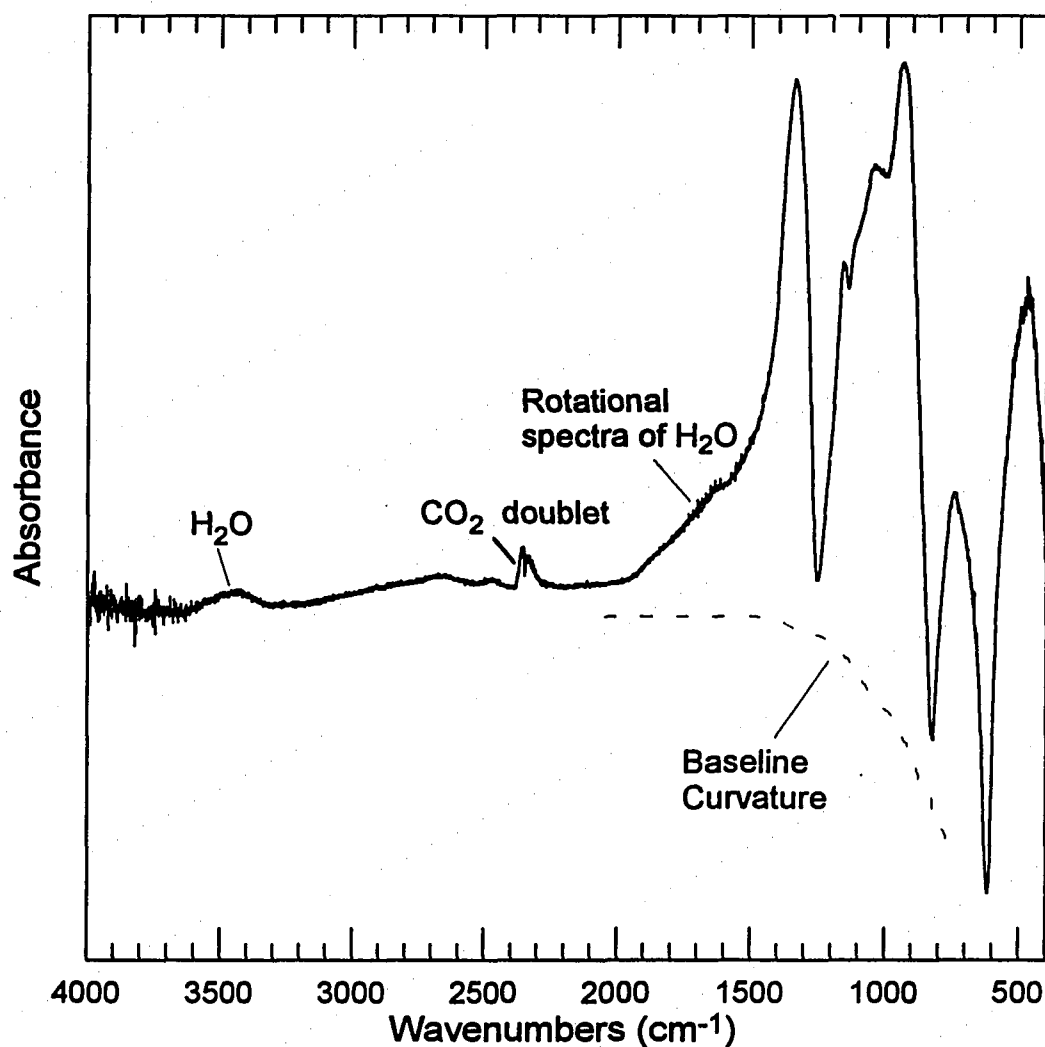


Figure 4.13 The MIR spectra of the 0.35 Na₂O + 0.65 P₂O₅ glass showing absorbance due to uncombined H₂O in the KBr, a doublet caused by residual CO₂ in the dry air within the spectrometer bench, H₂O rotational spectra due to residual H₂O in the dry air, and baseline curvature due to difference in thicknesses between the background KBr pellet and the sample pellet

4.3.1.1 Crystalline and Vitreous P_2O_5

The MIR spectrum of the H form of $c\text{-P}_4O_{10}$ is shown in Figure 4.14. The strongest absorbance modes are at 1400cm^{-1} , 1000cm^{-1} , 770cm^{-1} , and 590cm^{-1} . These absorbances arise from the $\nu(\text{P=O})_s$, $\nu(\text{POP})_{as}$, $\nu(\text{POP})_s$ and deformation modes of Q^3 structural units, respectively [111]. The less intense absorbances at 1700cm^{-1} , 1620cm^{-1} , 1290cm^{-1} , 1150cm^{-1} , and 550cm^{-1} arise from the stretching, combination, and deformation modes of a P-OH unit, as outlined in Table 4.13. Due to the strong absorbance of the crystalline material, the absorbance band at 1000cm^{-1} is clipped.

The MIR spectrum of $v\text{-P}_2O_5$ is shown in Figure 4.15. The spectrum is similar to those previously reported in literature [52, 53]. All absorbance bands in the MIR spectrum of $v\text{-P}_2O_5$ are broader ($\text{FWHM} \approx 100\text{cm}^{-1}$) than those in the MIR spectrum of $c\text{-P}_4O_{10}$ ($\text{FWHM} \approx 10\text{cm}^{-1}$). The strongest absorbances in the MIR spectrum of $v\text{-P}_2O_5$ are centered at 1395cm^{-1} , 995cm^{-1} , 800cm^{-1} and 480cm^{-1} . As in the MIR spectrum of the H form of $c\text{-P}_2O_5$, these absorbances arise from the $\nu(\text{P=O})_s$, $\nu(\text{POP})_{as}$, $\nu(\text{POP})_s$ and deformation modes of Q^3 structural units, respectively [111]. Less intense, broader bands are centered at 2750cm^{-1} , 1950cm^{-1} and 1750cm^{-1} which arise from the stretching and deformation modes of P-OH units.

4.3.1.2 The $\text{Li}_2\text{O}+\text{P}_2\text{O}_5$ System

The MIR spectra of lithium ultra-phosphate glasses are shown in Figure 4.16. As in previous MIR studies of ultra-phosphate glasses, the spectra are divided into four band complexes [14]. Complex I, centered near 1350cm^{-1} , consists of $\nu(\text{P=O})$ and $\nu(\text{PO}_2)_{as}$ stretching vibrations. Complex II, centered near 1000cm^{-1} , consists of the $\nu(\text{POP})_{as}$ and $\nu(\text{PO}_2)_s$ stretching vibrations. Complex III, centered near 750cm^{-1} , contains the $\nu(\text{POP})_s$ stretching vibrations and complex IV contains the deformation modes. As observed in crystalline ultra-phosphate materials [14], the high frequency broadening of complex II with the growth of bands between 1000 and 1200cm^{-1} ($\nu_{as}(\text{PO}_2)$) is correlated with increasing cation content. Additionally, the increasing intensity ratio of complex I to the $\nu(\text{POP})_{as}$

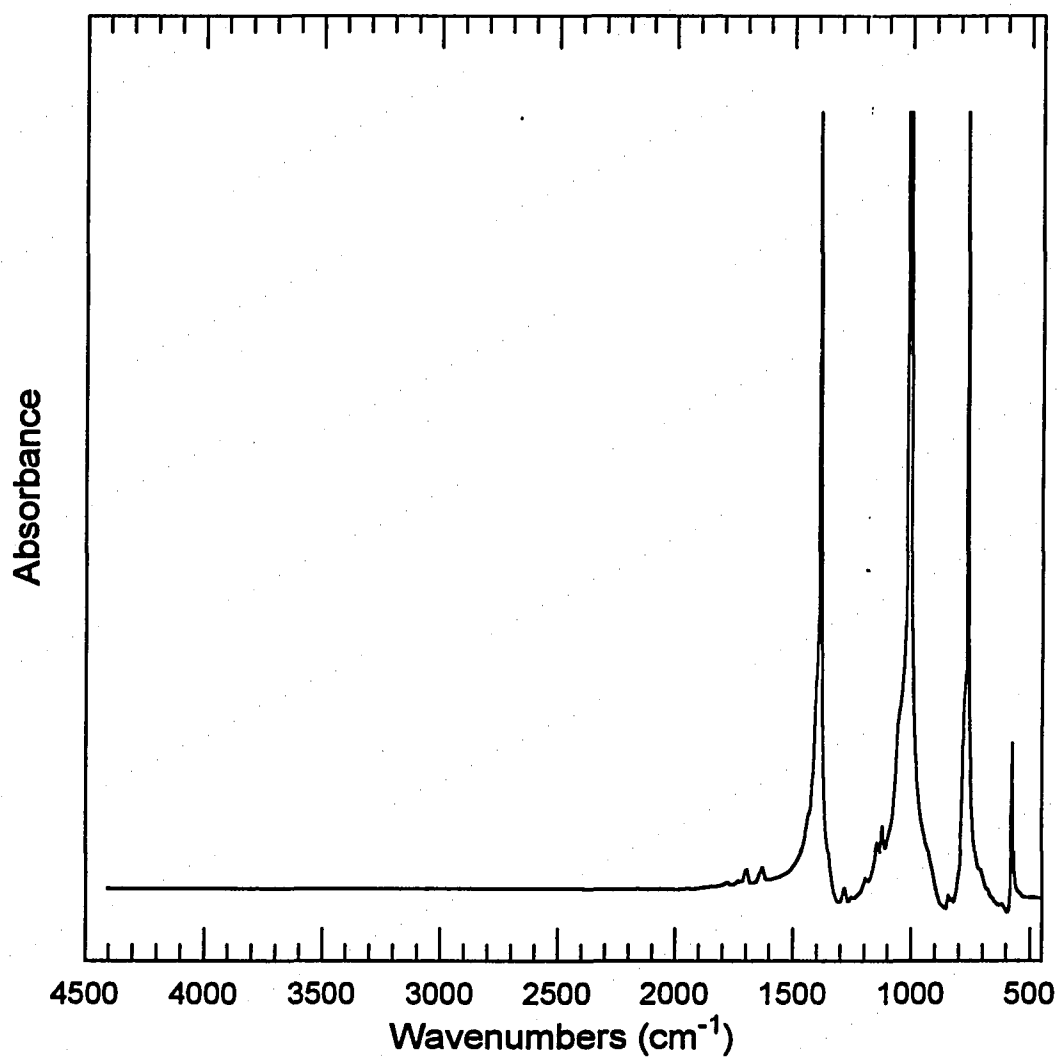


Figure 4.14 The MIR spectrum of the H form of crystalline P_4O_{10} .

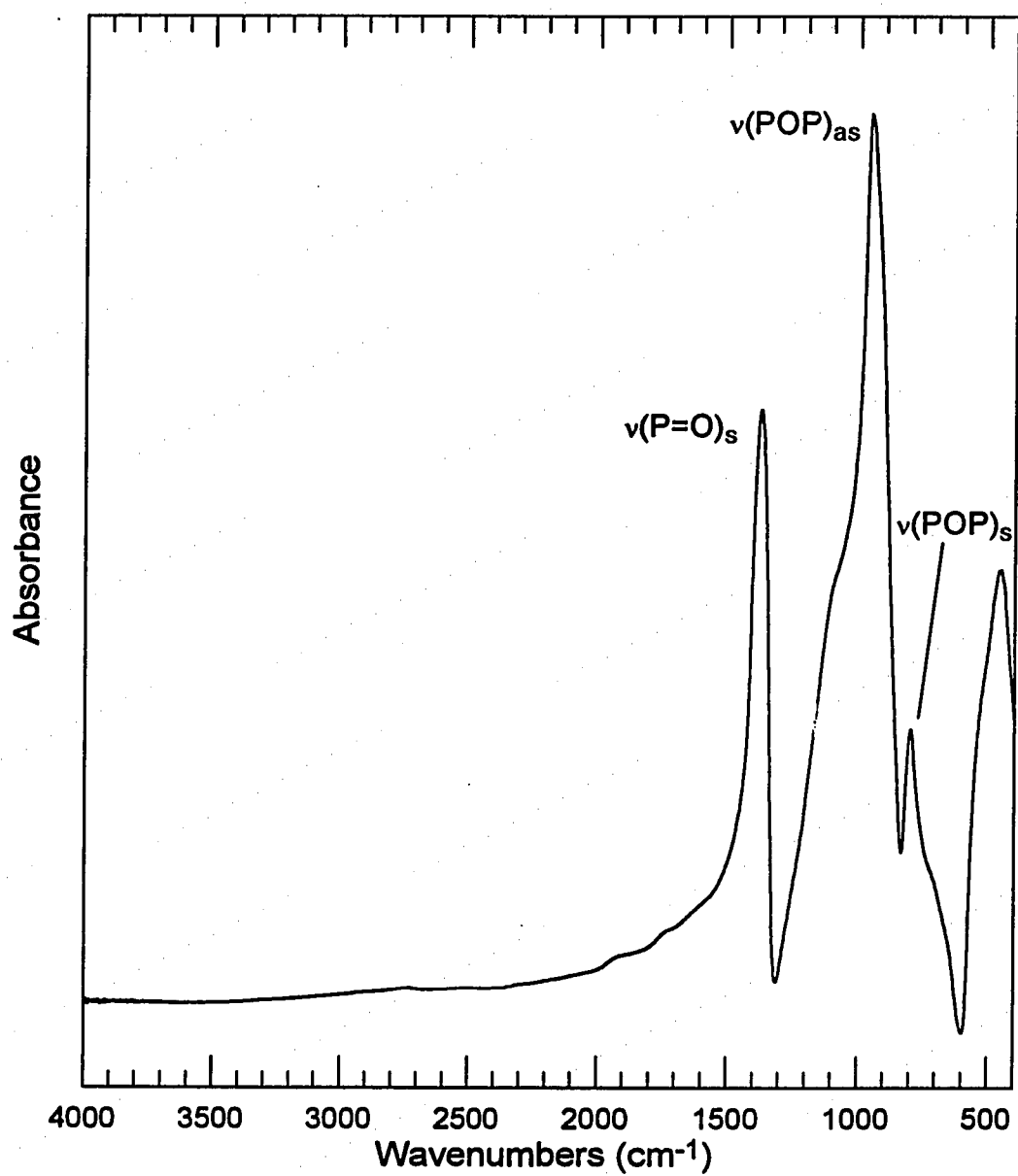


Figure 4.15 The MIR spectra of v-P₂O₅ indicating absorbances due to the symmetric and asymmetric stretches of Q³ units.

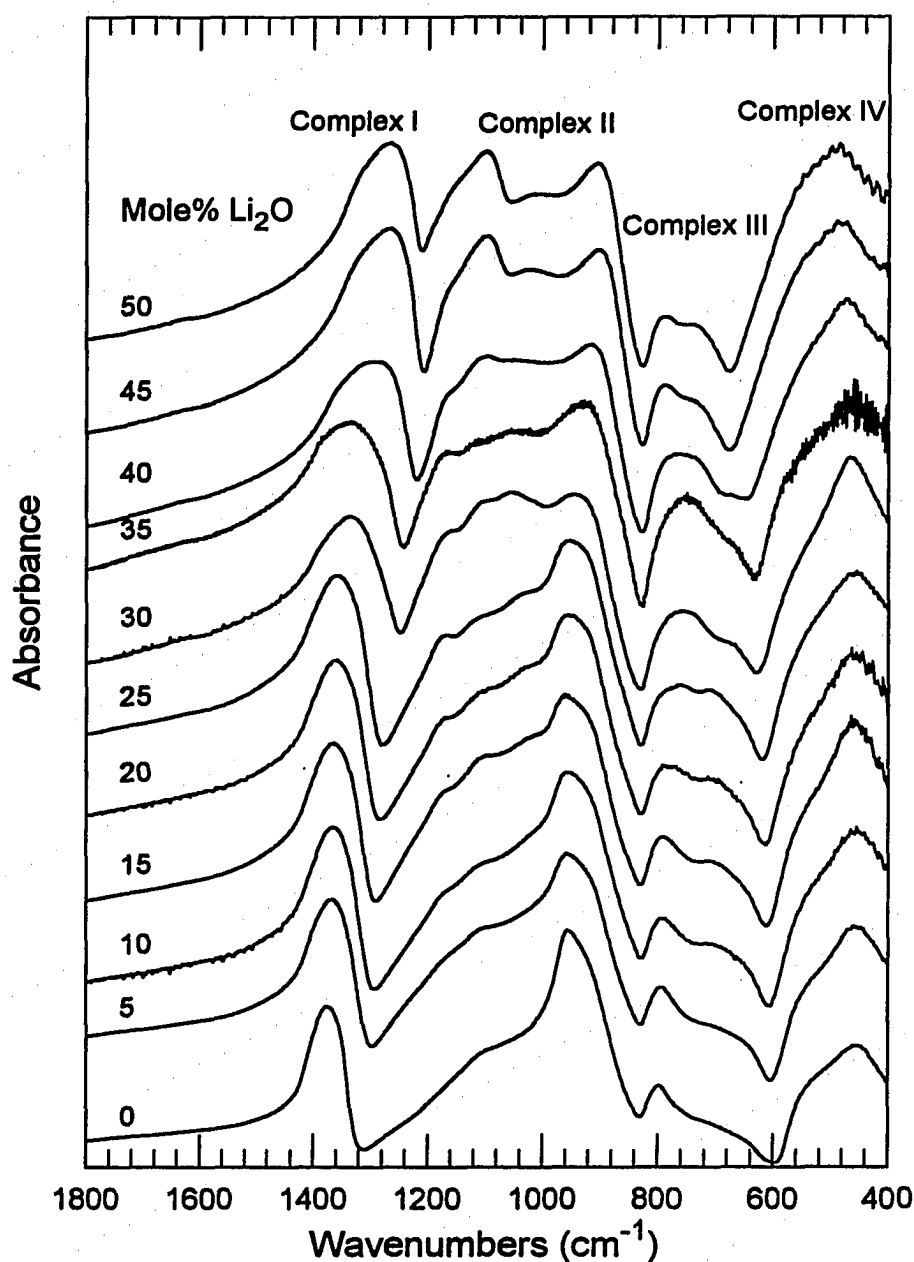


Figure 4.16 The MIR spectra of lithium ultra-phosphate glasses. The spectra can be divided into four band complexes. Complex I, centered near 1350cm^{-1} , consists of $\nu(\text{P}=\text{O})$ and $\nu(\text{PO}_2)_s$ stretching vibrations. Complex II, centered near 1000cm^{-1} , consists of the $\nu(\text{POP})_s$ and $\nu(\text{PO}_2)_s$ stretching vibrations. Complex III, centered near 750cm^{-1} , contains the $\nu(\text{POP})_s$ stretching vibrations and complex IV contains the deformation modes. The spectra have been offset to improve comparison.

Table 4.13 The wavenumbers of the centers of the different absorbance bands in the MIR spectra of lithium ultra-phosphate glasses and the vibrational modes assigned to those bands.

Li ₂ O (Mole%)											Assignment (cm ⁻¹)
5	10	15	20	25	30	35	40	45	50		
1358.3	1362.9	1362.9	1356.0	1356.0	1335.3	1335.3	1293.8	1266.1	1262.7		$\nu(\text{P}=\text{O})_{\text{a}}, \nu(\text{PO}_2)_{\text{as}}$
1088.7	1169.4	1165.9	1165.9	1165.9	1159.0	1162.4	1159.0				$\nu(\text{PO}_2)_{\text{s}}$
	1103.7	1096.8	1103.7	1103.7	1051.8	1058.8	1093.3	1093.3	1093.3		
943.5	951.6	958.5	1027.6	1034.6	941.2	927.4	917.1	1017.3	1010.4		$\nu(\text{POP})_{\text{as}}$
			951.6	948.2				899.8	903.2		
777.6	785.7	785.7	775.3	761.5	758.1	751.2	758.1	782.3	782.3		$\nu(\text{POP})_{\text{s}}$
	702.8	702.8	706.2	706.2	668.2			733.9	737.3		
445.9	450.5	457.4	453.9	453.9	464.3	471.2	467.7	481.6	485.0		Deformation Vibrations

vibrations ($\sim 950 \text{ cm}^{-1}$) is consistent with the creation of non-bridging oxygens at the expense of bridging oxygens.

4.3.1.3 $\text{Na}_2\text{O}+\text{P}_2\text{O}_5$

The IR spectra of sodium ultra-phosphate glasses are shown in Figure 4.17 and the absorbance assignments are given in Table 4.14. As in the absorbance spectra of lithium ultra-phosphate glasses, the sodium ultra-phosphate spectra can be divided into four regions of absorbance band complexes. The highest frequency complex in the spectra is in the range $1375\text{-}1250 \text{ cm}^{-1}$ and contains the symmetric stretch of the phosphoryl unit ($\nu(\text{P=O})_s$) and the asymmetric stretch of terminal oxygens on Q^2 units ($\nu(\text{PO}_2)_{as}$) [111]. Within complex II, absorbances in the range $1200\text{-}1100 \text{ cm}^{-1}$ result from the symmetric vibrations of terminal oxygens, $\nu(\text{PO}_2)_s$, while absorbances in the range $1050\text{-}850 \text{ cm}^{-1}$ are assigned to the asymmetric stretching modes bridging oxygens ($\nu(\text{POP})_{as}$). The symmetric stretches of bridging oxygens ($\nu(\text{POP})_s$) are found in complex III, $600\text{-}850 \text{ cm}^{-1}$, and complex IV contains the deformation modes. As is seen in crystalline ultra-phosphate materials, the high frequency broadening of complex II with the growth of bands between 1000 and 1200 cm^{-1} ($\nu_{as}(\text{PO}_2)$) is correlated with increasing cation content. Additionally, the increasing intensity ratio of complex I to the $\nu(\text{POP})_{as}$ vibrations is consistent with the creation of non-bridging oxygens at the expense of bridging oxygens, depolymerization of the phosphate network.

4.3.2 Raman Spectroscopy

While the use of IR and Raman techniques might appear redundant, the selection rules governing the coupling of light to particular vibrations are less stringent for Raman than IR. Therefore, the two techniques are often complimentary. In addition, depending on the width of the Rayleigh line, Raman spectroscopy allows spectra to be obtained at $<400 \text{ cm}^{-1}$, where ionic interactions can be studied. Also, the collection of polarized Raman spectra enables determination of the symmetries of vibrational modes.

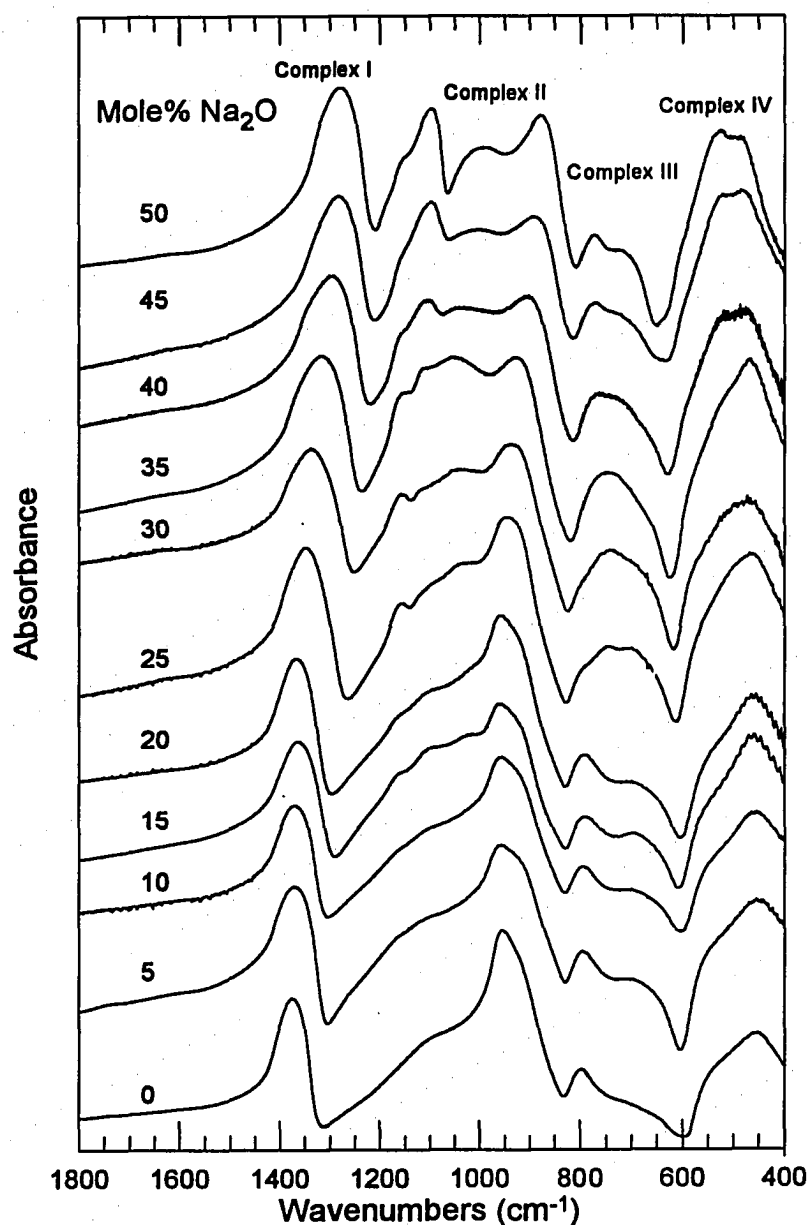


Figure 4.17 The infra-red spectra of sodium ultra-phosphate glasses. The spectra can be divided into four band complexes. Complex I, centered near 1350cm^{-1} , consists of $\nu(\text{P}=\text{O})$ and $\nu(\text{PO}_2)_s$ stretching vibrations. Complex II, centered near 1000cm^{-1} , consists of the $\nu(\text{POP})_s$ and $\nu(\text{PO}_2)_s$ stretching vibrations. Complex III, centered near 750cm^{-1} , contains the $\nu(\text{POP})_s$ stretching vibrations and complex IV contains the deformation modes. The spectra have been offset to improve comparison.

Table 4.14 The wavenumbers of the centers of the different absorbance bands in the MIR spectra of sodium ultra-phosphate glasses.

Na ₂ O (Mole%)												Assignment (cm ⁻¹)
0	5	10	15	20	25	30	35	40	45	50		
1370	1370	1370	1360	1360	1340	1330	1310	1294	1280	1270		$\nu(\text{P}=\text{O})_{\text{as}}, \nu(\text{PO}_2)_{\text{as}}$
(1100)	1170	1170	1160	1160	1150	1150	1150	1152	1150	1150		$\nu(\text{PO}_2)_{\text{s}}$
	1100	1100	1100	1100		1120	1110	1104	1100	1100		
			1030		1040	1040	1050	1038	1000	1000		$\nu(\text{POP})_{\text{as}}$
951	955	951	951	951	939	931	923	900	884	891		
794	789	789	786	786	741	737	745	765	714	770		$\nu(\text{POP})_{\text{s}}$
	695	695	693	693	697	697			764	717		
451	450	453	455	455	459	475	463	488	479	483		Deformation
									516	520		Vibrations

The depolarization ratio is defined as:

$$\rho = \frac{I_{\parallel}}{I_{\perp}} \quad (4.3)$$

where I_{\parallel} and I_{\perp} are the intensities of the Raman scatter at a given frequency shift with their plane of polarization perpendicular (HV) and parallel (HH) to that of the incident beam, respectively. In amorphous solids, ρ is between 0 and $\frac{3}{4}$. When $\rho < 0.1$, the vibration is considered highly symmetric. Also, polarized Raman spectra provide information about the symmetry of absorption modes not available using IR spectroscopy, such information is valuable when assigning vibration modes to absorption peaks in both Raman and IR spectra.

Generally, for a vibration to be IR-active it must result in a net dipole moment. For a vibration to be Raman active, the polarizability must differ for positive and negative values of the vibrational coordinate. Therefore, symmetric modes where all the atoms vibrate along equivalent directions, are generally strong in Raman and weak in IR. Figure 4.18 shows the Raman spectrum of c-NaPO₃ and MIR spectrum of c- Ca(PO₃)₂. Figure 4.18 illustrates the complimentary nature of the different methods. The asymmetric modes (PO₂ and POP) are less intense and symmetric modes (PO₂) and (POP) more intense in the Raman spectrum than those in the IR spectrum. Also, note the alkali oxide absorption band can be seen in the Raman spectra. The large increase in intensity at low wavenumbers in the Raman spectra is the onset of the Rayleigh line.

4.3.2.1 P₂O₅

Three Raman scattering studies of v-P₂O₅ can be found in literature [54, 112, 113]. The room temperature spectra of Bobovich [112] shows evidence of both Q² and Q¹ species suggesting contamination by H₂O or CaO. Only the high temperature (530°C) and room temperature studies by Galeener et al. [54, 113] show the characteristic symmetric P=O and P-O-P Raman lines expected for v-P₂O₅. The room temperature, unpolarised Raman spectra of anhydrous v-P₂O₅ obtained in this study, shown in Figure 4.19 is similar to the spectra

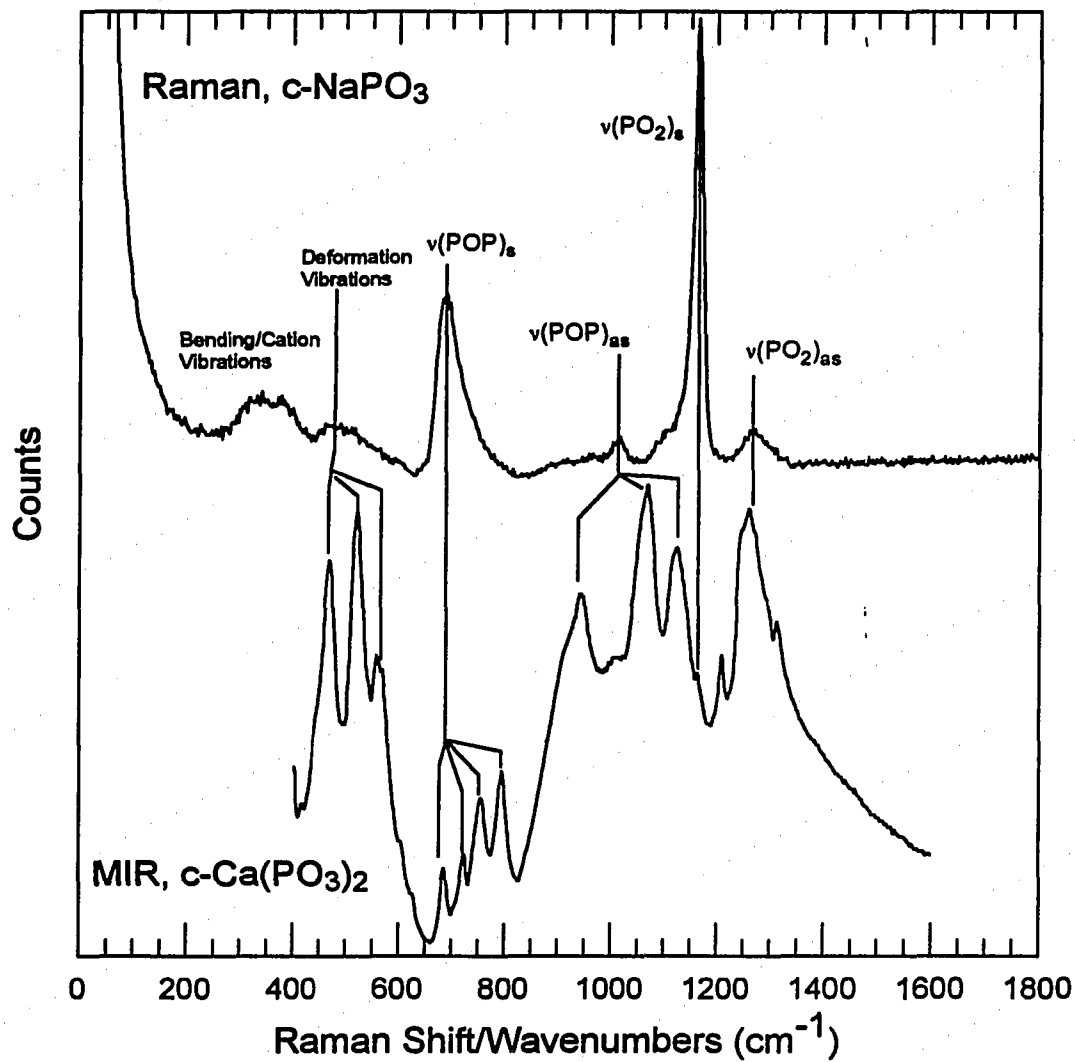


Figure 4.18 The raman spectra of c-NaPO₃ and MIR spectra of c-Ca(PO₃)₂, showing the differences between the two techniques.

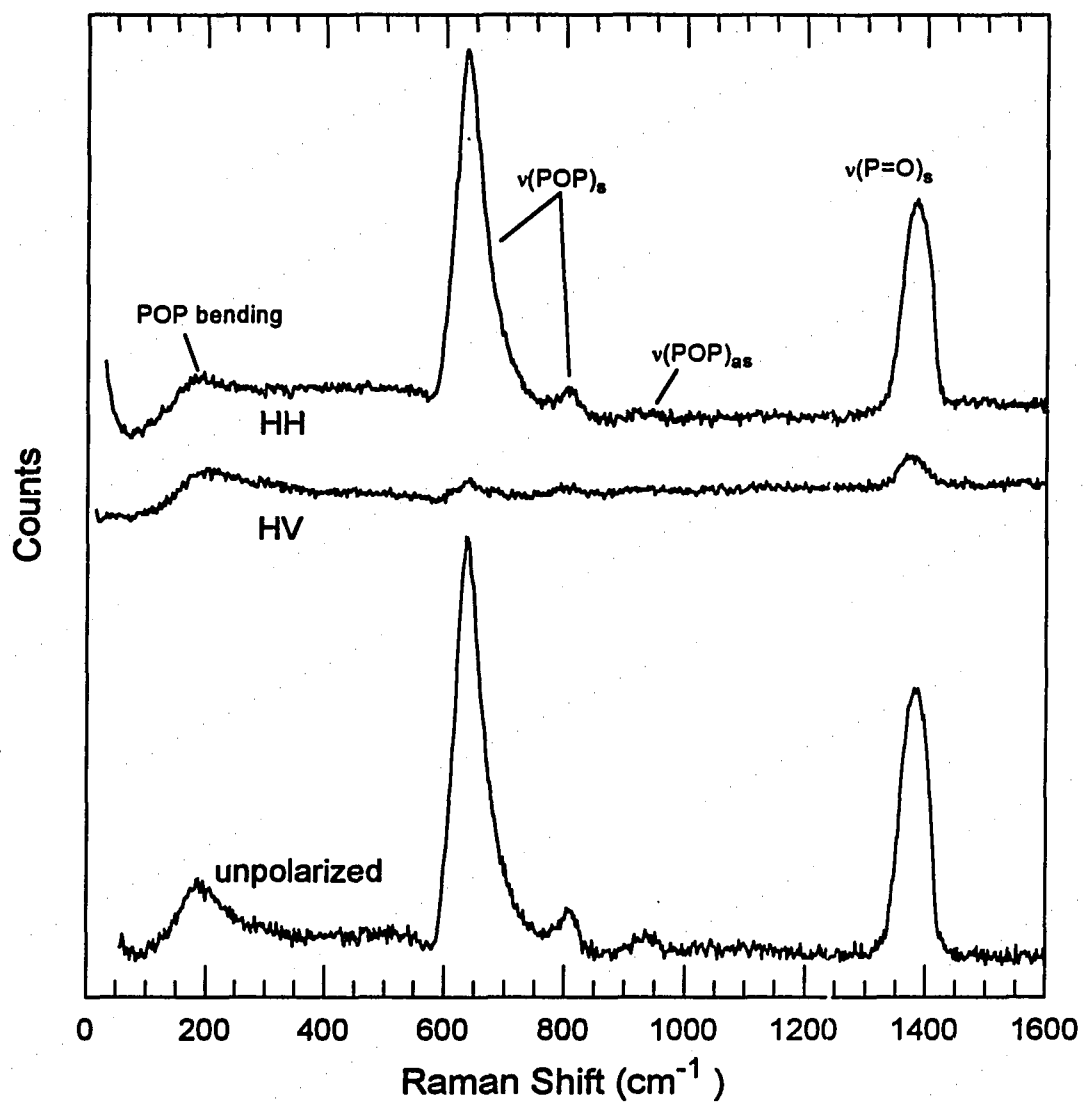


Figure 4.19 The unpolarized, HV polarized, and HH polarized Raman spectra of ν - P_2O_5 . The spectra have been offset to improve comparison.

reported by Galeener et al. The spectra has two strong lines at 1390 cm^{-1} ($\rho = 0.13$) and 640 cm^{-1} ($\rho = 0.005$) and much less intense lines at 810 cm^{-1} ($\rho = 0.75$) and 190 cm^{-1} ($\rho = 0.75$). The Raman line at 1390 cm^{-1} is due to the symmetric phosphoryl stretch, $\nu(\text{P}=\text{O})_s$, at 640 cm^{-1} to the $\nu(\text{POP})_s$ stretch, at 810 cm^{-1} to the $\nu(\text{POP})_{as}$ stretch and at 190 cm^{-1} to a P-O-P bending mode. Also, there is a very weak line at 910 cm^{-1} attributed to a $\nu(\text{POP})_{as}$ mode. Galeener reports another weak line near 1100 cm^{-1} not found in the present study.

4.3.2.2 The $\text{Li}_2\text{O}+\text{P}_2\text{O}_5$ System

Raman spectra were gathered for lithium ultra-phosphate glasses containing 0 to 45 mole% Li_2O , excluding the 40 mole% composition. The Raman spectra of lithium ultra-phosphate glasses are shown in Figures 4.20 and 4.21. The 0, 10, and 20 mole% Li_2O glass samples were relatively small and heavily fractured. Such samples yielded increased fluorescence which increased the overall count level resulting in higher levels of background noise. Due to the increased shot noise polarized Raman spectra were not collected for these samples.

Lithium phosphate glasses containing between 50 and 70 mole% Li_2O have been studied by Raman scattering [114- 117]. These studies show the main Raman scattering modes due to Q^2 units are at $\sim 1327\text{ cm}^{-1}$ ($\nu(\text{PO}_2)_{as}$), 1164 cm^{-1} ($\nu(\text{PO}_2)_s$), and 674 cm^{-1} ($\nu(\text{POP})_s$). As in the MIR spectra, the growth of a new scattering mode at $\sim 1200\text{ cm}^{-1}$ corresponds to an increasing cation content.

The Raman scattering spectra can be divided into two regimes. At compositions < 25 mole% alkali, there is little change in the Raman shift of the $\nu(\text{POP})_s$ and $\nu(\text{P}=\text{O})_s$ modes. The increase in intensity of Raman scatter at 1200 cm^{-1} and low frequency broadening of the $\nu(\text{P}=\text{O})_s$ are consistent with the depolymerization of the network as P-O Li^+ terminal oxygens are created from P-O-P bridging oxygens. At Li_2O contents > 20 mole% , the Raman scattering mode centered near 1327 cm^{-1} ($\nu(\text{P}=\text{O})_s$ and $\nu(\text{PO}_2)_{as}$) shifts to lower wavenumbers as does the $\nu(\text{POP})_s$ Raman scattering mode.

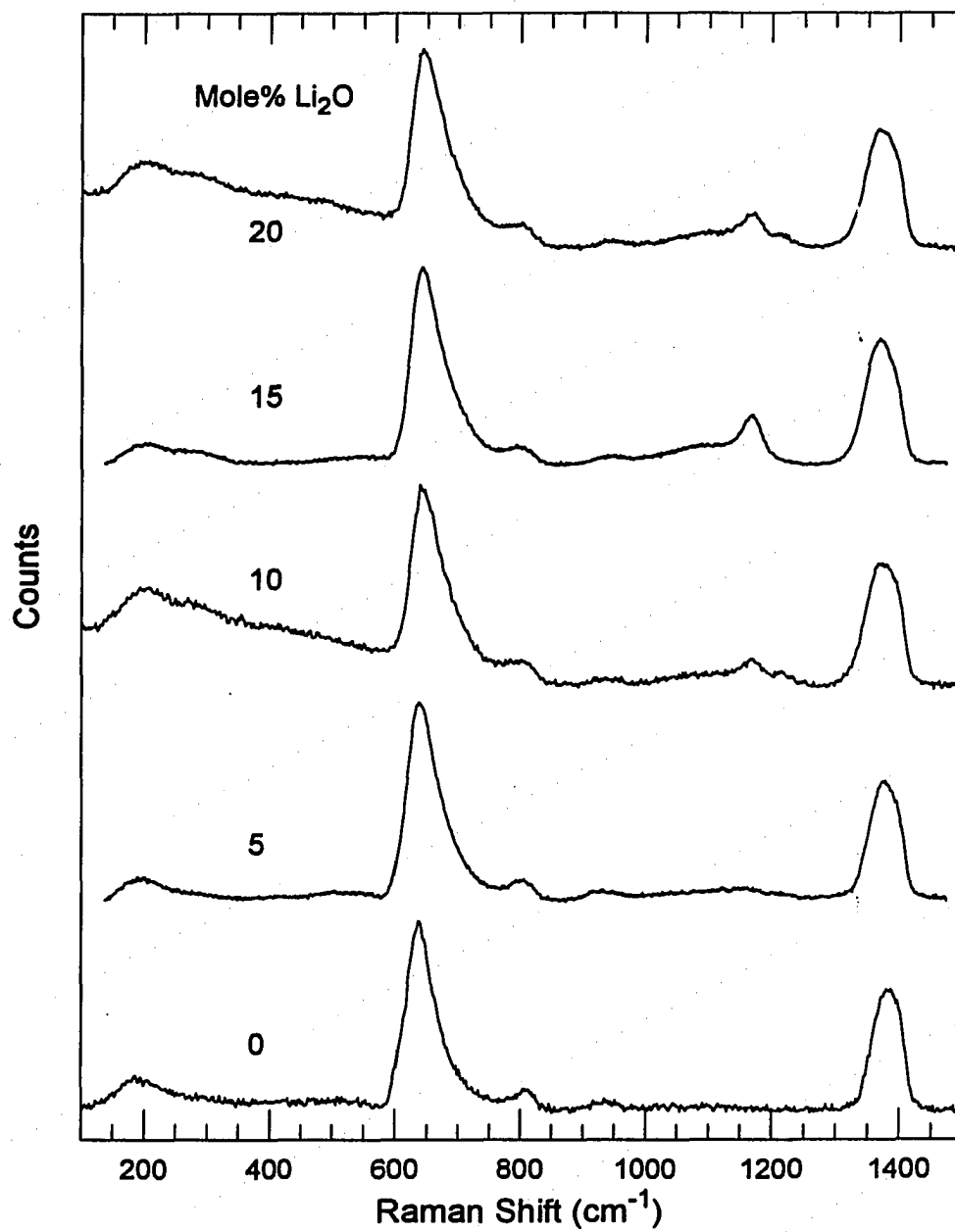


Figure 4.20 The raman spectra of lithium ultra-phosphate glasses from 0 to 20 mole% Li_2O . the spectra have been offset to improve comparison.

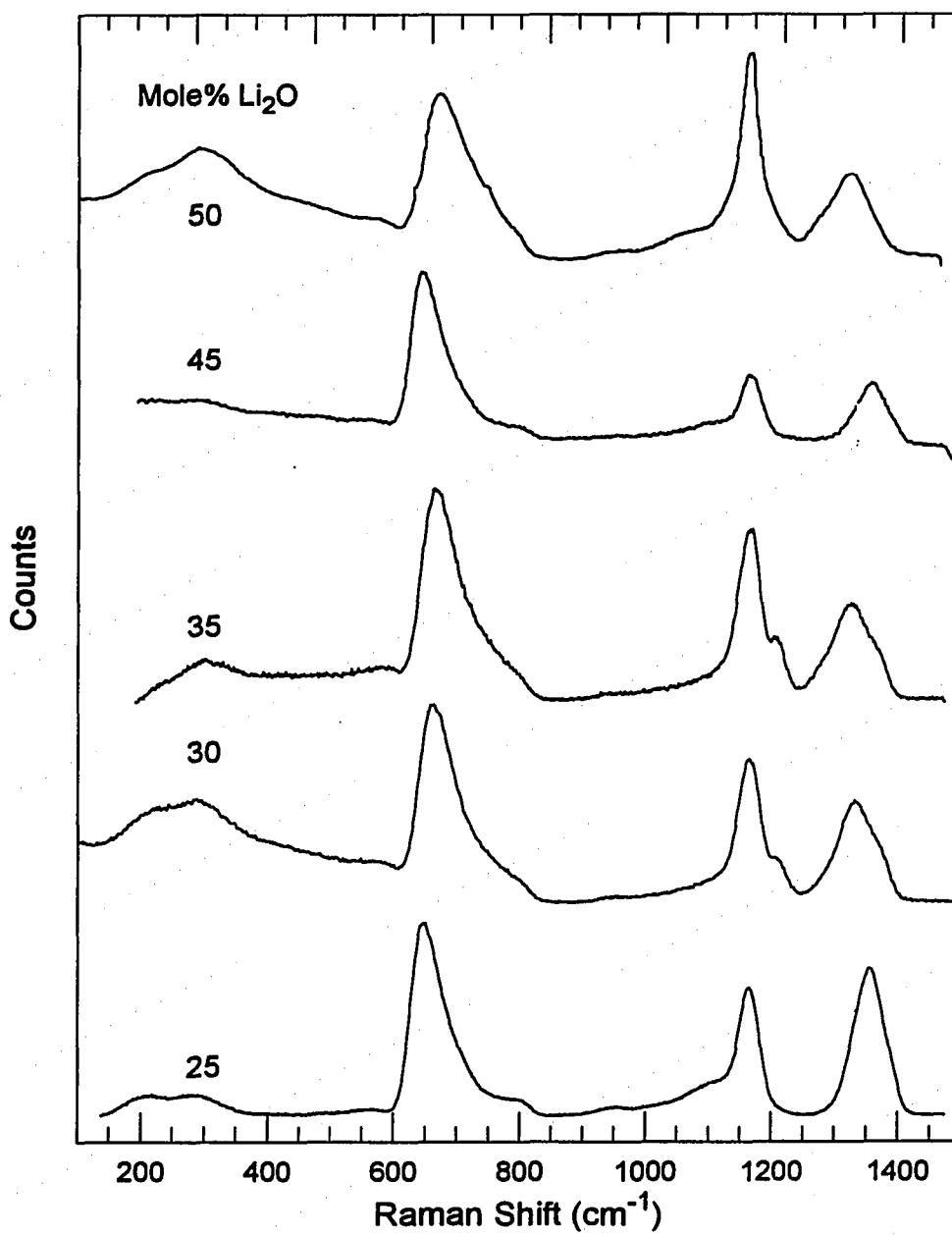


Figure 4.21 The raman spectra of lithium ultra-phosphate glasses from 0 to 20 mole% Li_2O . the spectra have been offset to improve comparison. The 50 mole% data is from reference [1].

Table 4.15 The wavenumbers of the centers of the different Raman scattering modes in lithium ultra-phosphate glasses. The 50 mole% data is from reference [1].

Mole% Li ₂ O									Assignment (cm ⁻¹)
0	5	10	15	20	25	30	35	50	
189.5	193.5	197.6 273.0	200.5 276.5	201.6 282.3	214.3 280.0	225.8 286.3	235.0 300.7	217.7 290.3	POP bending/ cation
500.0	521.9		515.0	491.9	559.9	572.6	577.2	573.7	deformation vibrations
637.1	635.9	641.1	639.4	645.2	649.8	665.3	667.1	674.0	v(POP) _g
806.5	801.8	806.5	798.4	798.4	801.8	798.4	791.5	798.4	
931.5	926.3	939.5 1085.0	943.5 1085.3	943.5 1096.8	953.9 1099.1	951.6	943.5	947.0 1064.5	v(POP) _{as}
	1144.0 1213.1	1169.4	1168.2	1169.4 1217.7	1164.7	1165.3 1209.7	1168.2 1206.2	1164.7	v(PO ₂) _g
1383.1	1375.6	1375.0	1372.1	1371.0	1354.8	1334.7	1327.2	1323.7	v(P=O) _g , v(PO ₂) _{as}

4.3.2.3 The $\text{Na}_2\text{O}+\text{P}_2\text{O}_5$ System

Nelson et al. [74] report the only Raman spectra of alkali ultra-phosphate glasses in open literature. The glasses contain a maximum of 75 mole% P_2O_5 and the Raman spectra are dominated by peaks at 690cm^{-1} , $(\text{POP})_{\text{sym}}$, and 1163cm^{-1} with less intense bands at 1290cm^{-1} , $\text{P}=\text{O}_{\text{sym}}$, and 290cm^{-1} , POP bend. Through comparison with the Raman spectra of crystalline $(\text{NaPO}_3)_n$ the intense line at 1163cm^{-1} has been assigned to the $(\text{PO}_2)_{\text{sym}}$ stretch representing the symmetric stretch of the Q^2 chain unit [4]. The asymmetric mode of this stretch, $(\text{PO}_2)_{\text{asym}}$, is at 1267cm^{-1} in the Raman spectra of crystalline $(\text{NaPO}_3)_n$, this makes the assignment of the mode at 1290cm^{-1} in the glassy spectra unresolved between the $\text{P}=\text{O}_{\text{sym}}$ stretch and the $(\text{PO}_2)_{\text{asym}}$ stretch. With increasing P_2O_5 content, the intensities of the $(\text{POP})_{\text{sym}}$ and $\text{P}=\text{O}$ (or $(\text{PO}_2)_{\text{asym}}$) bands increase as compared to the $(\text{PO}_2)_{\text{sym}}$ band while the $\text{P}=\text{O}$ (or $(\text{PO}_2)_{\text{asym}}$) peak shifts to higher frequency. Such changes are consistent with the conversion of Q^2 (chain) to Q^3 (3-D crosslinked) phosphate tetrahedral units, however, the spectra contain small features at 1000cm^{-1} suggesting the presence of water or hydroxyl groups in the glass which would create a disproportionately high fraction of Q^2 units.

Raman spectra were obtained for sodium ultra-phosphate glasses containing from 0 to 45 mole% Na_2O . Figure 4.22 and 4.23 shows and Table 4.16 lists the unpolarised Raman spectra of sodium ultra-phosphate glasses obtained in this study. shows the peak shift of the different Raman lines. As in the study of Nelson et al., the addition of alkali causes the $(\text{PO}_2)_{\text{sym}}$ mode to grow into the spectra near 1180cm^{-1} and become the largest and sharpest feature in the Raman spectra at the metaphosphate composition. Concomitant with the growth of the $(\text{PO}_2)_{\text{sym}}$ mode, the $(\text{POP})_{\text{sym}}$ and $(\text{POP})_{\text{asym}}$ modes, indicating the existence of BO's on the PO_4 tetrahedra, decrease in relative intensity. Also, the $(\text{POP})_{\text{sym}}$ mode moves to higher wavenumbers. The POP bending mode at 200cm^{-1} shifts to higher wavenumbers with increasing alkali and another bending mode grows in at 290cm^{-1} . The assignment of the peak at 1390cm^{-1} is well defined as the $\text{P}=\text{O}_{\text{sym}}$ stretch at the P_2O_5 composition, however, between 20 and 50 mole% alkali, this line begins shifting to lower wavenumbers, the peak shape becomes increasingly asymmetric and its intensity decreases as alkali is added. Due to the

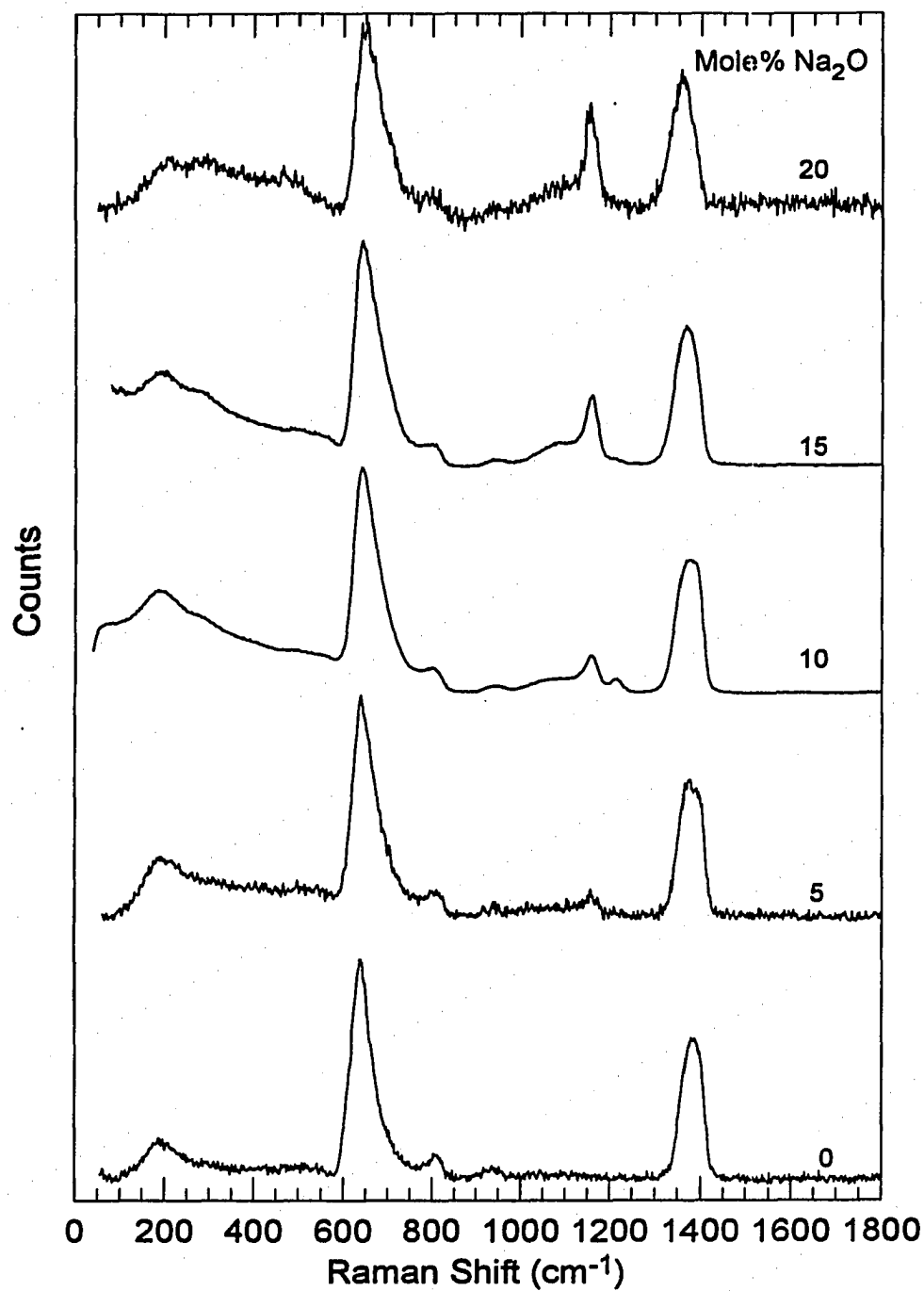


Figure 4.22 The Raman spectra of glasses in the system $x \text{ Na}_2\text{O} + (1-x) \text{ P}_2\text{O}_5$, where $0 \leq x \leq 0.25$. The spectra have been offset to improve comparison.

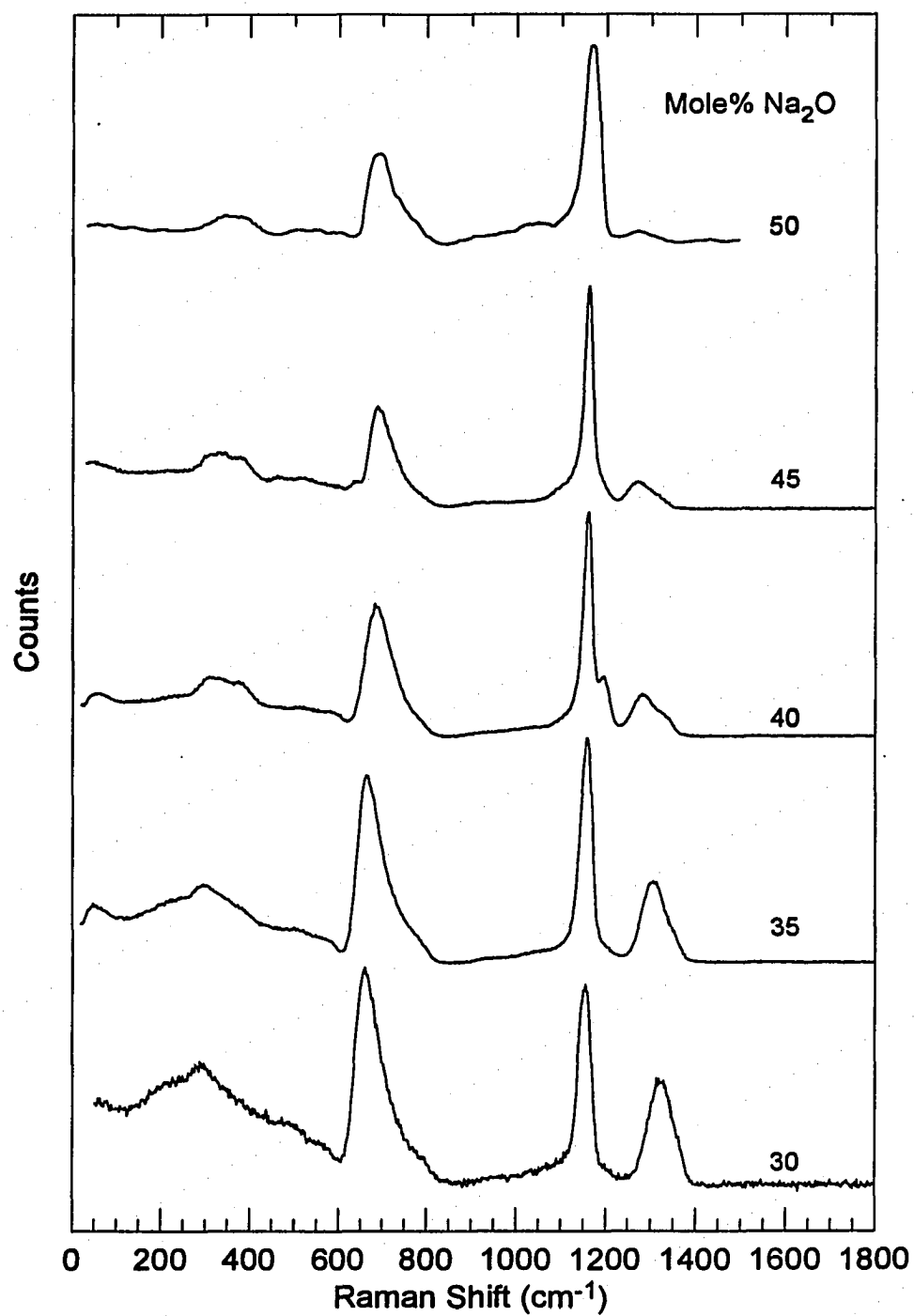


Figure 4.23 The Raman spectra of glasses in the system $x \text{ Na}_2\text{O} + (1-x) \text{ P}_2\text{O}_5$, where $0.30 \leq x \leq 0.45$. The spectra have been offset to improve comparison. The 50 mole% spectra is from ref. [74].

Table 4.16 The wavenumbers of the centers of the different Raman scattering modes in sodium ultra-phosphate glasses. The values in paraenthesis are the depolarization ratios.

Mole% Na ₂ O										Assignment
0	5	10	15	20	25	30	35	40	45	
189.5	184.3 (0.46)	189.5 (0.75) 274.2	193.5 (0.75) 282.3	205.6 294.4	209.7 286.3	209.7 (0.75) 286.3 (0.75)	235.0 (0.75) 300.7 (0.75)	304.1 (0.75) 373.3	328.3 (0.75) 380.2	POP bending/ cation
500.0	525.3	520.2	520.2	471.8	487.9	496.0	508.1 (0.75)	515.0	515.0	deformation vibrations
637.1	640.6 (0.186)	641.1 (0.04)	641.1 (0.004)	649.2	653.2	661.3 (0.415)	667.1 (0)	687.8 (0)	687.8	v(POP) _s
806.5	801.8 (0.43)	802.4 (0.375)	802.4 (0.5)	794.4	794.4	786.3	784.6	784.6		
931.5	940.1	939.5 1076.6 (0)	943.5 1084.7 (0)	939.5	947.6	959.7	943.5 1050.7			v(POP) _{as}
	1156.7 (~0)	1161.3 (0) 1213.7 (0)	1157.3 (0.007)	1157.3	1153.2	1153.2 (0.435)	1157.8 (0.005)	1161.3 (0) 1195.9 (0.19)	1161.3 (0.009)	v(PO ₂) _s
1383.1	1377.9 (0.269)	1375.0 (0.157)	1366.9 (0.175)	1358.9	1342.7	1322.6 (0.516)	1306.5 (0.236)	1282.3 (0.533)	1271.9 (0.454) 1330.6	v(P=O) _s , v(PO ₂) _{as}

shift of this peak, its assignment to either the $\text{P}=\text{O}_{\text{sym}}$ stretch or the $(\text{PO}_2)_{\text{asym}}$ stretch becomes unclear. Finally, with increasing alkali, cation modes, representing the weak alkali-oxygen stretches, have grown into the spectra between 50 and 60 cm^{-1} .

Another interesting feature in the spectra is the appearance of high frequency shoulders on both the $(\text{PO}_2)_{\text{sym}}$ and $(\text{PO}_2)_{\text{asym}}$, or $\text{P}=\text{O}$, for the 38 and 40 mole% sodium phosphate glasses. These features have not been assigned and are not observed in the Raman spectra of hydrated ultra-phosphate glasses [4].

4.3.2.4 High Temperature Raman Spectra

To investigate the high temperature dynamics of Raman-active vibrational modes, several high temperature Raman spectra were gathered for a 40 mole% Na_2O ultra-phosphate glass. The spectra were obtained using the same optical bench and configuration as was used to obtain the other Raman spectra. The glass sample was heated in situ within a tube furnace outfitted with windows to allow creation and detection of the Raman scatter. The phosphate glass sample was hermetically sealed inside a silica tube. The tube was specially made with a flat bottom to decrease scatter. The sample tube was hung in the furnace using platinum wire. Temperature was monitored by a thermocouple placed against the silica tube holding the glass sample. Raman spectra were gathered in 50-100°C increments to 900°C. The temperature was held at 900°C for 2hrs., then Raman spectra were gathered in 50-100°C increments down to room temperature. During cooling, the silica tube cracked at ~350°C due to the thermal expansion difference between the silica tube and phosphate glass.

Scattering in the low frequency region of the spectra was enhanced with increasing temperature due to increased thermal population of low energy vibrational states [118]. To account for such temperature dependence, Bose-Einstein populations were subtracted from each of the spectra [118].

The high temperature reduced Raman spectra of the 40mole% Na_2O ultra-phosphate glass are shown in Figures 4.24, 4.25, and 4.26. The peak centers of all Raman modes decrease with increasing temperature and FWHM of peaks increase.

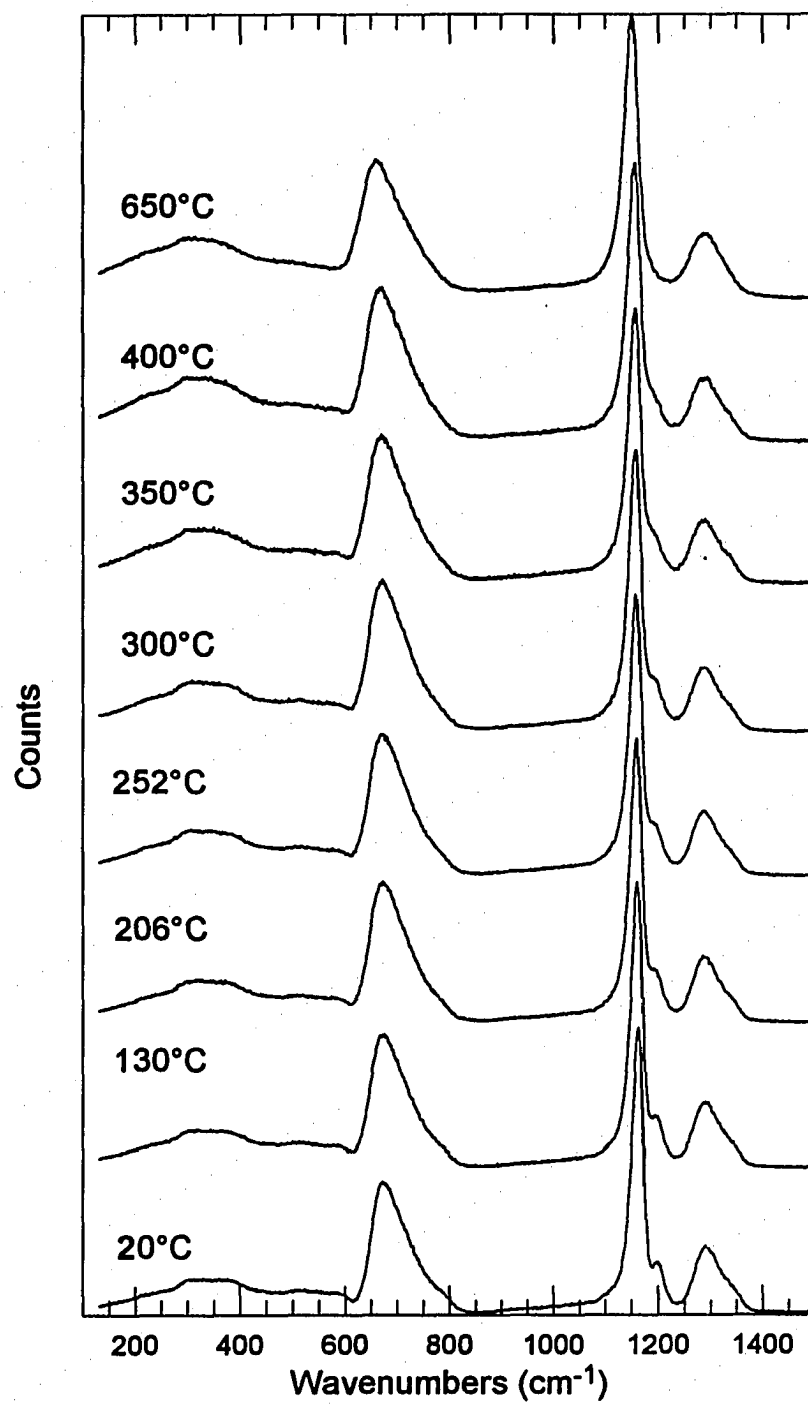


Figure 4.24 The Raman spectra of the glass 0.40 Na₂O + 0.60 P₂O₅ heated from room temperature to 650°C.

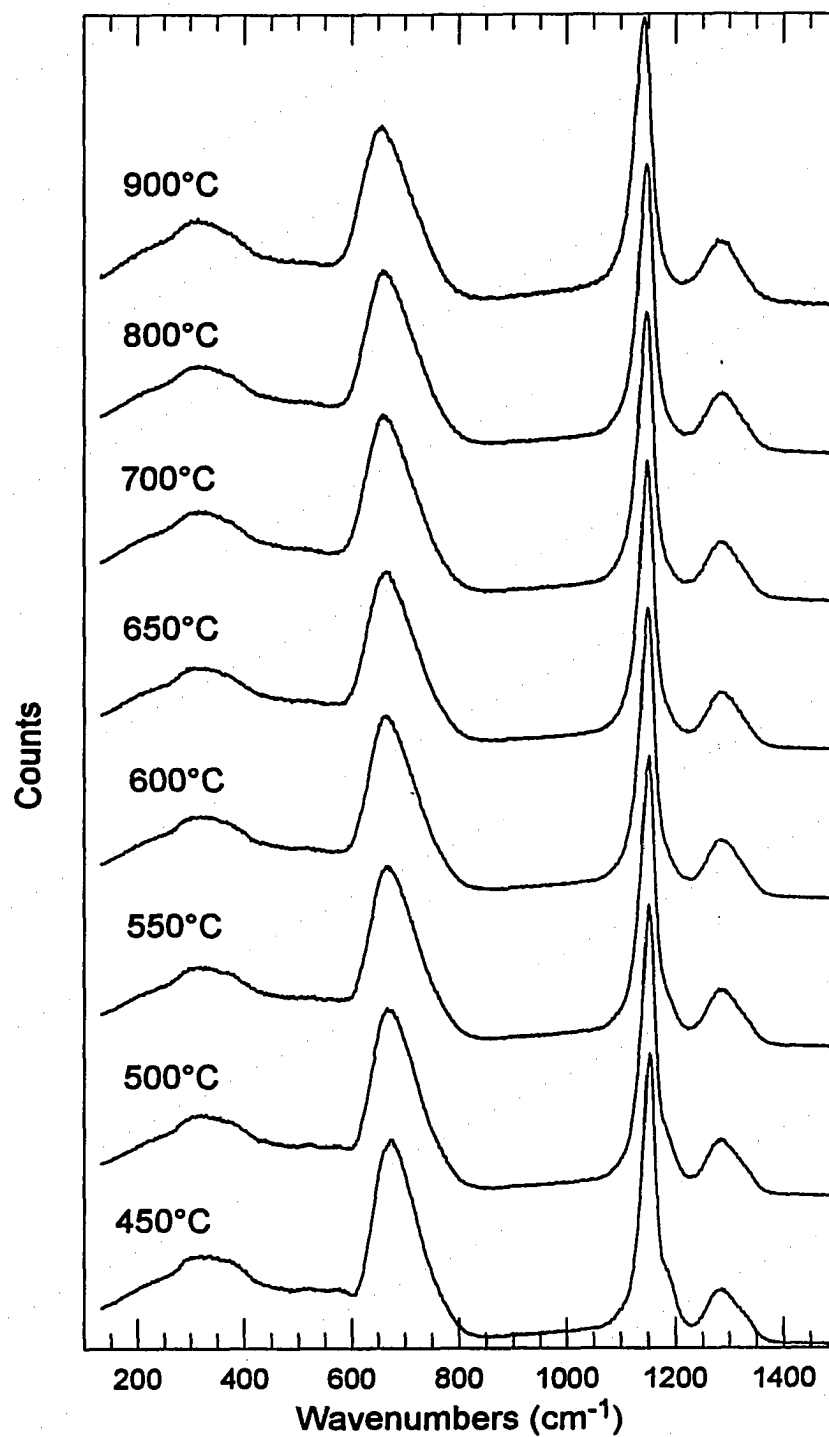


Figure 4.25 The Raman spectra of the glass $0.40 \text{ Na}_2\text{O} + 0.60 \text{ P}_2\text{O}_5$ cooled from 900°C to 450°C .

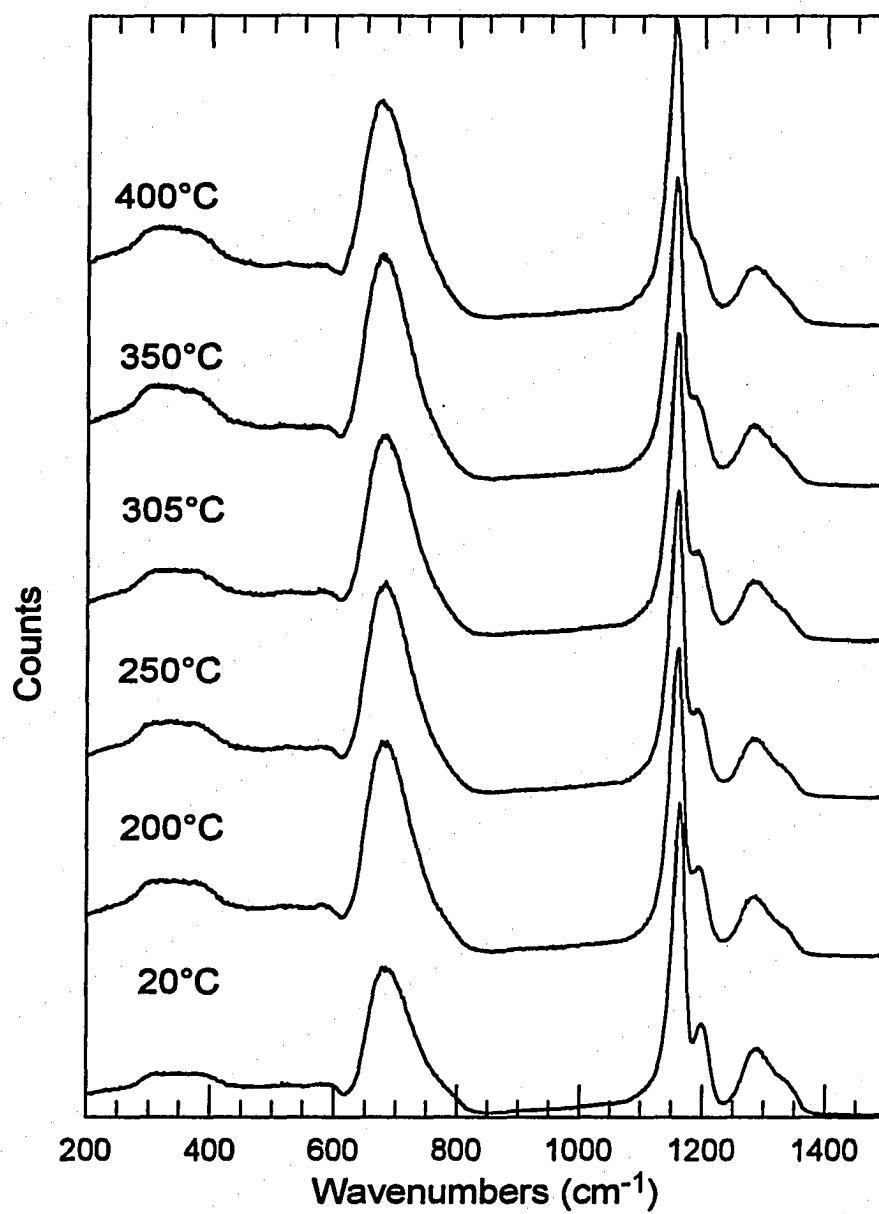


Figure 4.26 The Raman spectra of the glass $0.40 \text{ Na}_2\text{O} + 0.60 \text{ P}_2\text{O}_5$ cooled from 400°C to room temperature. The spectra have been offset to improve comparison.

4.3.3 ^{31}P MAS-NMR Spectroscopy

NMR analyses extract structural information from the interactions of nuclei with their environment. Interactions include those between nuclear magnetic dipole moments, those between nuclear electrical quadrupole moments and electric field gradients at the nuclear site, and chemical shifts generated by the particular electron distribution about a resonating nucleus. NMR spectra are obtained by placing a sample in a magnetic field thereby aligning all of the magnetizations. The magnetization is then tipped away from the principal axis and the precessional recovery of the magnetization to the principal axis induces a signal in a rf coil placed around the sample. Several of such free induction decays are signal averaged and their real part is Fourier transformed to give the NMR resonance absorbance spectrum. Resonances are reported in parts-per-million (ppm) away from the resonance of a standard material. For ^{31}P MAS-NMR the standard reference material is 85% for phosphoric acid solution. For solids NMR, the sample is spun at 54.7° to the external magnetic field to time-average the dipole-dipole interactions, which broaden the NMR resonances.

Because ^{31}P is a spin $\frac{1}{2}$ nuclei, the nuclear charge distribution is spherically symmetric, therefore, no quadrupole interactions exist and chemical shift is the dominant interaction. NMR chemical shifts are sensitive to variations in the structural environment which alter the electronic distribution around the resonating nucleus. Such changes include: the number and electronegativity of bonded ligands, the P-O-P bond angles, and the π -bond character of phosphate bonds. Like ^{29}Si MASS-NMR for the silicates [119], increasing polymerization of the phosphate network leads to increased shielding, hence more negative chemical shifts (Table 4.17).

In addition, the cation potential of modifying ligands can affect the chemical shift. For example, the chemical shift of the Q^2 resonance in NaPO_3 ($Z/a = 1.03\text{\AA}^{-1}$) is at -19 ppm while the same resonance in LiPO_3 ($Z/a = 1.47\text{\AA}^{-1}$) is at -23.2 ppm. Therefore, more σ electron withdrawal increases shielding of the nucleus. Lechter and Van Wazer [120] have summarized all such effects in the following relationship:

$$\Delta\delta_{\text{iso}} = a\Delta n_{\pi} + b\Delta\chi + c\Delta\theta_{\sigma} \quad (4.4)$$

where a , b and c are constants, Δn_{π} is the change in π bond order, $\Delta\chi$ is the change in electronegativity of the nearest neighbor atoms to P and $\Delta\theta_{\sigma}$ is the change in σ bond angle.

The isotropic chemical shift can be divided into the diagonal components of the chemical shift tensor in its principal axis system where:

$$\sigma_{\text{iso}} = 1/3 (\sigma_{11} + \sigma_{22} + \sigma_{33}). \quad (4.5)$$

Table 4.17 The approximate chemical shift ranges for different types of phosphate tetrahedra in phosphate materials.

Chemical Species	Chemical Shift Range (ppm)
Q^3	-55 to -35
Q^2	-30 to -18
Q^1	0 to 5
Q^0	8 to 15

In this axis system σ_{33} is aligned with the external field, therefore, when a molecule is axially symmetric (i.e. has C_{3v} symmetry), $\sigma_{11} = \sigma_{22}$. To better describe the symmetry of the tensor, the following relationships have been developed:

$$\delta = \sigma_{\text{iso}} - \sigma_{33} \quad (4.6)$$

$$\eta = (\sigma_{22} + \sigma_{11})/\delta. \quad (4.7)$$

For an axially symmetric tensor, the asymmetry parameter, η , is zero, and for a spherically symmetric tensor the anisotropy, δ , and asymmetry parameter are zero, when both are non-zero the tensor is asymmetric.

4.3.3.1 Vitreous P_2O_5

The ^{31}P MAS-NMR spectrum of v- P_2O_5 is shown in Figure 4.27. The spectrum was obtained on a Bruker spectrometer operating at 109.3 Mhz at a spinning speed of ~3.7 KHz. A single isotropic resonance was measured at -54.5 ppm (relative to an 85% H_3PO_4 solution), the remaining peaks are spinning sidebands. The isotropic chemical shift of -54.5 is consistent with those reported for v- P_2O_5 and crystalline branching phosphate units [16, 70], and is the resonance of a Q^3 species. The diagonal components of the chemical shift tensor were calculated using the graphical methods of Herzfeld and Berger [104] and are given in Table 4.18. The convention of the assignment of the principal components is that used by Hayashi and Hayamizu [121] where $|\sigma_{33} - \sigma_{iso}| > |\sigma_{22} - \sigma_{iso}| \geq |\sigma_{11} - \sigma_{iso}|$. The non-zero value of both δ and η indicate the chain P atoms are not axially symmetric.

4.3.3.2 The $Li_2O+P_2O_5$ System

The ^{31}P MAS-NMR spectra of lithium ultra-phosphate glasses are shown in Figures 4.28 and 4.29. The spectra were obtained on a Chemagnetics console interfaced to a General Electric 1280 data station at 80.8 Mhz and a spinning speed of ~6 kHz. Isotropic resonances were found in two chemical shift ranges, -54.2 ppm to -40.8 ppm and -34 ppm to -23ppm. The more shielded peak is the dominate feature up to 35mole% alkali, then at larger alkali concentrations the more deshielded peak is the dominant feature. The P species responsible for these resonances can be identified through comparison of their isotropic chemical shifts with those from a number of phosphate materials [16, 70, 71]. The more shielded resonances arise from Q^3 units while Q^2 units are responsible for the more deshielded resonances. The relative peak area of each site, including contributions from the respective spinning sidebands, to calculate the relative fraction of each phosphorus species (Table 4.18).

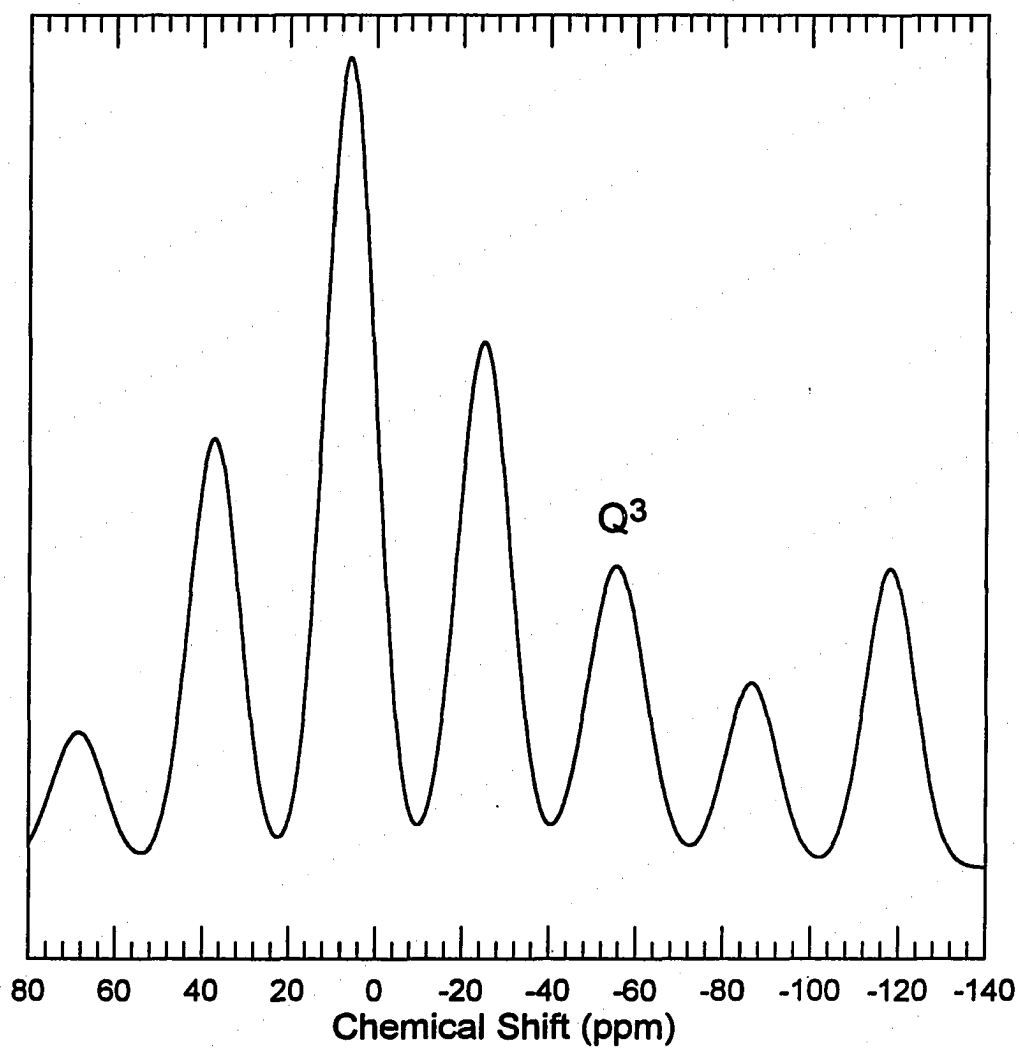


Figure 4.27 The ^{31}P MAS-NMR spectrum of $\nu\text{-P}_2\text{O}_5$. The peak labeled Q^3 is the resonance due to a Q^3 unit, the remaining peaks are spinning sidebands.

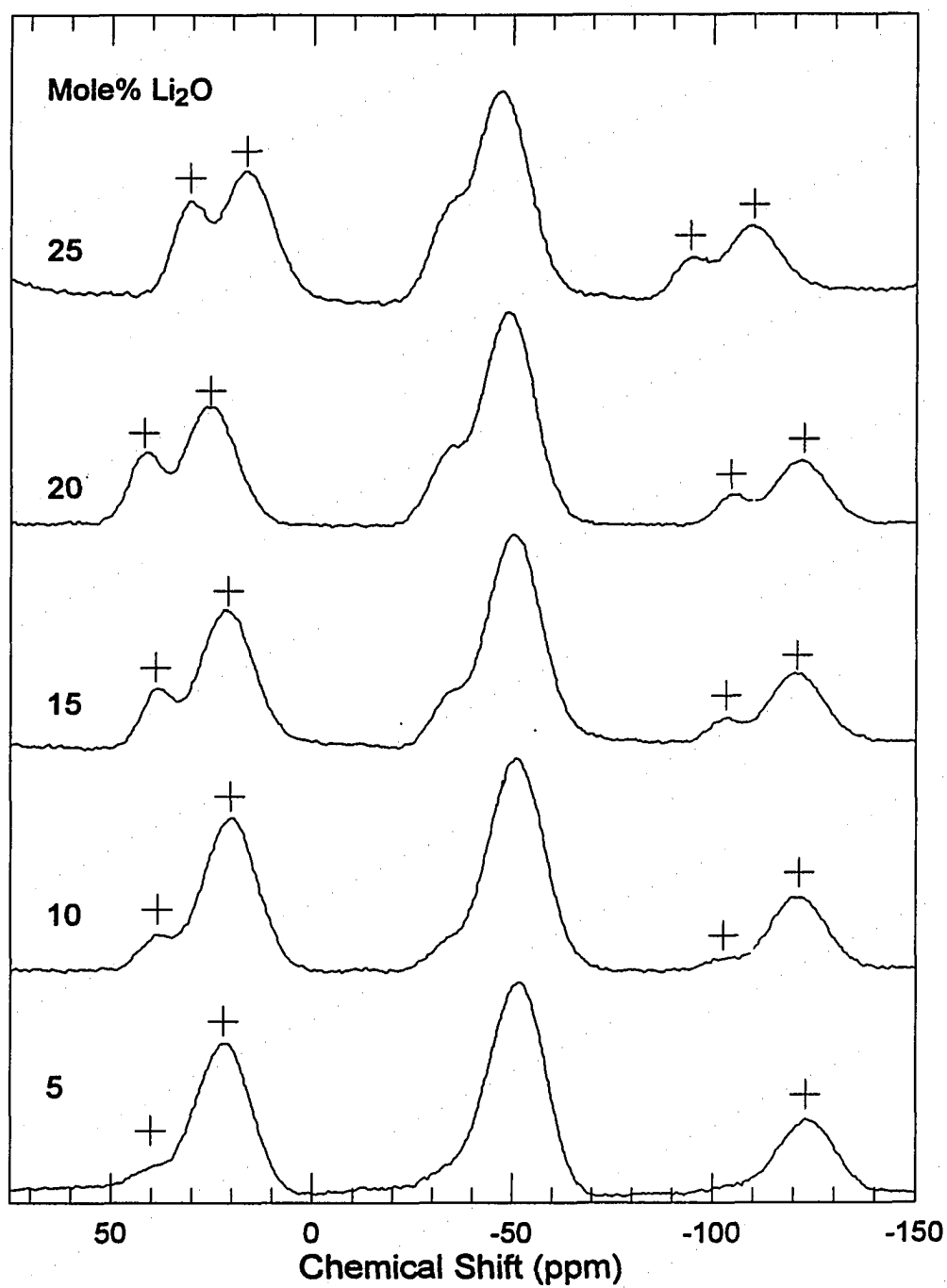


Figure 4.28 The ^{31}P MAS-NMR spectra of lithium ultra-phosphate glasses. The peaks marked with the (+) are spinning sidebands. The spectra have been offset to improve comparison.

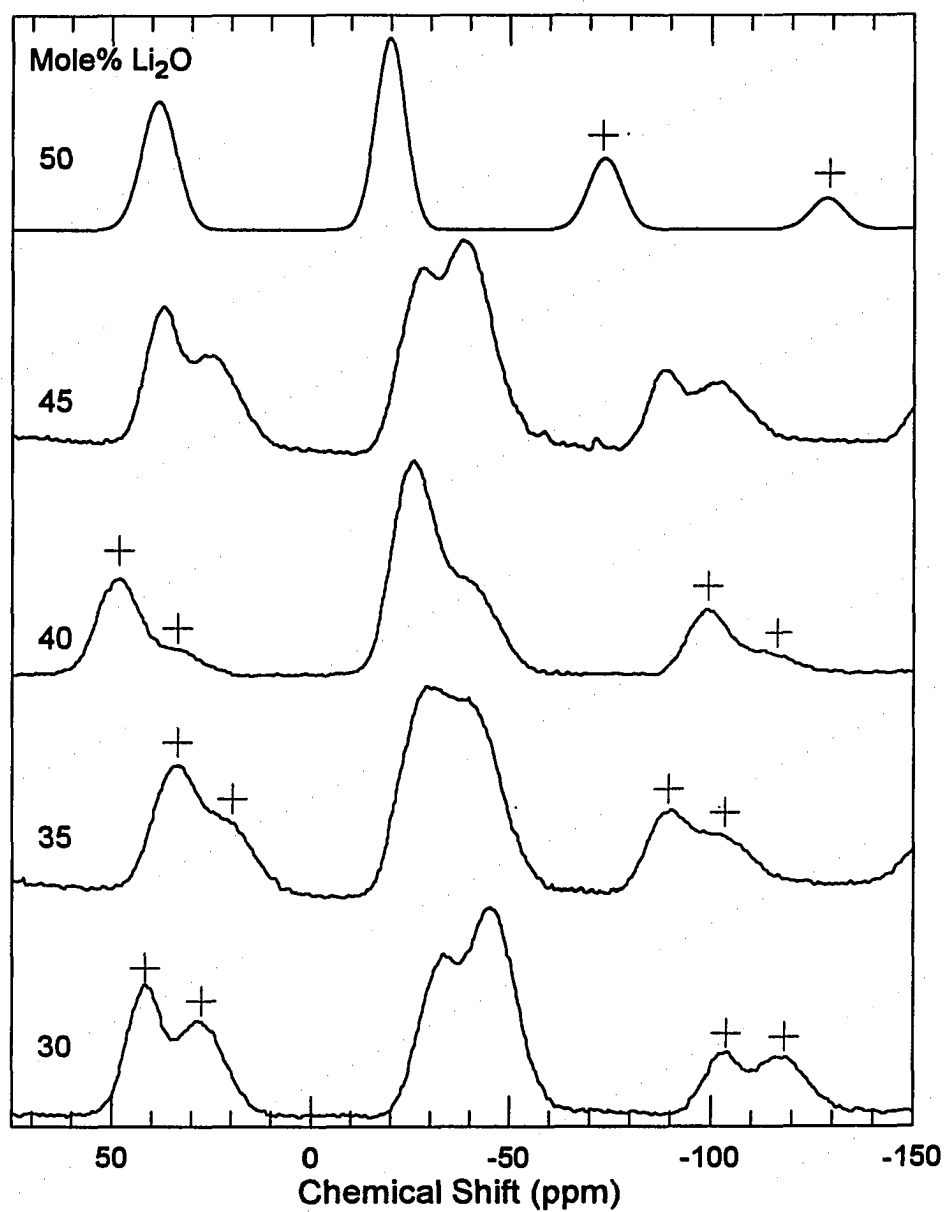


Figure 4.29 The ^{31}P MAS-NMR spectra of lithium ultra-phosphate glasses. The peaks marked with the (+) are spinning sidebands. The spectra have been offset to improve comparison.

Table 4.18 The Q^3 and Q^2 site distributions in the system $x \text{Li}_2\text{O} + (1-x) \text{P}_2\text{O}_5$ calculated from the ^{31}P MAS-NMR spectra.

Li_2O (mole%)	Q^3 (%)	FWHM (ppm)	Q^2 (%)	FWHM (ppm)
0	100	16.00	0	-
5	98.13	16.28	1.87	-
10	89.6	16.307	10.4	10.57
15	81.82	16.06	18.18	8.55
20	76.27	15.01	23.73	10.78
25	76.49	16.05	23.51	9.39
30	58.94	14.49	41.06	11.24
35	54.08	18.255	45.92	12.26
40	28.52	18	71.48	11.64
45	61.1	-	38.9	
50	0	-	100	10.1

The diagonal components of the chemical shift tensor were calculated using the graphical methods of Herzfeld and Berger [104] and are given in Table 4.19. The convention of the assignment of the principal components is that used by Hayashi and Hayamizu [121] where $|\sigma_{33} - \sigma_{iso}| > |\sigma_{22} - \sigma_{iso}| \geq |\sigma_{11} - \sigma_{iso}|$. For both Q^3 and Q^2 species, the non-zero value of both δ and η indicate the P atoms are not axially symmetric in either species. For the Q^3 species, the asymmetry parameter increases while δ decreases with increasing Li_2O content indicating significant modifications to the symmetry of the electron distributions around the P nucleus is occurring (Table 4.20). On the contrary, for the Q^2 species there is little change in the δ or η with increasing Li_2O content indicating no significant modifications to the symmetry of the electron distributions around the P nucleus is occurring. The FWHM of Q^3 peaks increases with those of Q^2 do not increase with the addition of Li_2O .

4.3.3.3 The $\text{Na}_2\text{O}+\text{P}_2\text{O}_5$ System

The ^{31}P MAS-NMR spectra of lithium ultra-phosphate glasses are shown in Figures 4.30 and 4.31. The spectra were obtained on a Chemagnetics console interfaced to a General Electric 1280 data station at 80.8 Mhz and a spinning speed of ~6kHz. Isotropic resonances

Table 4.19 The isotropic chemical shift and diagonal chemical shift tensor elements of glasses in the system $x \text{Li}_2\text{O} + (1-x) \text{P}_2\text{O}_5$.

Li_2O (mole%)	Q^3				Q^2			
	σ_{iso} (ppm)	σ_{11} (ppm)	σ_{22} (ppm)	σ_{33} (ppm)	δ_{iso} (ppm)	σ_{11} (ppm)	σ_{22} (ppm)	σ_{33} (ppm)
0	-54.2	73.6	23.6	-261	^a	^a	^a	^a
5	-53.4	58.1	14.5	-232.8	-34	^b	^b	^b
10	-51.7	65.87	-4.73	-216.2	-33.3	97.1	16.4	-213.4
15	-49.6	52.568	18.46	-219	-32.9	106.47	32.46	-237.6
20	-49	55.167	14.367	-216.5	-34	97.067	34.26	-233.3
25		^b	^b	^b		^b	^b	^b
30	-45.5	57.9	15.2	-209.6	-33.8	98.233	36.533	-236.1
35	-40.3	54.7	-21.9	-153.7	-29.5	82	0.9	-171.4
40	-40.8	65.23	-10.96	-176.7	-26	84.1	25.7	-187.8
50	^a	^a	^a	^a	-23	115.1	36.7	-220.8

^a No isotropic peak found.

^b Herzfeld-Berger parameters failed to converge.

Table 4.20 The anisotropy (δ) and asymmetry parameters (η) for lithium ultra-phosphate glasses.

Li_2O (mole%)	Q^3		Q^2	
	δ	η	δ	η
0	0.242248	-309.6	^a	^a
5	0.243032	-269.1	^b	^b
10	0.429145	-246.77	0.448084	-270.15
15	0.201018	-254.51	0.361501	-307.09
20	0.243534	-251.3	0.315124	-298.96
25	^b	^b	^b	^b
30	0.260207	-246.15	0.304899	-303.54
35	0.675525	-170.09	0.571529	-212.85
40	0.560765	-203.80	0.360939	-242.7
50	^a	^a	0.39636	-296.7

^a No isotropic peak found.

^b Herzfeld-Berger parameters failed to converge.

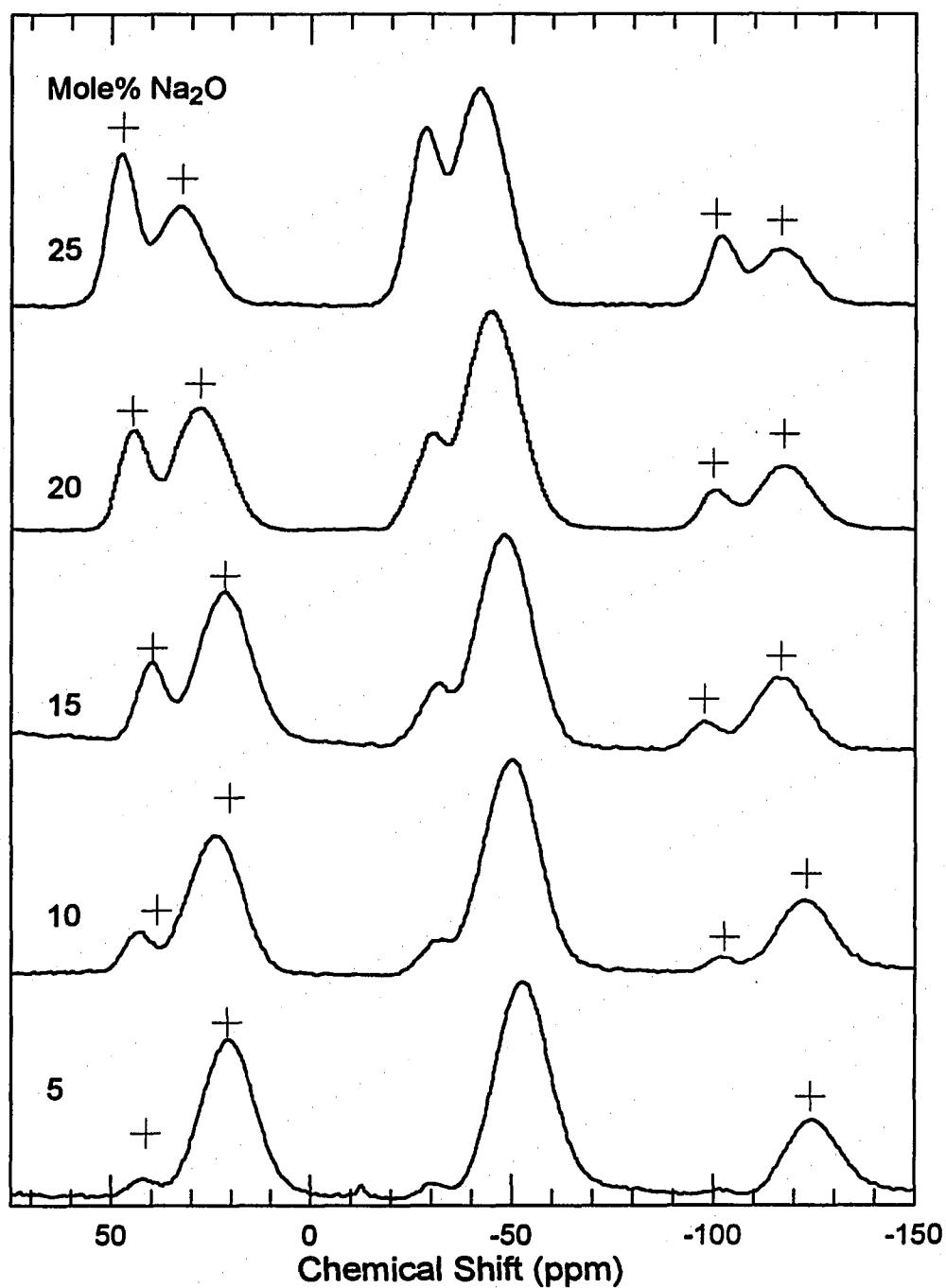


Figure 4.30 The ^{31}P MAS-NMR spectra of sodium ultra-phosphate glasses. The peaks marked with the (+) are spinning sidebands. The spectra have been offset to improve comparison.

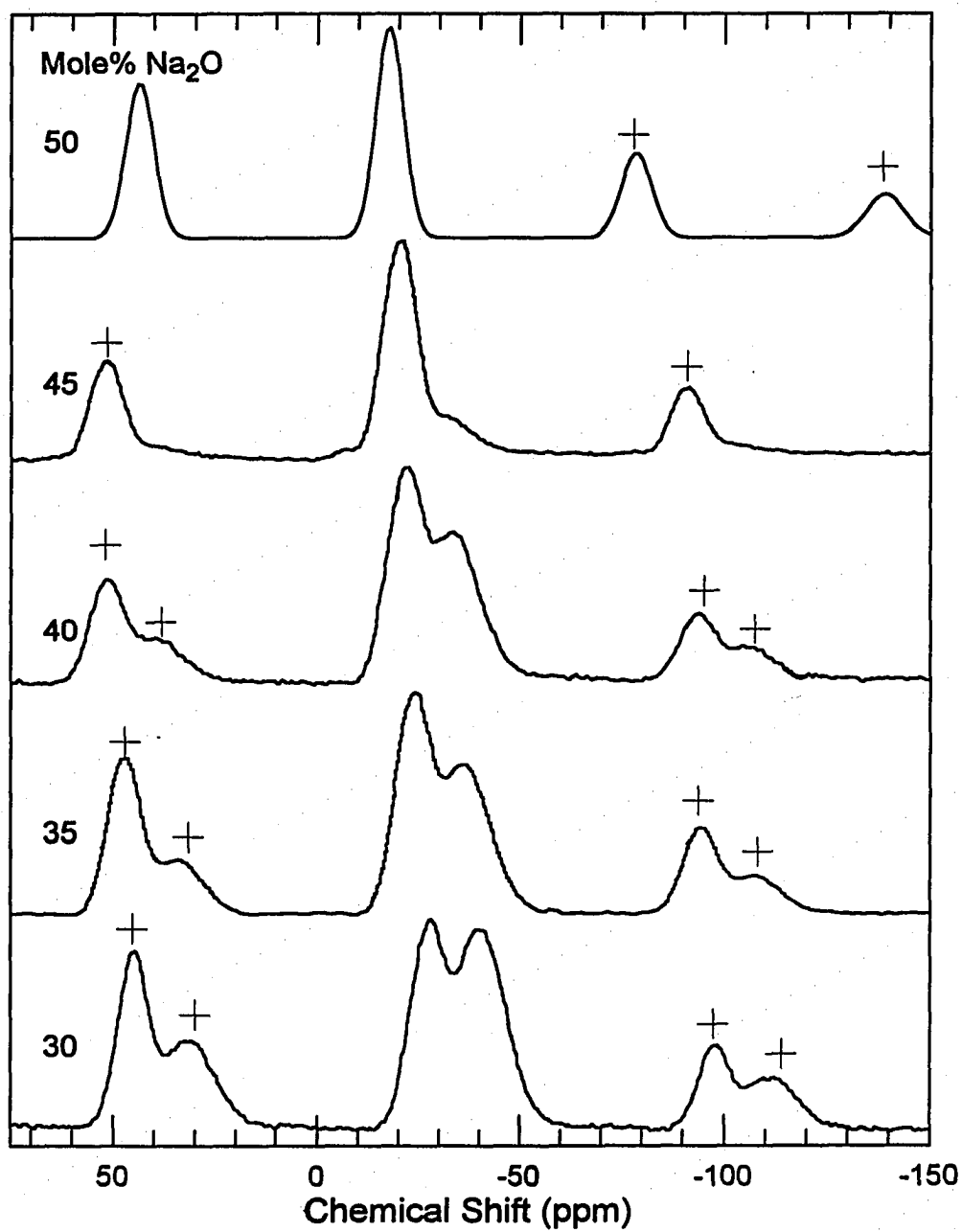


Figure 4.31 The ^{31}P MAS-NMR spectra of lithium ultra-phosphate glasses. The peaks marked with the (+) are spinning sidebands. The spectra have been offset to improve comparison.

were found in two chemical shift ranges, -54.2ppm to -40.8ppm and -34ppm to -23ppm. The more shielded peak is the dominate feature up to 35mole% alkali, then at larger alkali concentrations the more deshielded peak is the dominant feature. The P species responsible for these resonances can be identified through comparison of their isotropic chemical shifts with those from a number of phosphate materials [16, 70, 71]. The more shielded resonances arise from Q^3 units while Q^2 units are responsible for the more deshielded resonances. The relative peak area of each site, including contributions from the respective spinning sidebands, to calculate the relative fraction of each phosphorus species (Table 4.21).

Table 4.21 The Q^3 and Q^2 site distributions in the system x $Na_2O + (1-x) P_2O_5$ calculated from the ^{31}P MAS-NMR spectra.

Na_2O (mole%)	Q^3 (%)	FWHM (ppm)	Q^2 (%)	FWHM (ppm)	Q^1 (%)
0	100	16.00	0	-	-
5	95.52	16.32	4.48	6.16	-
10	90.53	16.33	9.47	8.58	-
15	82.57	15.90	17.43	8.90	-
20	75.00	16.01	25.00	8.89	-
25	63.34	14.95	36.67	8.82	-
30	52.75	14.58	47.25	9.75	-
35	40.34	15.17	59.66	9.71	-
40	42.10	15.14	57.9	10.09	-
45	9.64	12.28	85.61	9.76	4.75
50	0	-	100	8.5	-

The diagonal components of the chemical shift tensor were calculated using the graphical methods of Herzfeld and Berger [104] and are given in Table 4.22. The convention of the assignment of the principal components is that used by Hayashi and Hayamizu [121] where $|\sigma_{33} - \sigma_{iso}| > |\sigma_{22} - \sigma_{iso}| \geq |\sigma_{11} - \sigma_{iso}|$. For both Q^3 and Q^2 species, the non-zero value of both δ and η indicate the P atoms are not axially symmetric in either species (Table 4.23). For the Q^3 species, the asymmetry parameter increases while δ decreases with increasing Li_2O

Table 4.22 The chemical shift anisotropies of glasses in the system $x \text{Na}_2\text{O} + (1-x) \text{P}_2\text{O}_5$.

Na_2O (mole%)	Q^3				Q^2			
	δ_{iso} (ppm)	σ_{11} (ppm)	σ_{22} (ppm)	σ_{33} (ppm)	δ_{iso} (ppm)	σ_{11} (ppm)	σ_{22} (ppm)	σ_{33} (ppm)
0	-54.2	73.6	23.6	-261	^a	^a	^a	^a
5	-53.3	56.035	23.53	-239.4	-31.6	183.32	-18.24	-259.8
10	-50.2	61.867	11.767	-224.2	-32.9	125.13	54.533	-278.3
15	-48.6	59.633	22.333	-227.7	-32.2	109.06	36.967	-242.6
20	-45.4	62.3	9.6	-208.1	-31.6	95.1	48.1	-238
25	-42.8	59.867	8.167	-196.4	-29.1	87.9	36.9	-212.1
30	-40.4	51.933	14.733	-187.1	-28.2	97.167	48.067	-229
35	-36.8	64.267	-8.433	-166.2	-25.9	91.63	36.33	-205.6
40	-33.9	69.8	-11.4	-160.1	-22.1	^b	^b	^b
45	-36.3	54.967	-36.33	-127.5	-20.7	89.8	11.4	-163.3
50	^a	^a	^a	^a	-19	82	20	-160

^a No isotropic peak found.^b Herzfeld-Berger parameters failed to converge.Table 4.23 The anisotropy (δ) and asymmetry parameters (η) for Q^3 and Q^2 species in sodium ultra-phosphate glasses.

Na_2O (mole%)	Q^3		Q^2	
	η	δ	η	δ
0	0.242248	-309.6	^a	^a
5	0.174603	-279.2	0.883007	-342.4
10	0.287876	-261.0	0.287604	-368.1
15	0.208186	-268.7	0.34263	-315.6
20	0.323909	-244.1	0.227713	-309.6
25	0.336516	-230.4	0.278689	-274.5
30	0.253061	-220.5	0.244184	-301.6
35	0.561679	-194.1	0.307701	-269.5
40	0.643423	-189.3	^b	^b
45	1.000687	-136.8	0.54979	-213.9
50	^a	^a	0.440758	-211

^a No isotropic peak found.^b Herzfeld-Berger parameters failed to converge.

content indicating significant modifications to the symmetry of the electron distributions around the P nucleus is occurring. On the contrary, for the Q^2 species there is little change in the δ or η with increasing Li_2O content indicating no significant modifications to the symmetry of the electron distributions around the P nucleus is occurring. The FWHM of Q^3 peaks increases with those of Q^2 do not increase with the addition of Li_2O .

5. DISCUSSION

5.1 Vitreous P_2O_5

As described in Section 2.2.1, the structure of both $v\text{-}P_2O_5$ and the polymorphs of $c\text{-}P_4O_{10}$ are built from interconnected PO_4 tetrahedra each having three bridging and one terminal oxygen. The terminal oxygen on these species has been shown to be a $P=O$ [54, 56]. The ^{31}P MAS-NMR, Raman, and MIR spectra of the $v\text{-}P_2O_5$ prepared for this study are consistent with such a structure.

5.1.1 ^{31}P MAS-NMR

There is a single isotropic resonance at ~ -55 ppm in the ^{31}P MAS-NMR spectrum of $v\text{-}P_2O_5$ indicating the existence of only Q^3 species [16]. The linewidth of this peak is broad (1600Hz) when compared with linewidths in the ^{31}P MAS-NMR spectra of the polymorphs of crystalline P_2O_5 (~ 250 Hz) [16]. The significantly larger value reflects the inherent disorder of amorphous materials for the linewidth is proportional to the distribution of bond lengths and bond angles among the Q^3 species.

The chemical shift of the sheet form of $c\text{-}P_4O_{10}$ has isotropic resonances at - 61.2 and - 57.9 ppm while the molecular and branching forms have single resonances near -46 ppm [70, 16]. The splitting of the isotropic resonance of the Q^3 species in the sheet form of P_2O_5 is due to two different site symmetries for P [10, 17, 16]. The ^{31}P MAS-NMR spectrum of $v\text{-}P_2O_5$ does not show splitting of the isotropic peak, and the chemical shift value of ~ -55 ppm is intermediate to those of the sheet and branching forms of $c\text{-}P_4O_{10}$. Unlike $v\text{-}SiO_2$ where the chemical shift value is near the chemical shift of the corresponding crystal [122, 123] suggesting similar structures, the average Q^3 species in $v\text{-}P_2O_5$ are not similar to those in any of the polymorphs of $c\text{-}P_4O_{10}$. From the position of the Q^3 chemical shift the average structure of $v\text{-}P_2O_5$ resembles a mixture of the sheet and branching forms or interconnected sheets.

Evaluation of the ^{31}P anisotropic chemical shift tensor yields valuable information about the symmetry of phosphorus sites and the distribution of electron density around those sites. An ideal tetrahedron would be both axially and spherically symmetric and $\eta = \Delta\delta = 0$. However, on Q^3 tetrahedra, a large amount of electron density is localized on one bond ($\text{P}=\text{O}$) [54, 56]. Therefore, the species should be axially symmetric, having C_{3v} symmetry. The polymorphs of $\text{c-P}_4\text{O}_{10}$ are axially symmetric (Table 5.1) [16]. Contrary to the results of a previous study [16], the asymmetry parameter for $\text{v-P}_2\text{O}_5$ is not axially symmetric. The spectrum obtained in the present study contains less noise than the spectrum in ref. [16], suggesting the previous tensor analysis may be erred. In support, by analyzing static ^{31}P NMR spectra, Duncann et al. [70] found the ^{31}P shielding parameters of the O form of $\text{c-P}_4\text{O}_{10}$ are not axially symmetric, but $\eta = 0.10$ close to the value found for $\text{v-P}_2\text{O}_5$ ($\eta = 0.15$) in this study. The slight deviation from axial symmetry of the average P-site in $\text{v-P}_2\text{O}_5$ may be explained by the broad distribution of bond angles and bond lengths found in the amorphous material.

Table 5.1 The ^{31}P chemical shielding parameters of the polymorphs of $\text{c-P}_4\text{O}_{10}$ and glassy P_2O_5 .

Form	σ_{11} (ppm)	σ_{22} (ppm)	σ_{33} (ppm)	$\Delta\delta$ (ppm)	σ_{iso} (ppm)	η	Ref.
H	51.7	51.7	-244.4	296 ± 3	-46.7 ± 3	0	[16]
O	35.7	35.7	-211.2	247 ± 5	-46.5 ± 0.5	0	[16]
O	66	35	-240	296	-46	0.10	[70]
O'	24.3	24.3	-232.7	257 ± 3	-61.2 ± 0.3	0	[16]
	31.8	31.8	-237.2	269 ± 3	-57.9 ± 0.3	0	[16]
Glass	38.1	38.1	-240.9	279 ± 3	-54.9 ± 0.5	0	[16]
Glass	73.9	23.7	-261.6	334	-54.5 ± 2	0.15	This Study

The anisotropy of the ^{31}P -chemical shift, $\Delta\delta$, is larger than has previously been reported. Primarily, the change is due to a larger upfield component, σ_{33} . Given the near axial symmetry of the Q^3 species, the σ_{33} tensor axis lies along the $\text{P}=\text{O}$ and the σ_{11} and σ_{22} tensor axes lie in the same plane as the bridging oxygens. Therefore, σ_{33} is more shielded due to a

larger amount of electron density on the Q^3 terminal oxygen than on the bridging oxygens. This observation is consistent with the a Q^3 species consisting of three bridging oxygens and a single terminal oxygen.

5.1.2 Vibrational Spectra

Both the Raman and IR spectra of $v\text{-P}_2\text{O}_5$ resemble those obtained in previous studies [52, 54, 53, 88, and 112]. Figure 5.1 shows the vibrational modes giving rise to the peaks in the MIR and Raman spectra [124]. The main feature of the amorphous vibrational spectra corresponding to the crystalline spectra is a high frequency vibrational mode at $\sim 1390\text{cm}^{-1}$. This absorbance corresponds to the symmetric stretching of a $\text{P}=\text{O}$ terminal oxygen [54]. The peaks in the range $900\text{-}1200\text{cm}^{-1}$ and $600\text{-}850\text{cm}^{-1}$ correspond to asymmetric and symmetric stretches primarily involving bridging oxygens, $\nu(\text{POP})_a$ and $\nu(\text{POP})_{as}$. The low frequency peaks near 450 cm^{-1} are due to deformations of PO_4 tetrahedra [111]. The broad shoulder at 1140 cm^{-1} in the MIR spectrum of $v\text{-P}_2\text{O}_5$ is not seen in the Raman spectrum, but has been observed in previous Raman studies [54]. The relatively large amount of noise in the Raman spectrum may prohibit observation of this mode. The mode at 1140cm^{-1} has been tentatively assigned to longitudinal and transverse optical modes, similar to those found in the Raman spectra of SiO_2 , GeO_2 , and BeF_2 [125126]. The strength of the 1390cm^{-1} line suggests virtually every P atom in the glass has a double-bonded oxygen. The similarity between the frequencies of the $\text{P}=\text{O}$ mode in the glass and crystal suggest the PO_4 tetrahedra are similar, having similar amounts of π -bond delocalization.

The A_1 mode frequencies are similar in both gaseous P_4O_{10} and $v\text{-P}_2\text{O}_5$ [54]. However, the relative intensities of the modes are different and the Raman spectrum of $v\text{-P}_2\text{O}_5$ does not contain the low frequency modes found in the Raman spectrum of gaseous P_4O_{10} . Therefore, while both materials are built from similar PO_4 tetrahedra, in $v\text{-P}_2\text{O}_5$ the tetrahedra are not arranged in a P_4O_{10} cage as they are in gaseous P_4O_{10} .

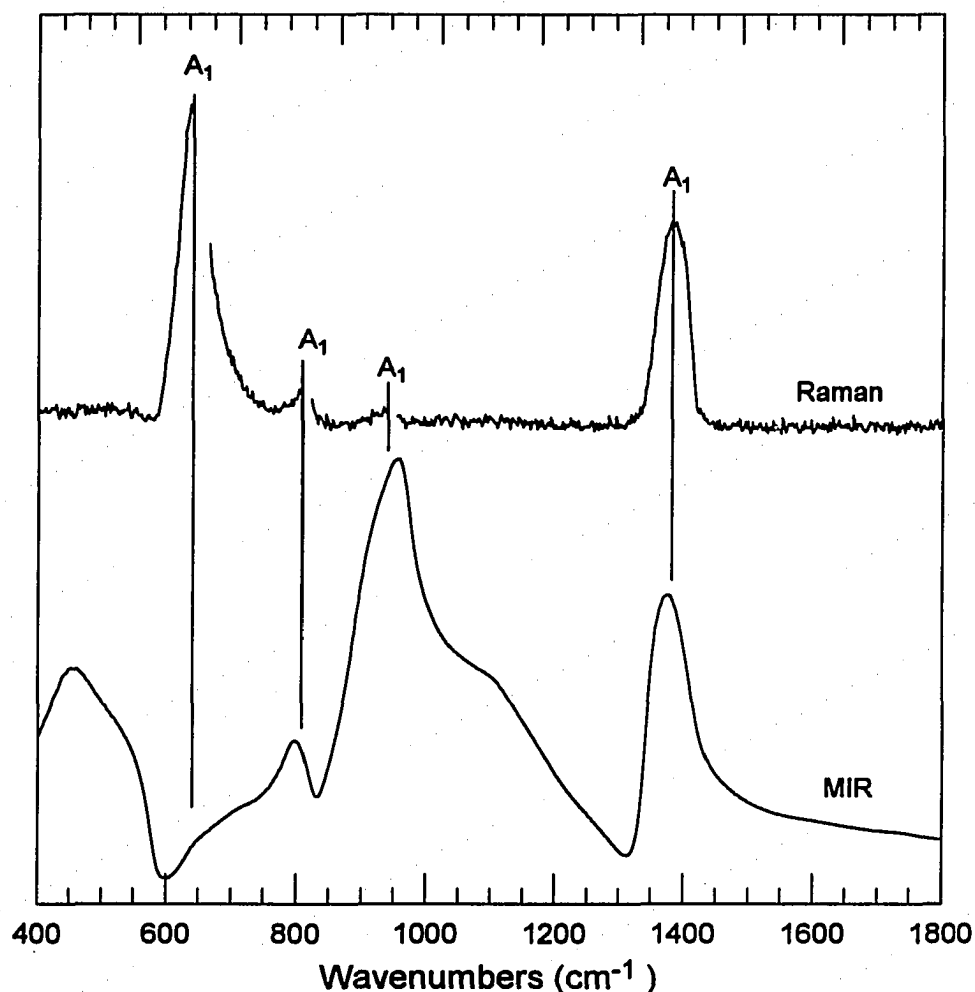


Figure 5.1 The MIR and Raman spectra of $v\text{-P}_2\text{O}_5$. The frequencies of non-degenerate A_1 vibrational modes are indicated [54].

5.1.3 Physical Properties

The density of $v\text{-P}_2\text{O}_5$ was found to be 2.47 ± 0.1 g/cc. This value is lower than the value of 2.52 g/cc reported by Patel et al. [127]. Both glasses had similar water contents, ~ 0.7 mole% H_2O ; however, the glass prepared by Patel et al. was quenched an order of magnitude slower than the P_2O_5 glass in this study. Therefore, the glass prepared in the present study has a higher fictive temperature and an expanded structure as compared to the glass prepared by Patel et al. Both densities are less than the branching (2.9g/cc) and sheet

(2.72 g/cc) polymorphs of $c\text{-P}_4\text{O}_{10}$, but larger than the molecular polymorph (2.3 g/cc). This observation is consistent with the structure of glassy P_2O_5 not consisting of molecular P_4O_{10} units, but the PO_4 tetrahedra form interconnected sheets or are 3-D branching.

The T_g for $v\text{-P}_2\text{O}_5$ found in this study (665K) is $\sim 75\text{K}$ higher than has previously been reported [46]. The discrepancy is undoubtedly due to water contamination. Studies have shown that H_2O acts as a modifier, depolymerizing the covalent network of phosphate glasses, thereby decreasing T_g [4]. For P_2O_5 glass prepared in this study, $<1\text{mole}\%$ H_2O is a conservative estimate of the water content, whereas water contents were not measured in the previous T_g study. The discovery that the T_g of $v\text{-P}_2\text{O}_5$ is 75K higher than previously reported impacts present theories surrounding the structure and dynamics of phosphate glasses.

The T_g for $v\text{-P}_2\text{O}_5$ is the highest of any alkali phosphate glass studied, contrary to previous theories. Kreidl stated, "...the weakest, low melting, pure P_2O_5 glass is structurally strengthened rather than weakened by the addition of RO or even R_2O ." [73]. Kreidl suggested the modifying cations would form ionic bonds with the terminal oxygens of Q^3 units thereby strengthening the network. On the contrary, this study shows the T_g of $v\text{-P}_2\text{O}_5$ is, in fact, larger than any alkali or alkaline earth phosphate glass. This result is consistent with $v\text{-P}_2\text{O}_5$ having a three dimensionally covalent bonding scheme which is depolymerized and weakened by the addition of ionic modifiers.

Previously, $v\text{-P}_2\text{O}_5$ has been described as the archetypal Arrhenius liquid [46]. Martin et al. [46] coupled their T_g with the viscosity data of Cormia [59] to compare $v\text{-P}_2\text{O}_5$ with other glass forming liquids on a reduced T_g plot (Figure 5.2). On a reduced T_g plot, those liquids where the cooperative motions necessary for viscous flow are discouraged by a 3-D covalent bonding scheme (e.g. SiO_2 and GeO_2) show little curvature. As the covalent bonding scheme is replaced by one dominated by non-directional ionic bonding, configurational degeneracy increases and so does the curvature in Figure 5.2. SiO_2 is considered the classic "strong" liquid while KCN is the model "fragile" liquid. According to the Adam-Gibbs theory of transport processes [8], the archetypal strong liquid should have a $C_p(l)/C_p(s)$ near 1 due to

the lack of configurational degeneracy in such a liquid. Conversely, at the free ion extreme, there are a large number of new configurations available for each broken bond and the additional energy required to activate all the additional degrees of freedom results in a large $C_p(l)/C_p(s)$. Therefore, if $v\text{-P}_2\text{O}_5$ were the model "strong" liquid, it should have a small $C_p(l)/C_p(s)$. Moreover, since rigidity, hence covalency, of the network is directly proportional to the strength of a liquid, $v\text{-P}_2\text{O}_5$ should have a higher, or equivalent T_g , to $v\text{-SiO}_2$.

When the T_g for $v\text{-P}_2\text{O}_5$ determined in the present study, $\sim 75\text{K}$ larger than that determined by Martin, was used in conjunction with the viscosity data of Cormia, P_2O_5 was found not to be the classic Arrhenius liquid (Figure 5.2). Cormia reports the water content of the phosphate liquid used to determine viscosity as $<1\text{mole}\% \text{H}_2\text{O}$. Likewise, $\leq 1\text{ mole}\% \text{H}_2\text{O}$ is a conservative estimate of the water content of the $v\text{-P}_2\text{O}_5$ prepared in this study. Martin does not report the water content of the $v\text{-P}_2\text{O}_5$ prepared in his study, however, given that water contamination decreases the T_g of phosphate glasses, one can assume there was $>1\text{mole}\% \text{H}_2\text{O}$ in the glass sample. P_2O_5 liquid not being the archetypal Arrhenius liquid supports proven theories of transport processes in glass-forming liquids.

Table 5.1 compares the T_g and $C_p(l)/C_p(s)$ as calculated by Martin to those found in the present study. Note the converse relationship between T_g and $C_p(l)/C_p(s)$. The T_g of the $v\text{-P}_2\text{O}_5$ prepared in this study is larger than the hydrated sample prepared by Martin, inversely, $C_p(l)/C_p(s)$ is smaller. Nonetheless, in both cases $v\text{-P}_2\text{O}_5$ has a T_g and $C_p(l)/C_p(s)$ are commensurate with sodium disilicate and sodium diborate, interestingly, all three of these systems have three covalent connections per glass forming cation.

5.2 Alkali Ultra-Phosphate Glasses

5.2.1 Site Distributions

Van Wazer hypothesized the evolution of the structure of binary phosphate glasses in his reorganization theory [128]. Based on liquid chromatography of polyphosphate glasses, reorganization theory assumes the addition of modifiers (excluding electron-acceptors) to $v\text{-}$

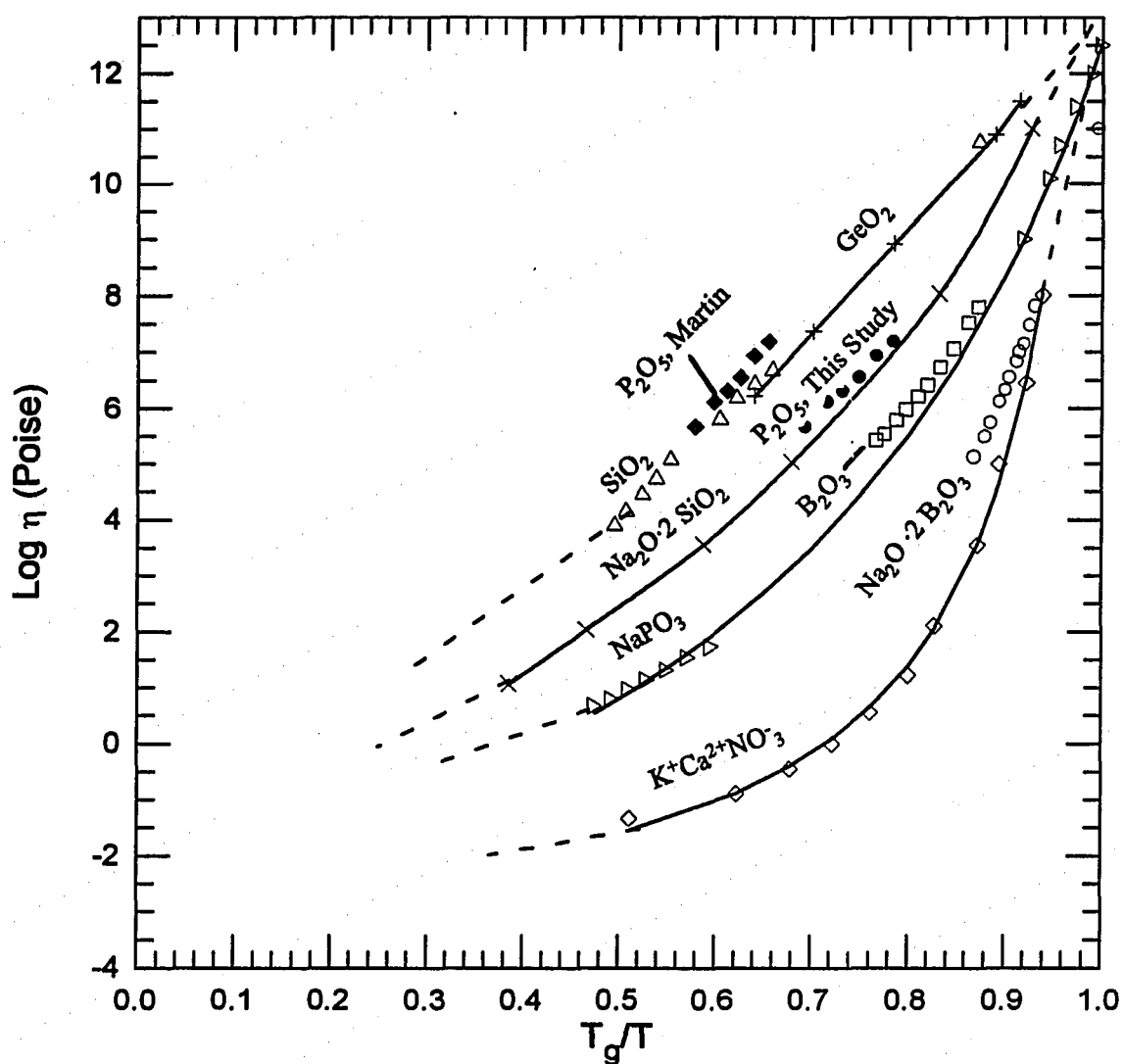
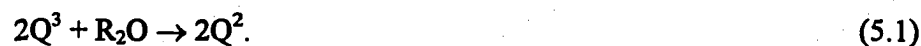


Figure 5.2 The dependence of viscosity on reduced T_g [46, 60]. Network liquids (SiO_2 and GeO_2) show Arrhenius behavior, but can be converted into non-Arrhenius liquids by decreasing the number of covalent interconnections. Although P_2O_5 contains no modifier, there are only three covalent interconnections whereas there are four in GeO_2 and SiO_2 . Therefore, P_2O_5 is not the archetypal Arrhenius liquid.

Table 5.2 The glass transition temperatures and $C_p(l)/C_p(s)$ ratios for the glass forming liquids in Figure 5.2

Liquid	T_g (K)	$C_p(l)/C_p(s)$
P_2O_5 (Martin)	537	1.2
SiO_2	1446	1
GeO_2	818	1.1
$Na_2O \cdot 2SiO_2$	713	1.18
P_2O_5 (This Study)	665	1.18
B_2O_3	553	1.49
$Na_2O \cdot P_2O_5$	555	1.34
$Na_2O \cdot 2B_2O_3$	706	
$K^+Bi^{3+}Cl^-$ (K:Bi = 1:2)	332	1.55
$K^+Ca^{2+}NO_3^-$ (K:Ca = 3:2)	306	1.5

P_2O_5 , depolymerizes the network by breaking bridging oxygen bonds to form non-bridging oxygens. Such structural depolymerization is described by the pseudo-reaction:



For the special case of ionic modifiers, such as alkali oxides, where no unreacted material and no composition gradients are anticipated, the disproportionation reaction:



is not expected. Therefore, the relative site populations in the ultra-phosphate region can be predicted from the alkali to phosphorus ratios.

Previously, liquid chromatography has been used to verify chemically simple depolymerization in polyphosphate glasses [18, 129]. However, chromatography techniques cannot be used at ultra-phosphate compositions because when the glass is dissolved, Q^3 branching points are hydrolyzed to form Q^2 species thus effectively changing the composition

of the glass. XPS O1s [56] and ^{31}P MAS-NMR [130] spectroscopies have successfully tested reorganization theory in the ultra-phosphate region by quantitatively measuring the BO/NBO ratio and Q^3/Q^2 ratio, respectively. However, only hydrated alkali ultra-phosphates have been studied where H_2O was treated as an additional structural modifier when calculating the modifier to phosphorus ratio. We can now test Van Wazer's reorganization theory on anhydrous glasses over the entire ultra-phosphate region. As shown in Figure 5.3, the site populations as determined by ^{31}P MAS-NMR are in excellent agreement with those predicted by reorganization theory.

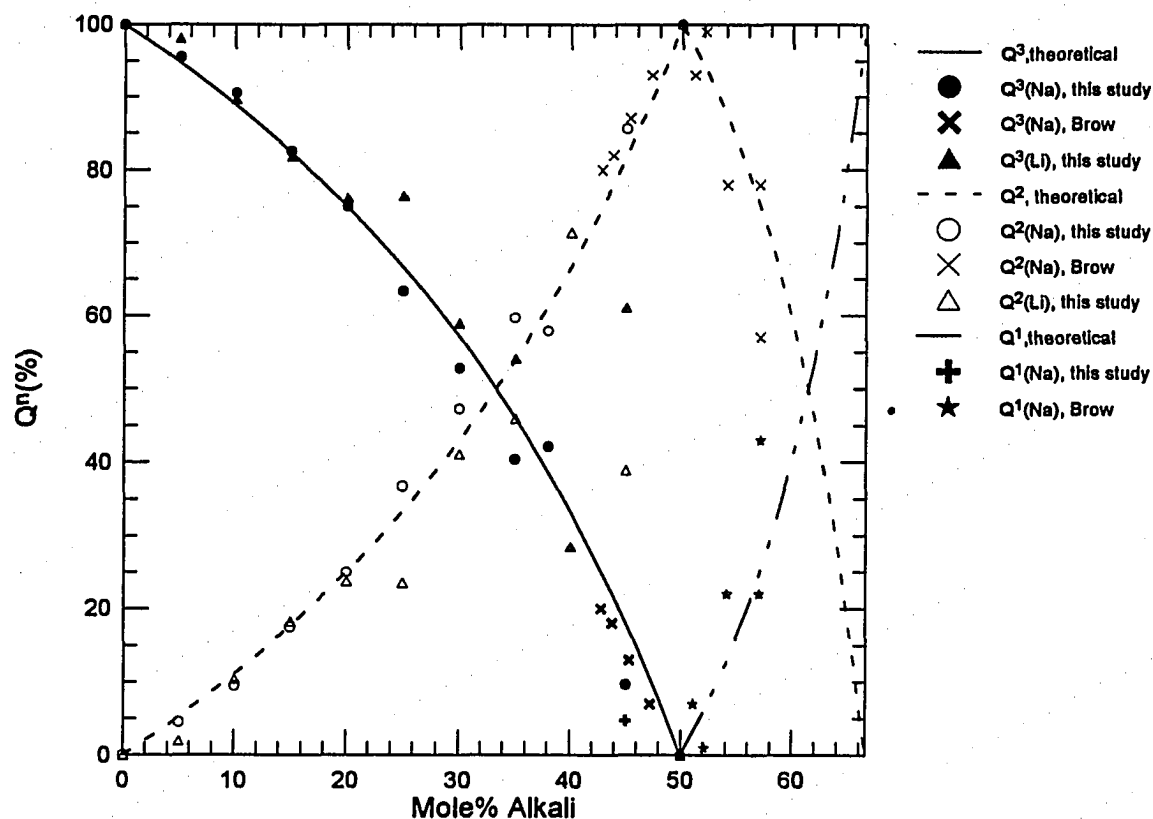


Figure 5.3 Q^3 , Q^2 , and Q^1 site distributions measured from the ^{31}P MAS-NMR spectra as compared to those predicted from the glass compositions using Equation (38).

Only at 45 mole% Na₂O does ³¹P MAS-NMR suggest the co-existence of Q¹ and Q³ species in these glasses, however, a separate peak was not resolved, only a broadening of the Q² resonance making the assignment to a Q¹ species tentative. Thus, site partitioning or phase separation into regions of high- and low- polymerization does not exist, in agreement with the ionic model of the Van Wazer model. As described by Brow [130], the best interpretation of the structural progression in alkali ultra-phosphate glasses is one of random co-polymerization of either Q² and Q³ species (>50 mole% P₂O₅) or Q² and Q¹ sites (<50mole% P₂O₅).

Vibrational spectra are qualitatively consistent with chemically simple depolymerization of the ultra-phosphate glasses. The growth of a new peaks near 1200cm⁻¹ (ν(PO₂)) concomitant with decrease in relative intensity of the peak centered near 1100cm⁻¹ (ν(POP)) and 800cm⁻¹ (ν(POP)) indicates the creation of non-bridging oxygens at the expense of bridging oxygens. This evolution is best seen in the Raman spectra (Figure 4.15).

5.2.2 Oxygen Bonding

While there exists millions of inorganic compounds based on phosphate tetrahedra, there are relatively few based on three- or five- coordinated phosphorus atoms. One reason tetrahedra are more stable is the energy contribution due to the existence of π bonding which is not present in the three- or five- coordinated compounds. In a tetrahedral ligand field, the energies of the d_{xz} and d_{yz} orbitals of the phosphorus atom are decreased relative to the other three d orbitals allowing π bonds to be formed with the p_x and p_y orbitals of the oxygen atoms. The degree of π bonding can be established through bond lengths [131].

In the molecular and branching polymorphs of c-P₄O₁₀ the terminal oxygen bond lengths average 1.43Å and bridging oxygen bond lengths average 1.60Å, yielding bond orders of 2 and 1, respectively. Therefore, most π bonding is localized on the terminal oxygen. In both glassy and crystalline sodium metaphosphate only two bond lengths can be identified: 1.48Å (P-BO) and 1.61Å (P-NBO) [132, 28]. Therefore, π-bonding is not localized on a single oxygen but is unevenly distributed among all four oxygens. In this way, the number of resonance structures increases with decreasing numbers of bridging oxygens until the

orthophosphate composition, where each non-bridging P-O bond has a bond order of 1.25[. While some unbalance in π -bonding is present in meta- and ortho-phosphate glasses and crystals, the greatest decrease in the unbalance of π -bond character is observed on going from the branching P_4O_{10} unit (Q^3) to the metaphosphate unit (Q^2).

5.2.2.1 *Vibrational Spectra*

Changes in the peak frequencies of vibrational modes are caused by changes in atomic masses, bond strengths, and bond angles. For example, Li has a smaller atomic mass than Na; therefore, the stretching frequencies in lithium ultra-phosphate glasses are at higher frequencies than those in sodium ultra-phosphate glasses. Additionally, π -bond shortening is well-known in crystalline and glassy phosphates [131], and it has been observed that bond angle changes accompany π -bond delocalization [10]. Any changes in bond length or bond angles due to π -bond delocalization will result in changes of the vibrational frequencies of normal modes of phosphate stretching vibrations. For example, changes in π -bonding on non-bridging oxygens between different Q-species results in their vibrational footprints being well separated, such evolution is best seen in the Raman spectra (Figure 5.4). In this way, delocalization of π -bond character results in a shift to lower frequencies of the NBO vibrational modes and shift to higher frequencies for the BO modes.

Figure 5.5 shows the stretching frequencies of the vibrational modes of Q^2 and Q^3 units in sodium and lithium ultra-phosphate glasses as determined from Raman and MIR spectroscopies. $\nu(\text{POP})_s$ and $\nu(\text{POP})_{as}$ represent the asymmetric and symmetric stretches of bridging oxygens, $\nu(\text{PO}_2)_s$ and $\nu(\text{PO}_2)_{as}$ are the stretches of non-bridging oxygen bonds on Q^2 species, and $\nu(\text{P=O})_s$ is the symmetric stretch of a terminal oxygen bond on a Q^3 species. The compositional dependence of the peak frequencies can be divided into three regions: region I (0 to ~20mole% alkali), region II (20 to ~45mole% alkali) and region III (45 to 50 mole% alkali).

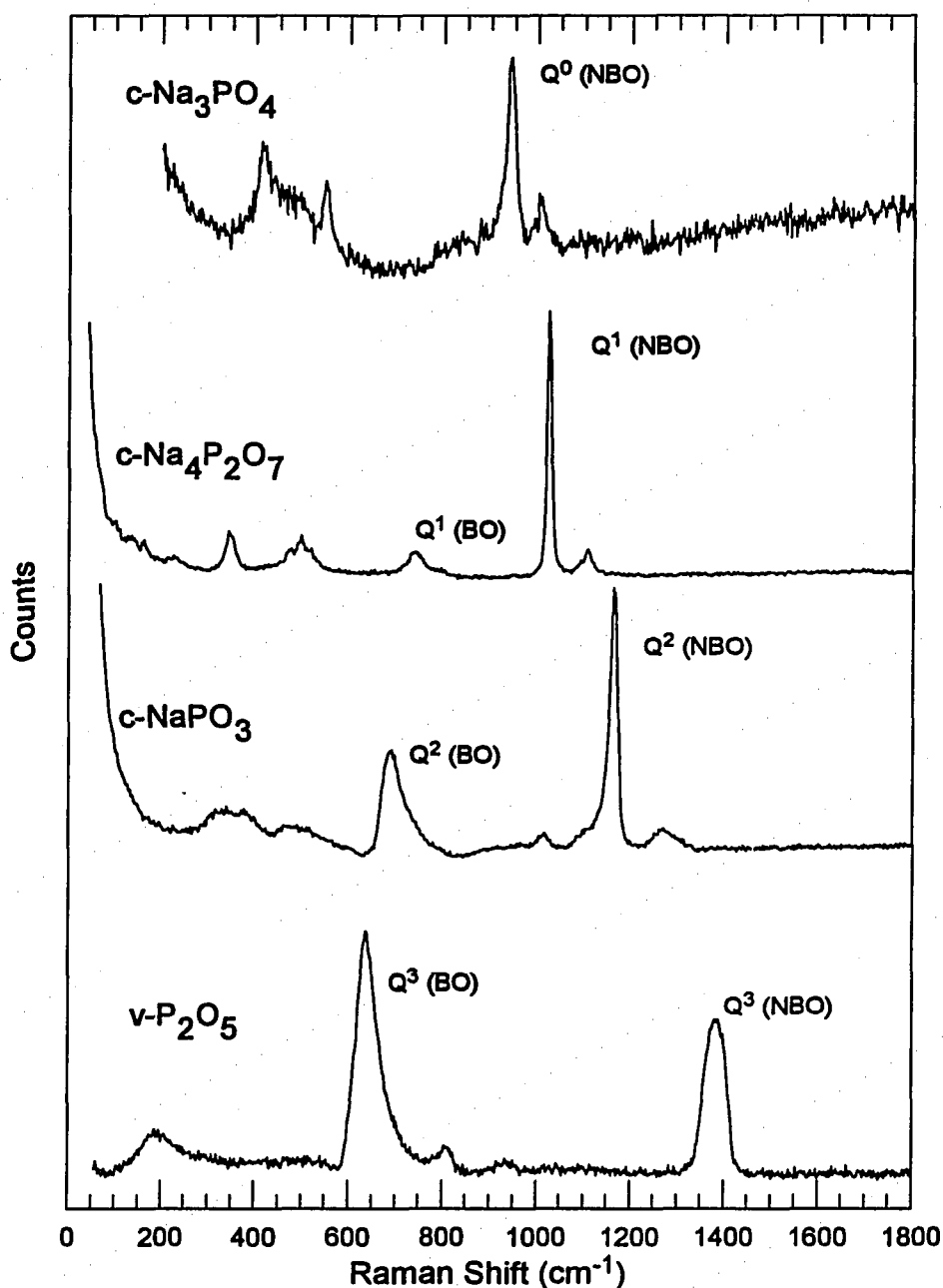


Figure 5.4 As the number of non-bridging oxygens per PO₄ tetrahedra increases, the P-NBO bond lengths decrease and P-BO bond lengths increase due to π -bond delocalization. Therefore, the vibrational frequencies of the NBO peaks decrease while those of the BO peaks increase. The largest amount of shift is seen on going from Q³ to Q² species. The crystal spectra were taken from ref. [74].

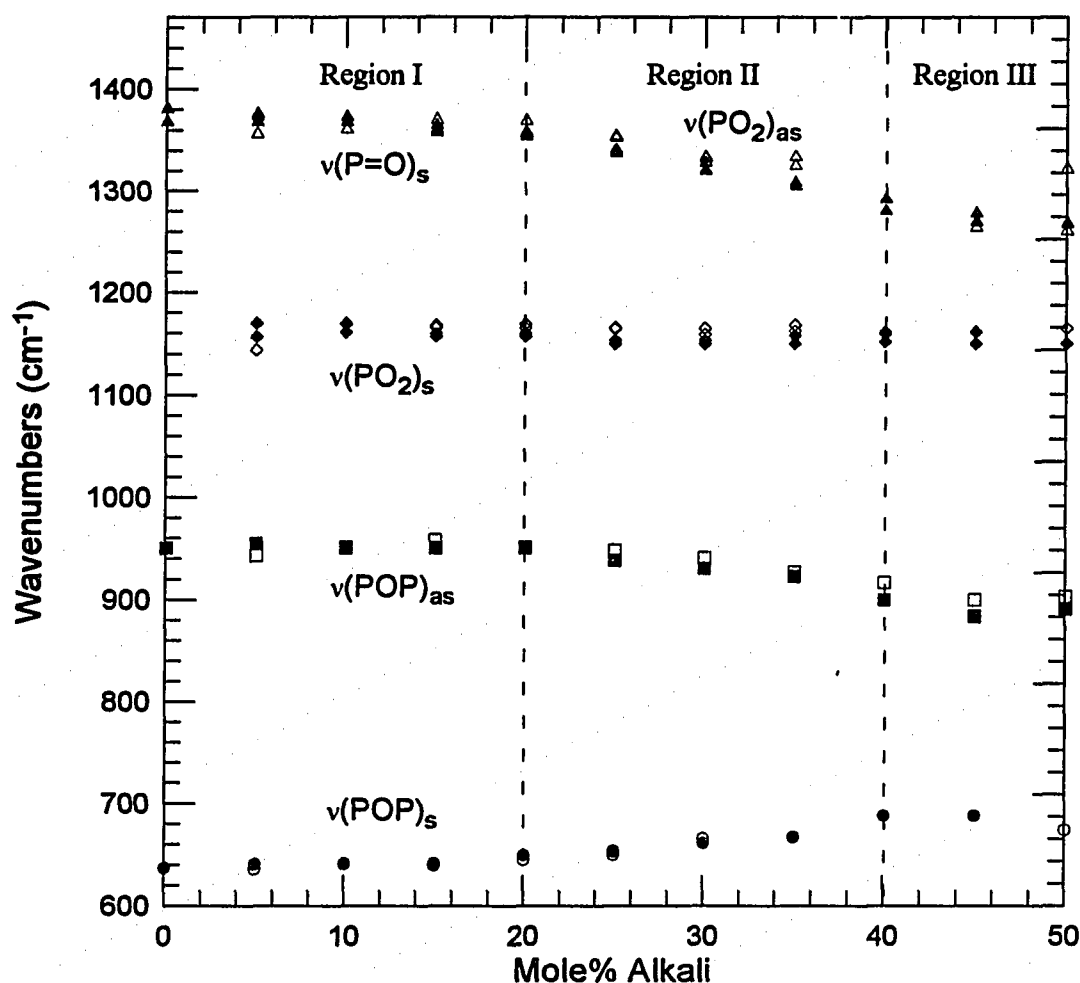


Figure 5.5 The peak frequencies of the vibrational modes of Q^2 and Q^3 species in sodium and lithium ultra-phosphate glasses as determined from Raman (open symbols) and MIR (filled symbols) spectroscopies. $\nu(\text{P=O})_s$ (\blacktriangle) is the stretching mode of a terminal oxygen on a Q^3 , $\nu(\text{PO}_2)_s$ (\blacktriangle) and $\nu(\text{PO}_2)_{as}$ (\blacklozenge) are the symmetric and asymmetric stretching modes of P-OM^+ terminal oxygens and $\nu(\text{POP})_s$ (\bullet) and $\nu(\text{POP})_{as}$ (\blacksquare) are the symmetric and asymmetric stretching modes of bridging oxygens. The compositional dependence of these peak frequencies can be divided into three regions.

In region I little peak shift is seen in the stretching frequencies of either bridging or non-bridging oxygens on either Q^3 or Q^2 species. Such constancy suggests no changes in oxygen bonding on Q^3 species or bonding between Q^3 species.

In region II, the peak center of the $\nu(P=O)_s$ mode decreases $\sim 125\text{cm}^{-1}$, the peak center of the $\nu(POP)_{as}$ mode decreases 45cm^{-1} , and the peak center of the $\nu(POP)_s$ mode increases 45cm^{-1} ; alternatively, the peak center of the $\nu(PO_2)_s$ mode shows little movement. The shift of the $\nu(P=O)_s$ to lower wavenumbers indicates the average terminal oxygen bond strength of Q^3 species is weakening with increasing depolymerization. Such weakening is most probably due to π -bond delocalization. Delocalization of π bond character is facilitated by an increase in P-O-P bond angle [10]. The shifts of the peak centers of the $\nu(POP)_{as}$ and $\nu(POP)_s$ stretching vibrations are consistent with larger POP angles as depolymerization increases [111].

In both glassy and crystalline metaphosphates, π -bonding is delocalized primarily over the terminal oxygen bonds. As shown in Figure 5.6, such delocalization results in the formation of resonance structures where no distinction can be made between $P=O$ terminal oxygens and $P-OM^+$ terminal oxygens [132, 28]. The constancy of the peak center of the $\nu(PO_2)_s$ mode over the entire ultra-phosphate region suggests Q^2 species at ultra-phosphate compositions are similar to those at the metaphosphate composition, having fully delocalized resonance structures. In support, the Q^2 species in crystalline CaP_4O_{11} , CaP_6O_{17} and α - $Ca(PO_3)_2$ have similar terminal and bridging oxygen bond lengths [15]. Given the changes in the $\nu(P=O)_s$, $\nu(POP)_{as}$, and $\nu(POP)_s$ modes in the same composition range, reconfiguration of π -bonding must be taking place on Q^3 species.

Analysis of the depolarization ratios of the $\nu(P=O)_s$ peak in the Raman spectra of the alkali ultra-phosphate glasses indicates a transformation of $P=O$ ($\nu(P=O)_s$) terminal oxygens on Q^3 species into $P-OM^+$ ($\nu(PO_2)_{as}$) terminal oxygens, where M is an alkali. Vibrational modes with depolarization ratios, ρ , of 0.1 or less are considered highly symmetric whereas modes with $\rho > 0.1$ are increasingly asymmetric [133]. Up to ~ 20 mole% alkali the depolarization ratio of the $\nu(P=O)_s$ mode remains near 0.14. In the same region where the

peak center of the $\nu(\text{P}=\text{O})_s$ mode shifts to lower wavenumbers, the depolarization ratio increases to near 0.5. Therefore, between 20 and 45 mole% alkali the terminal oxygens on Q^3 species are transformed from $\text{P}=\text{O}$ to $\text{P}-\text{O}^-\text{M}^+$ terminal oxygens. In support, the terminal oxygen bond lengths on Q^3 and Q^2 species in ultra-phosphate crystals are similar, with all terminal oxygens oriented towards counterions [15]. The question remains why π -bond delocalization on Q^3 species does not occur until 20mole% alkali.

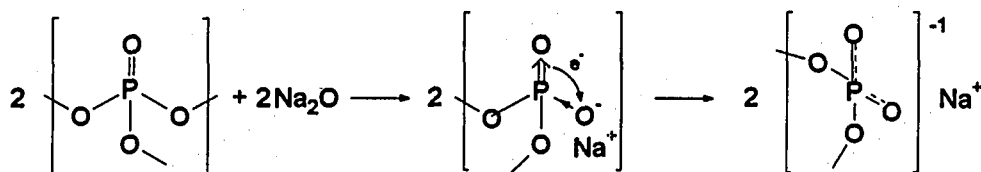


Figure 5.6 The creation of Q^2 species results in resonance structures where the counterion charge balances both terminal oxygens. The terminal oxygen lengths on Q^2 species are identical but are longer than the terminal oxygen bond length on Q^3 species.

In a recent paper by Statchel et al. [23] the authors examined the $\text{Q}^3:\text{Q}^2$ ratios instead of the percentages of each PO_4 group as a function of alkali, in the manner of Van Wazer [18]. Their analyses included a model of all the possible interconnections of Q^3 and Q^2 groups in the ultra-phosphate region. It is significant to note that at 20mole% alkali the $\text{Q}^3:\text{Q}^2$ ratio is 1:3, and, according to this model, every Q^3 species is covalently connected to one Q^2 and three Q^3 species. Therefore, at compositions >20 mole% alkali a second Q^2 is added to each Q^3 species. Presumably, the addition of a second Q^2 to a Q^3 species decreases the rigidity of the network enabling the $\text{O}-\text{P}(\text{Q}^3)-\text{O}$ bond angle to increase, facilitating π -bond delocalization.

Peak shift of the $\nu(\text{P}=\text{O})_s$, $\nu(\text{POP})_{as}$, and $\nu(\text{POP})_s$ peaks halts near 40 mole% alkali. Therefore, π -bond delocalization also ceases near 40 mole% alkali. At 40 mole% alkali the $\text{Q}^3:\text{Q}^2$ ratio is 2:3 and, assuming random co-polymerization of Q^3 and Q^2 species, Q^3 - Q^3 connections no longer exist. Interestingly, the moisture sensitivity of ultra-phosphate glasses decreases significantly in those glasses with >40 mole% alkali [4, 130]. Such behavior

suggests Q^3 - Q^3 bridges are unstable. In support, ultra-phosphate crystals show shortening of P-O bonds between Q^3 and Q^2 species; however, no shortening on those bonds bridging between Q^3 species. These results suggest π -bonding is preferentially delocalized onto Q^3 - Q^2 bridges, as shown in Figure 5.7. When only Q^3 - Q^2 and Q^2 - Q^2 bridges remain in the glass structure π -bond delocalization is complete.

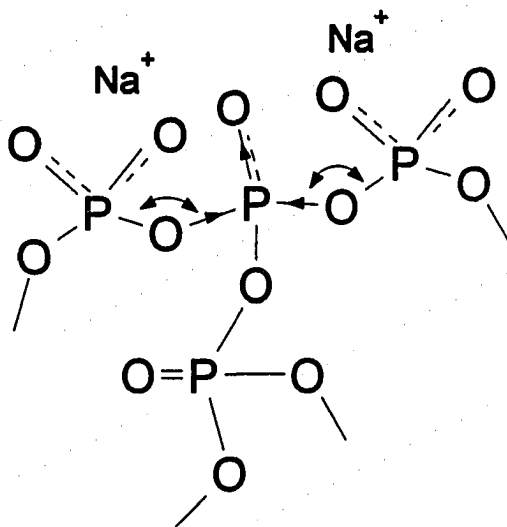


Figure 5.7 As the second Q^2 species is added to each Q^3 species (>20 mole% modifier), anionic repulsions between terminal oxygens results in an increase in $P(Q^2)$ -O- $P(Q^3)$ bond angles, shortening of Q^3 - Q^2 P-O bond lengths, lengthening of the P-O terminal oxygen bond length and conversion of the P=O terminal oxygens on Q^3 species into $P-O M^+$ terminal oxygens.

Beyond providing information about the short range structure of Q^3 and Q^2 species, the MIR spectra can also provide information about the network topology (the interconnection of Q^3 and Q^2 species). As shown in Figure 5.8, the shape of the MIR spectra of alkali ultra-phosphate glasses are similar in three distinct compositional regions: region I, 0-20 mole% alkali ; region II, 20-40 mole% alkali; region III, 40-50 mole% alkali. In region I the spectra closely resemble those in v - P_2O_5 and the sheet form of c - P_4O_{10} [15], suggesting the topology of the network is not changing. Between 20 and 40 mole% alkali, the shape of

the MIR spectra are similar to those of ultra-phosphate crystals where the network topology is dominated by large (12-16 membered) rings interconnected by 3- and 4-membered rings [15]. The similarity suggests the topology of alkali ultra-phosphate glasses in this composition regime likewise is dominated by rings of phosphate tetrahedra. Between 40 and 50 mole% alkali, the MIR spectra are consistent with a network that is chain dominated.

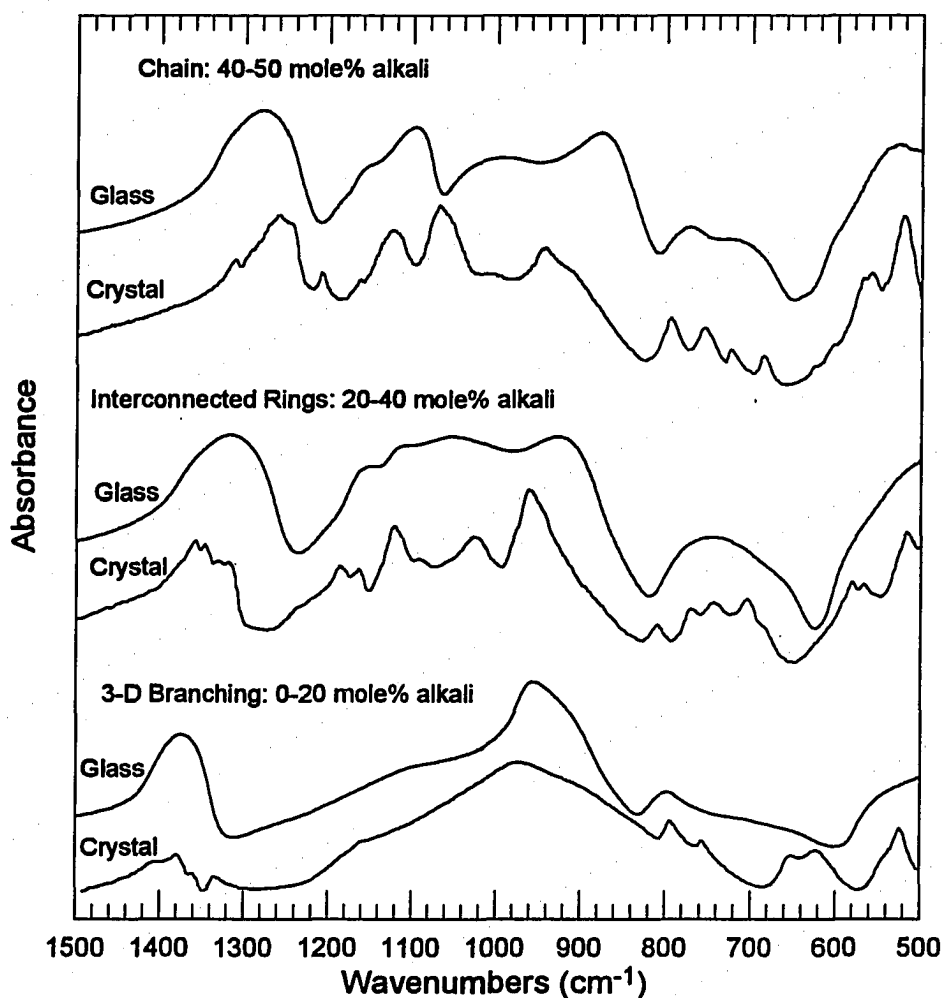


Figure 5.8 The shapes of the MIR spectra are similar in three distinct composition regions. Comparison of representative spectra from these regions with the MIR spectra of ultra-phosphate crystals [15] suggest the topologies of the glassy network are also different between these regions.

5.2.2.2 ^{31}P Chemical Shifts

The ^{31}P MAS-NMR isotropic chemical shifts of Q^3 and Q^2 units in sodium and lithium ultra-phosphate glasses are shown in Figure 5.9. ^{31}P chemical shifts have been found to be dependent on P-O-X bond angles [134, 135], field strength of countercations [62], and bond strength [136]. While semi-empirical models [134, 120] used to calculate the ^{31}P chemical shift indicate that changes in π -bonding result in the largest changes in chemical shift, the large number of factors influencing the ^{31}P chemical shift make analysis difficult..

Changes in electronegativity of ligands and/or changes in bond angles are not sufficient to explain the 10-20 ppm chemical shift differences between Q-sites in phosphorus materials [68]. Changes in π -bonding must be responsible for the large difference. For Q^3 species in glassy and crystalline P_4O_{10} , π -bonding is localized on terminal oxygens. Alternatively, for more depolymerized Q-species π -bonding is delocalized over all the terminal oxygens, in this way the distribution of electron density changes with extent of depolymerization of Q-sites. Therefore, as shown in Figure 5.9, the chemical shifts of different Q-sites are well separated. Chemical shifts of specific Q-sites vary due to changes in bond strengths, bond angles and ligand electronegativity.

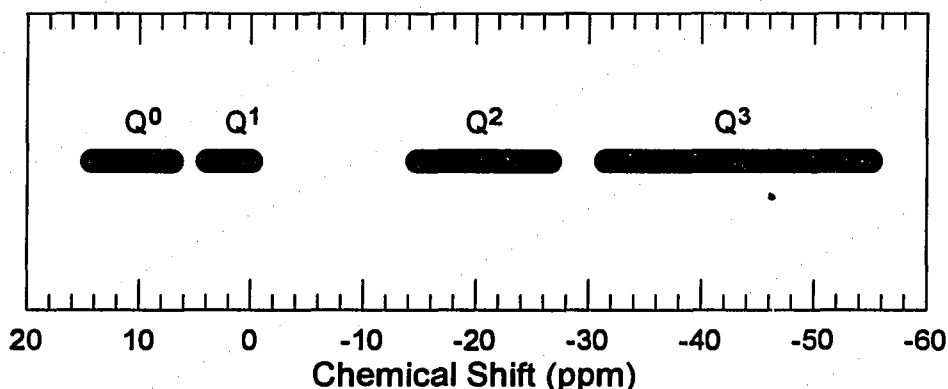


Figure 5.9 The relationship between Q-species and isotropic chemical shift [130].

As shown in Figure 5.10, the Q^2 -chemical shifts of lithium modified glasses are consistently more shielded than those of the sodium modified glasses. The larger electronegativity of Li over Na causes increased shielding of P nuclei. This result is consistent with previously reported [67, 137, 62] trends of the isotropic ^{31}P chemical shifts of Q^2 and Q^1 species in crystalline and glassy phosphates. With increasing countercation electronegativity, more electron density is shifted from the terminal oxygen to the countercation. Alternatively, on the P-O terminal oxygen bond, shared electron density is shifted onto the oxygen thereby increasing the shielding of the P nucleus. In addition to being dependent on the electron withdrawing power of the ligands, the isotropic Q^2 and Q^3 chemical shifts become more deshielded with increasing depolymerization.

Deshielding of ^{29}Si [138] and ^{31}P [62] chemical shifts with increasing depolymerization has been attributed to the averaging of compositionally dependent changes in electron distributions. This model assumes that there is a redistribution of charge within P-O bonds associated with the depolymerization of next-nearest-neighbor tetrahedra. Therefore, the deshielding of Q^3 -P species can be attributed to depolymerization of next-nearest-neighbor (NNN) Q^3 species to Q^2 species. Bridging oxygen P-O bonds on Q^2 species are more ionic than those on Q^3 species, as indicated by their longer bond lengths [15, 132]. Therefore, when a NNN Q^3 species is transformed into a Q^2 species, electron density on $\text{P}(Q^2)\text{-O}_b$ bonds is shifted toward the oxygen. In conjunction, electron density is shifted onto the Q^3 -P sharing this bridging oxygen, deshielding the Q^3 -P nuclei. Given random co-polymerization of the Q-sites, such changes in electron distributions of the Q^3 -P sites are averaged over the entire glass structure and the average chemical shift increases. Changes in optical basicity are consistent with such a macroscopic charge effect in phosphate glasses [61].

Interestingly, the compositional dependence of deshielding of Q^3 -P species is quenched for the more electronegative Li cation. Using an argument parallel to that given above, the dependence of Q^3 chemical shift on modifier could be due to the macroscopic charge effect.

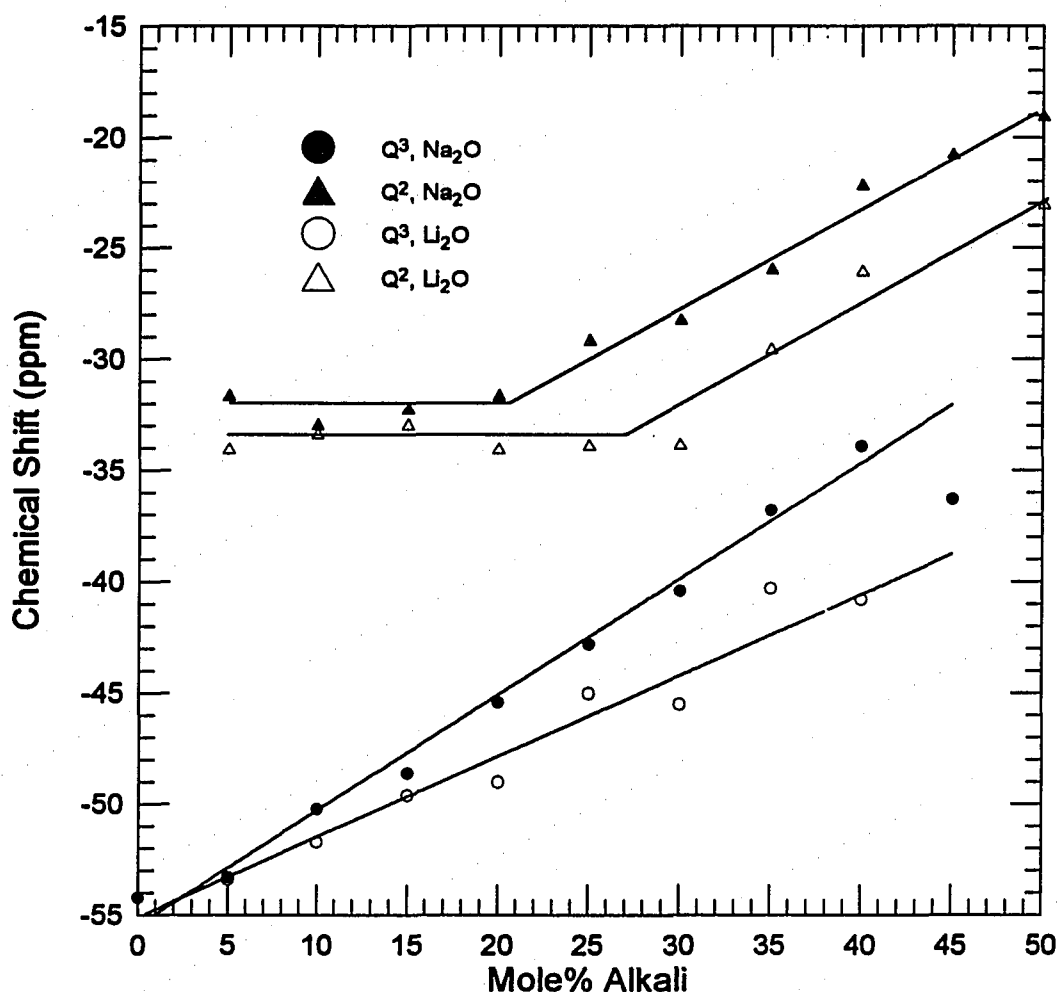


Figure 5.10 The ^{31}P isotropic chemical shifts of Q^3 (circles) and Q^2 (triangles) species in sodium and lithium ultra-phosphate glasses.

The amount of electron density shifted onto an oxygen bridging between a Q^2 and Q^3 species depends on the electron withdrawing power of the counteranion. However, the correlation between could also support the transformation of Q^3 terminal oxygens from $\text{P}=\text{O}$ to $\text{P}-\text{O}^-\text{M}^+$ species. For a $\text{P}=\text{O}$ terminal oxygen, a large amount of electron density is localized on the oxygen. When that terminal oxygen is transformed into a $\text{P}-\text{O}^-\text{M}^+$ terminal oxygen, some of that electron density is shared with the counteranion. In this way, shielding of the P is decreased.

The Q^2 -P chemical shift is insensitive to depolymerization between 0 and ~20 mole% alkali. According to the above model, such constancy suggests the glass consists of separate regions of Q^1 and Q^3 species which would not produce the macroscopic charge effect. In contrast, all other analyses suggest random co-polymerization. An alternate explanation considers the fractions and interconnections of Q-sites. At compositions < 20 mole% alkali, every Q^3 species is connected with at most one Q^2 species and there are no Q^2 - Q^2 connections. Therefore, Q^2 species are isolated from each other and experience no changes in next-nearest-neighbors with increasing depolymerization. There are no local changes in charge density hence no changes in macroscopic charge. Only at compositions >20 mole% alkali does the electron distribution of NNN Q^2 species start changing with the formation of Q^2 - Q^2 bridges and π -bond delocalization on Q^3 species.

Figure 5.11 shows the full width at half-maximum (FWHM) of the ^{31}P isotropic chemical shifts ($\pm 0.5\text{ppm}$) of Q^2 -P and Q^3 -P species in sodium and lithium ultra-phosphate glasses. Brow et al. [62] have observed a systematic increase in the FWHM of Q^2 units with increasing cationic potential. The increase in FWHM is suggestive of a larger amount of disorder in the glass, possibly due to wider distributions of P-O bond lengths and O-P-O and P-O-P bond angles. In support, the chains present in crystalline polyphosphates are more contorted when the cationic potential of the countercation is increased [139]. Although there is more scatter for the lithium ultra-phosphate data, our observations are consistent with increasing FWHM of Q^2 peaks with increasing countercation potential. Alternatively, cationic potential has little effect on the FWHM of Q^3 peaks up to 35 mole% alkali. At low alkali contents there is little interaction between the countercations and Q^3 species, whereas, at higher alkali contents vibrational spectra suggest P=O terminal oxygens convert to P-OM^+ terminal oxygens. Therefore, the cationic potential of the countercation influences the disorder of the Q^3 species.

As the amount of alkali is increased to ~40mole%, the ^{31}P FWHM of Q^2 species increase while the ^{31}P FWHM of Q^3 species decrease. Therefore, the structure of $v\text{-P}_2\text{O}_5$ is the most disordered of any alkali ultra-phosphate glass. Figure 5.12 shows there is a strong correlation

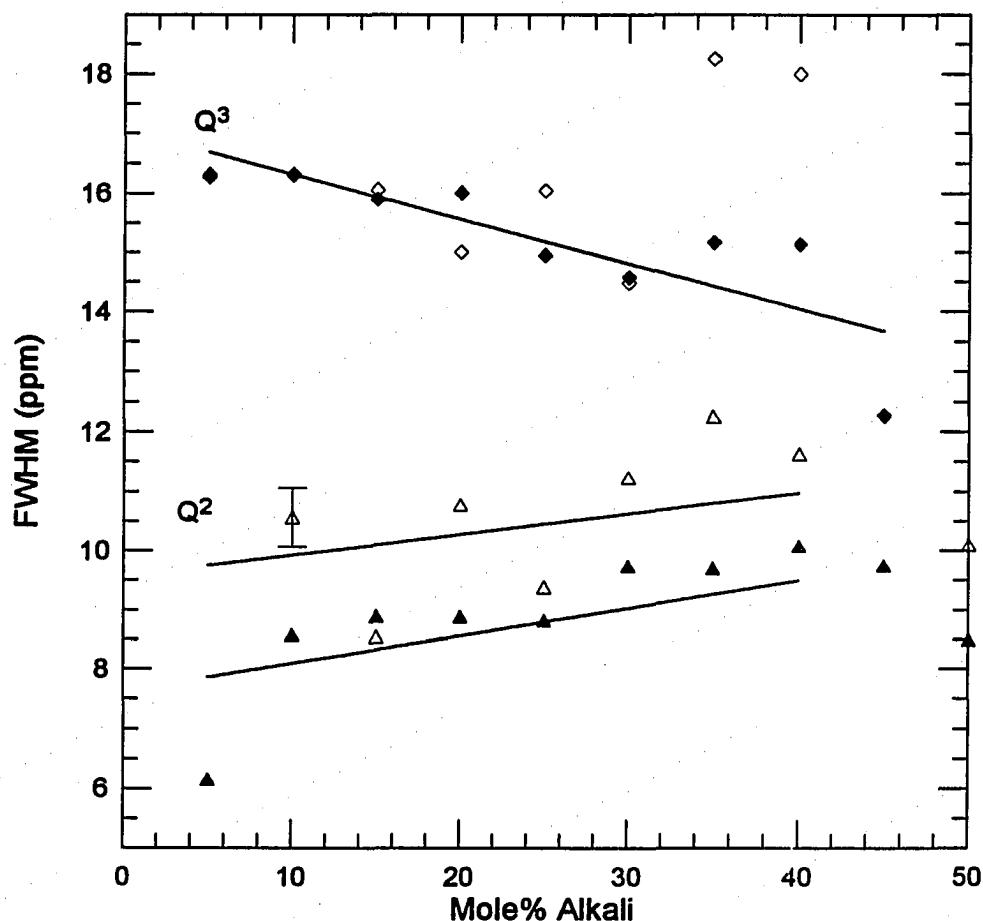


Figure 5.11 The relationship between the full width at half-maximum (FWHM) of the ^{31}P isotropic chemical shifts ($\pm 0.5\text{ppm}$) of Q^2 (triangles) and Q^3 (diamonds) species in sodium (solid symbols) and lithium (open symbols) ultra-phosphate glasses and alkali content. The lines represent linear least-squares best fits for the data.

between the degree of branching of the phosphate network and ^{31}P FWHM. Glasses formed from rigid, self-reinforcing, covalent bonding schemes have a wider distribution of bond lengths and angles compared to glasses where the covalent bonds have been replaced by non-directional covalent bonds. In support, XPS O1s spectra of sodium ultra-phosphate glasses indicate smaller distributions of oxygen sites with increasing depolymerization [20].

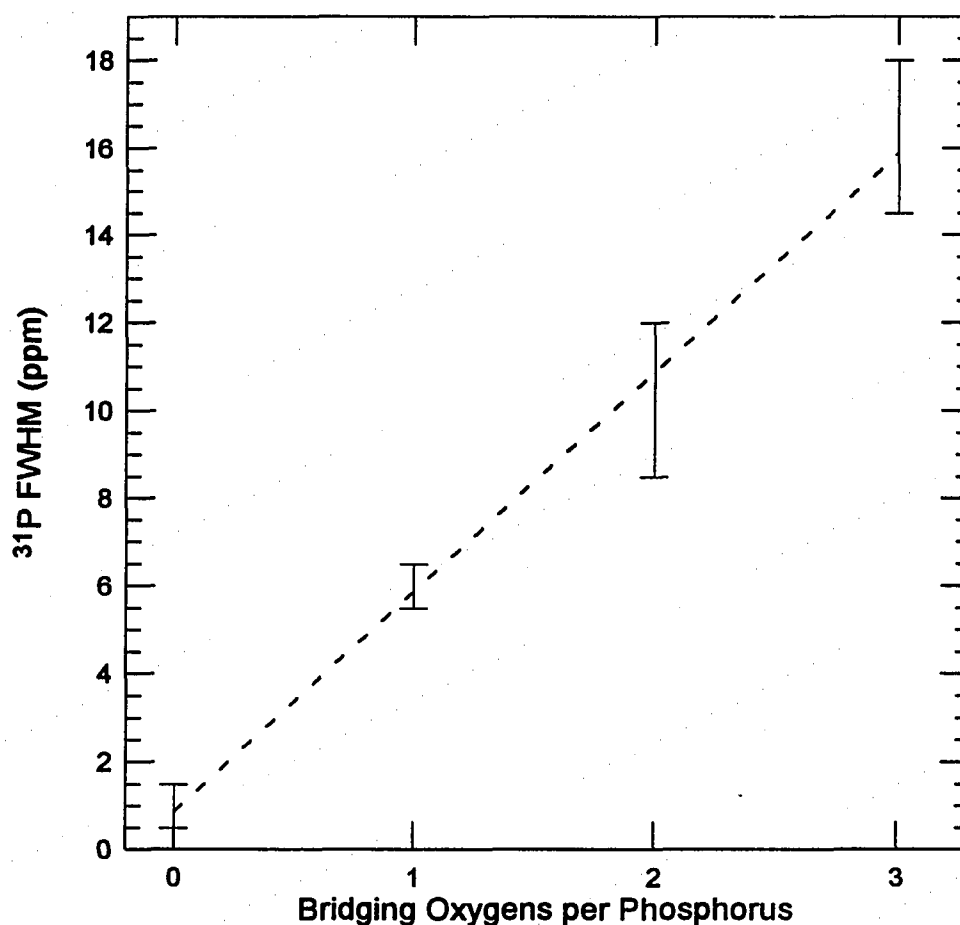


Figure 5.12 The relationship between ^{31}P FWHM and covalent interconnection of the network. The line represents the linear least-squares best fit for the data. The data for the Q^1 and Q^0 ^{31}P FWHM are from refs. [130, 61].

The decrease in Q^3 -FWHM is correlated with π -bond delocalization of the species. Alternatively, the increase in Q^2 -FWHM between 0 and 40 mole% alkali is correlated with the formation of ring structures which, as show for crystalline ultra-phosphates [15], have several equivalent sites for Q^2 species. The decrease in Q^2 -FWHM at compositions >40mole% alkali reflects the formation of chain structures where all Q^2 sites are similar.

Figure 5.13 shows the compositional dependence of the asymmetry parameters, η , of sodium and lithium ultra-phosphate glasses. The asymmetry parameter is a measure of the symmetry of electron density around the P nuclei. For example, Q^3 species in the crystalline

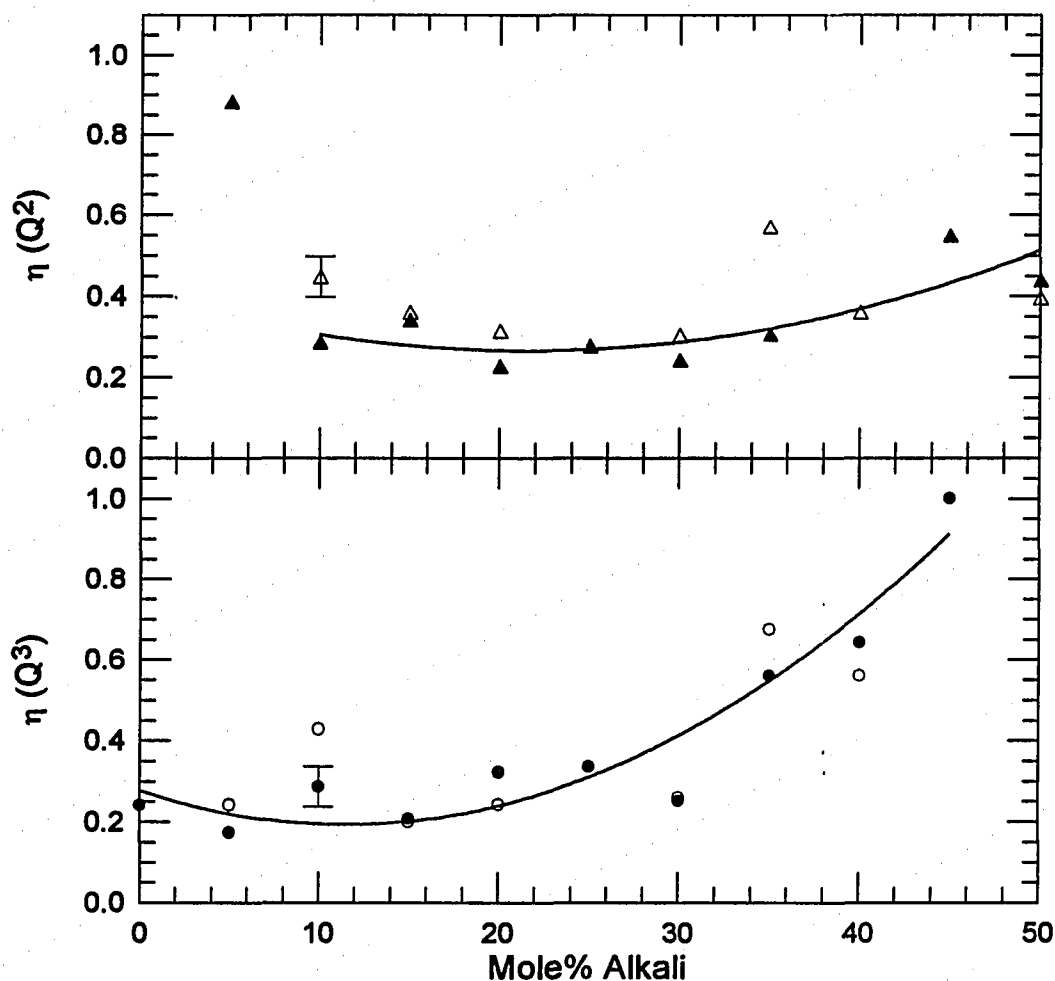


Figure 5.13 The asymmetry parameters of the ^{31}P chemical shift of Q^2 (triangles) and Q^3 (circles) species in lithium (filled symbols) and sodium (open symbols) ultra-phosphate glasses. The error for all measurements is estimated as ± 0.5 .

polymorphs of P_4O_{10} have C_{3v} symmetry and the electron density is symmetric around an axis adjacent to the terminal oxygen bond, therefore, $\eta=0$. Alternatively, for Q^2 species the electron density is not symmetric around a single axis but, at most, two-fold axis. Therefore, η for Q^2 species is a finite value larger than zero.

For alkali ultra-phosphate glasses, the asymmetry parameter of Q^2 -P species show little dependence on composition, with the exception of the outlying 5 mole% Na_2O point.

The intensity of the Q^2 resonance at 5 mole% alkali is weak and overlaps with the much stronger Q^3 resonance, therefore, the value of the asymmetry parameter is questionable. The asymmetry parameters of Q^2 species in alkaline earth phosphate glasses also show little dependence on composition [140]. Additionally, the asymmetry parameters of Q^2 species in crystalline and glassy metaphosphates [62] and glassy ultra-phosphates [140] show little dependence on the counteraction. Therefore, changes in Q^2 -P shielding due to changes in counteraction electronegativity or depolymerization are not localized on a particular bond, but are averaged over the entire tetrahedron. The increase in shielding of each of the three ^{31}P chemical shift tensors with increasing depolymerization support this observation. These findings are consistent with the formation of resonance structures on Q^2 units.

As in alkaline earth ultra-phosphate glasses [140], Q^3 species in alkali ultra-phosphate glasses are not axially symmetric. Therefore, the high symmetry found in Q^3 species of the crystalline polymorphs of $\text{c-P}_4\text{O}_{10}$ [16] is not present in the glassy state. The asymmetry parameter of Q^3 species are initially less than those of Q^2 species, then start increasing between 20 and 30 mole% alkali and become larger than those of Q^2 species by 40 mole % alkali. While changes in the asymmetry parameter is not correlated with changes in P shielding, Eckert et al. [141] have proposed that a 12° change in the S-P-S of $\text{S}=\text{SP}_{3/2}$ units, isostructural with Q^3 species, results in a substantial increase in the asymmetry parameter. An increase in O-P-O bond angle of Q^3 species starting between 20 and 50 mole% alkali is consistent with changes in the vibrational spectra, Section 5.2.2.1, and suggest p-bond delocalization is occurring in this same composition range. To further characterize the p-bond delocalization, the anisotropy of the chemical shift, $\Delta\delta$, can be examined.

The anisotropy of the ^{31}P chemical shift, $\Delta\delta$, increases with increasing depolymerization for both Q^3 and Q^2 species in lithium and sodium ultra-phosphate glasses (Figure 5.14). The approach often used to qualitatively describe the bonding geometry of phosphate materials through the ^{31}P chemical shift anisotropy is to consider each phosphate group as a perturbation of a tetrahedral $(\text{PO}_4)^{3-}$ ion. [70]. Changes in chemical shielding result from changes in angular momentum of the electrons including changes in electron

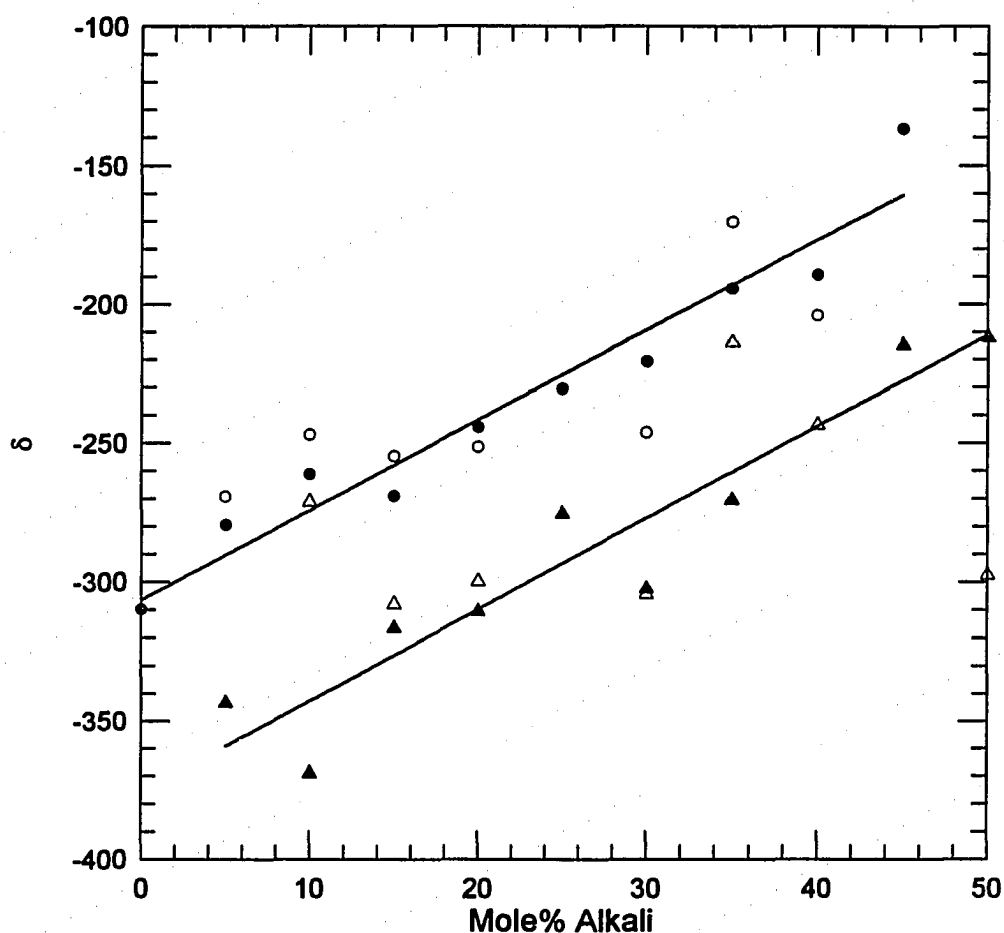


Figure 5.14 The ^{31}P chemical shift anisotropy ($\Delta\delta$) of Q^2 (triangles) and Q^3 (circles) species of sodium (filled symbols) and lithium (open symbols) ultra-phosphate glasses. The lines represent linear least squares fits of the sodium ultra-phosphate data.

density. In orthophosphate materials, where the bond order, hence π -bonding, is equivalent for all four oxygens on PO_4 tetrahedra the anisotropy is zero and the P site is spherically symmetric. For metaphosphates, π -bonding is localized on the terminal oxygens and the anisotropy increases. Studies of condensed metaphosphates have shown the σ_{33} axis lies in the $\text{O}_t\text{-P-O}_t$ plane while the σ_{11} tensor axis lies in the $\text{O}_b\text{-P-O}_b$ plane [70]. Therefore, the shielding along σ_{33} increases while the shielding along σ_{11} decreases. For the crystalline

polymorphs of P_4O_{10} , the Q^3 species are axially symmetric. The σ_{33} tensor axis is oriented adjacent to the $P=O$ terminal oxygen bond and the anisotropy is extremely large.

In $v\text{-}P_2O_5$, $\Delta\delta$ of Q^3 species (-310) is greater than the $\Delta\delta$ of Q^2 species (-210) in $v\text{-}NaPO_3$. However, at ultra-phosphate compositions, there are significant changes in the anisotropy of Q-sites. Given the constancy of η for Q^2 sites at ultra-phosphate compositions, the decreasing anisotropy with increasing depolymerization is consistent with electron density shifting from the terminal (σ_{33}) to the bridging oxygens (σ_{11}). This observation supports the strengthening of Q^3 - Q^2 bridges and Q^2 - Q^2 bridges with increasing depolymerization. Because η of Q^3 -P sites is a function of composition, analysis of Q^3 - $\Delta\delta$ is not as straightforward. However, Duncann et al. [70], suggest the difference between the two principal tensor components σ_{33} and σ_{22} reflects both changes in anisotropy and asymmetry and can therefore be used to differentiate between phosphate species.

Figure 5.15 shows the general dependence of $\sigma_{33}-\sigma_{22}$ on Q-site. Duncann et al. found that $\sigma_{33}-\sigma_{22}$ for a Q^3 species in a branching phosphate is larger than that of Q^2 species in a ring which is, on average, larger than that for a Q^2 species in a chain. They suggested that the value $\sigma_{33}-\sigma_{22}$ could be used to differentiate between Q-species. However, as shown in Figure 5.15, $\sigma_{33}-\sigma_{22}$ values for both Q^3 and Q^2 species in ultra-phosphate glasses cover the entire range of values. Therefore, Duncann et al. were incorrect assuming that the type of Q-site could be determined solely by $\sigma_{33}-\sigma_{22}$. However, we note a correlation between $\sigma_{33}-\sigma_{22}$ and topology of the network. MIR spectra suggest the topology of the ultra-phosphate network moves from branching to rings to chains of Q-species. The progression of $\sigma_{33}-\sigma_{22}$ values are consistent with such topological development. Between 0 and 20 mole% alkali the $\sigma_{33}-\sigma_{22}$ values are well within the branching range, then move through the ring range with increased alkali and are definitely in the chain range by the metaphosphate composition. Such a correlation is interesting, but must be used tentatively.

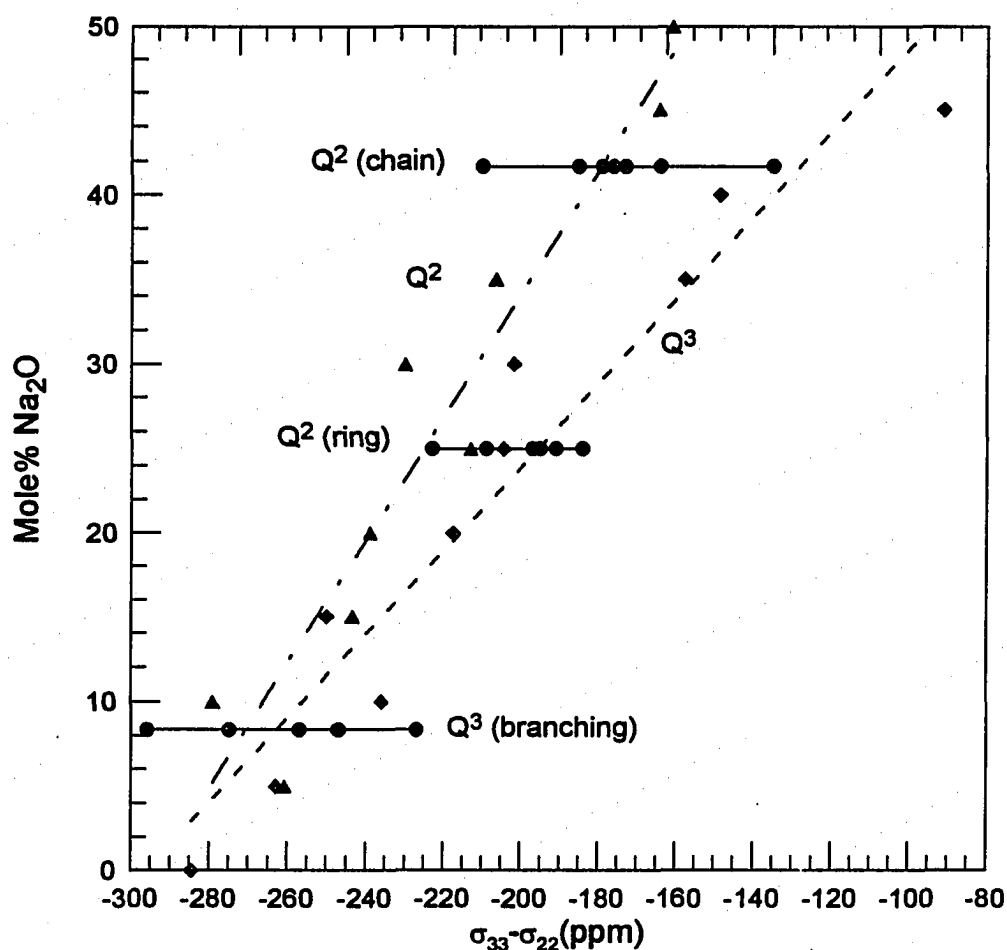


Figure 5.15 The relationship between type of phosphate group and the difference between upfield (σ_{33}) and intermediate (σ_{22}) chemical shielding tensors for crystalline phosphates [70, 71]. Also shown are the $\sigma_{33} - \sigma_{22}$ values for Q³ (— — —, ▲) and Q² (- - -, ◆) species in sodium ultra-phosphate glasses.

5.2.2.3 Summary

Q² species are introduced into the structure as fully delocalized species, as they are found at the metaphosphate composition. Little change is seen in the oxygen bonding of Q³ species at compositions < 20 mole% alkali. However, analyses are consistent with significant changes in oxygen bonding of Q³ species between 20 and 40 mole% alkali. Such changes include: (i) transformation of P=O to P-O-M⁺ terminal oxygens, (ii) increase of P(Q³)-O-P(Q²)

bond angles, and (iii) strengthening of Q^3 - Q^2 bridges. Contrary to the hypotheses that all π -bond delocalization occurs at compositions $<20\text{mole\%}$ alkali [142], we suggest that only at 20mole\% alkali is π -bond delocalization on every structural unit possible, not probable. The π -bond delocalization is initialized after 20mole\% alkali when Q^3 species are coordinated with a second Q^2 species. π -bond delocalization on Q^3 species terminates when Q^3 - Q^3 connections no longer exist, $\sim 40\text{mole\%}$ alkali. Furthermore, analyses are consistent with the network topology changing from branching to ring dominated and finally to chain dominated at the metaphosphate composition.

5.2.3 Glass Transition Temperatures

Figure 5.16 shows the calorimetric glass transition temperatures of sodium and lithium ultra-phosphate glasses obtained in the present study as compared to previously reported transition temperatures [7, 105]. The removal of H_2O has had a dramatic impact on the compositional trend of glass transition temperatures in the ultra-phosphate region.

Martin [7] reports the calorimetric glass transition temperatures of $x Li_2O + (1-x) P_2O_5$ glasses, where $0 \leq x \leq 0.5$, prepared in sealed silica tubes and, at compositions $> 30 \text{ mole\%}$ alkali, open silica crucibles in an inert atmosphere. This data shows a T_g minimum at $\sim 20 \text{ mole\%}$ alkali, additionally, for those glasses prepared in a sealed tube a T_g maximum was found near 40 mole\% alkali. The glass transition temperatures of lithium ultra-phosphate glasses reported by Martin are consistently less than those in the present study. Martin does not report the water contents of glasses used in his study, however, the larger deviations in T_g from the data updated here at low alkali concentrations are most probably due ingressed water which is known to decrease the T_g in proportion to the amount of water present [4]. Similarly, the previously reported glass transition temperatures of hydrated ($\sim 20\text{mole\%}$ H_2O) sodium ultra-phosphate glasses fall below those of the anhydrous ($0.75 \pm 0.6 \text{ mole\%}$ H_2O) sodium ultra-phosphate glasses prepared in this study.

The glass transition temperatures of both lithium and sodium ultra-phosphate glasses exhibit a minimum near 20 mole\% alkali. Such a minimum is considered anomalous. PO_4 tetrahedra

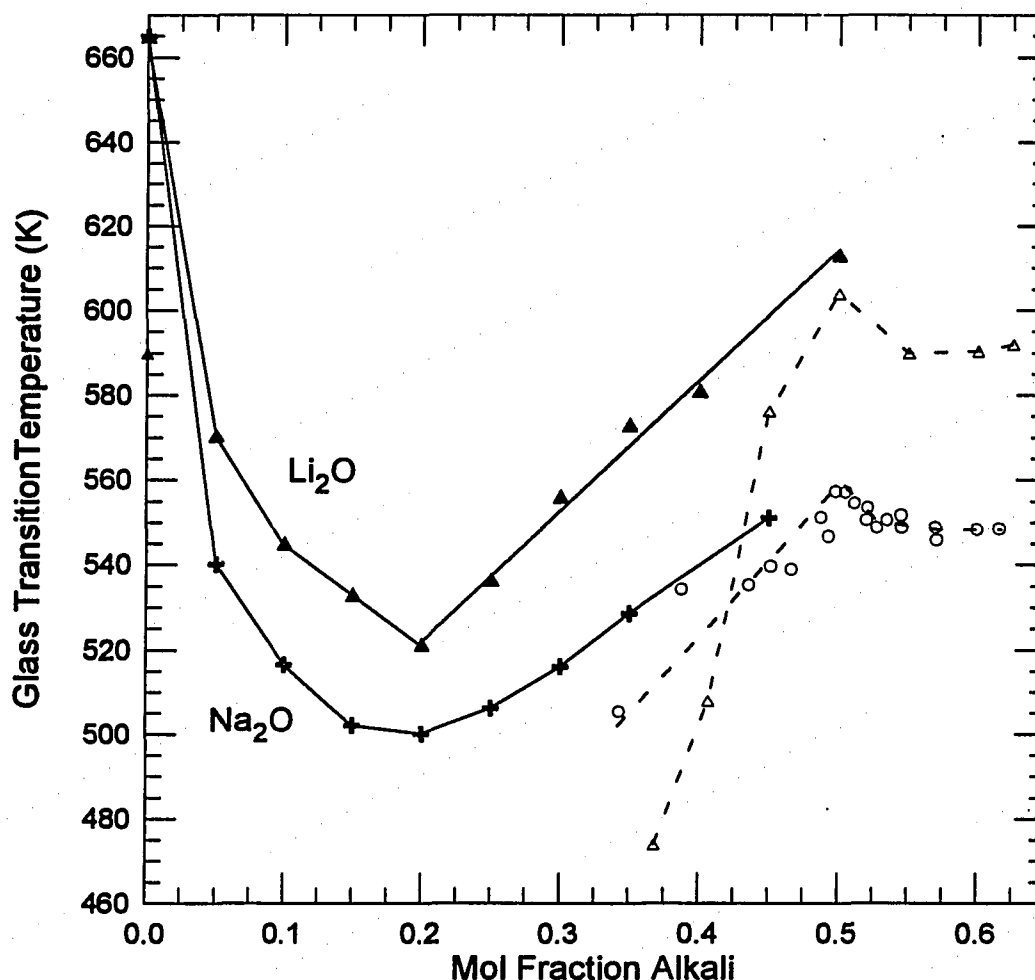


Figure 5.16 The glass transition temperatures of anhydrous lithium (▲) and sodium (+) as compared to hydrated lithium (Δ) [7] and sodium (○) [105] ultra-phosphate glasses.

are as basic as, and similar to SiO_4 tetrahedra in silicate materials [73]. In silicate glasses, the addition of alkali results in chemically simple depolymerization of the network, as we have shown, chemically simple depolymerization is also observed in phosphate glasses. However, with increasing depolymerization of silicates T_g decreases, with the exception of those systems where there is phase separation. Given the similarities between simple alkali phosphate and alkali silicate glass forming systems, the T_g of ultra-phosphate glasses should decrease with increasing depolymerization. Kreidl, however, points out the chief and significant difference

between silicate and phosphate materials is that the pentavalence of P introduces terminal oxygens in the absence of network modifiers [73].

Kreidl and others [73, 142] have suggested the addition of polarizing cations (Na^+ , Li^+ etc.) to P_2O_5 glass will convert the $\text{P}=\text{O}$ terminal oxygens to $\text{P}-\text{O}^-\text{M}^+$ terminal oxygens thereby progressively strengthening the network. According to this structural model, P_2O_5 glass would have the lowest T_g of any binary alkali phosphate glass. Alternatively, Figure 5.16 shows P_2O_5 glass has the highest T_g of any binary lithium or sodium phosphate glass.

Analysis of the oxygen bonding of ultra-phosphate glasses, Section 5.2.2, revealed that between 0 and 20 mole% alkali there is no conversion of $\text{P}=\text{O}$ to $\text{P}-\text{O}^-\text{M}^+$ terminal oxygens on Q^3 species, as suggested by Kreidl. However, the terminal oxygens on Q^2 species are both $\text{P}-\text{O}^-\text{M}^+$ terminal oxygens across the entire ultra-phosphate region. Apparently, the introduction of such Q^2 species does not strengthen the network, but the network is initially weakened, as in the simply constituted silicates.

Between 20 and 40 mole% alkali, the terminal $\text{P}=\text{O}$ oxygens are transformed into $\text{P}-\text{O}^-\text{M}^+$ terminal oxygens on those Q^3 species connected to two Q^2 species. Therefore, with the addition of one Q^2 species: (i) one bridging oxygen is converted to a non-bridging oxygen, (ii) at least one terminal $\text{P}=\text{O}$ oxygen is converted into a $\text{P}-\text{O}^-\text{M}^+$ terminal oxygens. The increased ionic interconnection alone cannot explain the increase in T_g given the continuing depolymerization. We have shown that π -bonding is not located on Q^3-Q^3 bridges, but is concentrated on Q^3-Q^2 and Q^2-Q^2 bridges. The increasing numbers of the stronger Q^3-Q^2 and Q^2-Q^2 bridges over the weaker Q^3-Q^3 bridges with increasing depolymerization, strong directional bonding along Q^2-Q^2 chains and increased ionic interconnection of the glass cooperate to increase T_g between 20 and 50 mole% alkali. Therefore, unlike most oxide based glass systems, oxygen bonding plays a significant role in determining the properties of ultra-phosphate glasses.

5.2.4 Density

Figure 5.18 shows the densities of sodium and lithium ultra-phosphate glasses go through a minimum at 20 mole% alkali. Similarly, Figure 5.17 shows the densities of magnesium and calcium ultra-phosphate crystals [15] are significantly less than either the sheet or branching form of $c\text{-P}_4\text{O}_{10}$, however the density increases between 33.3 and 50 mole% modifier. Therefore, as with sodium and lithium ultra-phosphate glasses, the density of ultra-phosphate crystals must go through a minimum between 0 and 33.3 mole% total modifier.

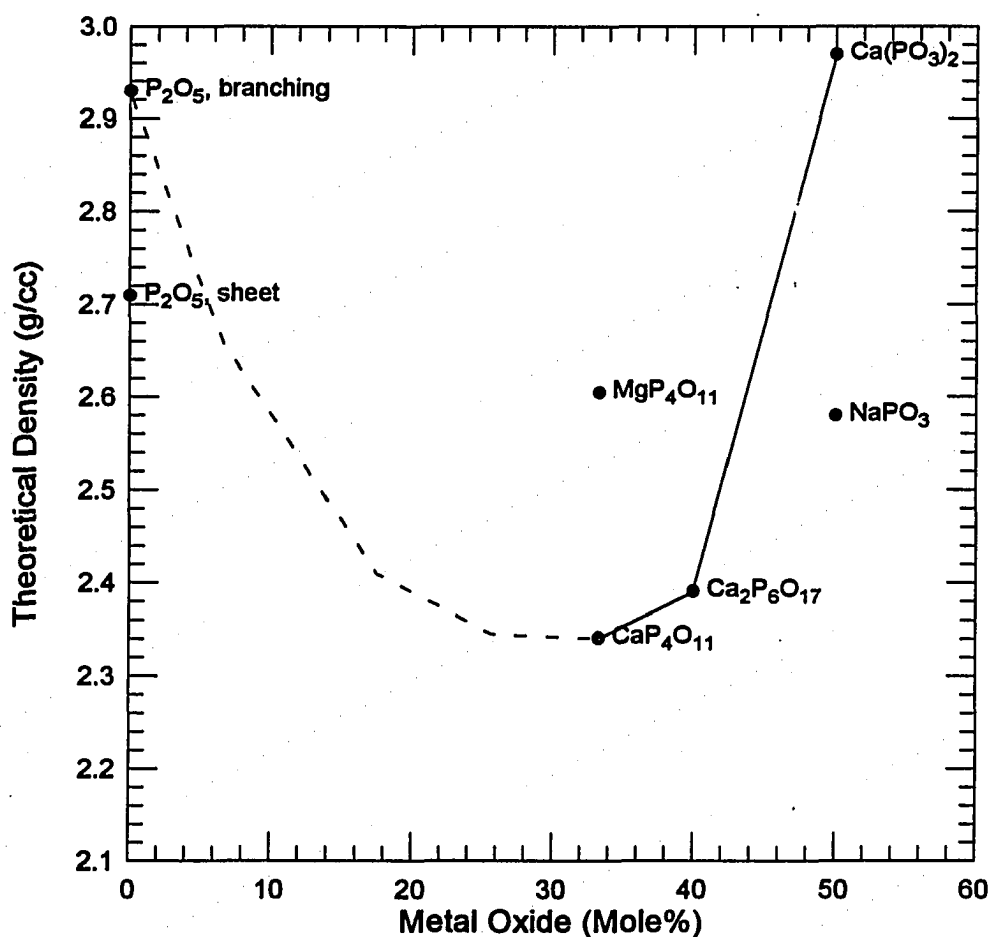


Figure 5.17 The densities of several crystalline ultra-phosphates. Densities have been calculated from lattice parameters [15].

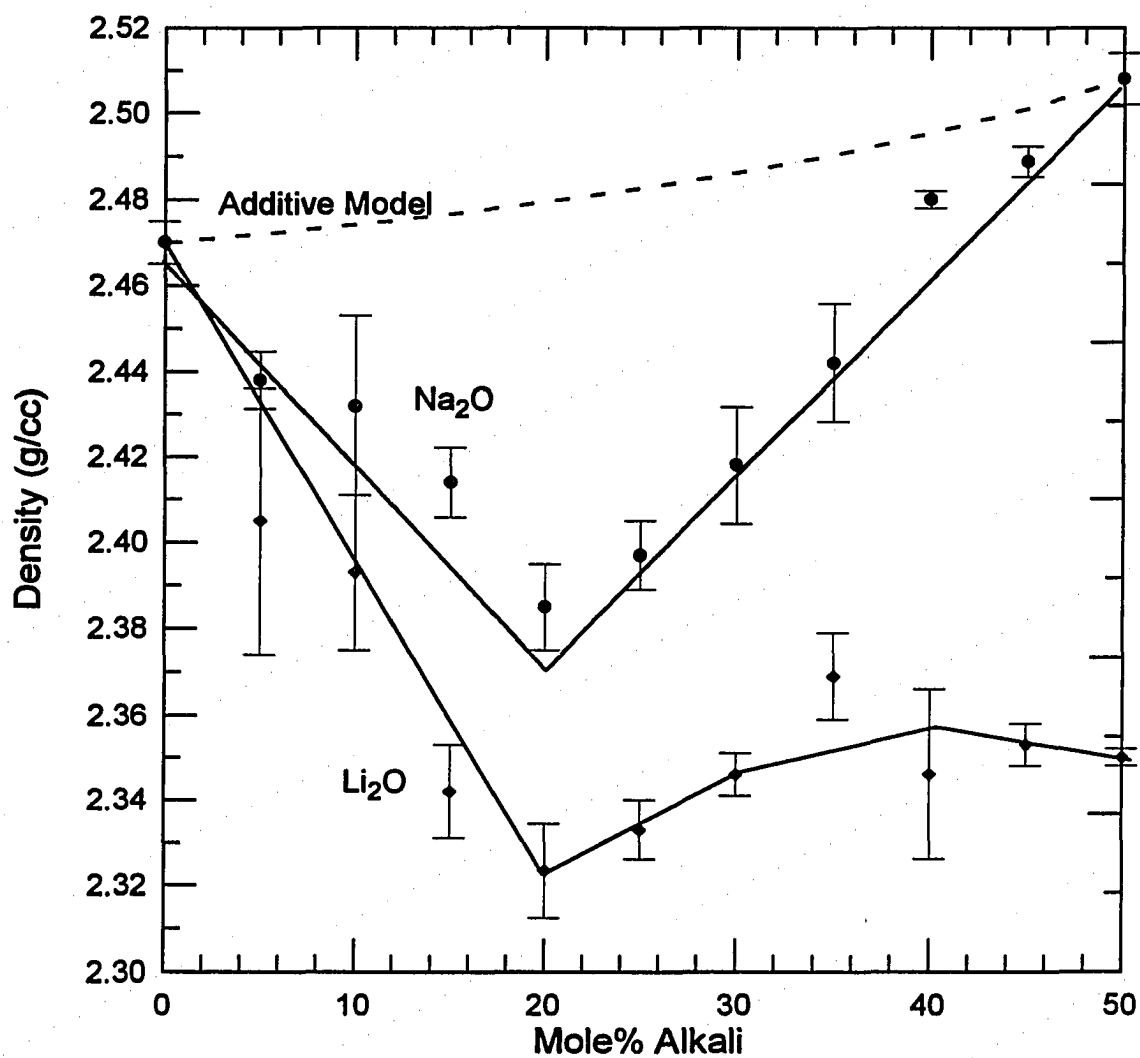


Figure 5.18 The densities of both lithium (♦) and sodium (•) ultra-phosphate glasses show a minimum at 20 mole% alkali. The data cannot be accurately modeled using a simple additive model (----).

Given the chemically simple depolymerization of the alkali ultra-phosphate glasses, their densities should be a smooth function of composition. Assuming that the average density of a Q^3 unit in $v\text{-P}_2\text{O}_5$ and the average density of a Q^2 unit at the metaphosphate composition are characteristic of their respective densities at ultra-phosphate compositions, an additive model [143] can be used to predict density. Figure 5.18 shows such a model deviates significantly from the experimental densities of the sodium ultra-phosphate glasses. Similarly, additive models do not predict the crossing density curves of simple alkali silicate systems or the turning points in the density curves of simple borate glasses [144].

The so-called "boron anomaly" in simple alkali borates is due to the compositional dependence of the coordination number of boron. The molar volume of four-coordinated boron species is less than the three coordinated species, therefore, density becomes dependent on the fraction of four-coordinated species. We have shown P ions stay in a tetrahedral arrangement over the entire glass forming region, therefore, the T_g minimum in ultra-phosphate glasses is not a result of a change in P-coordination.

The density cross-over of sodium and potassium silicates is due to the larger size of potassium (K) ions. The interstices of the loose $(\text{SiO}_4)^{4-}$ network can accommodate most of the Na cations with little expansion; however, the larger K cations greatly expand the network and at high alkali content the density of potassium silicates drops below that of sodium silicates. Conversely, the cavities of the silicate network are significantly larger than the small Li cations and the network contracts, presumably the larger cationic potential of Li plays a role in the contraction of the network. Whether similar compositionally dependent changes in network expansion cause the density minimum in alkali ultra-phosphate can be determined by examining the molar volume.

Figure 5.19 shows the molar volume of sodium and lithium ultra-phosphate glasses. For Figure 5.19, molar volume was calculated as volume per mole of phosphate tetrahedra ($Q^3 + Q^2$). In this way, if countercations are filling the interstices of the network without expanding the network, no change in volume should be seen. The molar volume of P_2O_5 is higher than SiO_2 [145], indicating the silicate network is more compact. It is significant to

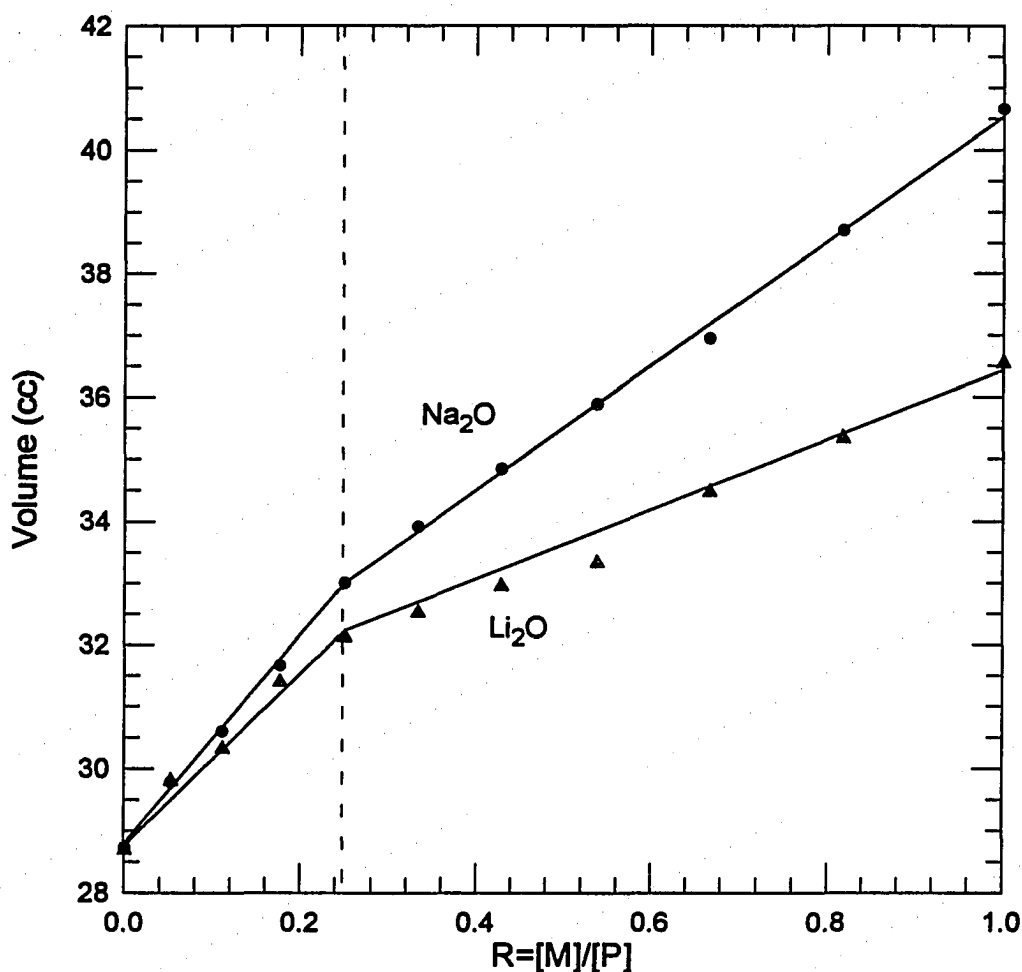


Figure 5.19 The molar volumes of lithium (▲) and sodium (●) ultra-phosphate glasses. The network expands at a significantly faster rate at low alkali concentrations.

note that the terminal oxygen present on P_2O_5 in the absence of alkali increases the free volume of the phosphate network. The molar volume of both sodium and lithium ultra-phosphate glasses increases with increasing alkali content. Therefore, the network is expanding with increasing depolymerization. However, between 0 and 20 mole% alkali, the rate of expansion is significantly greater than that between 20 and 50 mole% alkali.

Expansion of the glassy network is a result of either (i) increasing free volume or (ii) changes in structural species, i.e. longer bonds or larger bond angles. As discussed in Section

5.2.2, ultra-phosphate Q^2 species are structurally similar to metaphosphate Q^2 species having fully delocalized resonance structures with two non-bridging oxygens. The network expands as shorter terminal $P=O$ bonds on Q^3 species are replaced by longer $P-OM^+$ terminal oxygen bonds of Q^2 species, however, such expansion should be a smooth function of alkali content given the chemically simple depolymerization. Furthermore, vibrational and magnetic resonance spectra indicate little change in Q^3 species at compositions < 20 mole% alkali. Expansion of the phosphate network must be due to increases in the free volume of the network.

As discussed in Section 5.1, the topology of P_2O_5 glass resembles the sheet form of $c-P_4O_{10}$. In the sheet form of $c-P_4O_{10}$, the structure resembles corrugated sheets of six Q^3 species [15] with extremely close terminal-oxygen bridging-oxygen distances between sheets, $\sim 3\text{\AA}$ [10]. As in the sheet form of $c-P_4O_{10}$, the topologies of all known ultra-phosphate crystals [15] are dominated by rings composed of from four to sixteen PO_4 tetrahedra. The topology of alkali ultra-phosphate glasses with < 20 mole% alkali most probably consists of "islands" of branching Q^3 species interconnected by Q^2 species. ^{31}P MAS NMR chemical shifts in this low alkali region are consistent with non-random co-polymerization of Q^3 and Q^2 species. Presumably, the modifying cations are not evenly dispersed throughout the network but are grouped inside of ring structures as shown in Figure 5.20. Additionally, the terminal oxygens of both Q^3 and Q^2 species are oriented toward the center of these large rings. Due to repulsion between the terminal oxygens and repulsion between countercations, the interior of the rings contain a significant amount of free volume. The form of such rings can be gleaned from the structures of ultra-phosphate crystals (Figure 5.20).

At 20 mole% alkali every Q^3 species is coordinated with one Q^2 species and isolated "islands" of the tightly packed, branching Q^3 species are not present. Moreover, dramatic changes in oxygen bonding, hence bond lengths and angles, begin near 20 mole% alkali. Therefore, as modifier is added past 20 mole% alkali, network expansion slows because: (i) the necessary amount of free volume to accommodate the countercations is present (ii) bridging bonds between Q^3 and Q^2 species are shortening due to changes in π -bonding and

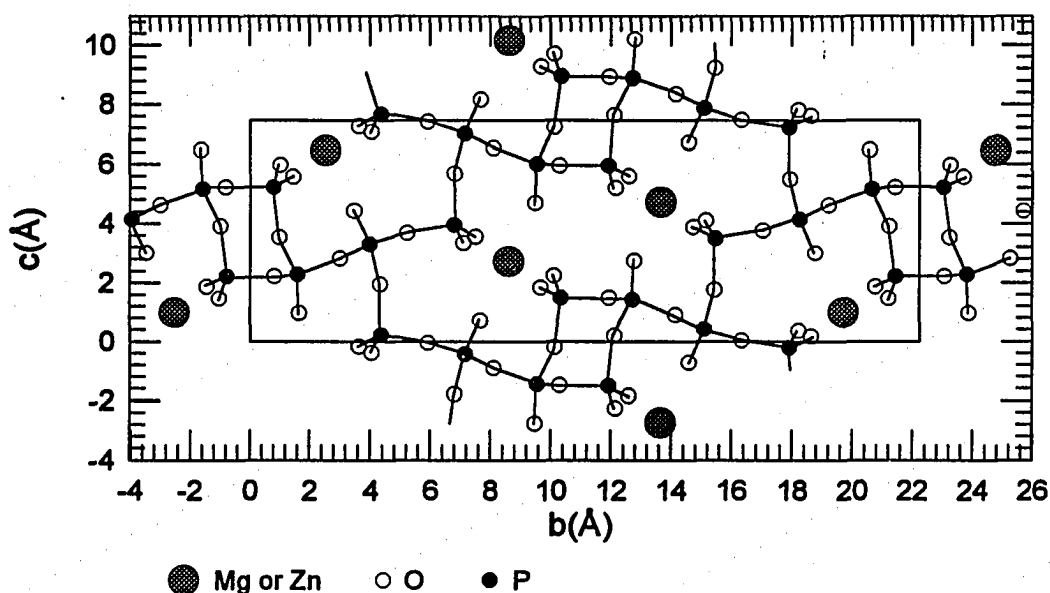


Figure 5.20 The crystal structure of an ultra-phosphate showing the large amount of free volume [15]. The square represents the projection of a unit cell in the b-c plane.

(iii) the tightly packed islands of Q^3 species no longer exist. Because the amount of free volume is not increasing, density increases. The densities of lithium ultra-phosphate glasses are less than those of sodium ultra-phosphate glasses because less network expansion is required to accommodate the much smaller lithium counterions.

5.2.5 Heat Capacity and Structural Relaxation

The investigation of structural relaxation in ultra-phosphate glasses was undertaken primarily to characterize P_2O_5 glass. P_2O_5 glass was previously found to be the archetypal Arrhenius liquid and, therefore, should have single relaxation time kinetics [46]. Modeling the enthalpy relaxation of P_2O_5 glass should return fitting parameters corresponding to such kinetics, $\beta=1$. However, as discussed in Section 5.1, P_2O_5 glass is not the model Arrhenius liquid, but has a $\Delta C_p(T_g)$, T_g , and viscosity commensurate with an intermediate liquid and, therefore, a spectrum of relaxation times.

The focus of the structural relaxation study has been shifted to characterizing structural relaxation around the T_g minimum. Unlike other glassy systems where T_g is most affected by depolymerization of the covalent network or changes in coordination of the glass-forming cation, in ultra-phosphate glasses T_g is dependent on changes in oxygen bonding. The sensitivity of heat capacities, activation enthalpies, and breadth of spectrum of relaxation times to changes in oxygen bonding may provide important clues into their origin.

The solid state heat capacities of all the ultra-phosphate glasses show the characteristic temperature dependence found in most glassy systems. The development of heat capacity as the temperature of the solid rises from 0°K has previously been described in terms of the progressive excitation of quantized vibrational energy states [147]. In the liquid state, all such states are excited and there is no change in the liquid heat capacity. In the transition region between the glassy and liquid state, heat capacity often "overshoots" the value of the equilibrium liquid state heat capacity. The magnitude of this overshoot is proportional to the degree which the glass is out of equilibrium.

At constant volume, the law of Dulong and Petit predicts the maximum heat capacity for a solid is $3R \text{ g atom}^{-1}$. The $3R$ values for the alkali ultra-phosphate glasses were calculated on a mole basis. Formally, the conversion between C_v and C_p is calculated from the expression :

$$C_p - C_v = \frac{TV\alpha^2}{\beta} \quad (5.3)$$

From Equation (40), the difference between heat capacity values are much smaller than the experimental error for the glasses in this study, therefore, we make the approximation $C_p = C_v$. As shown in Figure 5.21, the glassy heat capacities of the sodium ultra-phosphate glasses approach, but do not exceed the maximum value of $3R$.

The magnitude of the glassy state heat capacity is a measure of the average characteristic temperature of the bonds responsible for the configurational changes associated

with the liquid state [146]. In glasses such as SiO_2 , where there is a three-dimensional network, the Si-O bonds must be fully excited to enter the liquid state. Si-O bonds have high characteristic temperatures, therefore, the glassy state heat capacity of SiO_2 reaches 100% of the Dulong-Petit value. Alternatively, for materials such as glycerine, which is a molecular liquid, the weaker intermolecular bonds are broken to produce the configurational changes necessary to enter the liquid state. Therefore, the glassy heat capacity of glycerine reaches only 25% of the Dulong-Petit value. Generally, the magnitude of the glassy state heat capacity in relation to the $3R$ value is a qualitative measurement of the average bond strength of the material and changes should correspond to changes in glass transition temperature.

Given the above discussion, $\%3R$ should decrease with increasing depolymerization as covalent bonds (high characteristic temperature) are replaced with non-directional ionic bonds (low characteristic temperature). As shown in Figure 5.21, $\%3R$ does decrease with depolymerization until $\sim 20\text{mole}\% \text{ Na}_2\text{O}$ then increases monotonically up to the metaphosphate composition. Such a trend is consistent with our model of oxygen bonding in ultra-phosphate glasses.

Between 0 and 20 mole% alkali, bridging oxygens are converted to non-bridging oxygens and the average bond strength of the network decreases. At compositions >20 mole% alkali, the strengths of $\text{Q}^3\text{-Q}^2$ and $\text{Q}^2\text{-Q}^2$ bridges increase and P=O terminal oxygens on Q^3 species are converted into P-OM^+ terminal oxygens. The total number of bonds, ionic + covalent, increases as does the strength of the covalent bonds, therefore, the average bond strength of the network increases.

Similar to $\%3R_n$, the activation enthalpy of a glass is a measure of the average amount of energy necessary to rearrange the structural species in a glass. The amount of energy required is dependent on the number of covalent bonds, the strength of the bonds (covalent and ionic) and the interconnection of the species. Whereas, $C_p(l)/C_p(s)$ is not sensitive to changes in oxygen bonding (strength of bonds), activation enthalpy should be. Figure 5.22 shows that activation enthalpy does scale with the glass transition temperature going through a minimum at 20 mole% sodium, as predicted. Hodge has shown there is a correlation

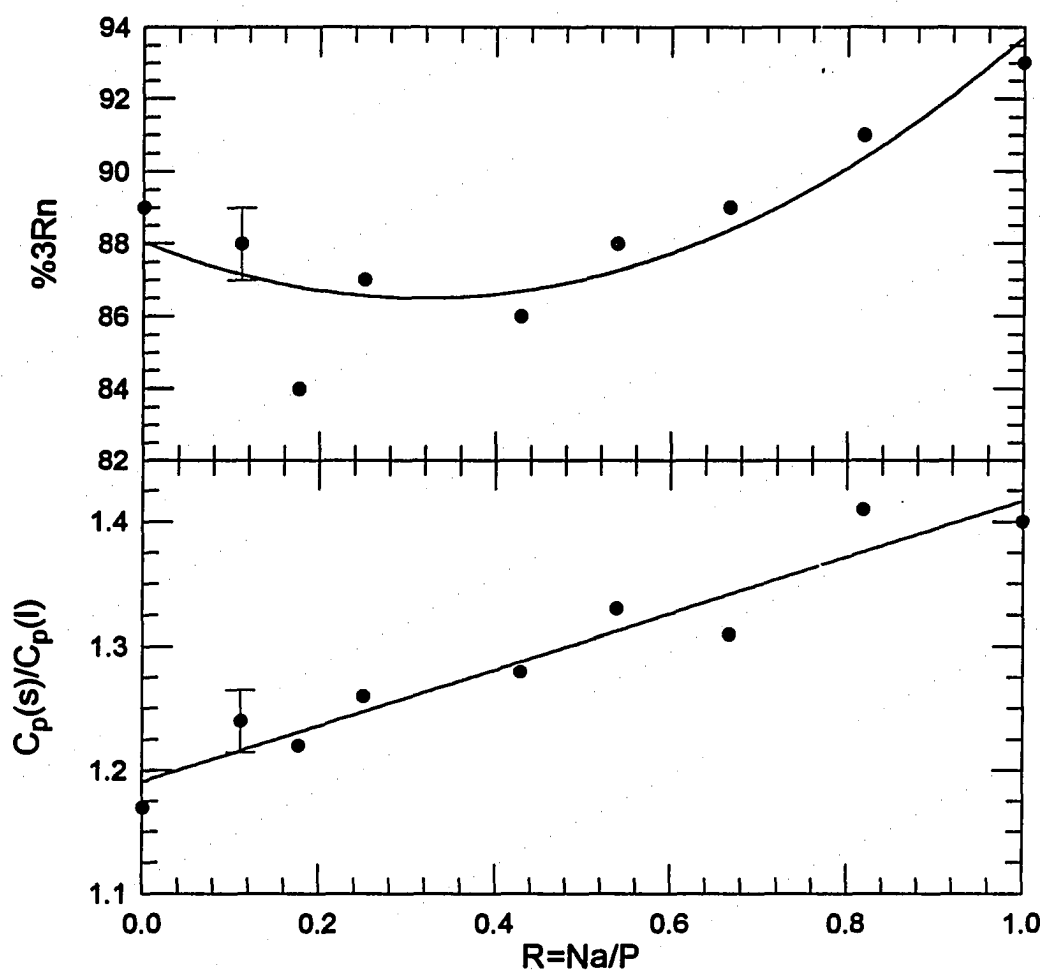


Figure 5.21 The $C_p(l)/C_p(s)$ at T_g increases with increasing depolymerization, while %3Rn goes through a minimum. The error bars are applicable to all measurements.

between activation enthalpy and the breadth of the spectrum of relaxation times; however, such a correlation exists only when materials having similar glass transition temperatures are considered. For the case of alkali ultra-phosphate glasses, there is significant variation in transition temperatures between compositions. Therefore, activation enthalpy for structural relaxation cannot be used to probe the spectrum of relaxation times. We now consider what correlations can be made between heat capacity and the spectrum of relaxation times.

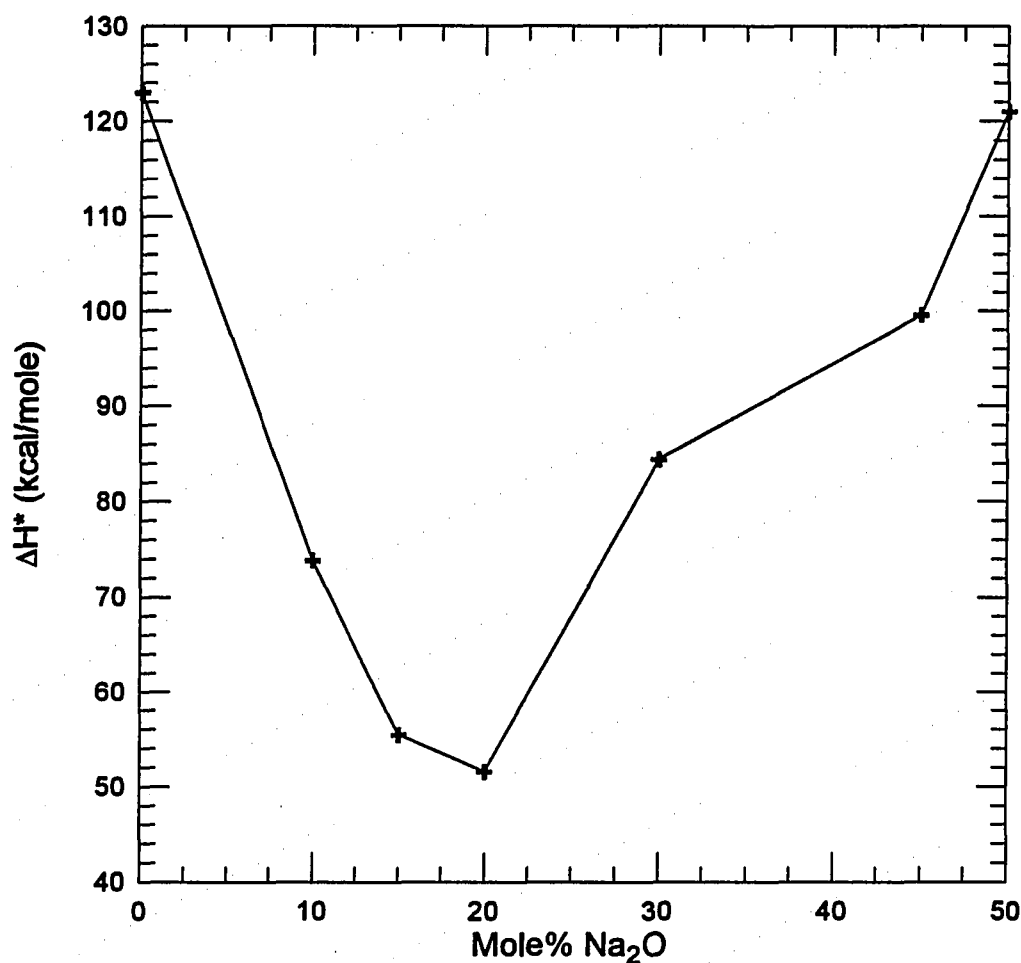


Figure 5.22 The activation enthalpies, ΔH^* , of several sodium ultra-phosphate glasses.

Differences between the liquid heat capacity, $C_p(l)$, and the solid heat capacity, $C_p(s)$, are the result of changes in configurational degeneracy. Liquids like SiO_2 and GeO_2 , where the self-reinforcing, covalent network bonding opposes changes in short and intermediate range order with increasing temperature have limited configuration degeneracy. The amount of configurational degeneracy is proportional to the amount of energy available to activate the translational and rotational degrees of freedom. Therefore, 'strong' liquids have small $C_p(l)/C_p(s)$ ratios. As bonding becomes more non-directional with the introduction of ionic bonds, the number of possible particle arrangements increases for a given energy input and the

$C_p(l)/C_p(s)$ ratio increases. Given the chemically simple depolymerization of the phosphate network, $C_p(l)/C_p(s)$ of ultra-phosphate glasses should increase monotonically with increasing NBO/BO ratio. As shown in Figure 5.21 the $C_p(l)/C_p(s)$ ratio of sodium ultra-phosphate glasses are a linear function ($r^2=0.92$) of the NBO/BO (Na/P) ratio. This observation indicates that the $C_p(l)/C_p(s)$ ratio is insensitive to the significant changes in oxygen bonding in the alkali ultra-phosphate glasses.

Similarly, $C_p(l)/C_p(s)$ is insensitive to changes in cation potential of countercations, for example, $C_p(l)/C_p(s)$ for LiPO_3 is ~ 1.31 compared to ~ 1.34 for NaPO_3 . Presumably, the more covalent nature of bonds formed by countercations with higher cation potentials do decrease the average configurational degeneracy but not to the same degree as changing the degree of depolymerization. More generally, $C_p(l)/C_p(s)$ scales inversely with T_g , because the factors affecting T_g , degree of depolymerization and cationic potential, also affect configurational degeneracy. However, changes in T_g due to oxygen bonding are unique to the alkali ultra-phosphate systems.

In an attempt to further define the structural relaxation of the sodium ultra-phosphate glasses, heat capacity curves were fit using a semi-empirical model. A full description of the model and modeling procedures are given in Section 2.3. Specifically, we desired to determine the compositional dependence of the spectrum of relaxation times, β , responsible for structural relaxation. Bohmer et al. [147] have shown that the fragility, m , of a glass-forming liquid is given as:

$$m = \left. \frac{d \log \langle \tau \rangle}{d(T_g/T)} \right|_{T=T_g} \quad (5.4)$$

where τ is the relaxation time for structural rearrangement. Interestingly, the spectrum of relaxation times can be probed using a number of different techniques including dielectric spectroscopy, viscoelastic modulus measurements, quasielastic light scattering experiments,

and others and the non-exponential behavior is often approximated using the KWW equation. By gathering beta parameters from a number of techniques and a variety of materials Bohmer et al. Have found a correlation between fragility and β . Most betas are concentrated along the line:

$$m = 250 - 320\beta, \quad (5.5)$$

If the materials are limited to network liquids (SiO_2 , GeO_2 , etc.) m varies ± 15 for a given β . As was discussed in Section 0, the $C_p(l)/C_p(s)$, T_g , and reduced viscosity of $v\text{-P}_2\text{O}_5$ are similar to those for B_2O_3 and $\text{Na}_2\text{O} \cdot 2\text{SiO}_2$. In support of these materials having similar distributions of relaxation times, Table 5.3 shows the β for $v\text{-P}_2\text{O}_5$ found in this study is similar to those found for B_2O_3 and $\text{Na}_2\text{O} \cdot 2\text{SiO}_2$. It appears the dimensionality of the covalent interconnection of the network plays the significant role in determining the spectrum of relaxation times. Therefore, as alkali is added and the network is depolymerized and β should increase. The increasing $C_p(l)/C_p(s)$ of alkali ultra-phosphate glasses is consistent with such a trend, as is the increasing fragility of reduced T_g viscosity curves with increasing depolymerization [4]. Alternatively, the betas determined from enthalpy relaxation fits increase with increasing depolymerization. Given the poor quality of a majority of the enthalpy relaxation fits and the poor correlation of fragility with b given small changes fragility, little significance is afforded to the compositional dependence of the betas.

5.3 The Melt Processing Dependence of Properties

Martin [7] showed the glass transition temperatures of lithium ultra-phosphate glasses with between 35 and 50 mole% Li_2O were dependent on preparation technique. The glass transition temperatures of lithium ultra-phosphate glasses prepared in a open crucible within a dry box fell consistently below those prepared in sealed silica crucibles. Moreover, a maximum in T_g was found for those glasses prepared in the sealed tube. Martin observed the significant difference in preparation technique was quench rate. Both sealed tube and open

Table 5.3 The T_g , fragility and non-exponentiality parameter of representative glass forming liquids [147].

Glass former	T_g (K)	$m(T_g)$	$\beta(T_g)$
SiO ₂	1500	20	0.70
GeO ₂	818	20	1.00
B ₂ O ₃	554	32	0.60
Na ₂ O·2SiO ₂	728	45	0.60
P ₂ O ₅ ^a	666	45	0.59
KCN	343	93	0.45

^a From the present study.

crucible preparations were held at 1000°C, however, open crucible preparations were splat quenched at 1000°C/min. while sealed tube preparations were quenched at ~0.1°C/min. From these observations, Martin hypothesized the structures of these phosphate liquids are highly temperature dependent.

At high temperatures the available thermal energy is on the order of the free-energy difference between the two different structures available to the liquid, therefore, entropy considerations would favor structures where more configurational disorder exists; less connected structures. At lower temperatures the driving force towards a more-connected structure is larger than the available thermal energy, in this case the lower free energy, less-connected structures are preferred. Therefore, at $T \gg T_g$ all phosphate liquids share the same disordered, less-connected IRO, it is the quench rate that determines the non-equilibrium (glassy state) IRO. A rapid quenching rate (splat quenching) allowed the high temperature, disordered IRO to be "frozen" into the glass, while the polymerization process necessary to produce a more-connected glass was kinetically arrested. However, a slow quench rate (sealed tube preparation) allowed the necessary time for polymerization to take place, creating a more connected structure.

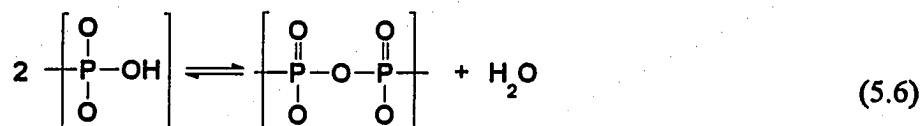
To explore this hypothesis Martin [7] proposed an experiment where a melt would be sealed in a closed ampoule and then subjected to isothermal holds for increasing periods of time. At the end of each hold the melt would be rapidly quenched to room temperature in

order to freeze in the equilibrium structure of the liquid into the non-equilibrium glass, and the T_g measured

A glass that was initially cooled at $1000^\circ\text{C}/\text{sec}$ was hermetically sealed inside a gold DSC sample pan and then subjected to heat treatments aimed at replicating glass formation using a slow cooling rate, $0.01^\circ\text{C}/\text{sec}$. The sample was first soaked at $T \approx T_g$ (600°C) for increasing periods of time, where T_g was measured after each hold. T_g increased ≈ 150 K after soaking 25 hrs. at 600°C . The sample was then soaked at 900°C for 12 hrs., to simulate a fast cooling rate, and T_g was measured again. T_g decreased ≈ 150 K to a value very near the same as the "as prepared" value of 450 K. Reproducibility was tested by reheating the sample to 600°C for 48 hrs. and T_g was found to again increase by ≈ 150 K. Martin hypothesized these phenomena were the result of highly processing dependent IRO structures in the alkali phosphate liquids he studied; however, he did not define the structures present. For this study, repeated attempts at repeating this experiment were not successful.

A 40 mole% Li_2O glass was batched, held at 600°C for 17 hrs., quenched to room temperature, and T_g was measured. The same sample was then resealed in a silica tube, reheated to 900°C , held at that temperature for 17 hrs., quenched to room temperature at the same rate as the first sample, and T_g was measured. Finally, the 600°C preparation was repeated. Contrary to the findings of Martin, T_g was not higher for the glass held at 600°C but was 60°C higher for the glass held at 900°C and the T_g did not change after the final 600°C melt anneal. Similar results were found for the 40 mole% Na_2O ultra-phosphate glass composition. The absence of "switchability" of the glass transition temperature is due to the methods used by Martin to measure the processing dependence.

P_2O_5 forms an azeotrope with boiling water at 850°C [148]. Therefore, the reversible pseudo-reaction:



will be driven to the left at temperatures $> 800^{\circ}\text{C}$, and to the right at temperatures $< 800^{\circ}\text{C}$ [99]. To analyze the melt processing dependence of his glass, Martin sealed a powdered glass sample in a gold pan and carried out the experiments in a differential scanning calorimeter. Experience using gold DSC pans has shown them to not be hermetic, and are not sold as being hermetic. Therefore, when the small sample was held at 600°C Equation 43 was driven to the right and the T_g of the glass increased as the structure was polymerized. Alternatively, when the glass was held at 900°C Equation 43 was driven to the left and the structure was depolymerized and T_g decreased. For our preparations, glasses were sealed in an evacuated silica ampoule and H_2O contamination was not a factor. A parallel argument can explain the perceived quenching rate dependence of the glass transition. Those glasses prepared in the open crucibles absorbed free H_2O in the dry box, thereby depolymerizing the phosphate glass and decreasing T_g as compared to those glasses prepared in sealed tubes where the amount of free H_2O was small.

Although not in the manner described by Martin, the glass transition temperatures of alkali ultra-phosphate glasses are dependent on melt processing (Figure 5.23). The T_g of sodium metaphosphate glass is dependent on preparation technique. Sodium metaphosphate glasses prepared in a sealed, evacuated silica tube with increasing melt annealing times had equivalent glass transition temperatures, however, those glasses prepared in silica tube open to the atmosphere showed glass transition temperatures and crystallization temperatures $\sim 30\text{K}$ higher. Interestingly, remelting of the glass prepared in the sealed ampoule within an open ampoule results in an increased T_g .

Initially, it was presumed that the difference in T_g of the metaphosphate composition was due to ingressed water since it is well known that the amount of residual water in a phosphate melt can be decreased with melt time thereby increasing T_g [99]. However, a qualitative inspection of the MIR spectra reveals the same amount of water in the phosphate glass. Moreover, the T_g of the 45 mole% Na_2O composition is 20K higher than that of the metaphosphate prepared in the silica crucible. If there were water retention, a lower T_g would be expected for the 45 mole% composition where the glass was made with the same starting

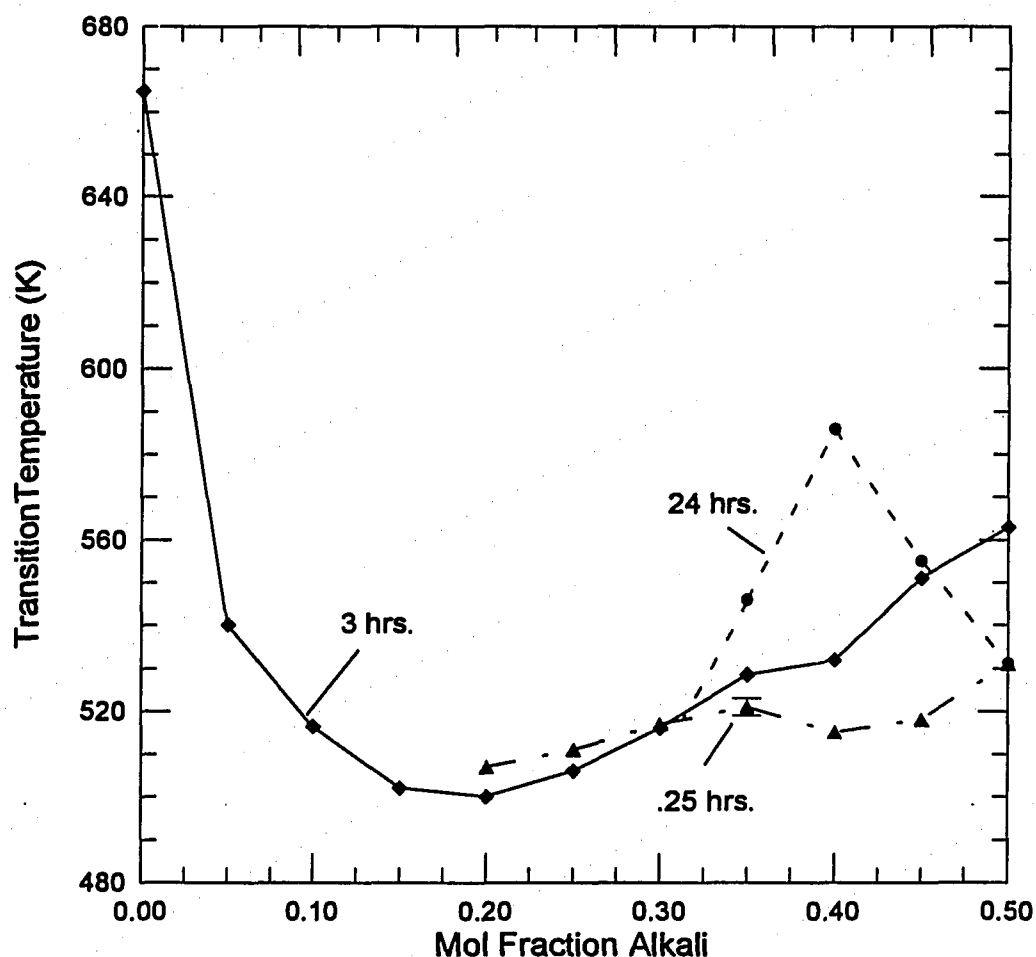


Figure 5.23 The glass transition temperatures ($\pm 3^\circ\text{C}$) of sodium ultra-phosphate glasses held at 900°C for 0.25hrs (\blacktriangle , - - -), 3hrs. (\blacklozenge , —), and 24hrs. (\bullet , - - -). At the metaphosphate composition, T_g was independent of melt annealing time for all sealed tube preparations. The higher T_g resulted from preparing sodium metaphosphate in an open silica crucible.

material. Possibly, due to the low water vapor pressure in the sealed silica tube technique, preferential linkages are forming in the metaphosphate melt.

It has been shown that the structure of Graham's salt, $(\text{NaPO}_3)_n$, consists of high-molecular weight polyphosphate chains, cyclic trimetaphosphate rings ($\text{Na}_3\text{P}_3\text{O}_9$), and higher order rings [128]. At higher preparation temperatures and/or lower water vapor pressures more trimetaphosphate rings and longer polyphosphate chains are found in the crystal. The

formation of these rings is thought to be promoted by the formation of long, coiled polymetaphosphate chains which develop into $\text{Na}_3\text{P}_3\text{O}_9$ rings in the melt. In a sealed silica tube the water vapor pressure is extremely low when compared to an open air crucible. This could promote the development of a large fraction of $\text{Na}_3\text{P}_3\text{O}_9$, or higher order rings in the melt significantly decreasing the strength of the glass and reducing T_g . However, as shown in Figure 5.24, the MIR spectra of the glass prepared in a sealed tube is virtually identical to the MIR spectra of the glass prepared in an open crucible. While the formation of small rings would undoubtedly result in strained Q-sites and changes in the MIR spectra, the formation of large rings (5-membered) may not lead to such strain and the MIR spectra of such a structure would be similar to that of a chain metaphosphate, as in Figure 5.24. Further quantitative work is required to better understand the structures responsible for the difference in T_g .

Interestingly, the T_g of lithium metaphosphate glass is not dependent on preparation technique. Both open crucible and sealed tube preparations result in similar glass transition temperatures. While a number of crystalline ring structures are known for sodium ultra-phosphate glasses, a review of the literature could find no ring lithium metaphosphate crystals. Such an observation is consistent with the proposed model for the structural changes giving rise to the processing dependence of the T_g .

The T_g of the 40 mole% sodium ultra-phosphate glass increases with melt annealing time. As shown in Figure 5.25, T_g increases $\sim 70\text{K}$ after holding the melt 900°C for 15 hours. Similarly, as shown in Figure 5.26 the density of the 40mole% Na_2O glass increases significantly with melt annealing time. The densities of the glasses held at 900°C for 15 minutes could not be accurately measured because they were heavily fractured. Similar variations in properties have been observed for amorphous GeO_2 and binary alkali borate glasses.

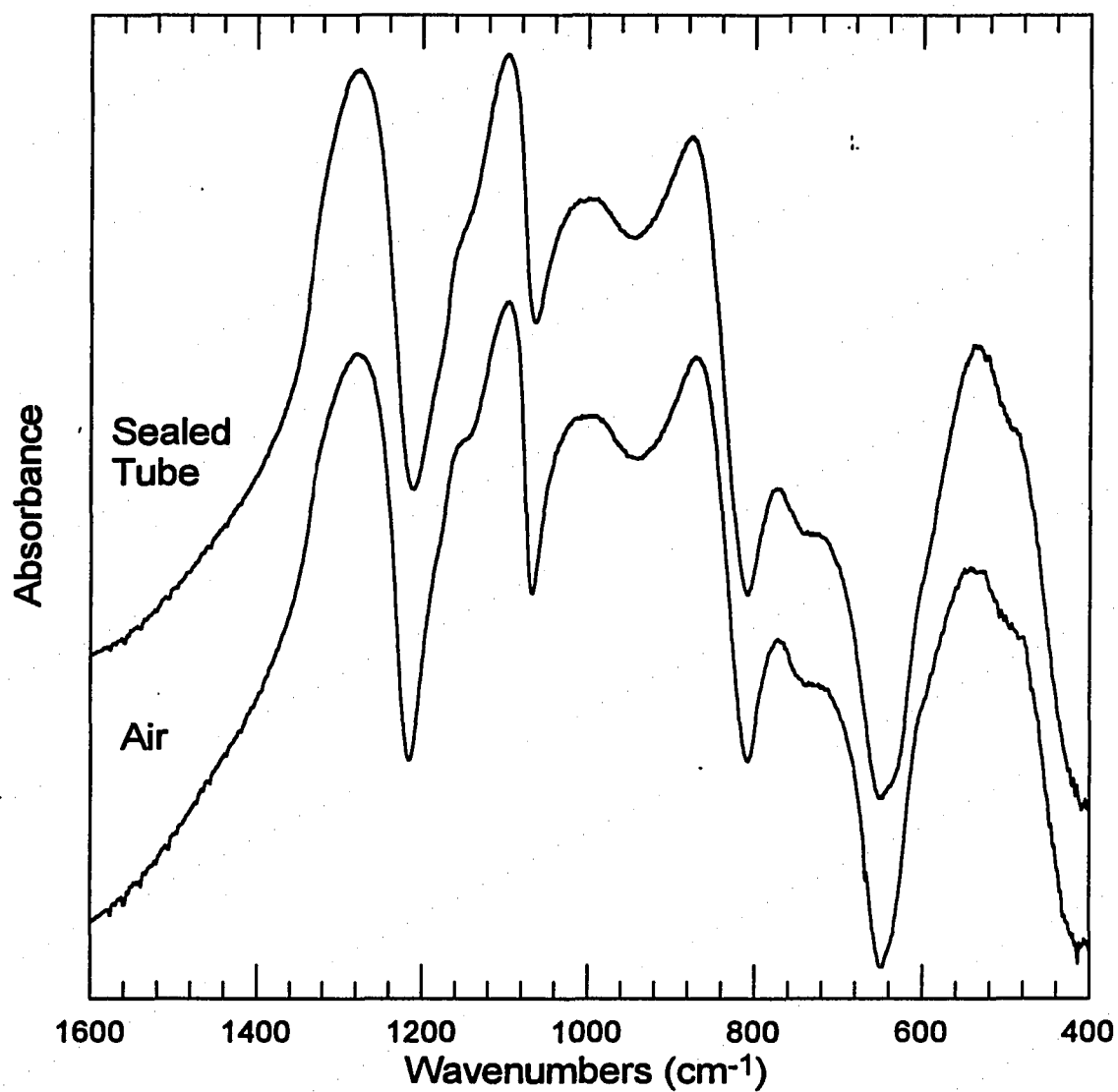


Figure 5.24 The MIR spectra of sodium metaphosphate glasses prepared in a sealed crucible and open crucible. There is virtually no difference in the spectra.

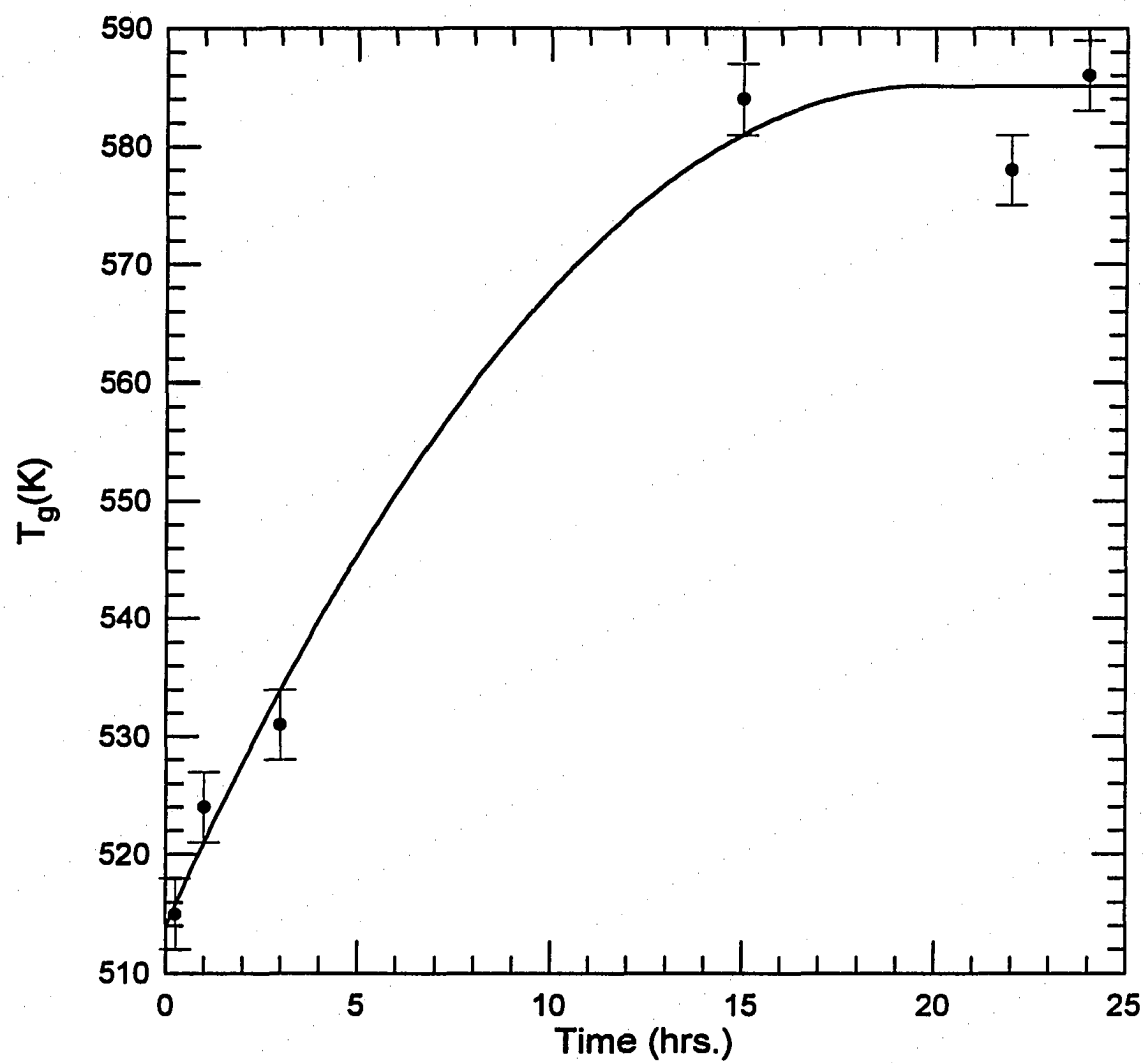


Figure 5.25 The glass transition temperatures of the 40 mole% Na_2O glass as a function of hold time at 900°C . All glasses were quenched at identical rates.

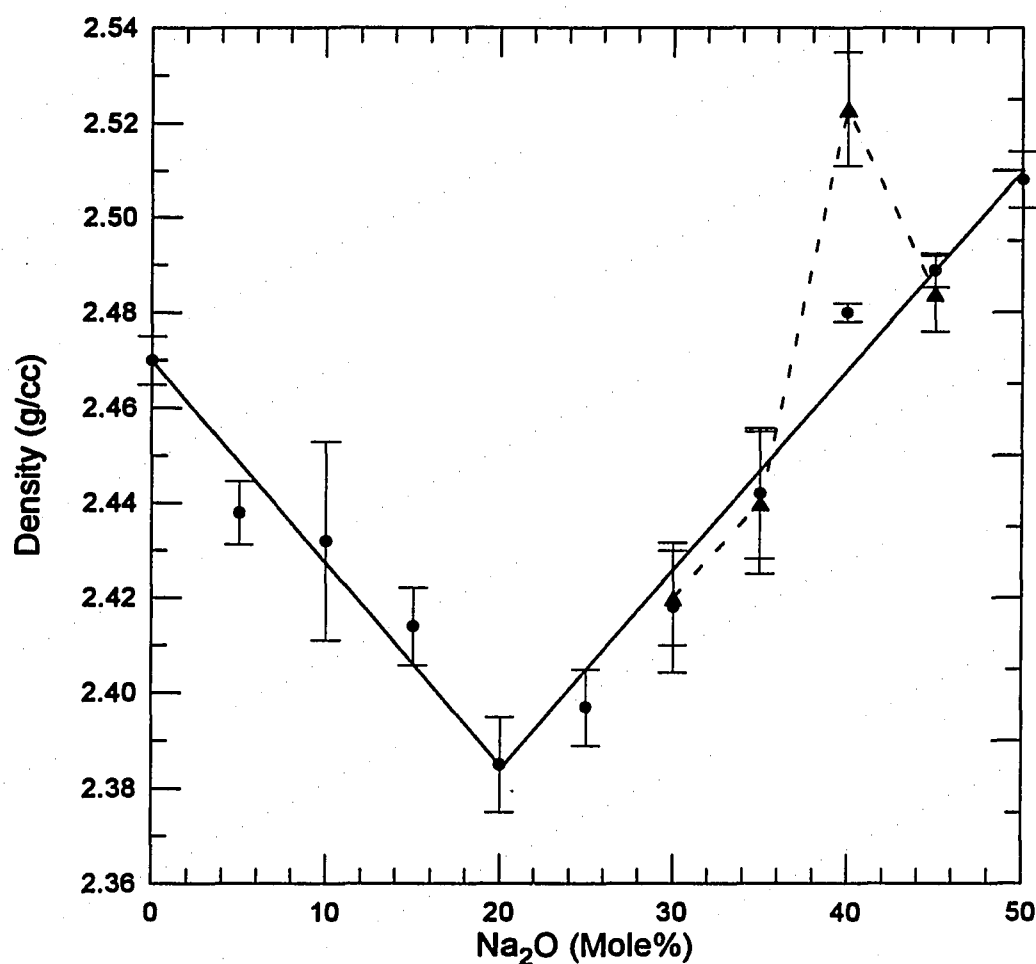


Figure 5.26 The densities of sodium ultra-phosphate glasses after melt annealing for 3 hrs. (●, —) and 24 hrs. (▲, ----).

The properties of amorphous GeO_2 have been shown to be dependent on melt temperature [87-93]. The slowly relaxing process responsible for the melt processing dependence of the properties is the equilibration of oxygen-related defects. At present, we have no evidence suggesting a similar mechanism is present in alkali ultra-phosphate glasses. Sodium triborate glasses prepared using identical melt temperatures and quench rates exhibited decreasing electrical conductivity, density and IR absorptivity with increasing annealing time of the melt at 850°C [94]. The origin of the melt processing dependence of

the properties is the transformation of tetrahedrally coordinated boron to less compact triangularly coordinated boron units. The transformation between the borate species is ~ 10 orders of magnitude slower than the structural relaxation responsible for changes in viscosity. Possibly there are similar slowly relaxing structures in ultra-phosphate glasses which are not formed until the melt is held for many hours.

The average relaxation time for structural relaxation of a melt is given by:

$$\langle \tau_r \rangle = \eta_s / G_\infty, \quad (5.7)$$

where η_s is the shear viscosity and G_∞ is the infinite time shear modulus. For sodium metaphosphate glass $\eta_s = 4.67$ Pascal at 846°C [149] and $G_\infty = 10^{10}$ dyne/cm² is a reasonable estimate for amorphous materials, thus, $\tau_s \approx 4.9 \times 10^{-9}$ s. The structure should reach equilibrium at an average of $5 \times \tau_s$ or $\approx 2 \times 10^{-8}$ s at 846°C . Therefore, structural equilibrium should be reached almost instantaneously at 900°C . At temperatures just above T_g , $\tau_s \sim$ seconds and the structure of the amorphous solid is dependent on the structure of the supercooled liquid. The relaxation time is a broad distribution due to the distribution of bond angles and bond lengths in amorphous materials. It is possible that the process responsible for the changing T_g has a relaxation time in the long tail of the relaxation time distribution. In the alkali borates the slowly relaxing structure involves the formation of four-coordinated borons, therefore, the development of such structures can be studied by examining the MIR absorbance spectra.

The MIR spectra of a 40mole% Na_2O ultra-phosphate glass after holding for 1 and 22 hrs at 900°C are shown in Figure 5.27. Also shown in Figure 5.27 are the MIR spectra of ring-dominated calcium ultra-phosphate crystals and the MIR spectra of a chain-dominated calcium metaphosphate crystal [15]. There are significant differences between the glassy spectra. In the MIR spectrum of the glass held at 900°C for 15hr. the $\nu(\text{P}=\text{O})_s$ (or $\nu(\text{PO}_2)_{as}$) mode is shifted to lower wavenumbers, the intensity of the $\nu(\text{PO}_2)_{as}$ modes are concentrated near 1100cm^{-1} , and the POP modes are more separated than in the spectrum of the 1 hr. glass. Note that band complex II and band complex III of the 15hr. glass and chain metaphosphate

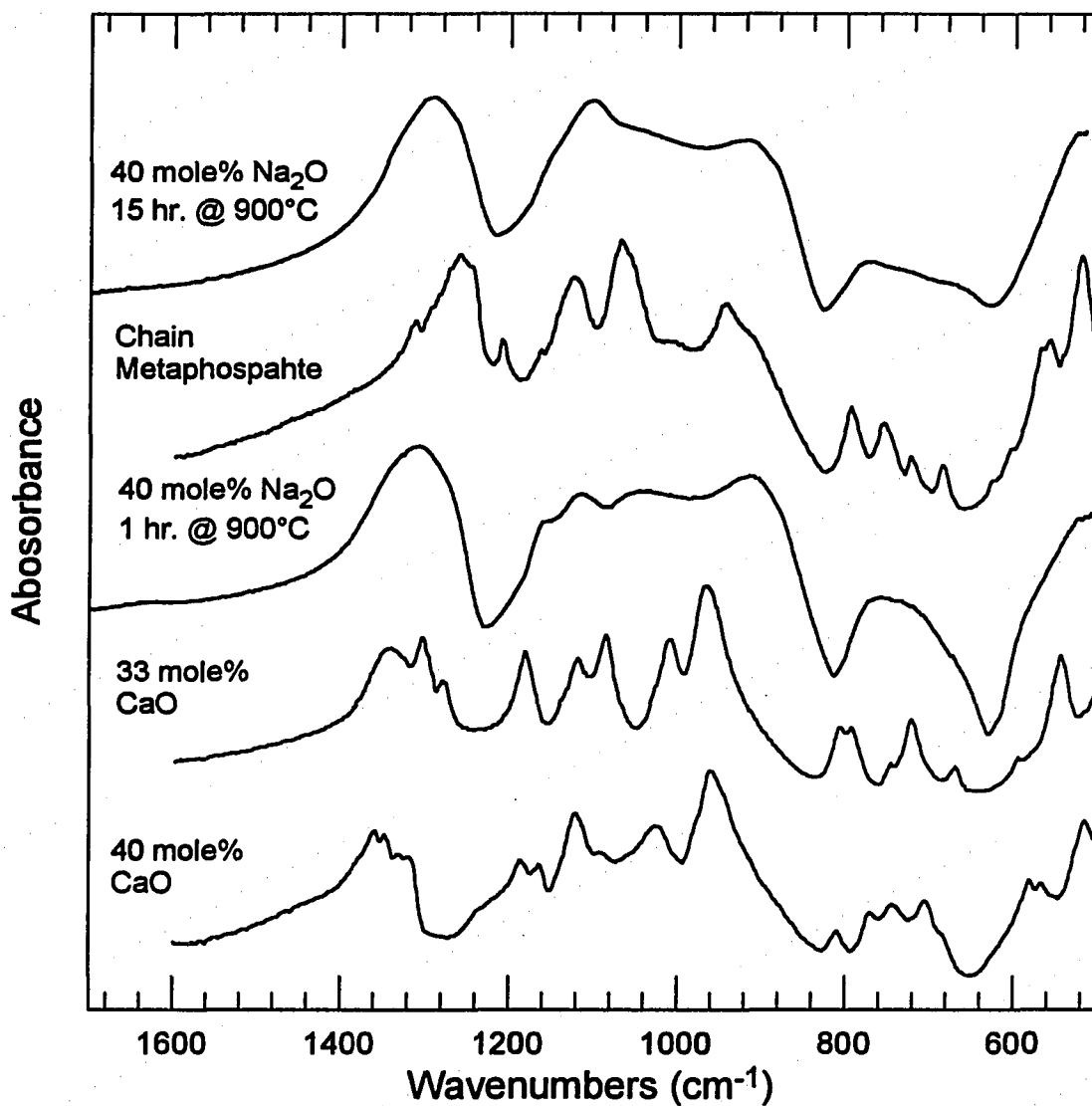


Figure 5.27 The MIR spectra of a 40mole% Na_2O ultra-phosphate glass after holding for 1 and 22 hrs at 900°C . The MIR spectrum of the 40mole% Na_2O glass held at 900°C for 1hr. resembles the MIR spectra of ring-dominated calcium ultra-phosphate crystals [15]. Alternatively, the MIR spectrum of the 40mole% Na_2O glass held at 900°C for 15hr. resembles the MIR spectra of the chain-dominated calcium metaphosphate crystal [15].

are similar, but complex I is at higher wavenumbers in the 15 hr. glass spectra. Likewise, the band complexes of the 1hr. glass and the cyclic calcium phosphate crystals are similar.

The MIR spectra suggest the change in structure is driven by enthalpy as opposed to entropy considerations, as suggested by Martin [7]. It has been shown, Section 5.2.2, that movement of the $\nu(\text{P=O})_s$ (or $\nu(\text{PO}_2)_{as}$) mode to lower wavenumbers corresponds to a decrease in the asymmetry of π -bonding on phosphate tetrahedra. Therefore, the structure of the 15hr. glass is in a more symmetric, lower energy, configuration than that of the 1hr. glass. The MIR spectra suggest the structure of the 1hr. glass is best represented by rings while that of the 15hr. glass is best represented as interconnected rings. The question remains why the formation of chain structures would reach completion ten orders of magnitude slower than the bulk structure relaxes.

Interestingly, the Raman spectra of this same composition shows high frequency shoulders on both the $\nu(\text{PO}_2)_{as}$ and $\nu(\text{PO}_2)_s$ peaks. The shoulders are well-defined and well-separated from the $\nu(\text{PO}_2)_{as}$ and $\nu(\text{PO}_2)_s$ peaks and appear to be variants of the $\nu(\text{PO}_2)_{as}$ and $\nu(\text{PO}_2)_s$ stretching vibrations. Their appearance on the high frequency side of the main $\nu(\text{PO}_2)_{as}$ and $\nu(\text{PO}_2)_s$ peaks suggests a strained structure and their appearance as distinct bands, rather than a broadening of the main band, suggests a specific structure. Similar defect modes have been found in various forms of silica [150].

Prominent in the Raman spectra of high surface area silica materials are two bands at 606 and 495 cm^{-1} given the designations D1 and D2, respectively, which cannot be explained through conventional random network models of fused silica [150]. Galeener [151] found the D1 and D2 bands arise from vibrationally-decoupled four-fold and three-fold siloxane rings, respectively. These small rings are found mainly in high-surface area silicates because they form through condensation of surface hydroxyl groups and are therefore, susceptible to hydroxyl attack. Similarly, the Raman spectra of a hydrated sodium ultra-phosphate glass containing 40mole% total modifier ($\text{Na}_2\text{O}+\text{H}_2\text{O}$) does not show high frequency shoulders on either the $\nu(\text{PO}_2)_{as}$ or $\nu(\text{PO}_2)_s$ peaks[74] suggesting that the species giving rise to the high

frequency shoulders are strained. To further investigate these bands, we performed a high temperature Raman study of a 40mole% sodium ultra-phosphate glass.

As shown in Figures 5.28 and 5.29, the high frequency shoulders on the main $(\text{PO}_2)_{\text{sym}}$ and $(\text{PO}_2)_{\text{asym}}$ modes were found to disappear when the glass was heated above T_g and into the melt (900°C) and then reappear as the glass was cooled through T_g . Interestingly, these peaks did not disappear until $>200^\circ\text{C}$ above T_g ($\sim 257^\circ\text{C}$). Therefore, the peaks must be representative of a strained structure which relaxes much slower than the cooperative rearrangements necessary for the glass to move into the liquid state. Moreover, after holding for two hours at 900°C the fraction of strained species increases significantly. The numbers of these strained species is proportional to the increase in T_g . From the shape of the MIR spectra, as discussed above, it is unlikely the strained species are representative of small rings in the structure. Alternatively, we suggest the strained species are representative Q^3 units bridging between chains. This hypothesis is consistent with a maximum in T_g at 40 mole% alkali.

The crosslinking of chains will increase the glass transition temperature of a glass, providing ring structures are not formed. Between 40 and 50 mole% alkali and at long anneal times, rings are not formed and Q^3 species cross-link chains of Q^2 species thereby increasing T_g . As the network is further polymerized between 40 and 20 mole% alkali, ring structures are formed and weak Q^3 - Q^3 linkages are formed, and T_g decreases.

The melt processing dependence of the fraction of rings in ultra-phosphate glasses is consistent with the increase in density with increasing melt anneal times. Chain structures undoubtedly pack more efficiently than ring structures. Furthermore, the density should increase as chain structures are cross-linked and free-volume decreases. Therefore, at 40 mole% alkali where the maximum amount of crosslinking of chains takes place, without formation of ring structures, density increases.

In conclusion, it must be emphasized that our model of the structural changes leading to the melt anneal dependence of alkali ultra-phosphate glasses has not been confirmed, but is

consistent with experimental results. A significant amount of work is required to elucidate the structures leading to such unique processing dependence.

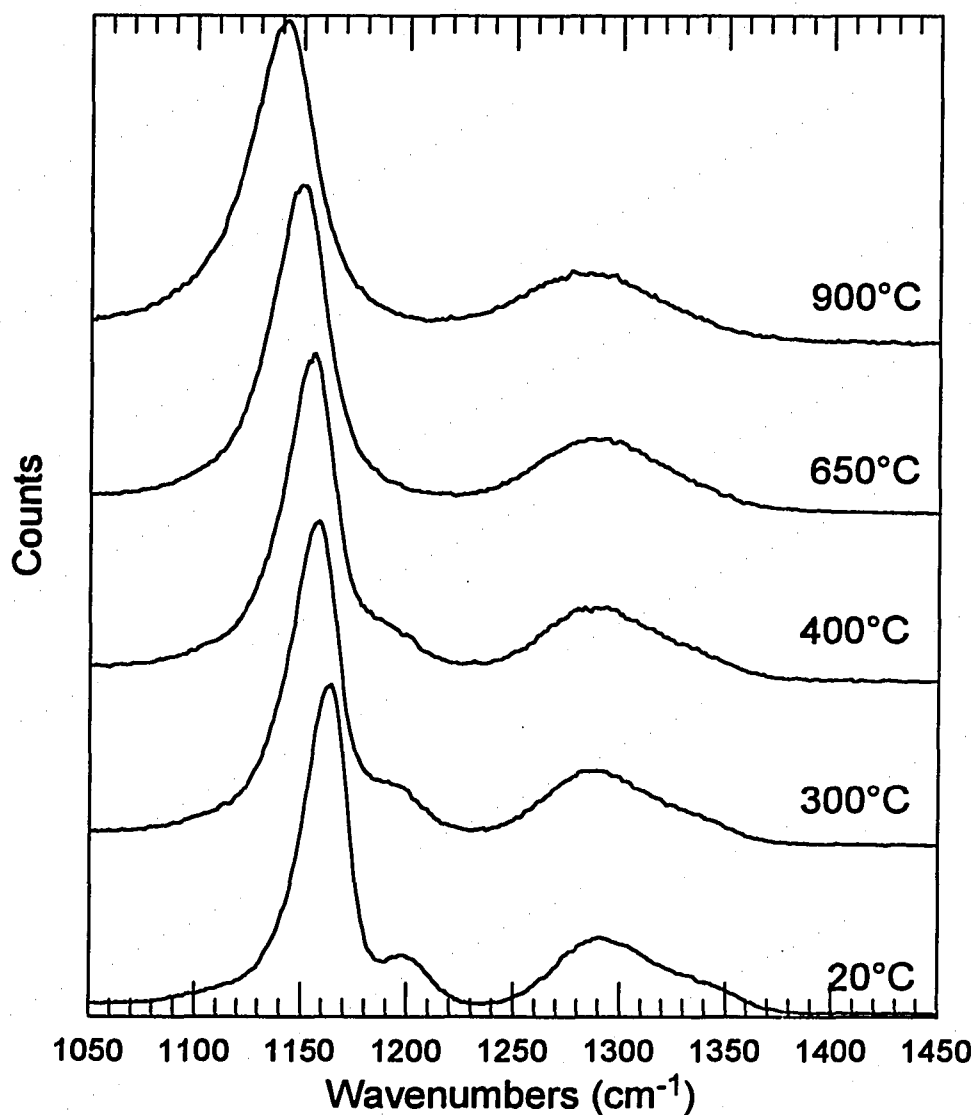


Figure 5.28 The Raman spectra of a 40mole% sodium ultra-phosphate glasses on heating from room temperature to 900°C.

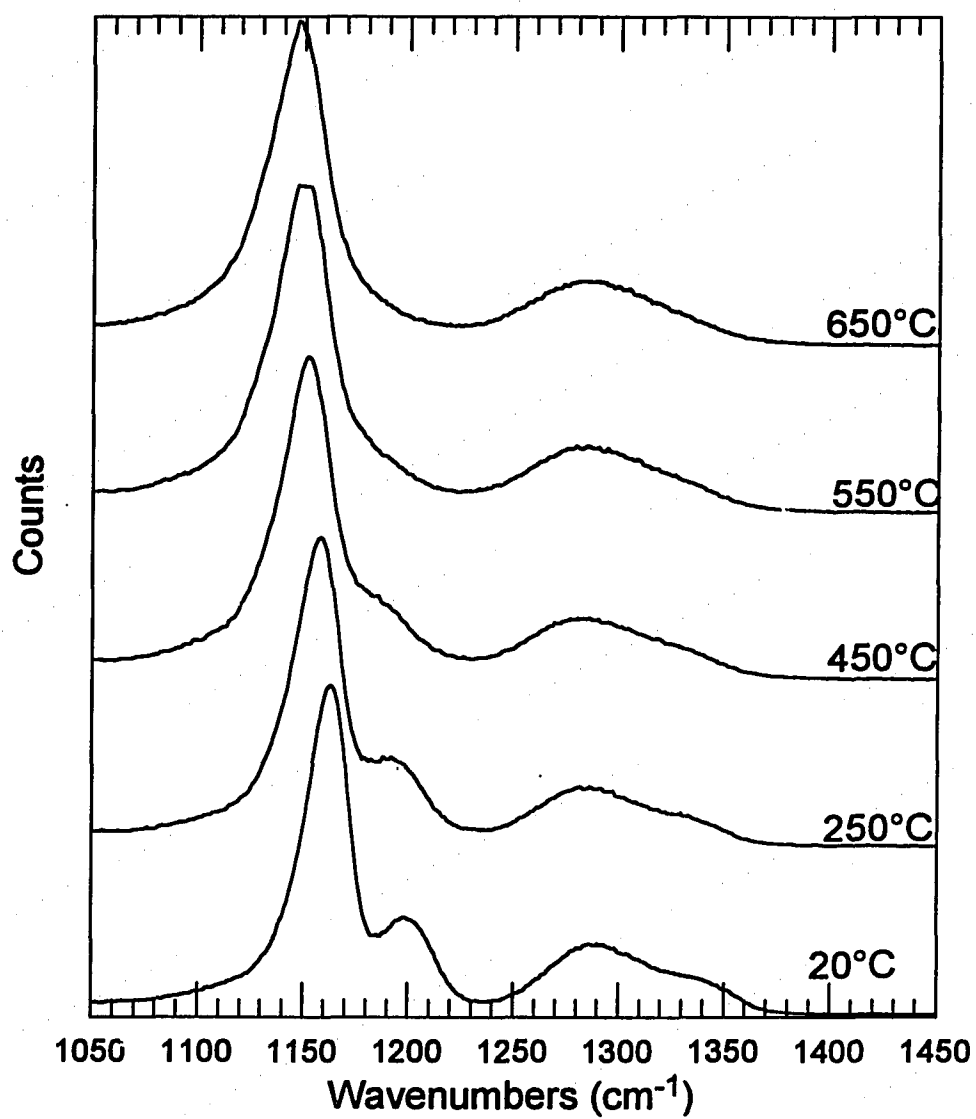


Figure 5.29 The Raman spectra of a 40mole% sodium ultra-phosphate glasses on heating from room temperature to 900°C.

6. CONCLUSIONS

Given the simplicity binary alkali phosphate glass systems studied, the objectives of the research were straightforward:

- Prepare anhydrous alkali ultra-phosphate glasses.
- Characterize the structures of these glasses.
- Determine the compositional dependence of key physical properties and their dependence on structure.
- Explore the extent and form of the melt processing dependence of properties.
- Confirm single relaxation time kinetics for amorphous P_2O_5 .

We have prepared anhydrous (0.75 ± 0.6 mole% H_2O) sodium and lithium ultra-phosphate glasses across the entire ultra-phosphate region. We have shown the depolymerization of the three-dimensional network of amorphous P_2O_5 with the addition of alkali follows the simple models developed by Van Wazer [18]. Analyses are consistent with the topology of the network changing from branching to ring dominated to chain dominated with increasing depolymerization. Additionally, we found that oxygen bonding changes both on depolymerized (Q^2) species and branching (Q^3) species. While Q^2 species are introduced as fully delocalized units, the delocalization of π -bond character on Q^3 units is dependent on the $Q^3:Q^2$ ratio.

Anomalous glass transition and density minima were found at 20 mole% alkali. The glass transition temperature minimum was found to be a result in the changes in oxygen bonding which occur at 20 mole% alkali. At compositions >20 mole% alkali, the transformation of $P=O$ terminal oxygens on Q^3 species to $P-OM^+$ terminal oxygens and the strengthening of Q^3-Q^2 and Q^2-Q^2 bridges over Q^3-Q^3 bridges cooperate to increase the average strength of the network with increasing depolymerization. The density minimum is due to a rapid expansion of the network between 0 and 20 mole% alkali. The expansion is

hypothesized to be due to the formation of ring structures which contain the counterions in their interior.

$v\text{-P}_2\text{O}_5$ was found not to be the archetypal Arrhenius liquid but to have a T_g , $C_p(l)/C_p(s)$, fragility and spectrum of relaxation times consistent with other glass forming liquids having similar bonding. The spectrum of relaxation times did not scale with glass transition temperature but increased with increasing depolymerization. The insensitivity of the spectrum of relaxation times to the changes in oxygen bonding suggests non-exponentiality is most correlated with degree of covalent interconnection, not the strength of such interconnections.

We have shown that structure of ultra-phosphate glasses with compositions near 40 mole% alkali are strongly dependent on melt annealing. At short melt anneal times ring structures are thought to dominate the network topology, however, at long melt anneal times, chain structures dominate the topology. Such dependence of structure on melt anneal is consistent with experimental results, however, more research needs to be done to explore melt processing dependence of glass-forming liquids in order to elucidate whether such structures exist and why their relaxation times are long at such high temperatures.

LIST OF REFERENCES

- [1] W.H. Zachariason, *J. Am. Chem. Soc.*, **54**, 3841 (1932).
- [2] For recent reviews of the structures and some of the properties of phosphate glasses see (a) S.W. Martin, *Eur. J. Sol. State Inorg. Chem.*, **28**, 163-205 (1991). (b) S.W. Martin, *J. Amer. Ceram. Soc.*, **74**, 1767-84 (1991).
- [3] W.L.Hill, G.T. Faust, and S.B. Hendricks, *J. Amer. Chem. Soc.*, **65**, 794-802 (1947).
- [4] P.E. Gray and L.C. Klein, *Glass Tech*, **23** [4], 177-79 (1982).
- [5] P.E. Gray and L.C. Klein, *Glass Tech*, **24** [4], 202-206 (1983).
- [6] N.H. Ray and C.J. Lewis, *J. Mater. Sci.*, **7**, 47-51 (1972).
- [7] S.W. Martin, Ph.D. Dissertation, Purdue University (1986).
- [8] G. Adams and J. Gibbs, *J. Chem. Phys.*, **43**, 139 (1965).
- [9] B. Beagley, D.W.J. Cruickshank, and T.G. Hewitt, *Trans. Faraday Soc.*, **63**, 836 (1967).
- [10] D.W.J. Cruickshank, *Acta Cryst.*, **17**, 677 (1964).
- [11] G.C. Hampson and A.J. Stiosick, *J. Amer. Chem. Soc.*, **60**, 1814 (1938).
- [12] D.W.J. Cruickshank, *Acta. Cryst.*, **17**, 679 (1964).
- [13] C.H. MacGillavry, H.C.J. De Decker, and L.M. Nijland, *Nature*, **164**, 448-449 (1949).
- [14] J.R. Van Wazer and K. A. Holst, *J. Am. Chem. Soc.*, **72**, 639 (1950).
- [15] K. Meyer, H. Hobert, A. Barz, and D. Stachel, *Vibrational Spectroscopy*, **6**, 323-332 (1994).
- [16] A. -R. Grimmer and G.-U. Wolf, *Eur. J. Solid State Inorg. Chem.*, **28**, 221-232 (1991).
- [17] H.C.J. De Decker, *Rec. Chim. Pays-Bas*, **60**, 413-427 (1941).
- [18] J.R. Van Wazer, *J. Amer. Cer. Soc.*, **78** [22], 5709-5726 (1956).
- [19] D.P. Craig, A. Maccoll, R.S. Nyholm, L.E. Orgel, and L.E. Sutton, *J. Chem. Soc.*, **332** (1954).
- [20] R. K. Brow, Sandia National Laboratories, Private communication.

- [21] J.R. Van Wazer and E.J. Griffith, *J. Amer. Ceram. Soc.*, **77**, 6140 (1955).
- [22] D. Stachel, H. Paulus, I. Svoboda, and H. Fuess, *Z. Krist.*, **202**, 117-118 (1992).
- [23] D. Stachel, C. Bätz-Dölle, and H. Reiss, *Bol. Soc. Esp. Ceram. Vid.*, **31-C**, 3 (1992).
- [24] D. Stachel, H. Paulus, C. Guenter, and H. Fuess, *Z. Krist.*, **199**, 275-276 (1992).
- [25] C. Baez-Doelle, D. Stachel, I. Svoboda, and H. Fuess, *Z. Krist.*, **203**, 282-283 (1993).
- [26] W.L. Hill, G.T. Faust, and D.S. Reynolds, *Am. J. Sci.*, **242**, 457 (1944).
- [27] W.L. Hill, G.T. Faust, and D.S. Reynolds, *Am. J. Sci.*, **242**, 542 (1944).
- [28] A. McAdam, K.H. Jost, and B. Beagley, *Acta Cryst.*, **B24**, 1621 (1968).
- [29] Von K. H. Jost, *Acta Cryst.*, **16**, 623 (1963).
- [30] D. W. J. Cruickshank, *Acta Cryst.*, **17**, 681 (1964).
- [31] Von K. H. Jost, *Acta Cryst.*, **14**, 779 (1961).
- [32] A.G. Nord and K.B. Lindberg, *Acta Chim. Scand.*, **A29**, 1 (1975).
- [33] P.M.T. Averbuch-Pouchot, A. Durif, and M. Bagieu-Beucher, *Acta Cryst.*, **C39**, 25-26 (1983).
- [34] Von K. H. Jost, *Acta Cryst.*, **17**, 1539 (1964).
- [35] H.M. Ondik, *Acta Cryst.*, **18**, 226 (1965).
- [36] Par M. Bagieu-Beucher, A. Durif, and J.C. Guitel, *Acta Cryst.*, **B31**, 2264 (1975).
- [37] E. D. Eanes and H.M. Ondik, *Acta Cryst.*, **15**, 1280 (1962).
- [38] Par A. Durif, M.T. Averbuch-Pouchot, and J.C. Guitel, *Acta Cryst.*, **B31**, 2680 (1975).
- [39] Von O.H. Jarchow, *Acta Cryst.*, **17**, 1253 (1964).
- [40] H.M. Ondik, S. Block, and C. H. MacGillavry, *Acta Cryst.*, **14**, 555 (1961).
- [41] H.M. Ondik, *Acta Cryst.*, **17**, 1139 (1964).
- [42] D.W.J. Cruickshank, *Acta Cryst.*, **17**, 675 (1964).
- [43] J.K. Fawcett, V. Kocman, and S.C. Nyburg, *Acta Cryst.*, **B30**, 1979 (1974).

- [44] Laugt, *Acta Cryst.*, **B28**, 201 (1972).
- [45] K.-H. Jost, *Acta Cryst.*, **19**, 555 (1965).
- [46] S.W. Martin and C.A. Angell, *J. Phys. Chem.*, **90**, 6736-6740 (1986).
- [47] K. Takahashi, In Advances in Glass Technology, Vol. 1, (Plenum, New York, 1962), pp. 366-376.
- [48] A.V. Gladkov, *Zh. Fiz. Khim.* **31** [5], 1002-1004 (1957).
- [49] K. Takahashi, N. Mochida, H. Matsui, S. Takeuchi, and Y. Gohshi, *J. Ceram. Soc. Jpn.*, **84**[10], 482-490 (1976).
- [50] E. Kordes, *Z. Anorg. Allg. Chem.*, **241** [1], 1-38 (1939).
- [51] Bh. V.J. Rao, *J. Am. Ceram. Soc.*, **48** [6], 311-319 (1965).
- [52] J. Wong, *J. Non-Cryst. Solids*, **20**, 83-100 (1976).
- [53] D. Stachel and H. Reiss, *Wiss. Z.-Friedrich-Schiller-Univ. Jena: Natuwiss. Reiche*, **39**(2/3), 292-7 (1990).
- [54] F.L. Galeener and J.C. Mikkelsen, *Sol. St. Comm.*, **30**, 505 (1979).
- [55] A.C. Wright, R.A. Hulme, D.I. Grimley, R.N. Sinclair, S.W. Martin, D.L. Price, and F.L. Galeener, *J. Non-Cryst. Solids* **129**[1] (1991).
- [56] R. Gresch, W. Müller-Warmuth, and H. Dutz, *J. Non-Cryst. Solids*, **34**, 127-136 (1979).
- [57] A. Higazy and B. Bridge, *Phys. Chem. Glasses*, **24** [5], 122 (1983).
- [58] (a) S. Saka and J.D. MacKenzie, *Non-Cryst. Solids*, **6**, 145 (1971). (b) N.H. Ray, *J. Non-Cryst. Solids*, **15**, 423 (1974).
- [59] R.L. Cormia, J.D. Mackenzie, and D.J. Turnbull, *J. Appl. Phys.*, **34**[4], 2245 (1963).
- [60] C.A. Angell in *Relaxation in Complex Systems* (Proceedings of the Workshop on Relaxation Processes, Blacksburg, VA, July 1983); K. Ngai, G.B. Smith, Eds., (National Technical Information Service, U.S. Department of Commerce: Washington, D.C., 1985) p. 3; *J. Non-Cryst. Solids*, **59**, 137 (1976).
- [61] J.A. Duffy and M.D. Ingram, *J. Of Non-Cryst. Solids*, **21**, 373 (1976).

- [62] R.K. Brow, C.C. Phifer, G.L. Turner, and R.J. Kirkpatrick, *J. Amer. Cer. Soc.*, **74**, 1287-90 (1991).
- [63] M. Villa and K.R. Carduner, *Phys. Chem. Glasses*, **28**, 131-132 (1987).
- [64] S. Prabhakar, K.J. Rao, and C.N.R. Rao, *Chem. Phys. Lett.*, **139**, 96-102 (1987).
- [65] S. Hayashi and K. Hayamizu, *J. Solid State Chem.*, **80**, 195-200 (1989).
- [66] I.L. Mudrakovskii, V.P. Shmachkova, N.S. Kotsarenko, and V.M. Mastikhin, *J. Phys. Chem. Solids*, **47**, 335-339 (1986).
- [67] G.L. Turner, K.A. Smith, R.J. Kirkpatrick, and E. Oldfield, *J. Mag. Res.*, **70**, 408-415 (1986).
- [68] E.R. Andrew, D.J. Bryant, E.M. Cashell, and B.A. Dunell, *Chem. Phys. Lett.*, **77**, 614-617 (1981).
- [69] A.R. Grimmer and U. Haubenreisser, *Chem. Phys. Lett.*, **99**, 487-490 (1983).
- [70] D.C. Duncan and D.C. Douglass, *Chem. Phys.*, **87**, 339-349 (1984).
- [71] L. Griffiths, A. Root, R.K. Harris, K.J. Packer, A.M. Chippendale, and F.R. Tromans, *J. Chem. Soc. Dalton Trans.*, 2247-2251 (1986).
- [72] R.K. Brow, *J. Non-Cryst. Solids*, to be published.
- [73] N.J. Kreidl, *Glass Science and Technology*. Volume 1. Glass-Forming Systems, N.J. Kreidl, D.R. Uhlmann, Eds., (Academic Press, New York, 1983), p. 192
- [74] C. Nelson and D.R. Tallant, *Phys. Chem. Glass*, **26** [4], 119-122 (1985).
- [75] R.A. Hulme, Ph.D. Dissertation, University of Reading, (1991).
- [76] U. Hoppe, G. Walter, and D. Stachel, *Phys. Chem. Glass*, **33** [6], 216-221 (1992).
- [77] See, for example, A.E.R. Westman and P.A. Gartaganis, *J. Amer. Chem. Soc.*, **40** [9], 293-299 (1957).
- [78] A.Q. Tool, *J. Amer. Ceram. Soc.*, **29** [9], 240-53 (1946).
- [79] O.S. Narayanaswamy, *J. Amer. Cer. Soc.*, **54**[10], 491-98 (1971).
- [80] H.N. Ritland, *J. Amer. Cer. Soc.*, **39**[12], 403-406 (1956).

- [81] P.B. Macedo and A. Napolitano, *J. Res. Nat. Bur. Stand.-A. Phys. and Chem.*, **71A**[3], 231-238 (1967).
- [82] M. Goldenstein, in
- [83] C.T. Moynihan, P.B. Macedo, C.J. Montrose, P.K. Gupta, M.A. Debolt, J.F. Dill, B.E. Dom, P.W. Drake, A.J. Easteal, P.B. Elterman, R. P. Moeller, H. Sasabe, and J.A. Wilder, *Ann. N.Y. Acad. Sci.*, **279**, 15-35 (1976).
- [84] C.P. Lindsey and G.D. Patterson, *J. Chem. Phys.*, **73**, 3348 (1980).
- [85] C.T. Moynihan, A.J. Easteal, and J. Wilder, *J. Phys. Chem.*, **78**[26], 2673-2677 (1974).
- [86] M.A. DeBolt, A.J. Eastel, P.B. Macedo, and C.T. Moynihan, *J. Amer. Cer. Soc.*, **59**[1-2], 16-21 (1976).
- [87] R.H. Magruder, D.L. Kinser, and R.A. Weeks, *J. Non-Cryst. Solids*, **71**, 95 (1985).
- [88] F.L. Galeener and R.H. Geils, The Sturcture of Non-Crystalline Materials, P.H. Gaskell, Ed. (Taylor and Francis, London, 1977) p. 223.
- [89] H. Bohm, *Phys. Chem. Glasses*, **11**, 177 (1977).
- [90] R.H. Magruder, D.L. Kinser, R.A. Weeks and J.M. Jackson, *J. Appl. Phys.*, **57**, 345 (1985).
- [91] J.M. Jackson, M.E. Wells, G. Kordas, D.L. Kinser, R.A. Weeks and R.H. Magruder, *J. Appl. Phys.* **58**, 2308 (1985).
- [92] R.A. Weeks and D.L. Kinser, *Diff. Defect Data*, **53&54**, 117 (1987).
- [93] E.I. Kamitsos and M.A. Karakassides, *Phys. Chem. Glass.*, **30**, 235 (1989).
- [94] W.C. Huang, H. Jain, E.I. Kamitsos, and A.P. Patsis, *J. Non-Cryst. Solids*, **162**, 107-117 (1993).
- [95] T.R. Meadowcroft and F.D. Richardson, *Trans. Faraday Soc.*, **61**[1], 54-70 (1966).
- [96] A.E.R. Westman and J. Crowther, *J. Amer. Ceram. Soc.*, **37**[9], 420-26 (1954).
- [97] E. Kordes, W. Vogel, and R. Feterowsky, *Z. Eledtrochem.*, **57**[4], 282-89 (1953).
- [98] W. Bues and H.W. Gehrke, *Z. Anorg. Allg. Chemie*, **288**, 291-306 (1956).
- [99] N.H. Ray, *J. Of Polymer Science*, **11**, 2169-2177 (1973).

- [100] H. Ebendorff-Heidepriem, W. Seeber, and D. Ehrt, *J. of Non-Cryst. Solids*, **163**, 74-80 (1993).
- [101] M.J. O'Neill, *Analytical Chemistry*, **38**, 1331 (1966).
- [102] D.C. Jennings and G.T. Furukawa, *J. Amer. Chem. Soc.*, **75**, 522 (1952).
- [103] J. Krogh-Moe, *Phys. Chem. of Glasses*, **3** 61-62 (1962).
- [104] J. Herzfeld and A. E. Berger, *J. Chem. Phys.*, **73**[12], 6021-6030 (1980).
- [105] Physical Sciences Data, Vol. 15, Handbook of Glass Data: Part B, Single Component and Binary Non-Silicate Oxide Glasses., O.V. Mazurin, M.V. Streltsina, T.P. Shvaiko-Schvaikovskaya, Eds. (Elsevier, Amsterdam, 1985)
- [106] R. Wasche and R. Bruckner, *Phys. Chem. Glasses*, **27** [2], 87-94 (1986).
- [107] G.J. Exarhos and W.M. Risen, *Solid State Comm.*, **11**[5], 755-758 (1972)
- [108] G.J. Exarhos and W.M. Risen, *Chem. Phys. Lett.*, **10**[4], 484-486 (1971).
- [109] C. Nelson and G.J. Exarhos, *J. Chem. Phys.*, **71**[7], 2739-2747 (1979).
- [110] A. Abdel-Kader, A. A. Higazy, and M. M. Elkholy, *J. Mat. Sci.*, **2**, 157-163 (1991).
- [111] D.E.C. Corbridge, *Appl. Chem.*, **6**, 456-465 (1956).
- [112] Ya. S. Bobovich, *Optical Spectroscopy (Engl. Trans.)*, **13**, 274-282 (1962).
- [113] F.L. Galeener, J.C. Mikkelsen, R.H. Geils and W.J. Mosby, *Appl. Phys. Lett.*, **32**[1], 34-36 (1978).
- [114] M. Tatsumisago, Y. Kowada, and T. Minami, *J. Non-Cryst. Solids*, **150**, 207-211 (1992).
- [115] M. Villa, G. Chiodelli, and M. Scagliotti, *Solid State Ionics*, **18 & 19**, 382-387 (1986).
- [116] Y. Kowada, H. Adachi, M. Tatsumisago, and T. Minami, *Nippon Seramikkusu Kyokai Gakujutsu Ronbunshi*, **98**, 109-109 (1990).
- [117] Y. Kowada, H. Adachi, M. Tatsumisago, and T. Minami, *Phys. Chem. Glasses*, **34**, 10-11 (1993).
- [118] F. L. Galeener and P.N. Sen, *Phys. Rev.*, **B17**, 1928 (1978).

- [119] C.M. Schramm, B.H.W.S. DeJong, and V.E. Parziace, *J. Am. Chem. Soc.*, **106**, 4396-4402 (1984).
- [120] J.H. Lechter and J.R. Van Wazer, *J. Chem. Phys.*, **44**, 815 (1966).
- [121] S. Hayashi and K. Hayamizu, *Bull. Chem. Soc. Jpn.*, **62**, 3061-68 (1989).
- [122] R. Dupree and R.F. Pettifer, *Nature*, **308**, 523 (1984).
- [123] K.A. Smith and C.S. Blackwell, *Nature*, **302**, 223 (1983).
- [124] W. Chang, Z. Jin, and X. Zou, *Phys. Lett. A*, **159** 361-364 (1991).
- [125] F.L. Galeener and G. Lucovsky, *Phys. Rev. Lett.*, **37**[22], 1474-1478 (1976).
- [126] F.L. Galeener, G. Lucovsky, and R.H. Geils, *Solid State Comm.*, **25**, 405-408 (1978).
- [127] N.D. Patel, B. Bridge and D. N. Waters, *Phys. Chem. Glasses*, **24** [5], 122-129 (1983).
- [128] J.R. Van Wazer, Phosphorus and Its Compounds, Vol. 1 Chemistry, J.R. Van Wazer, Eds. (Interscience Publishers, Inc., New York, 1958).
- [129] B.C. Sales and L.A. Boatner, *J. Amer. Cer. Soc.*, **70**, 615 (1987).
- [130] R.K. Brow, R.J. Kirkpatrick and G.L. Turner, *J. Non-Cryst. Solids*, **116**, 39-45 (1990).
- [131] L. Pauling, *J. Phys. Chem.*, **56**, 361 (1952).
- [132] K. Suzuki and M. Ueno, *J. de Phys.*, **46**, C8-261(1985).
- [133] J.F. Emerson and P.J. Bray, Experimental Techniques of Glass Science, C.J. Simmons and O. H. El-Bayoumi, Eds. (The American Ceramic Society, 1993), p. 53.
- [134] U. Sternberg, F. Pietrowski, and W. Priess, *Z. Phys. Chem.*, **168**, 115-128 (1990).
- [135] D. Muller and E. Jahn and G. Ladwig, *Chem. Phys. Lett.*, **109**, 332(1984).
- [136] A.K. Cheetham, N.J. Clayden, C.M. Dobson, and R.J.B. Jakeman, *J. Chem. Soc., Chem. Commun.*, 195-197 (1986).
- [137] J. H. Lechter and J.R. Van Wazer, Topics in Phosphorus Chemistry, Vol. 5., J. H. Lechter and J.R. Van Wazer, Eds. (Interscience, New York, 1967), pp 75-226.

- [138] R. Dupree, D. Holland, P.W. McMillan and R.F. Pettifer, *J. Non-Cryst. Solids*, **68**, 399 (1984).
- [139] F. Liebau, Structure and Bonding in Crystals, II, M. O'Keefe and a. Navrotsky, Eds. (Academic Press, New York, 1981), pp. 197-232.
- [140] P. Losso, B. Schnabel, C Jager, U. Sternberg, D. Stachel, and D.O. Smith, *J. Non-Cryst. Solids*, **143**, 265-273 (1992).
- [141] H. Eckert, C. S. Liang, and G. D. Stucky, *J. Phys. Chem.*, **93**, 452-457 (1989).
- [142] J. Wong and C.A. Angell, Glass Structure by Spectroscopy, , J. Wong and C. A. Angell, Eds. (Marcel Dekker, Inc., New York and Basel, 1976) p. 172.
- [143] A. Winkelmann and O. Schott, *Ann. Phys*, **51**, 730-746 (1894).
- [144] W. Vogel, Chemistry of Glass, N. Kreidl and E. Lense Eds. (American Ceramic Society, Westerville, OH, 1985).
- [145] H. Scholze, *Glass Ind.*, **546** [10,11,12], 546-551 (1966).
- [146] J.S. Hagerty, A.R. Cooper, and J.H. Heasley, *Phys. Chem. Glasses*, **9**[2], 132 (1968).
- [147] R. Bohmer, K.L. Ngai, C.A. Angell, and D.J. Plazek, *J. Chem. Phys.*, **99** [5], 4201-4209 (1993).
- [148] J.R. Van Wazer, Inorganic Polymers, F.G.A. Stone and W.A.G. Graham, Eds., (Academic Press, New York, 1962).
- [149] P.E. Gray and L.C. Klein, *Phys. Chem. Glasses*, **27** [6], 241-244 (1986).
- [150] D.R. Tallant, B.C. Bunker, C.J. Brinker, and C.A. Balfe, *Mat. Res. Soc. Symp. Proc.*, **73**, 261-267 (1986).
- [151] F.L. Galeener, R.A. Barrio, E. Martinez, and R.J. Elliot, *Phys. Rev. Lett.*, **53**, 2429 (1984).

ACKNOWLEDGMENTS

Support for this work was provided by Sandia National Laboratories, the National Science Foundation through grant numbers NSF-DMR-87-01077, NSF-DMR-91-04460, and NSF-DMR-93-45554 and by the Iowa State University Research Foundation, College of Engineering, and Materials Science and Engineering Department. Acknowledgment is made to Dr. Richard Brow, Dr. David Tallant, Dr. Roger Assink, Dr. Alan Irwin, and Dr. Prabhakar for their help in collecting and analyzing data.

Acknowledgment is made to Dr. Steve W. Martin for his guidance and allowing almost totally independent research. Special thanks to Dr. David Martin for his constant support and friendship. Thanks are also due to Dr. Richard Brow for allowing me to spend two very rewarding summers at Sandia National Laboratories. Finally, I would like to recognize the many members of the Glass and Optical Materials research group who I have had the pleasure working with: Donny Bloyer, Hitendra Patel, Mark Wagner, Mark Quillin, Peter Shin, Jaephil Cho, Susan VanKirk, Sheila Grant, Julia Sills, Kirk Garrett, Joe Kincs and Abdouleh Soufiane.

**APPENDIX A: THE HEAT CAPACITIES OF SODIUM ULTRA-
PHOSPHATE GLASSES**

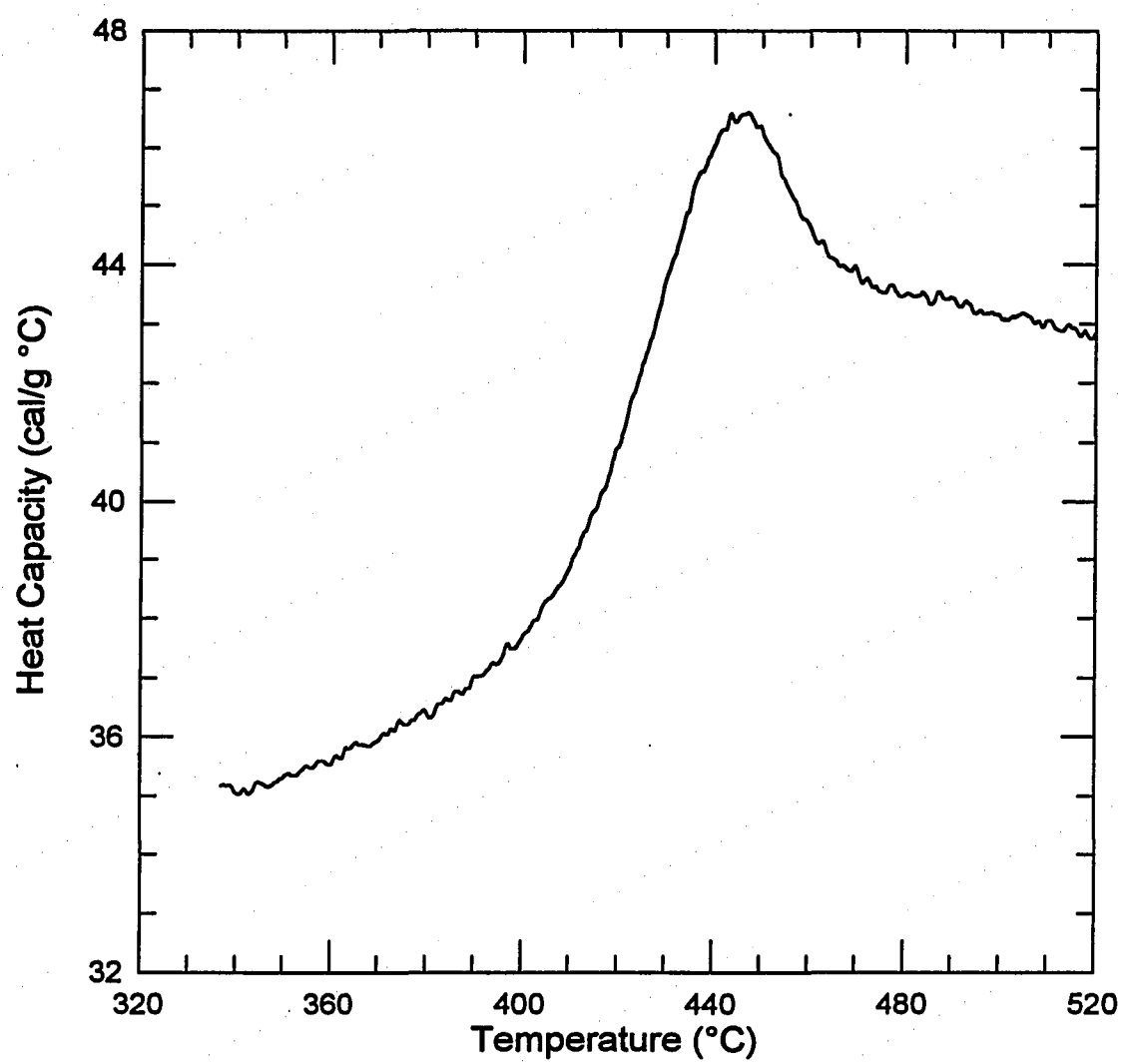


Figure A.1 The heat capacity of $v\text{-P}_2\text{O}_5$.

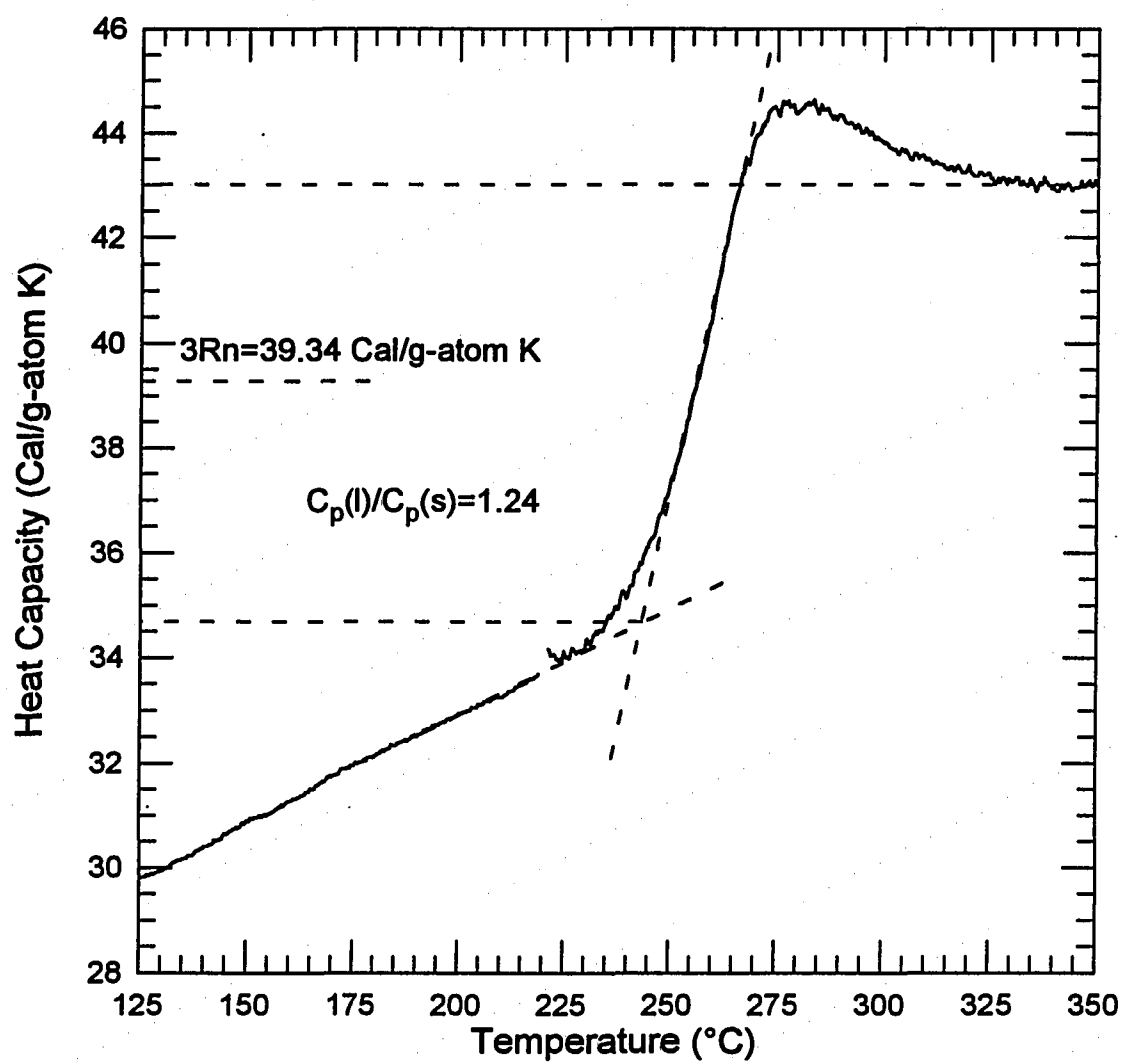


Figure A.2 The heat capacity of 0.10 Na₂O + 0.90 P₂O₅ glass.

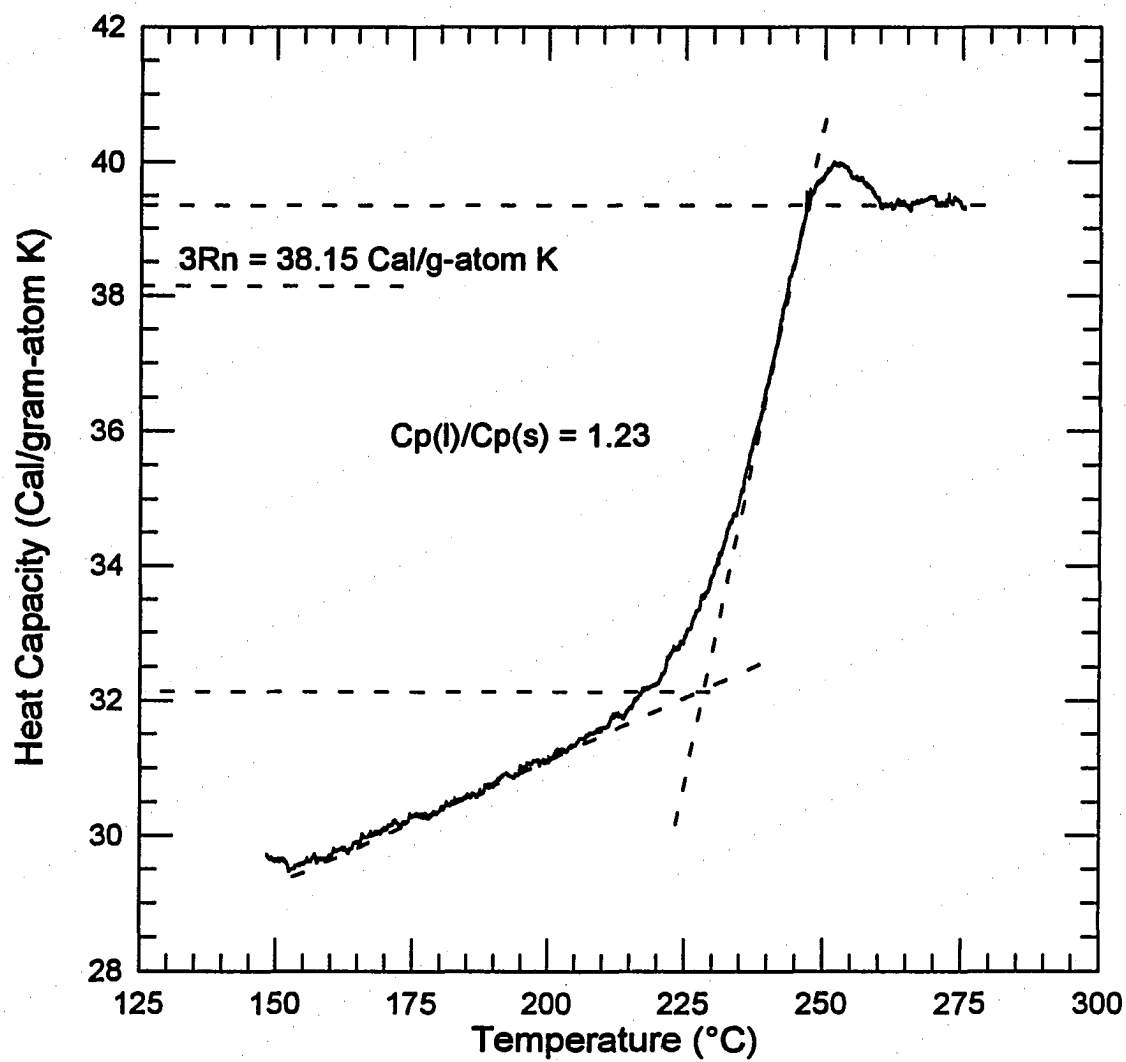


Figure A.3 The heat capacity of $0.15 \text{ Na}_2\text{O} + 0.85 \text{ P}_2\text{O}_5$ glass.

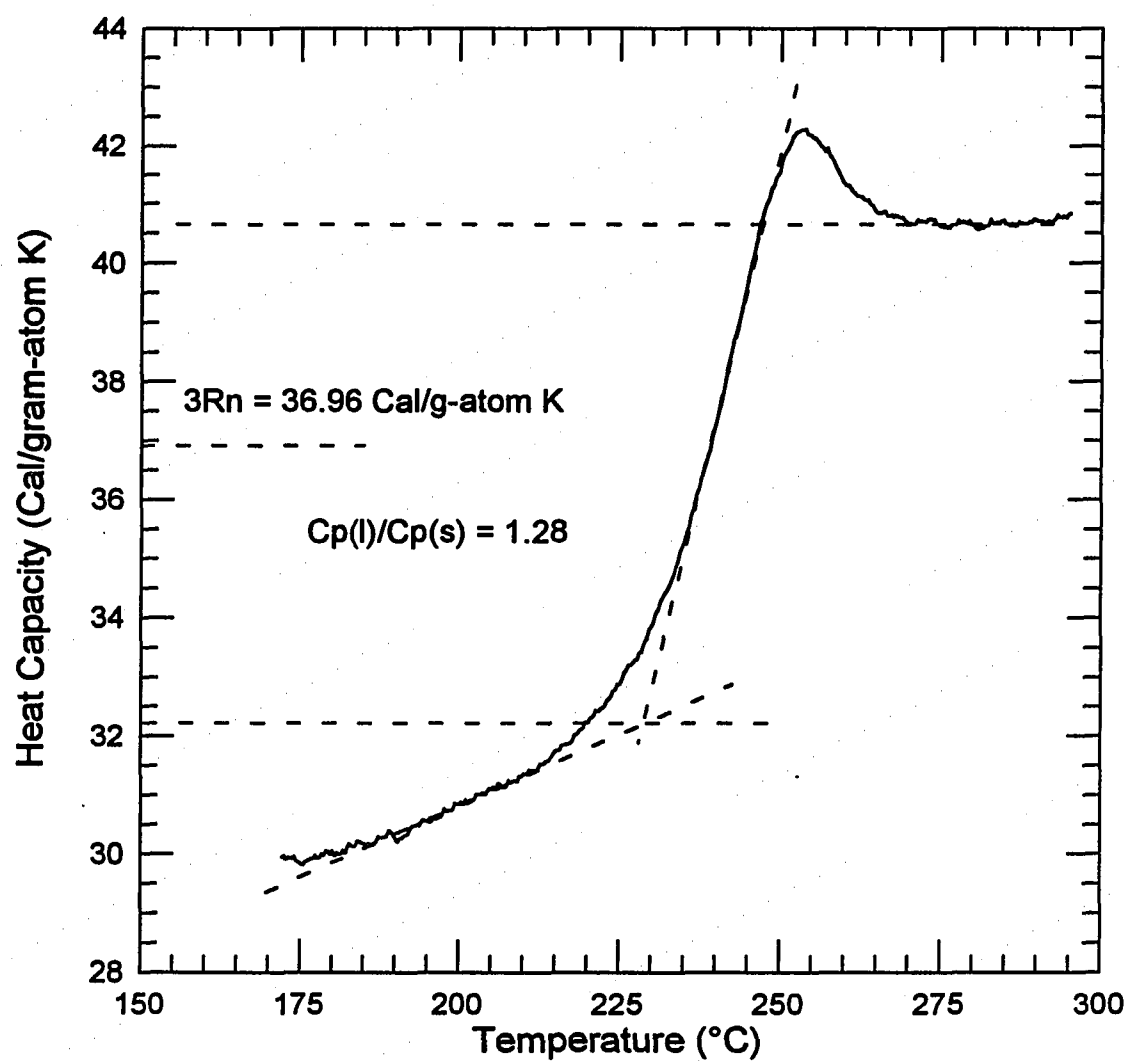


Figure A.4 The heat capacity of $0.20 \text{ Na}_2\text{O} + 0.80 \text{ P}_2\text{O}_5$ glass.

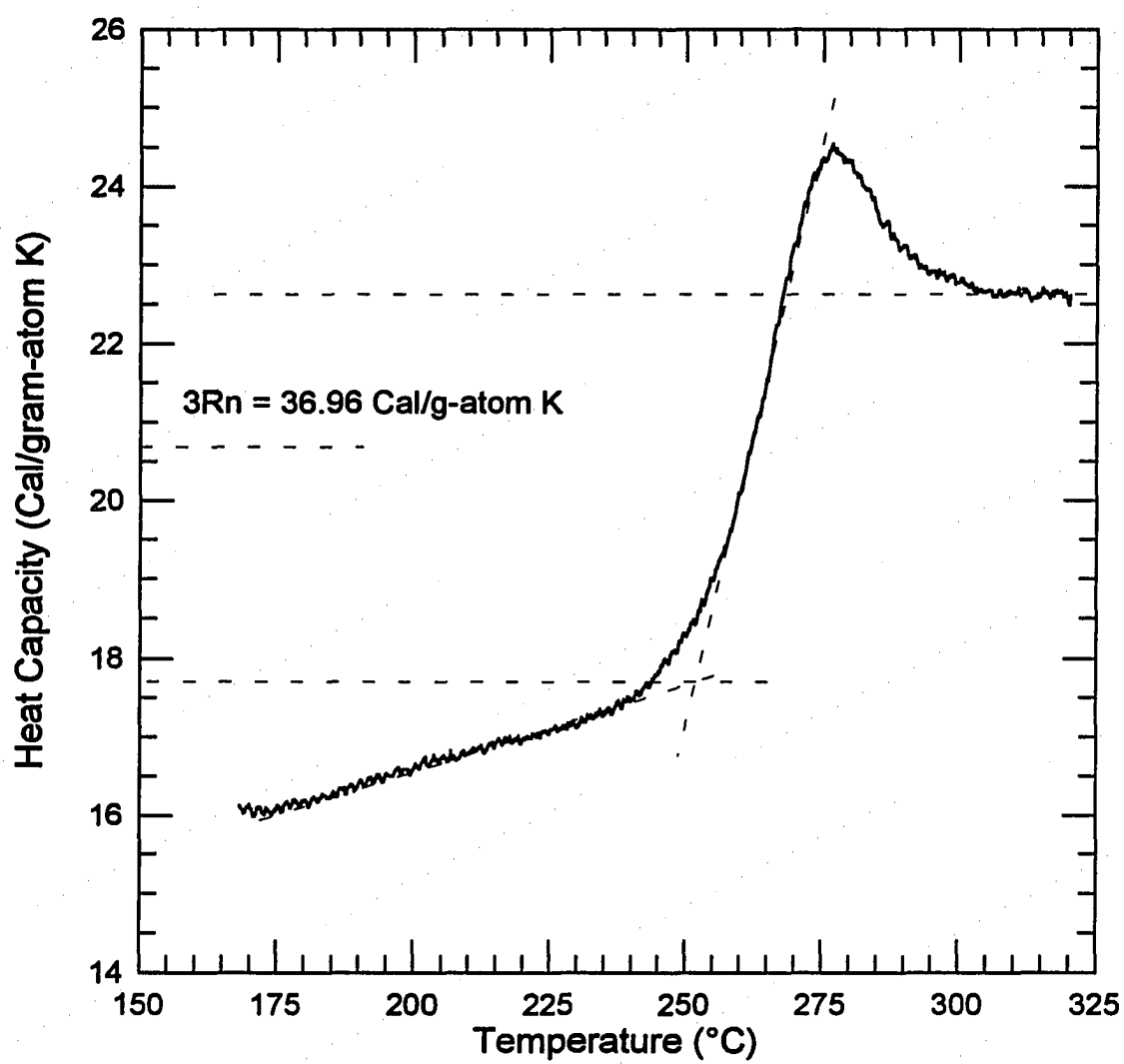


Figure A.5 The heat capacity of 0.30 Na₂O + 0.70 P₂O₅ glass.

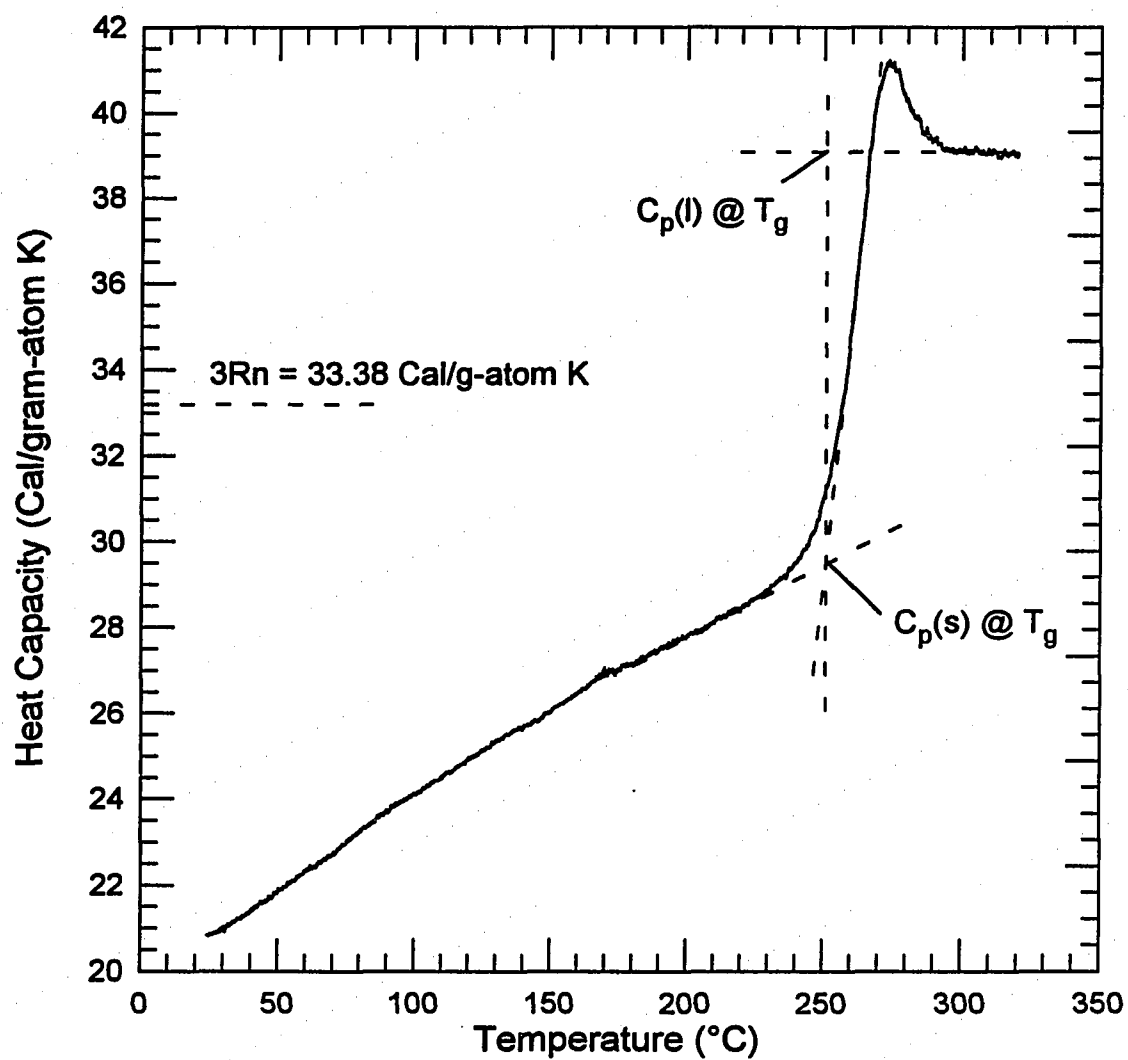


Figure A.6 The heat capacity of $0.35 \text{ Na}_2\text{O} + 0.65 \text{ P}_2\text{O}_5$ glass.

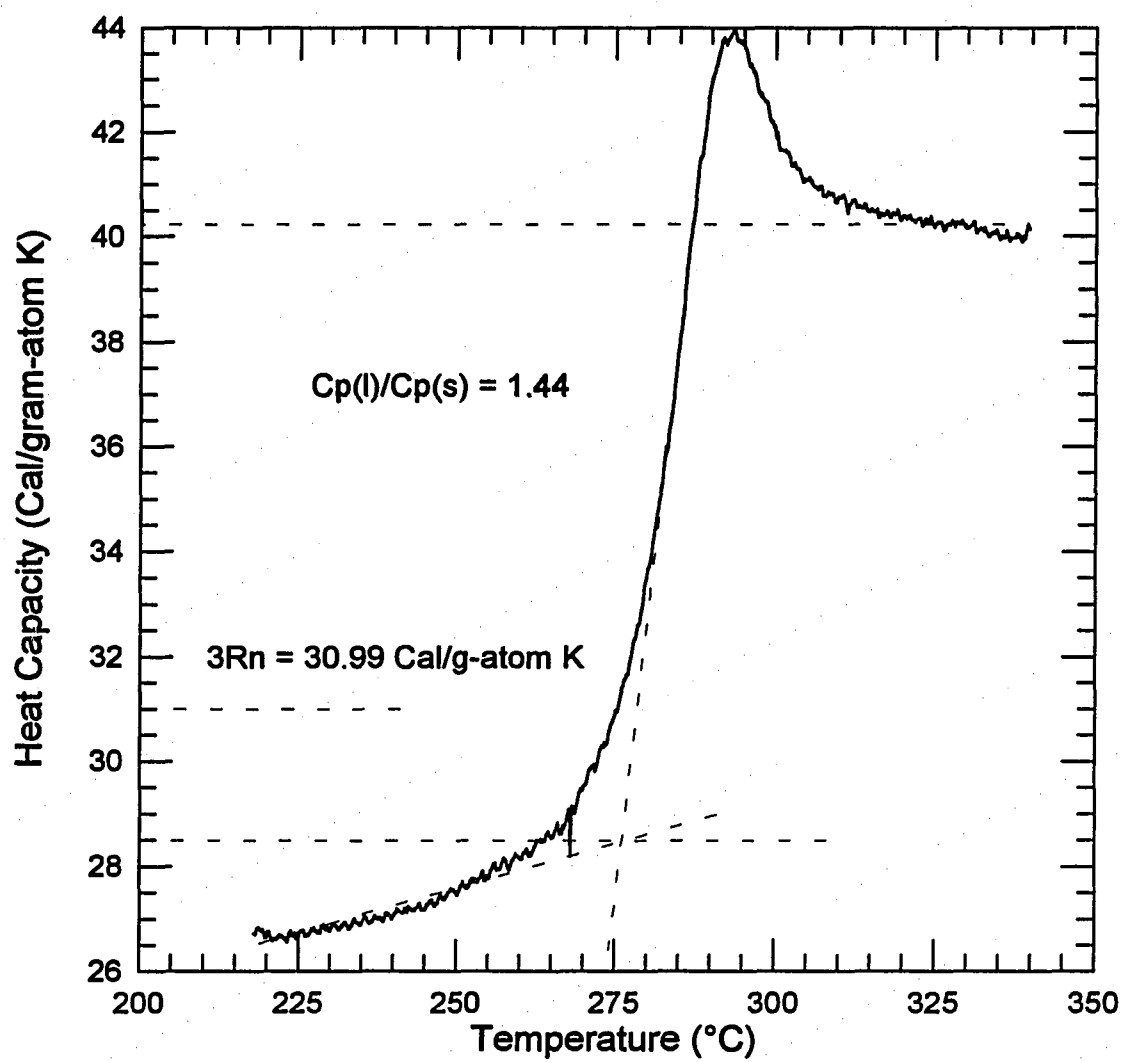


Figure A.7 The heat capacity of $0.45 \text{ Na}_2\text{O} + 0.55 \text{ P}_2\text{O}_5$ glass.

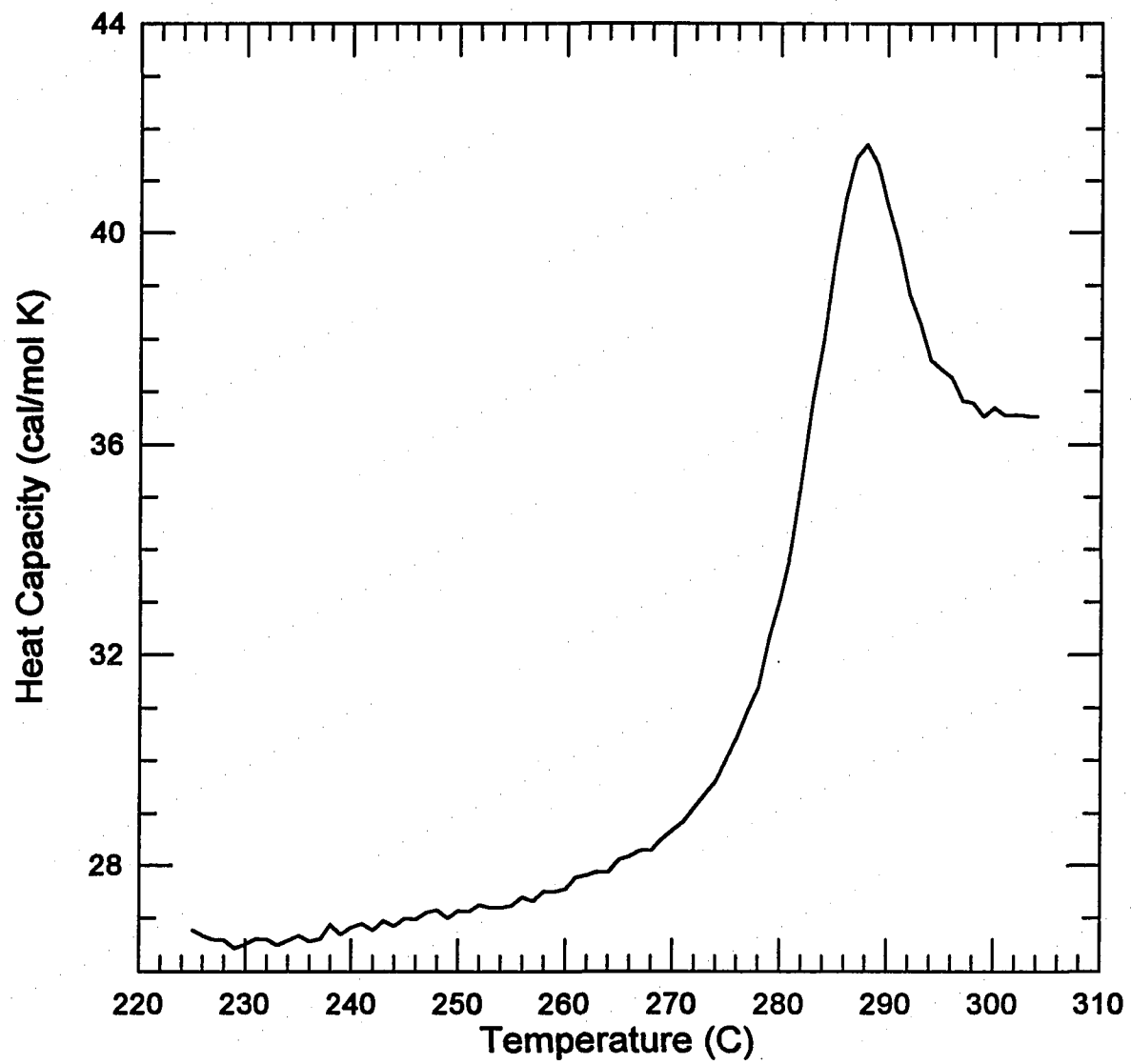


Figure A.8 The heat capacity of 0.50 Na₂O + 0.50 P₂O₅ glass.

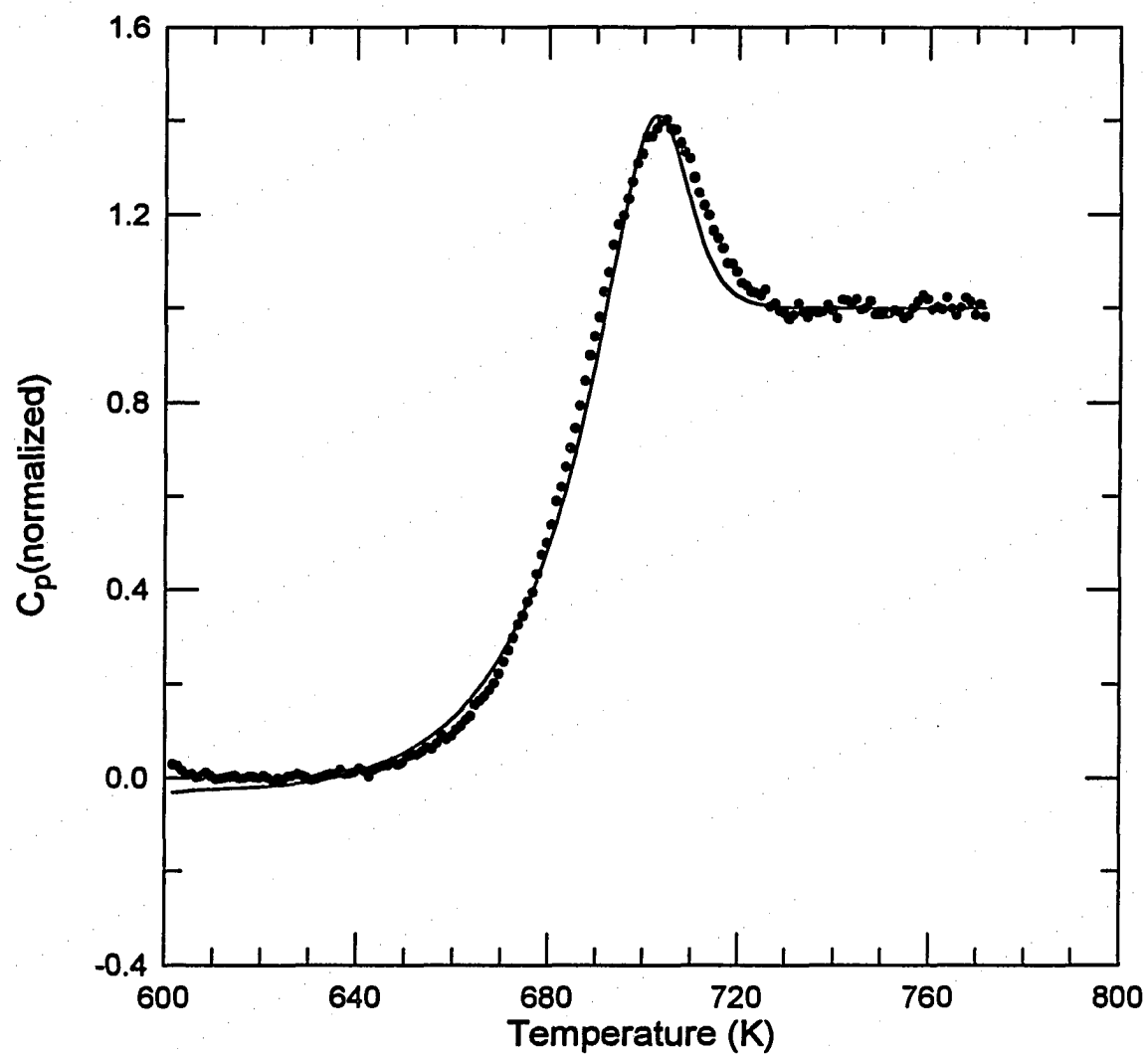


Figure A.9 The normalized heat capacity of $v\text{-P}_2\text{O}_5$ determined experimentally (\bullet) and calculated (—).

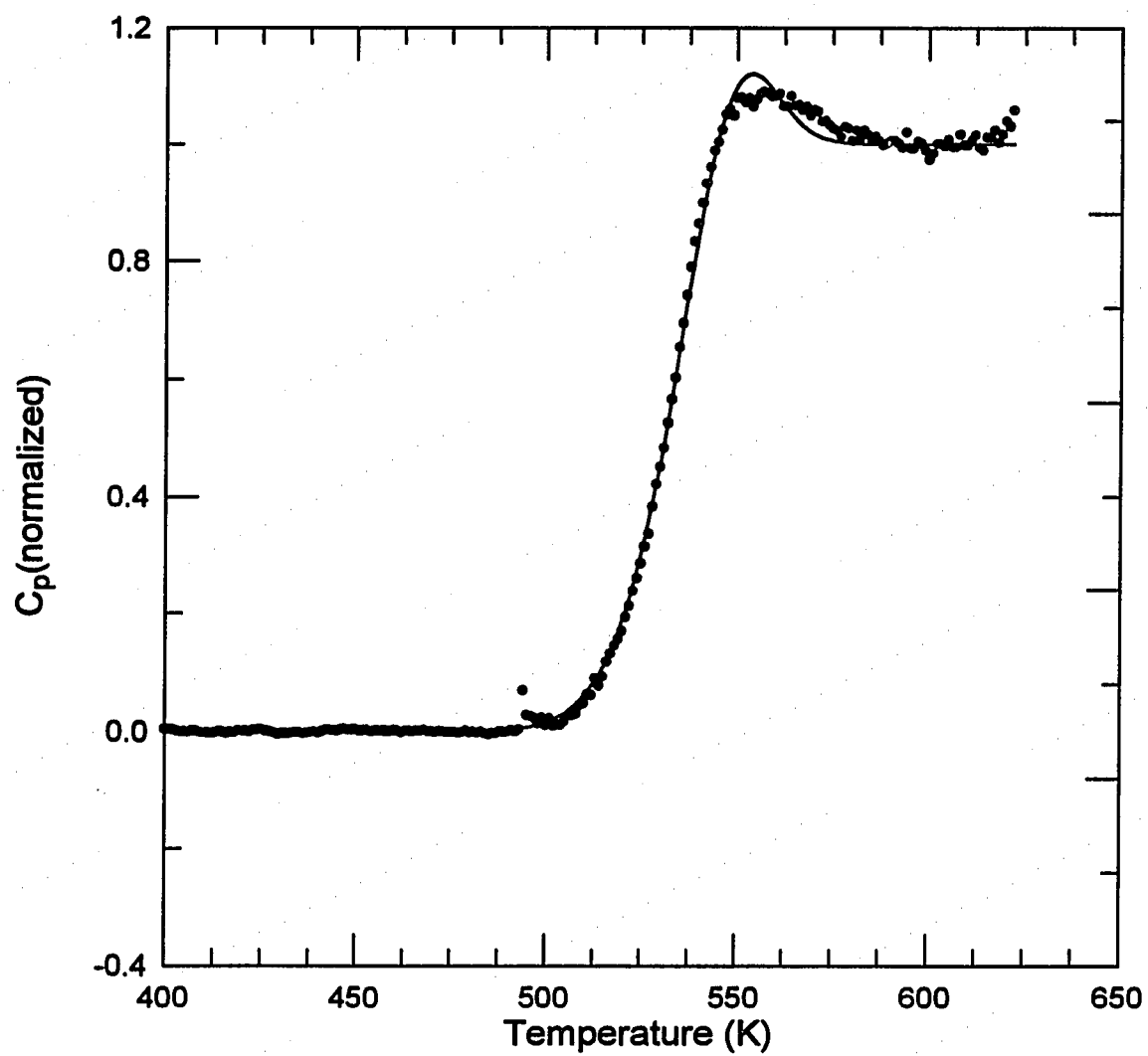


Figure A.10 The normalized heat capacity of $0.10 \text{ Na}_2\text{O} + 0.90 \text{ P}_2\text{O}_5$ glass determined experimentally (•) and calculated (—).

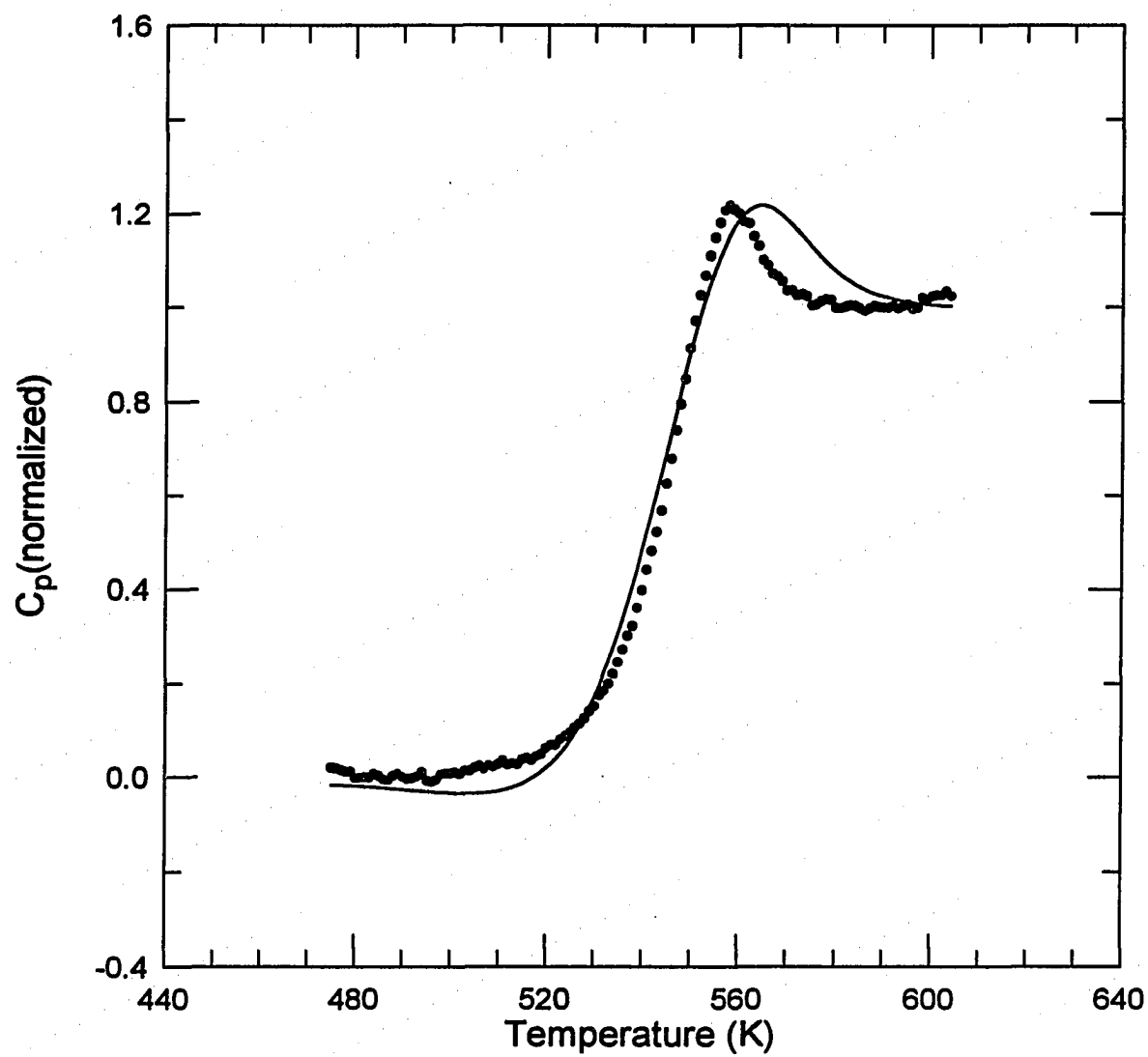


Figure A.11 The normalized heat capacity of 0.20 Na₂O + 0.80 P₂O₅ glass determined experimentally (•) and calculated (—).

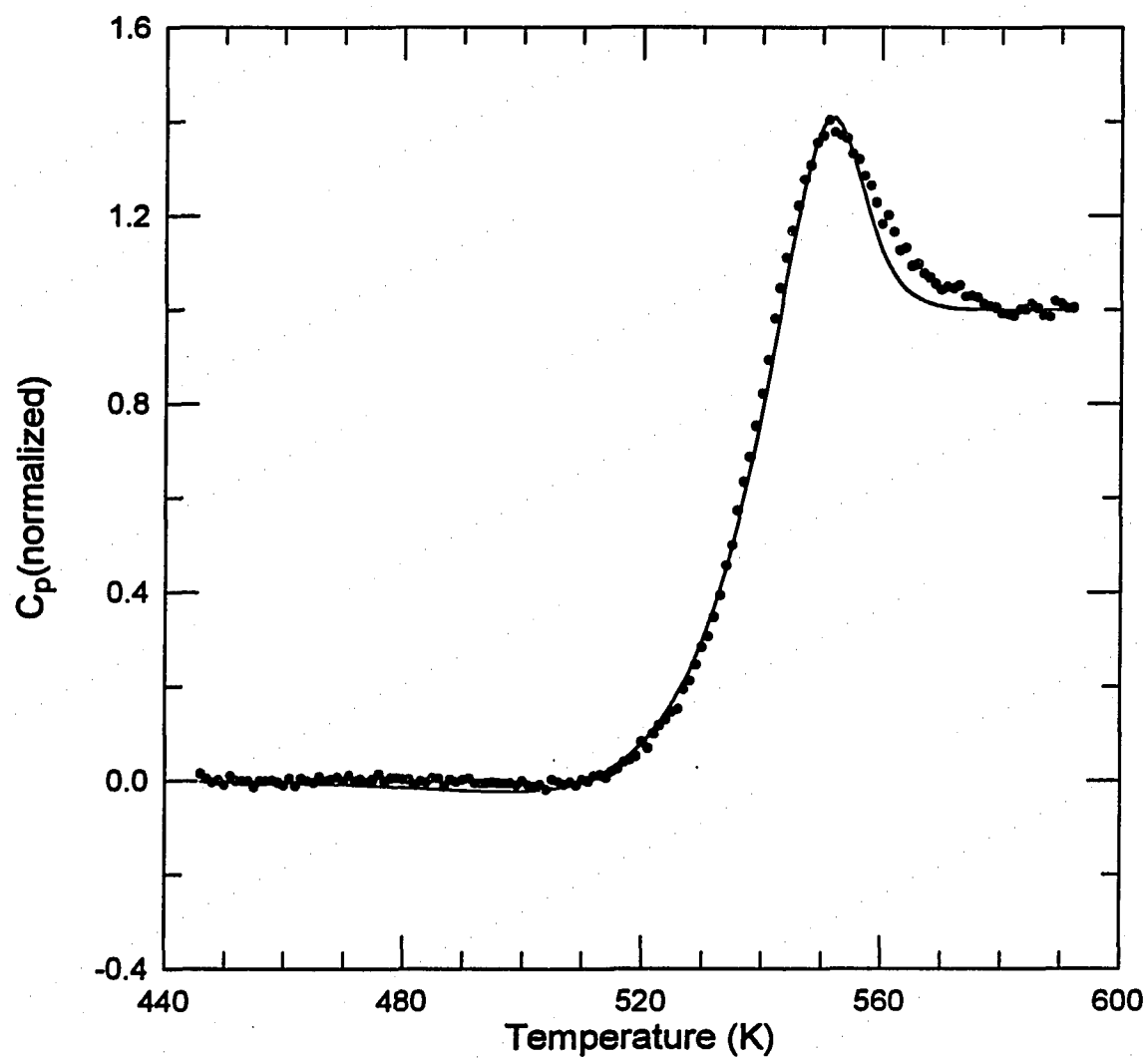


Figure A.12 The normalized heat capacity of $0.30 \text{ Na}_2\text{O} + 0.70 \text{ P}_2\text{O}_5$ glass determined experimentally (•) and calculated (—).

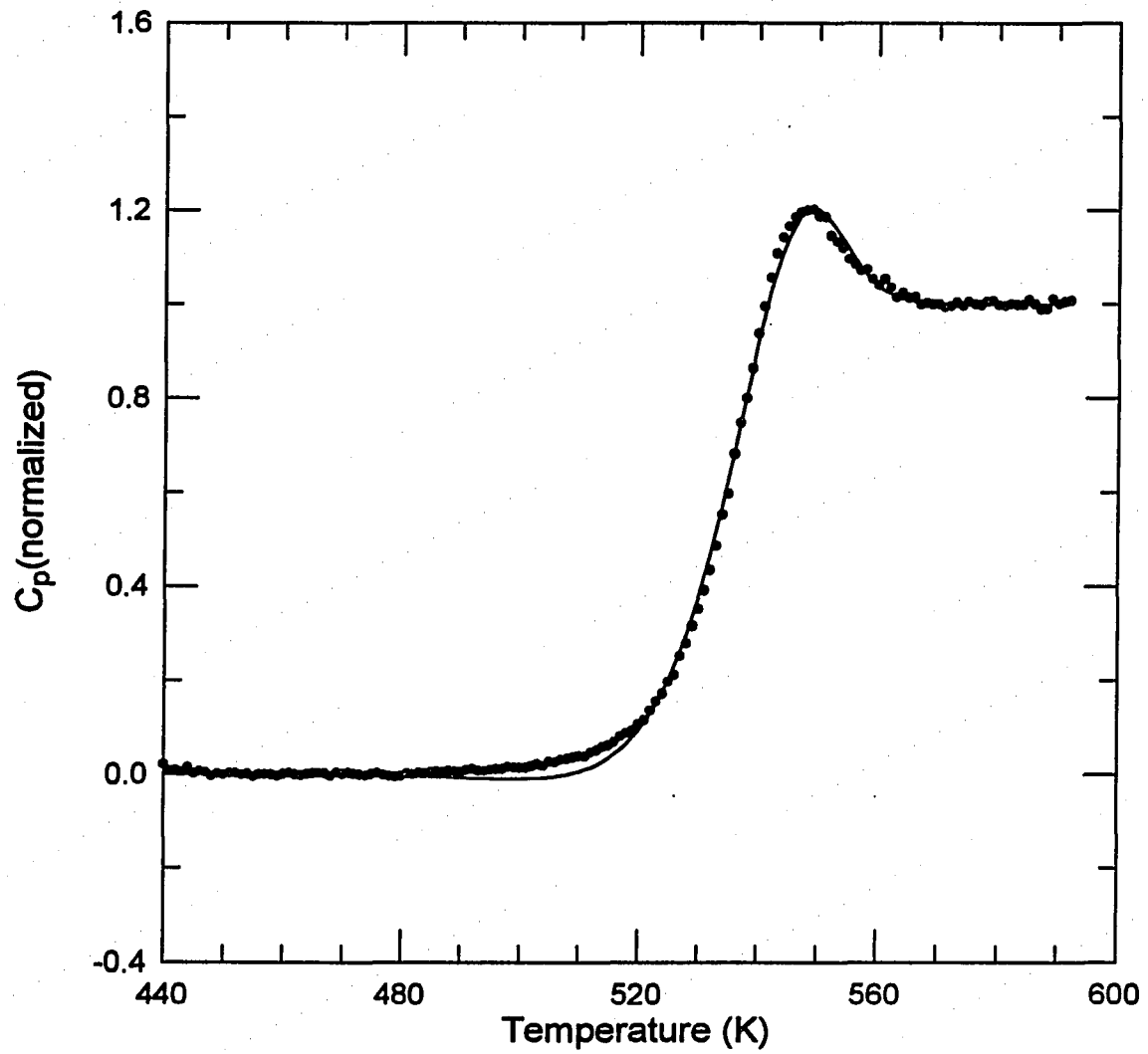


Figure A.13 The normalized heat capacity of $0.35 \text{ Na}_2\text{O} + 0.65 \text{ P}_2\text{O}_5$ glass determined experimentally (•) and calculated (—).

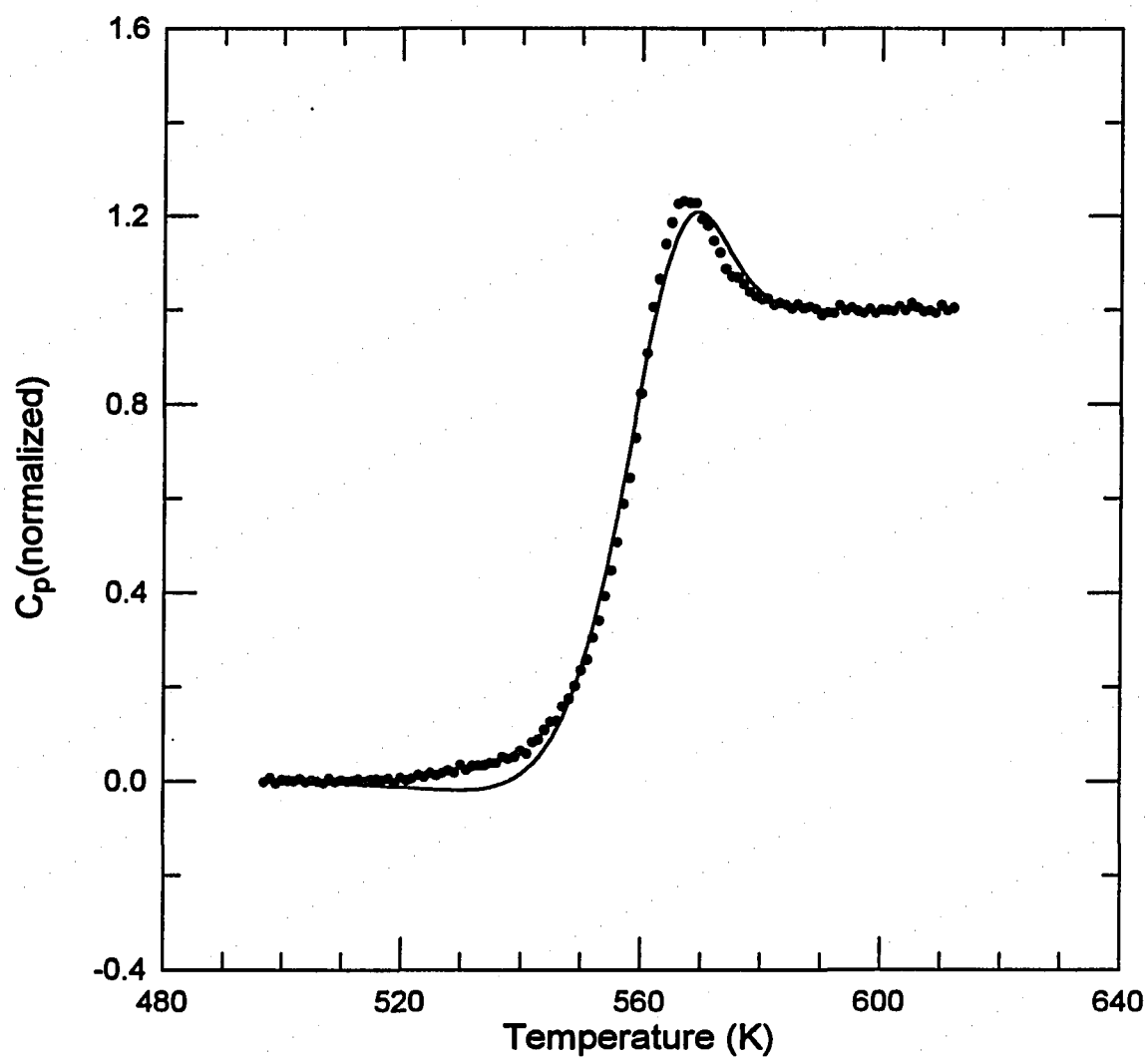


Figure A.14 The normalized heat capacity of 0.45 Na₂O + 0.55 P₂O₅ glass determined experimentally (•) and calculated (—).

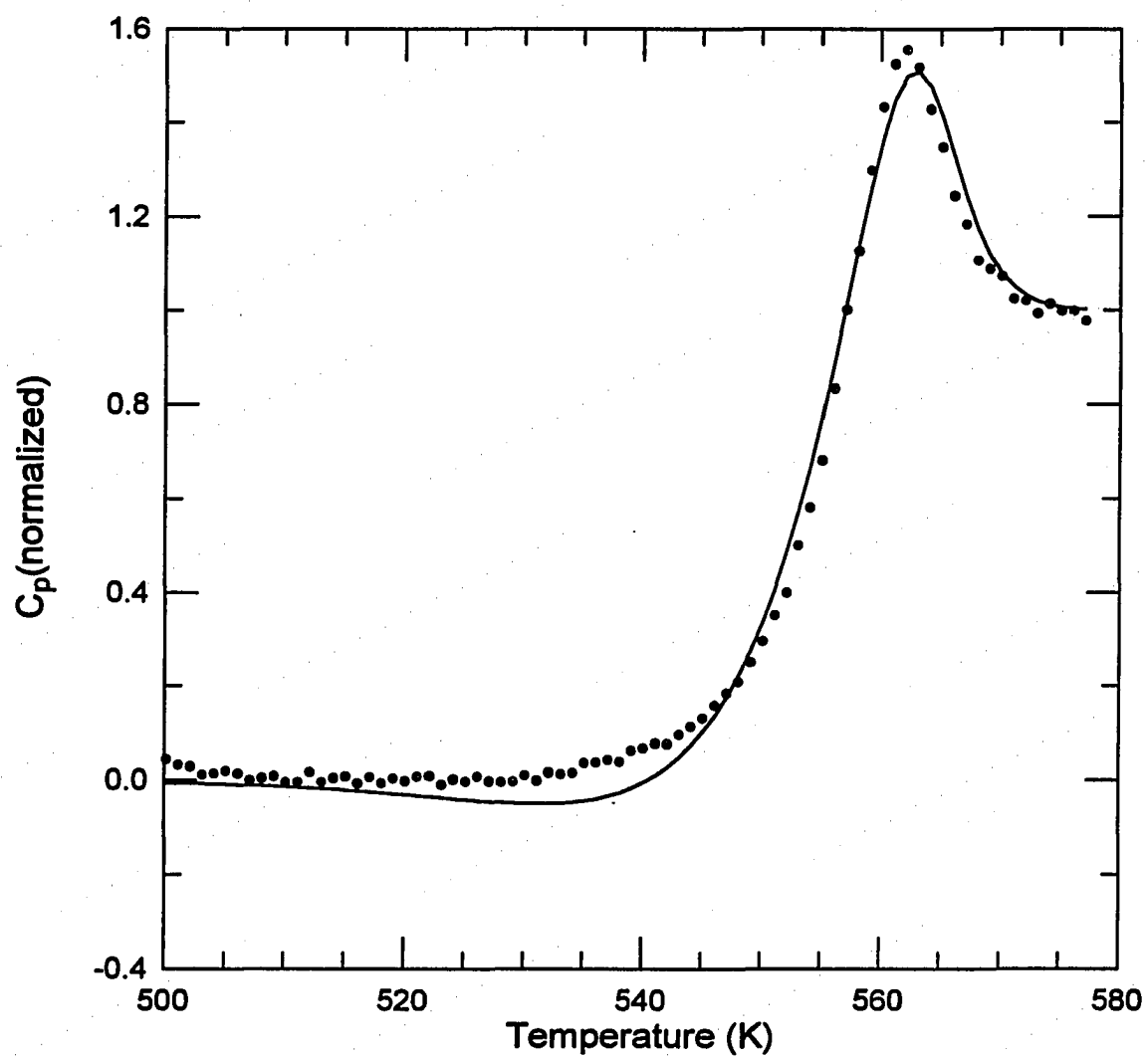


Figure A.15 The normalized heat capacity of $0.50 \text{ Na}_2\text{O} + 0.50 \text{ P}_2\text{O}_5$ glass determined experimentally (\bullet) and calculated (—).

**APPENDIX B: THE INFRA-RED SPECTRUM OF SODIUM AND
LITHIUM ULTRA-PHOSPHATE GLASSES**

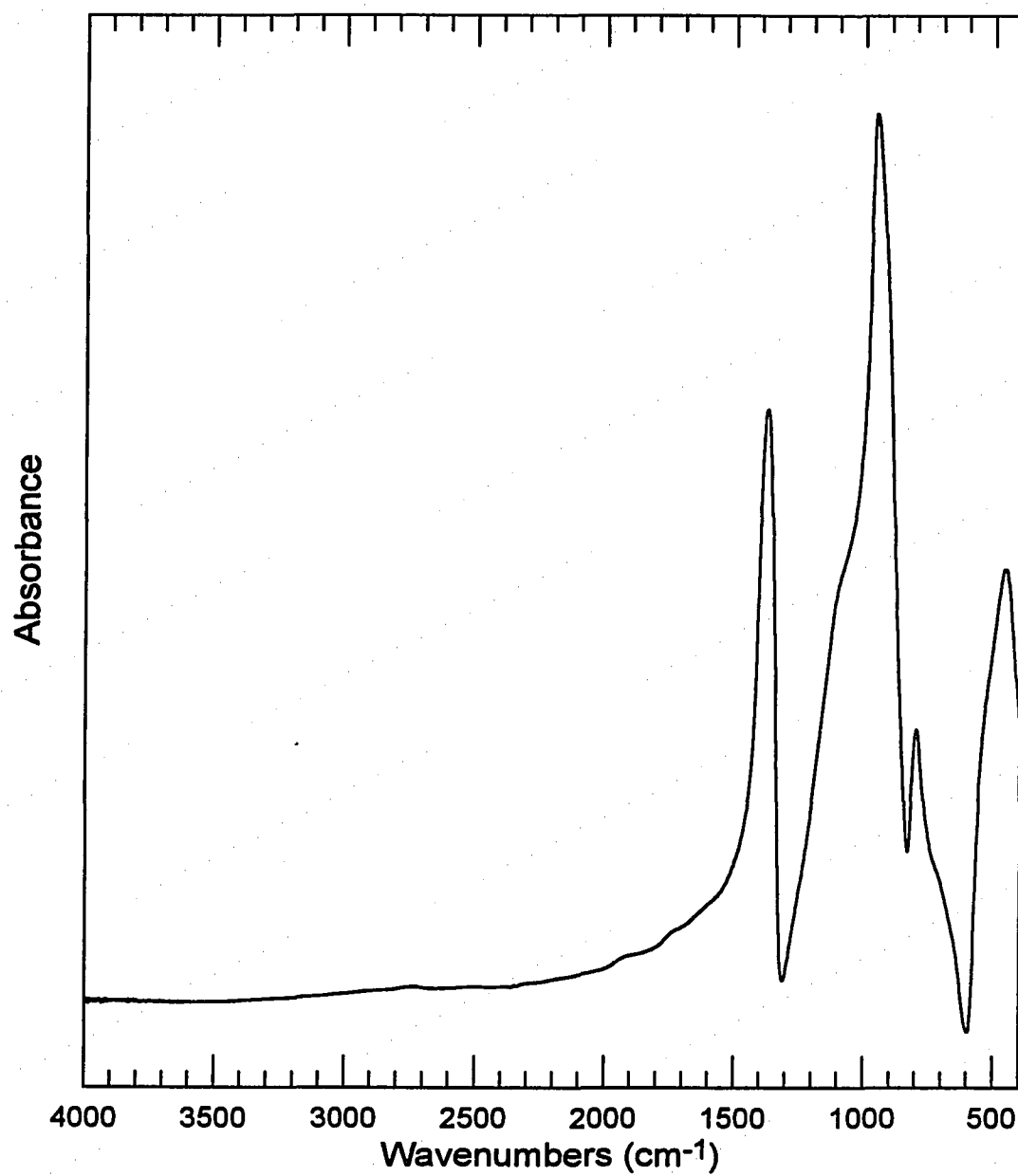


Figure B.1 MIR spectrum of ν - P_2O_5

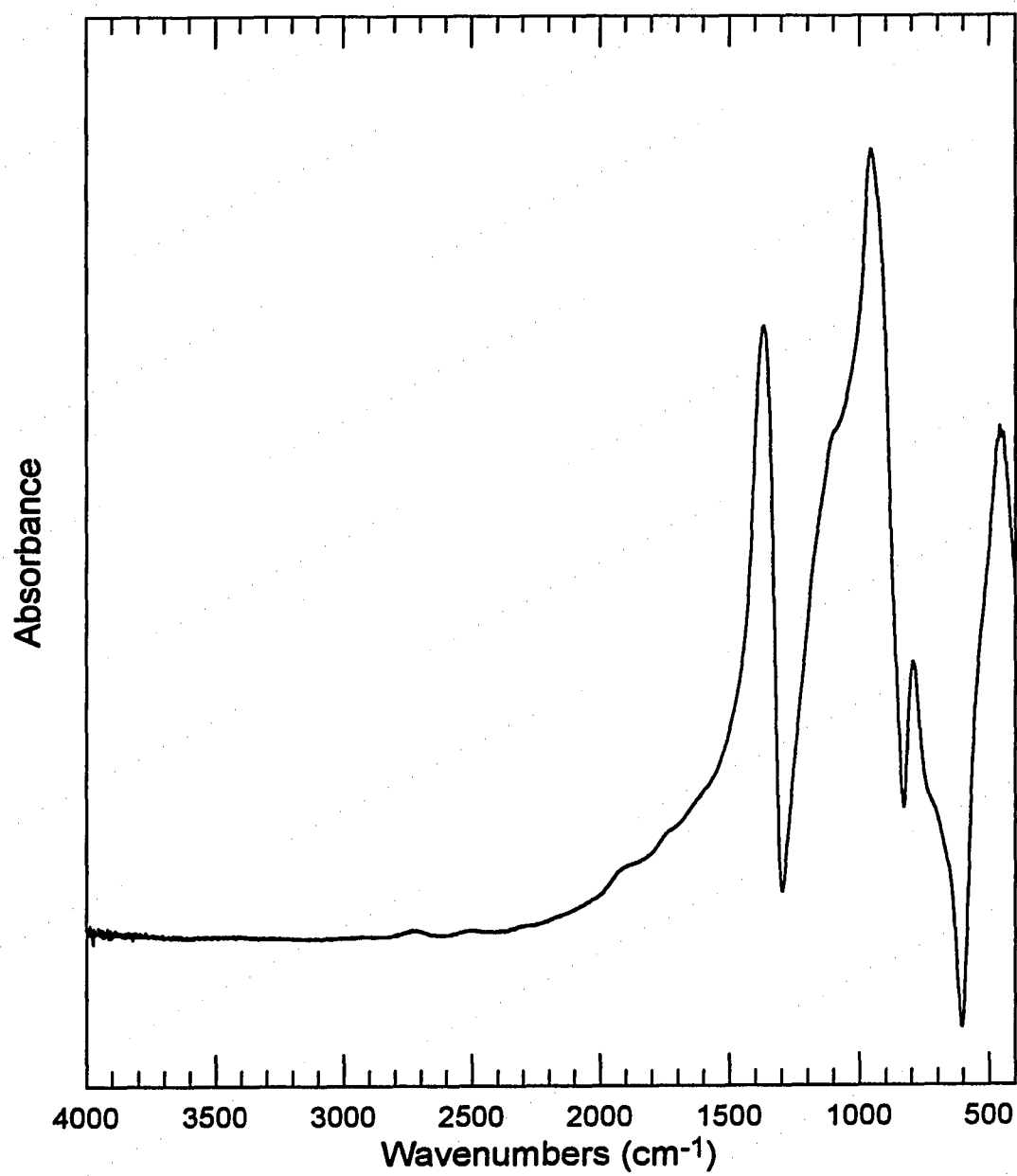


Figure B.2 MIR spectrum of 0.05 Li₂O + 0.95 P₂O₅ glass.

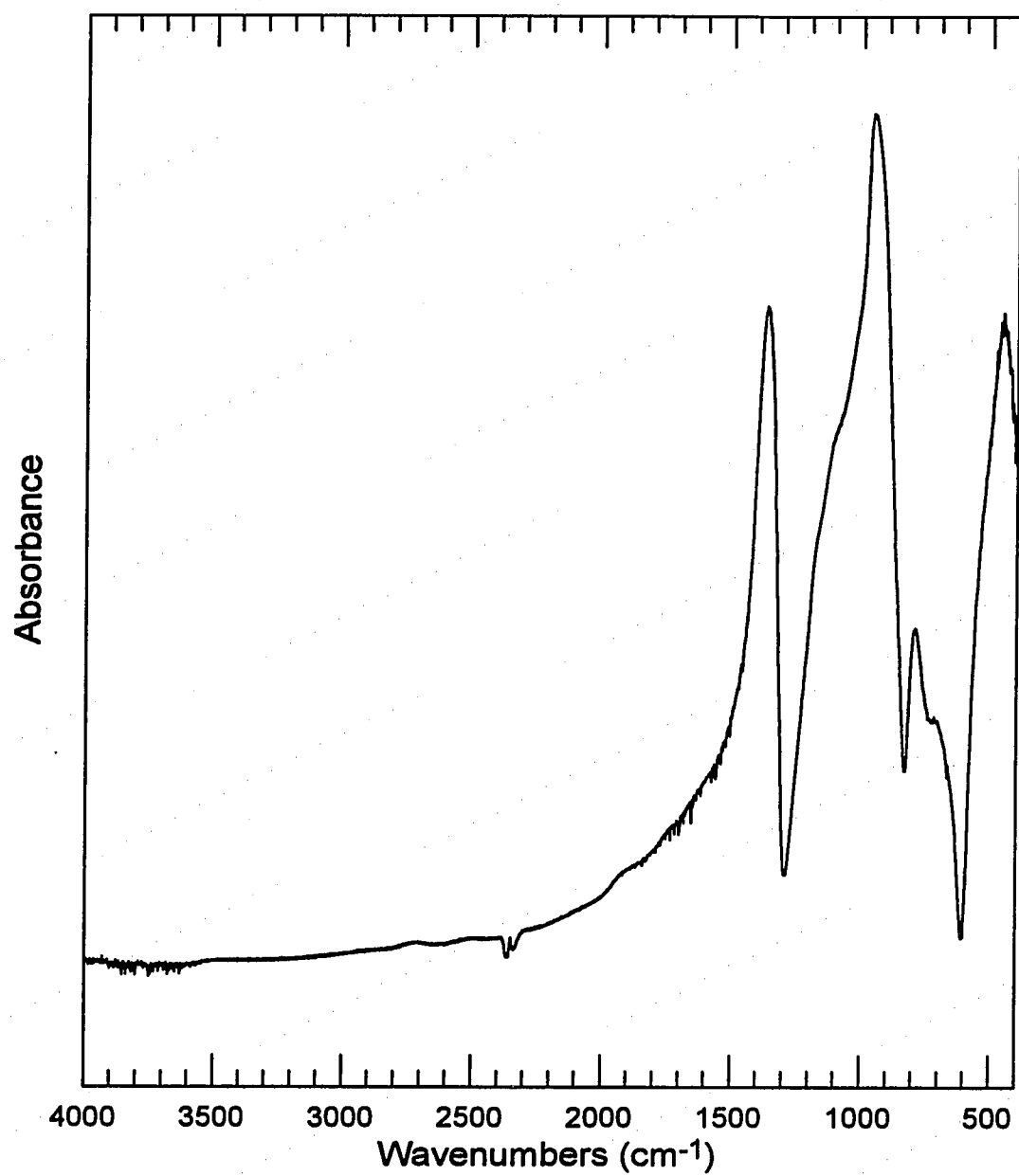


Figure B.3 MIR spectrum of 0.10 Li₂O + 0.90 P₂O₅ glass.

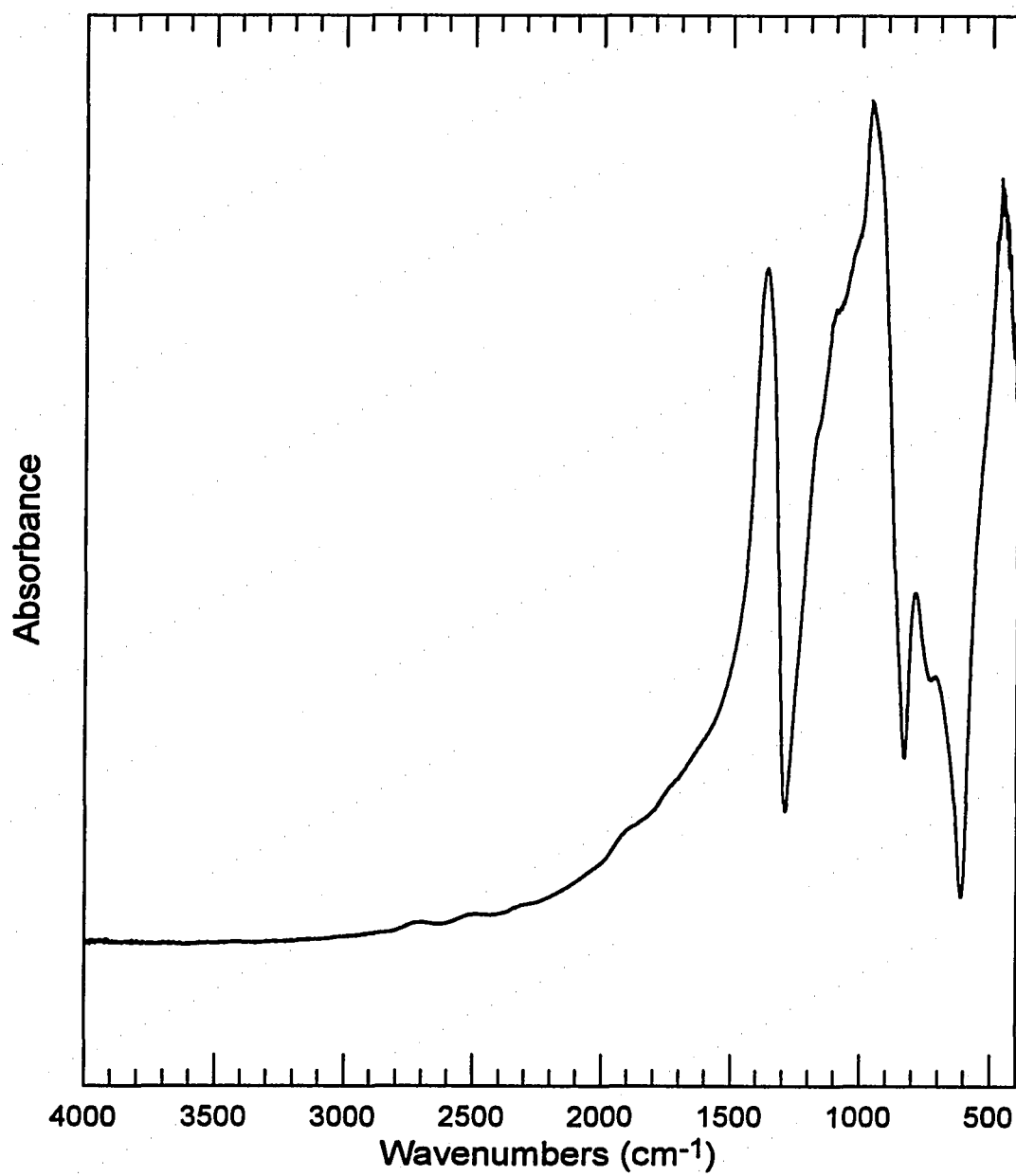


Figure B.4 MIR spectrum of 0.15 Li₂O + 0.85 P₂O₅ glass.

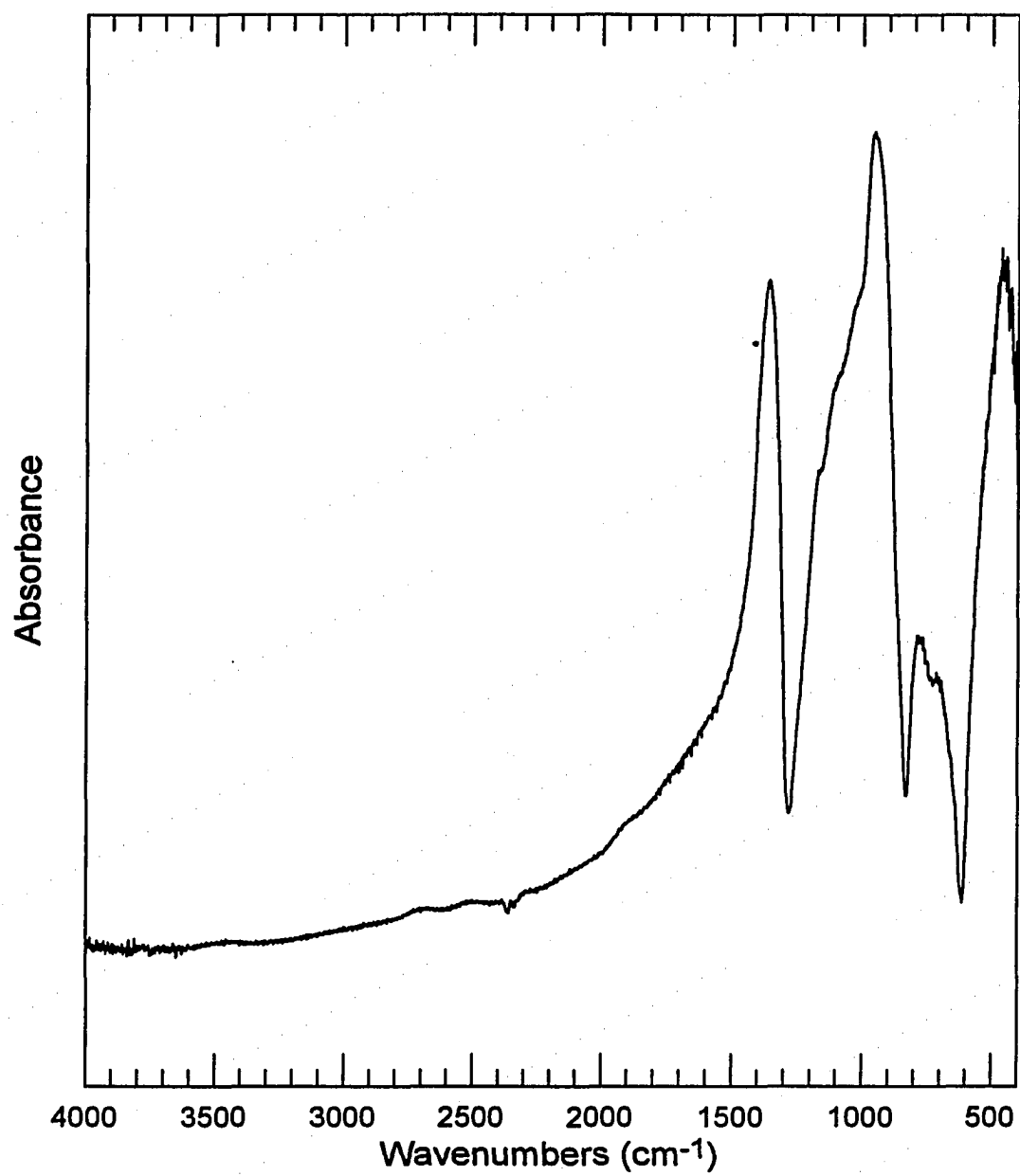


Figure B.5 MIR spectrum of 0.20 Li₂O + 0.80 P₂O₅ glass.

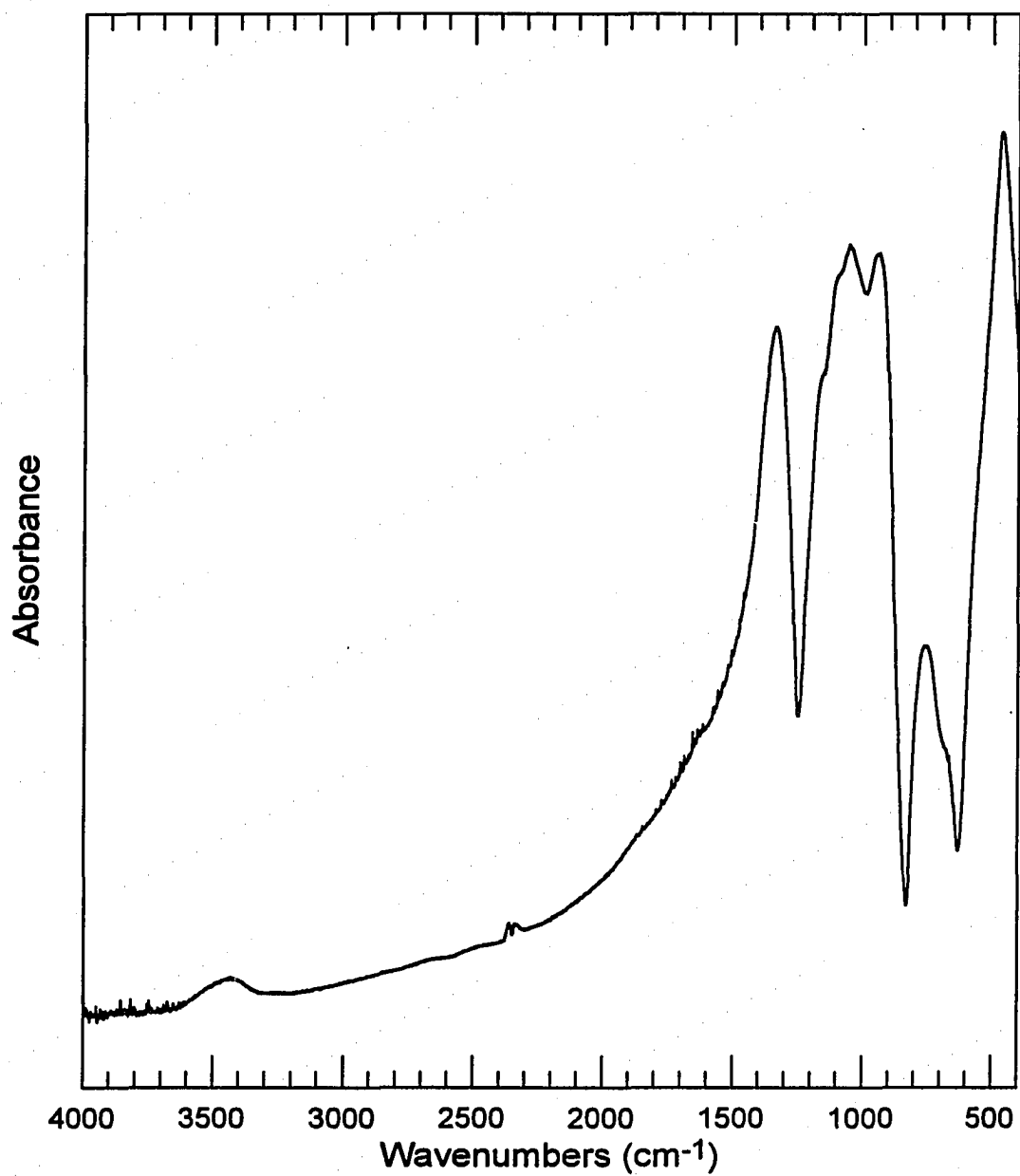


Figure B.6 MIR spectrum of 0.30 Li₂O + 0.70 P₂O₅ glass.

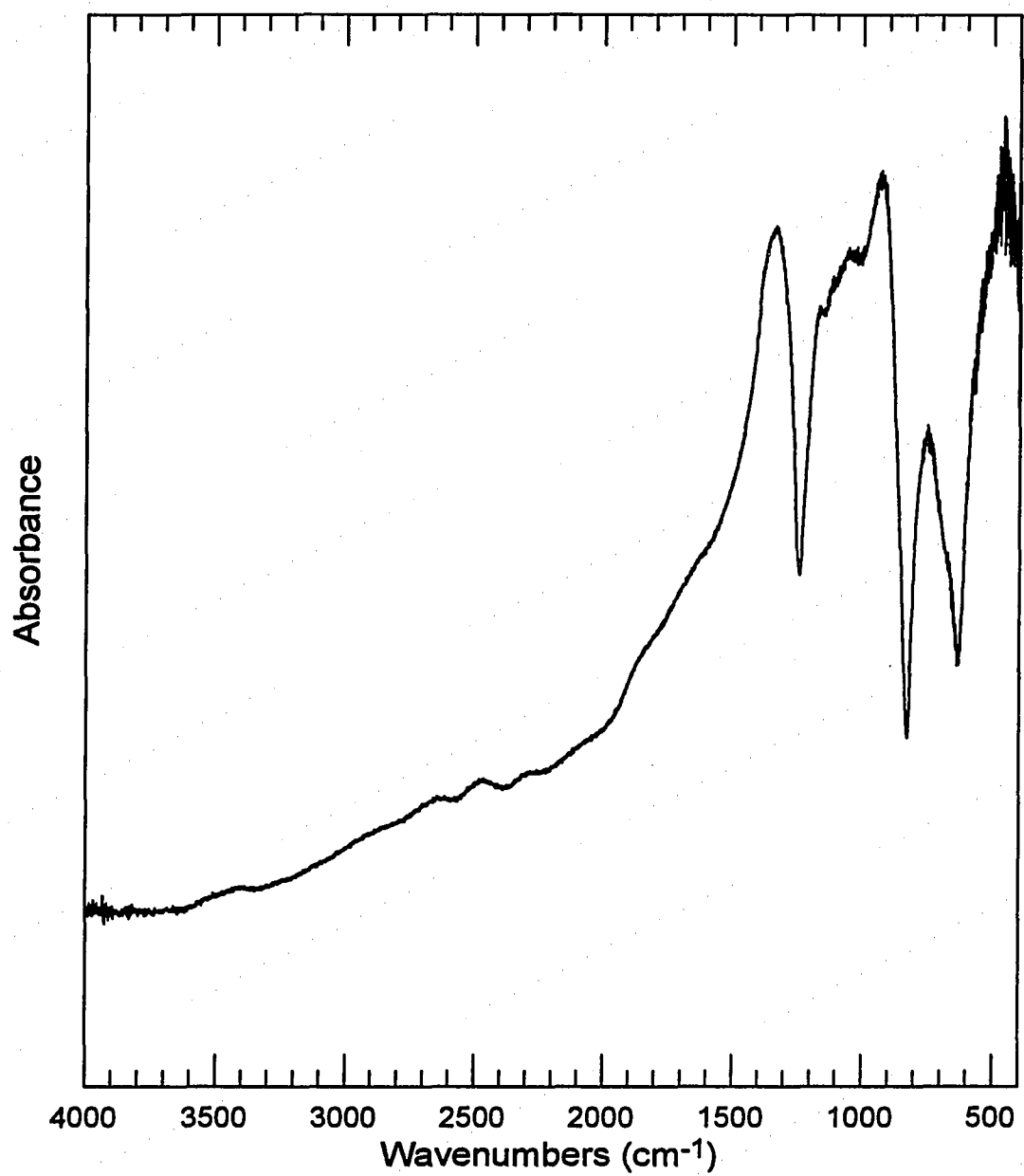


Figure B.7 MIR spectrum of 0.35 Li₂O + 0.65 P₂O₅ glass.

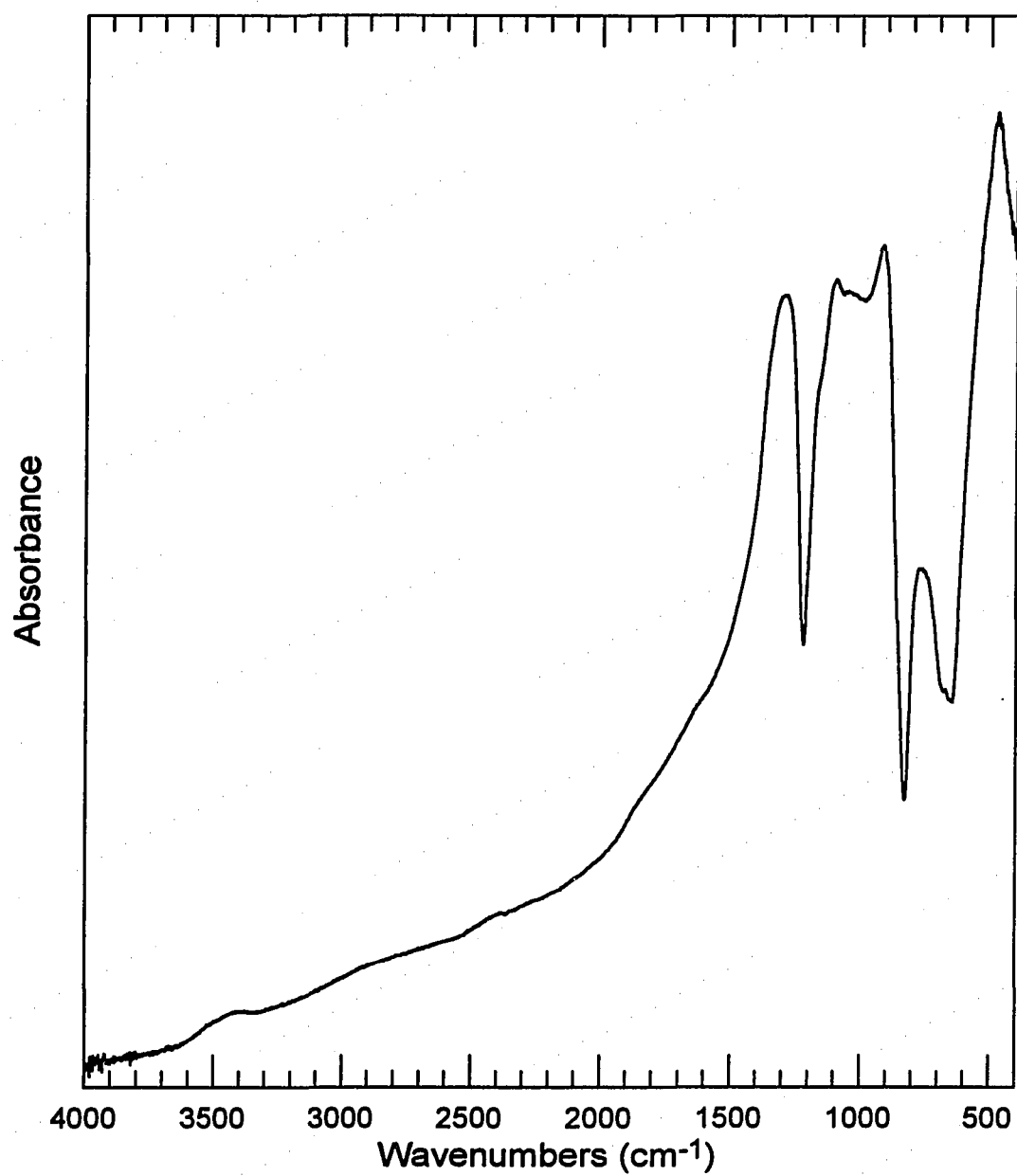


Figure B.8 MIR spectrum of 0.40 Li₂O + 0.60 P₂O₅ glass.

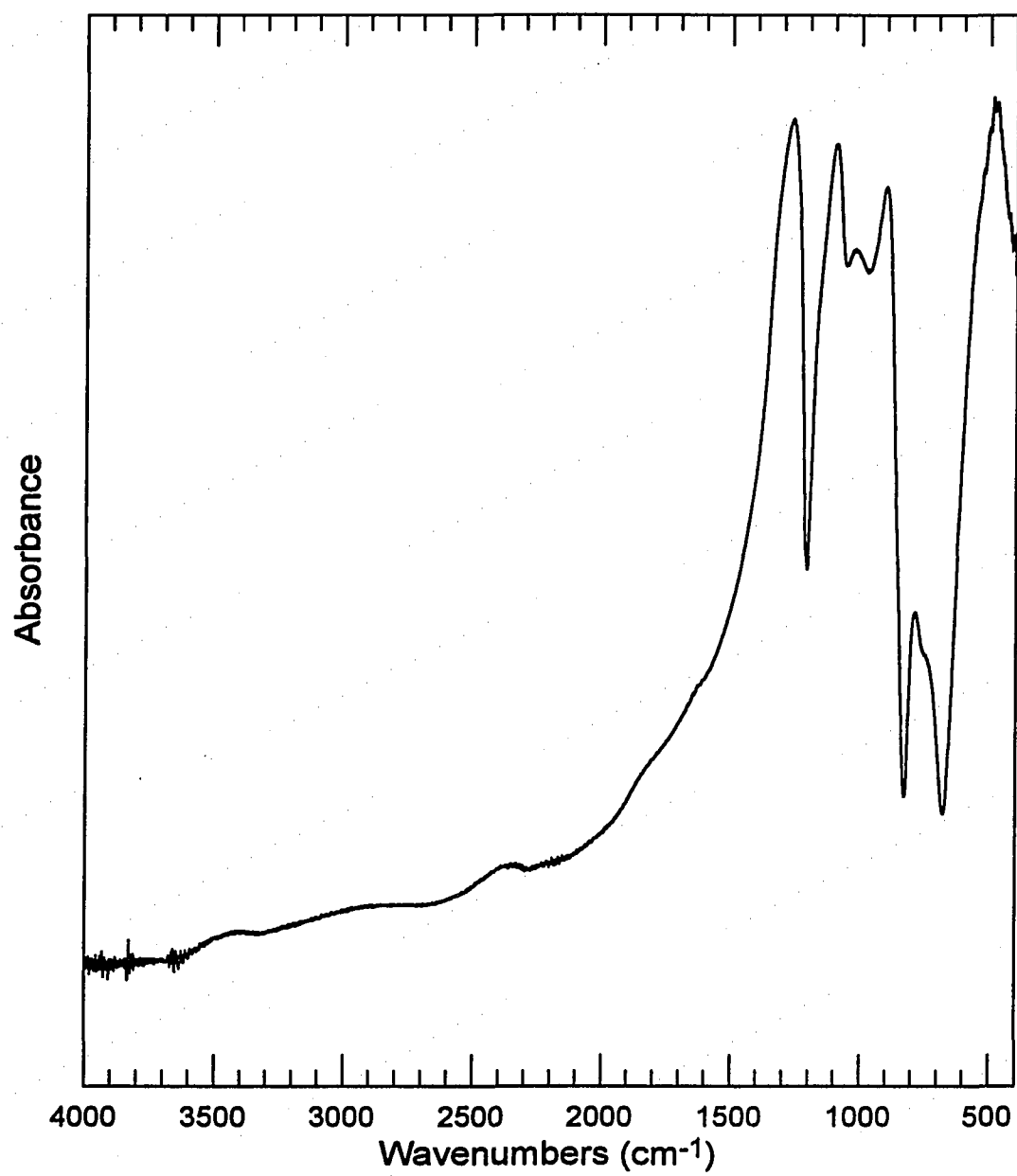


Figure B.9 MIR spectrum of 0.45 Li₂O + 0.55 P₂O₅ glass.

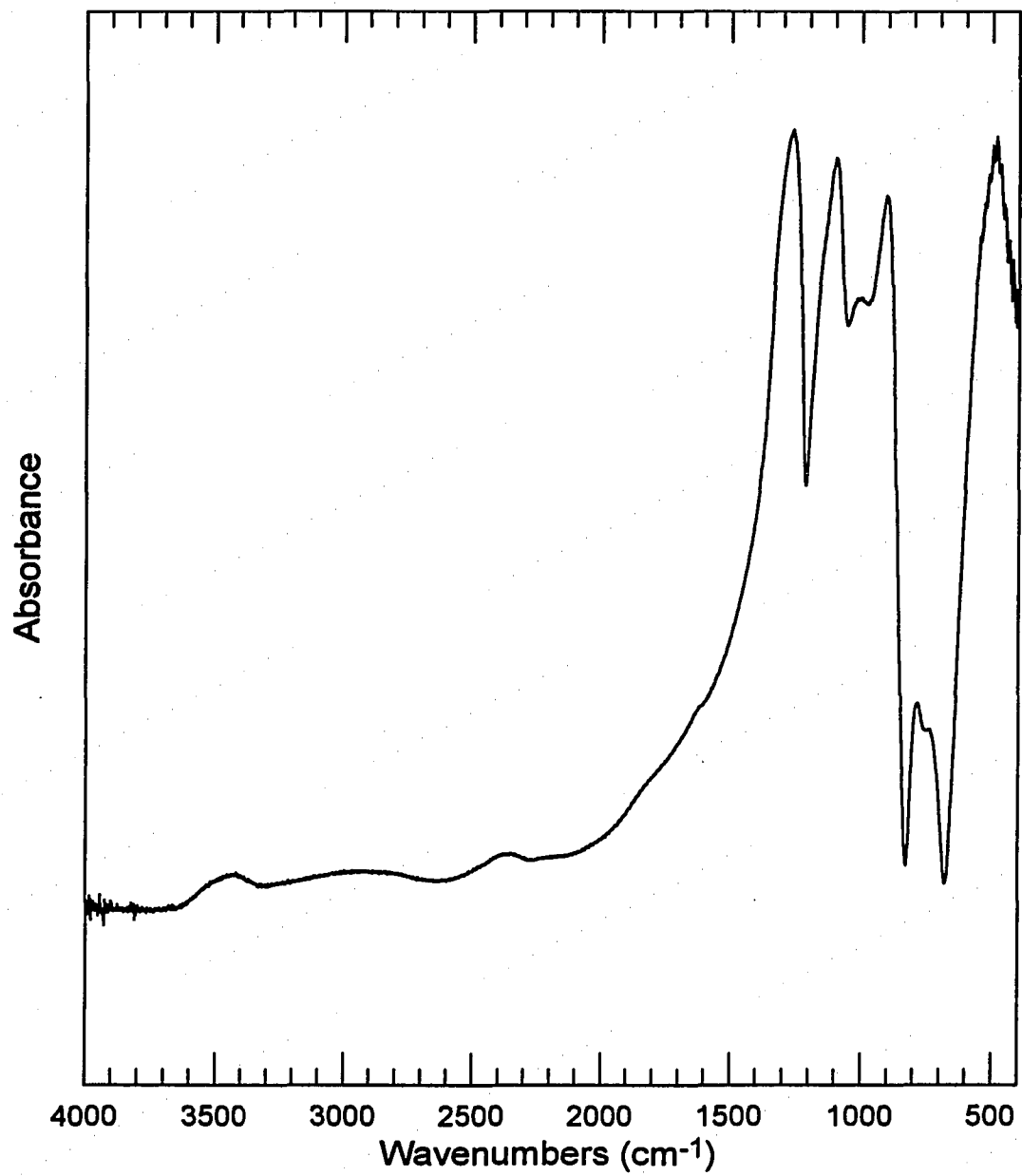


Figure B.10 MIR spectrum of 0.50 Li₂O + 0.50 P₂O₅ glass.

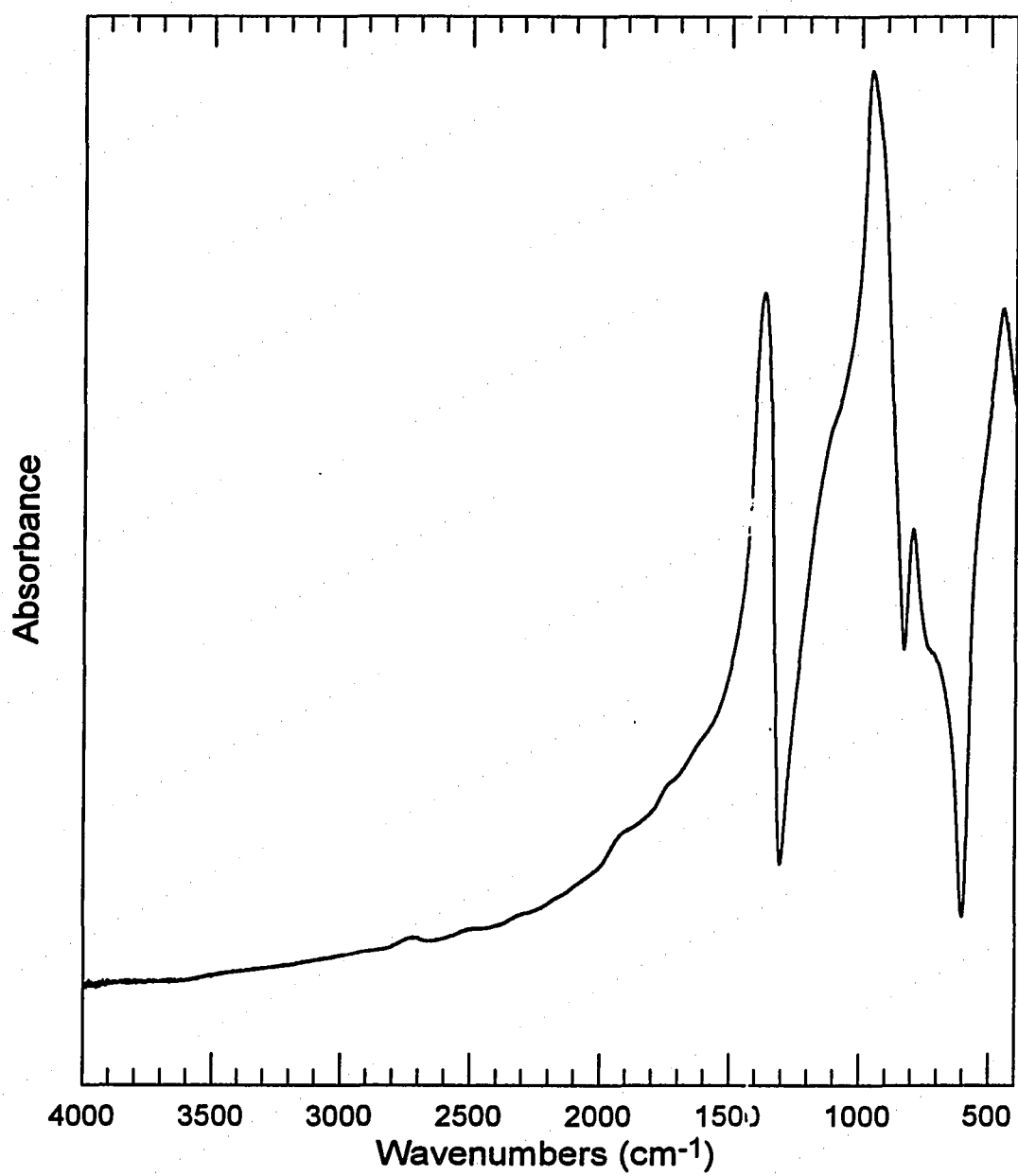


Figure B.11 MIR spectrum of 0.02 Na₂O + 0.98 P₂O₅ glass.

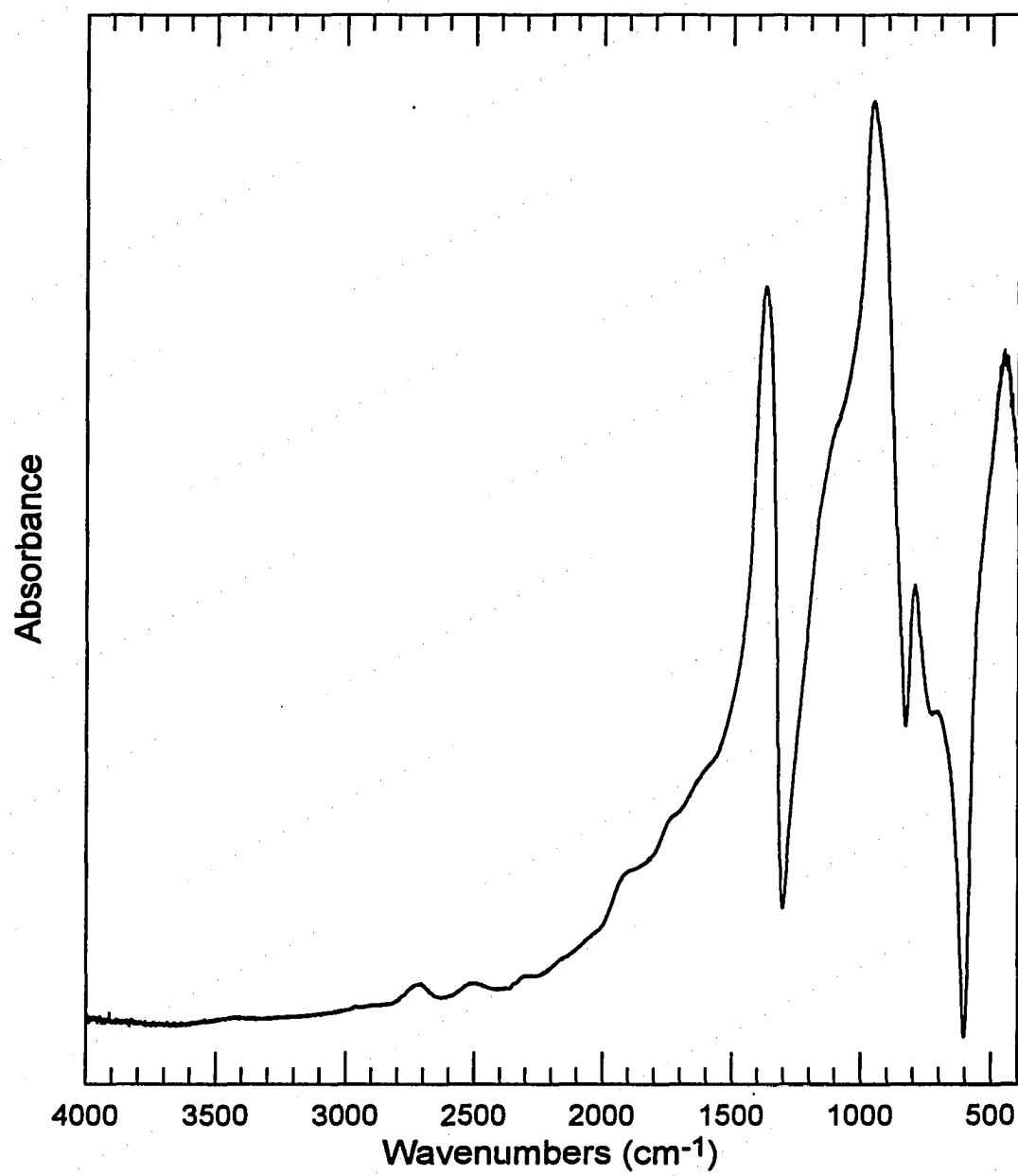


Figure B.12 MIR spectrum of 0.05 Na₂O + 0.95 P₂O₅ glass.

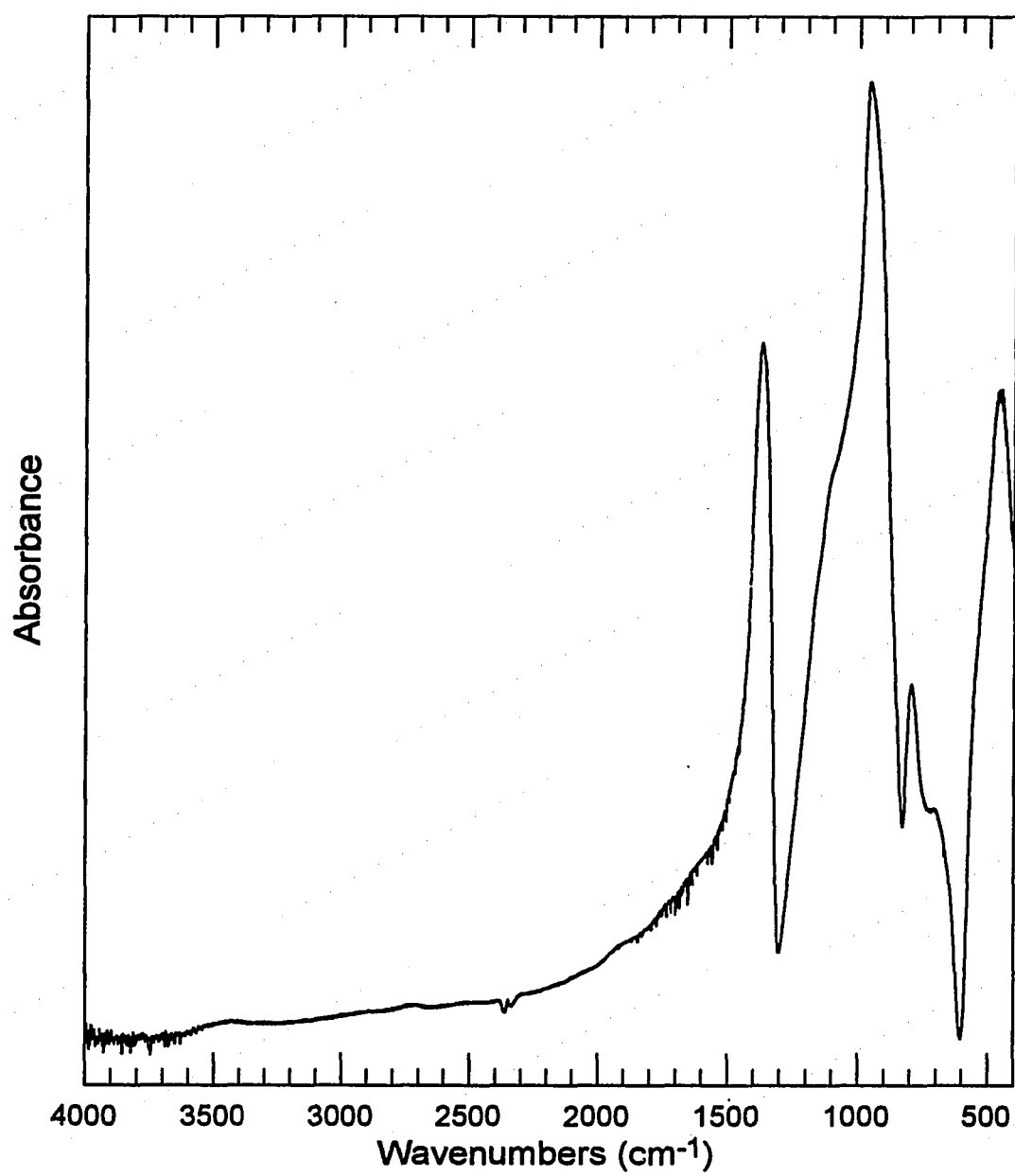


Figure B.13 MIR spectrum of 0.10 Na₂O + 0.90 P₂O₅ glass.

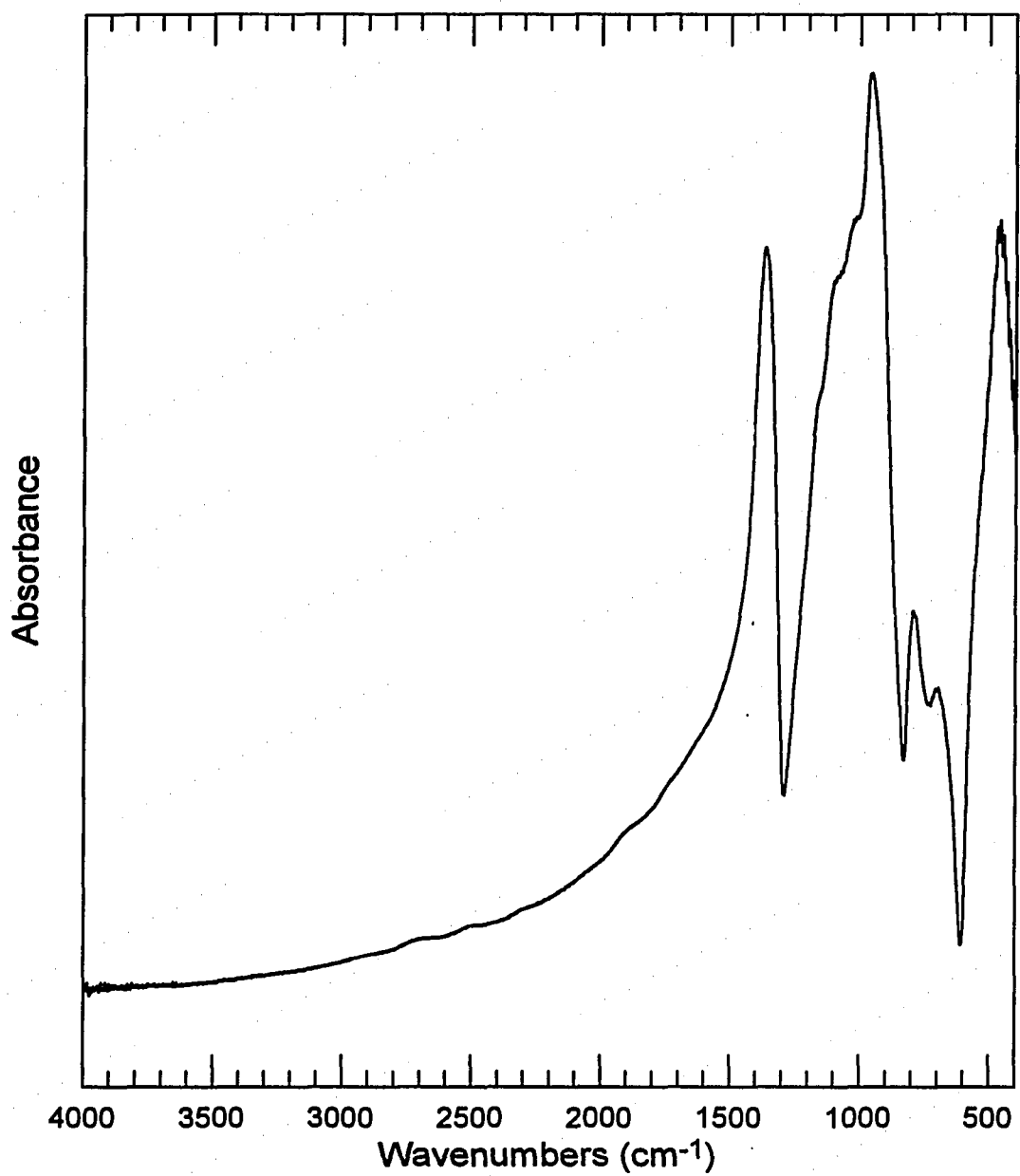


Figure B.14 MIR spectrum of 0.15 Na₂O + 0.85 P₂O₅ glass.

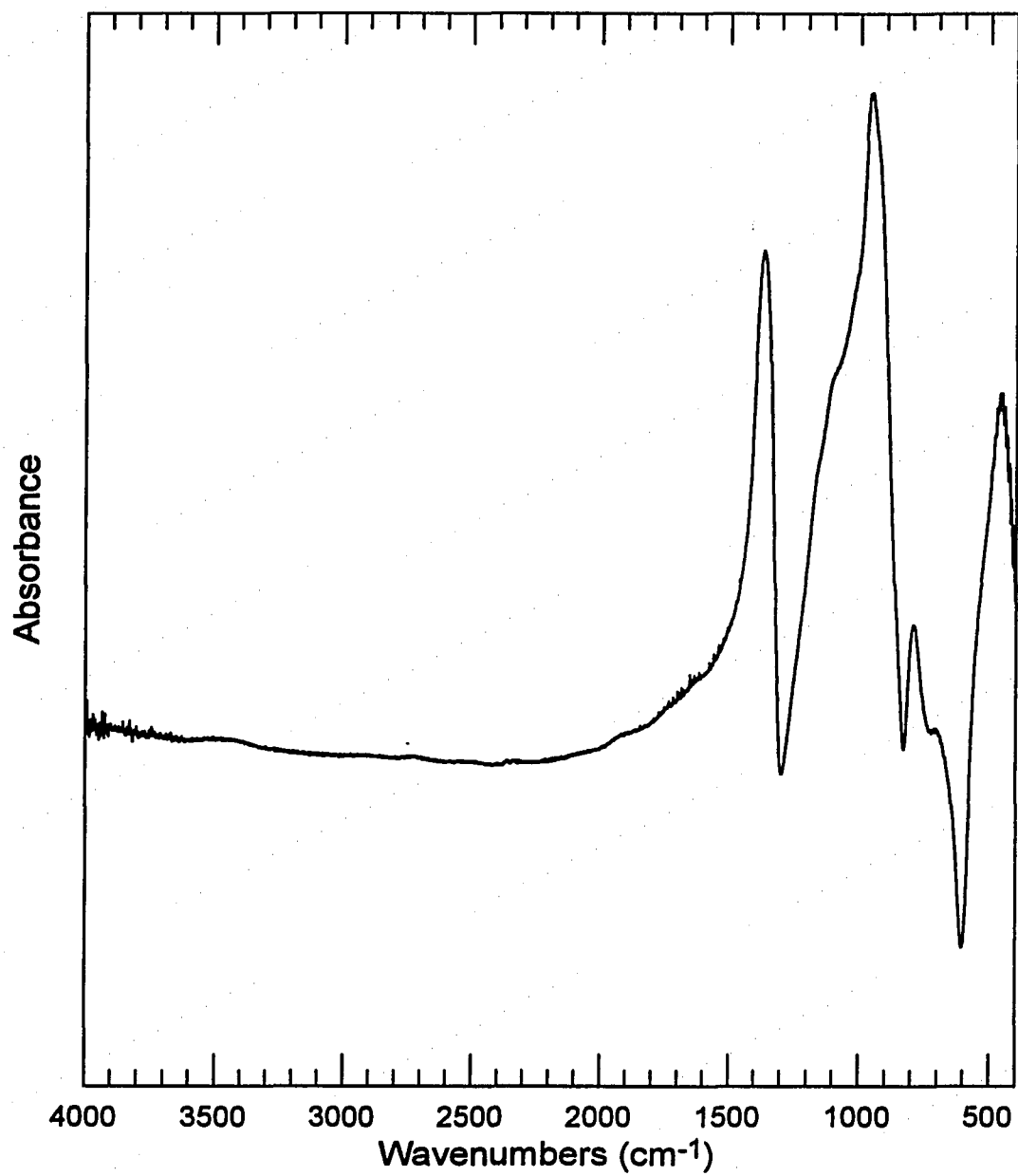


Figure B.15 MIR spectrum of 0.20 Na₂O + 0.80 P₂O₅ glass.

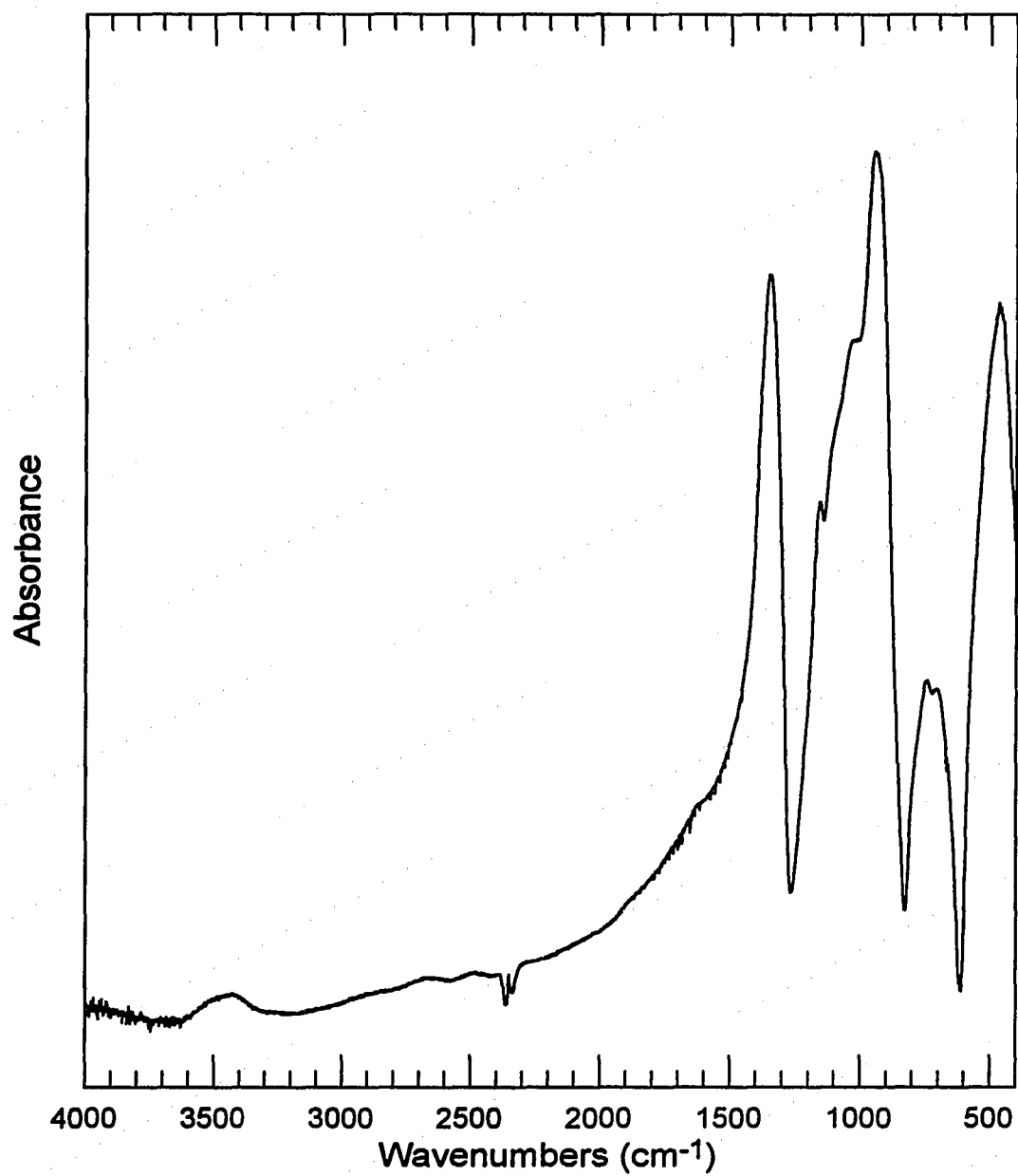


Figure B.16 MIR spectrum of 0.25 Na₂O + 0.75 P₂O₅ glass.

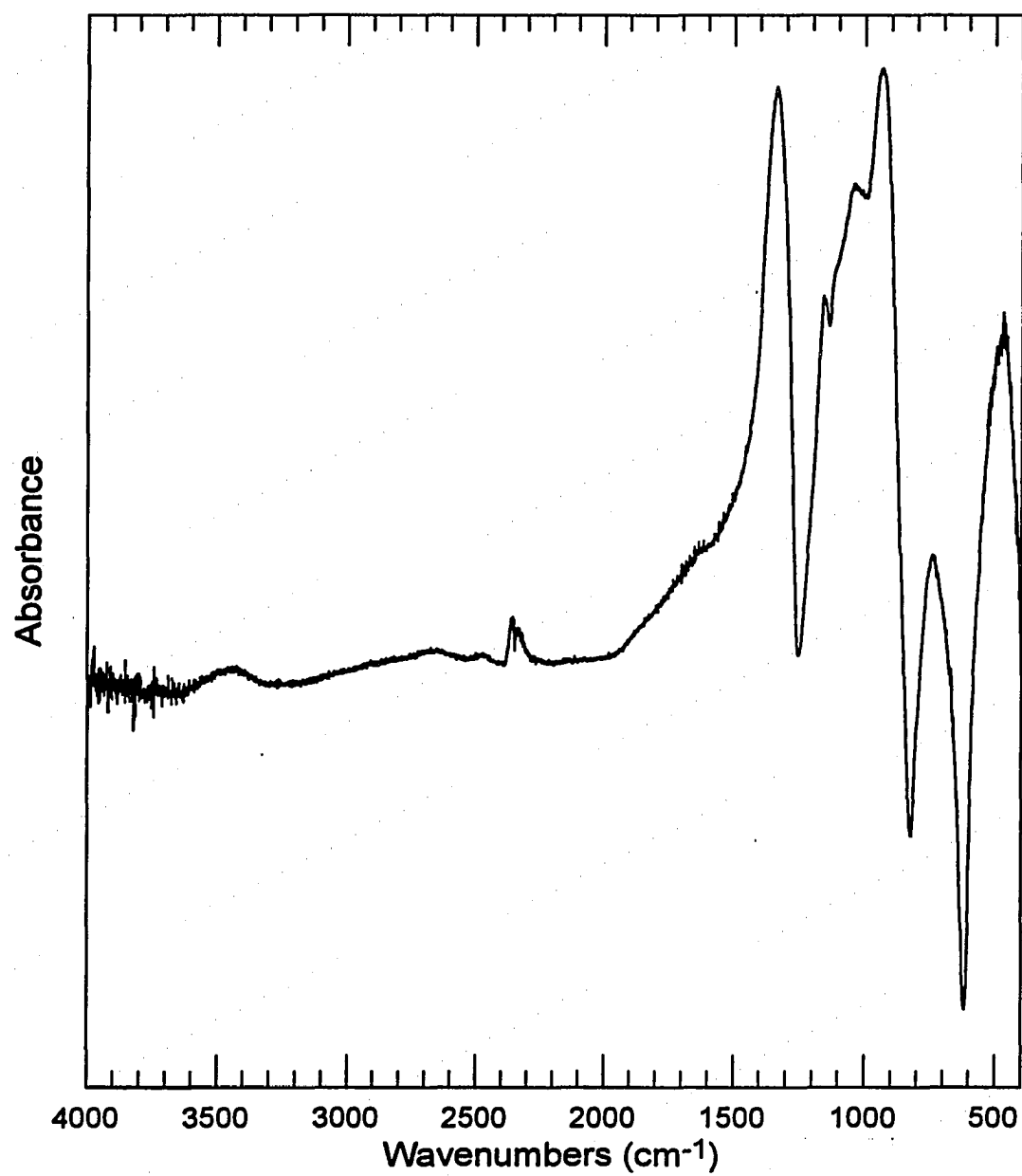


Figure B.17 MIR spectrum of 0.30 Na₂O + 0.70 P₂O₅ glass.

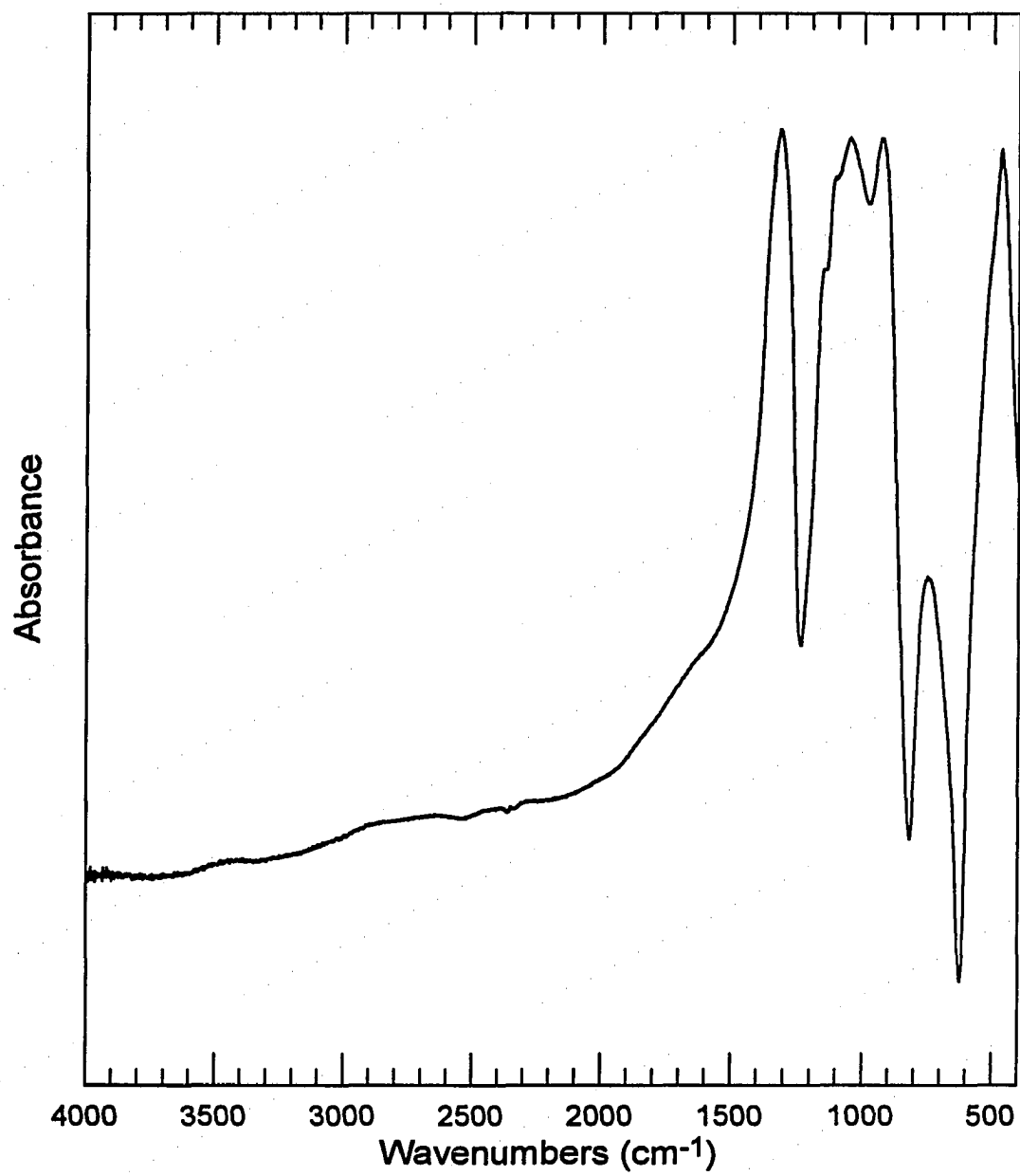


Figure B.18 MIR spectrum of 0.35 Na₂O + 0.65 P₂O₅ glass

**APPENDIX C: THE RAMAN SPECTRUM OF SODIUM AND
LITHIUM ULTRA-PHOSPHATE GLASSES**

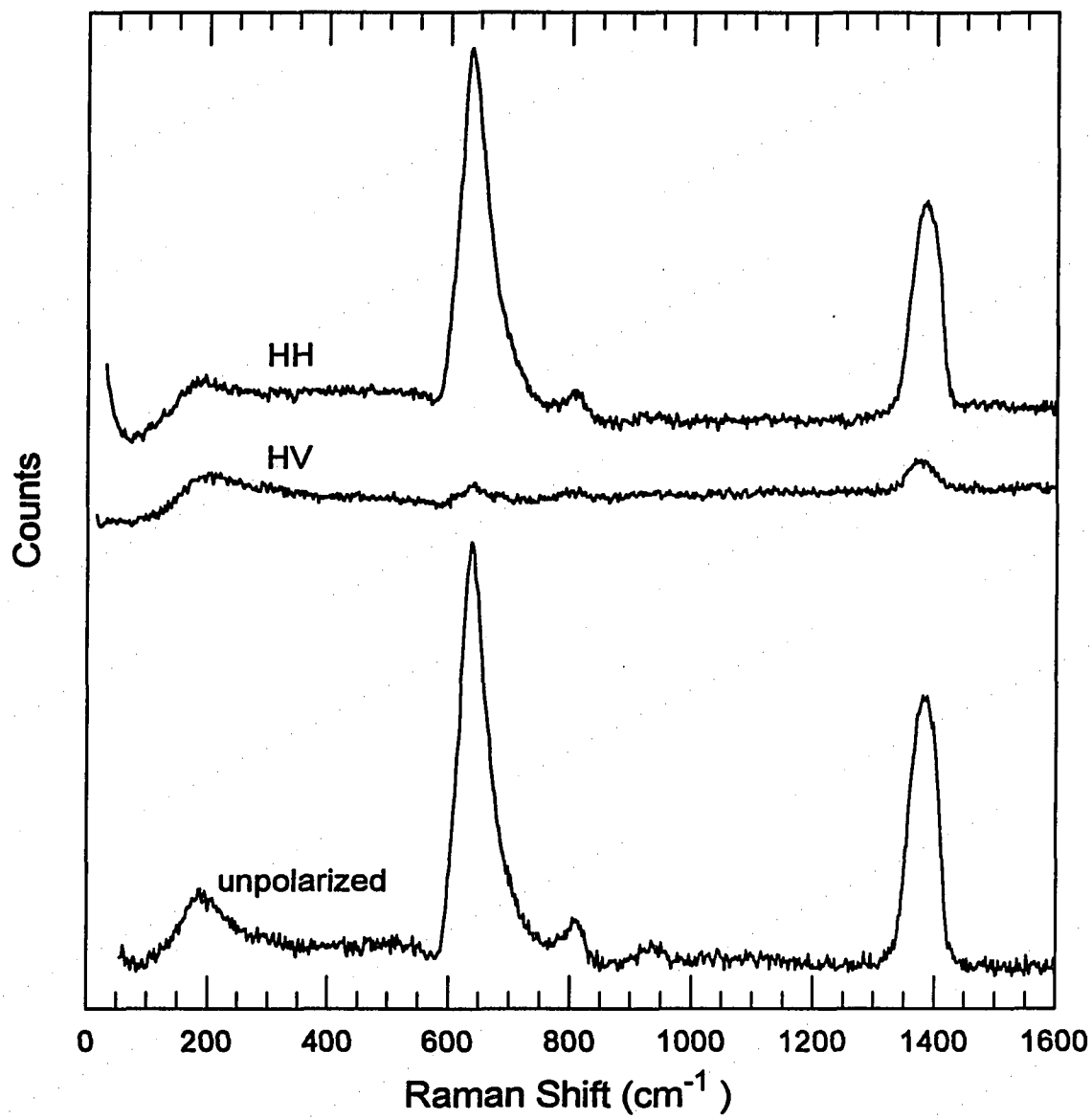


Figure C.19 The unpolarized, HV polarized, and HH polarized Raman spectrum of ν -P₂O₅.

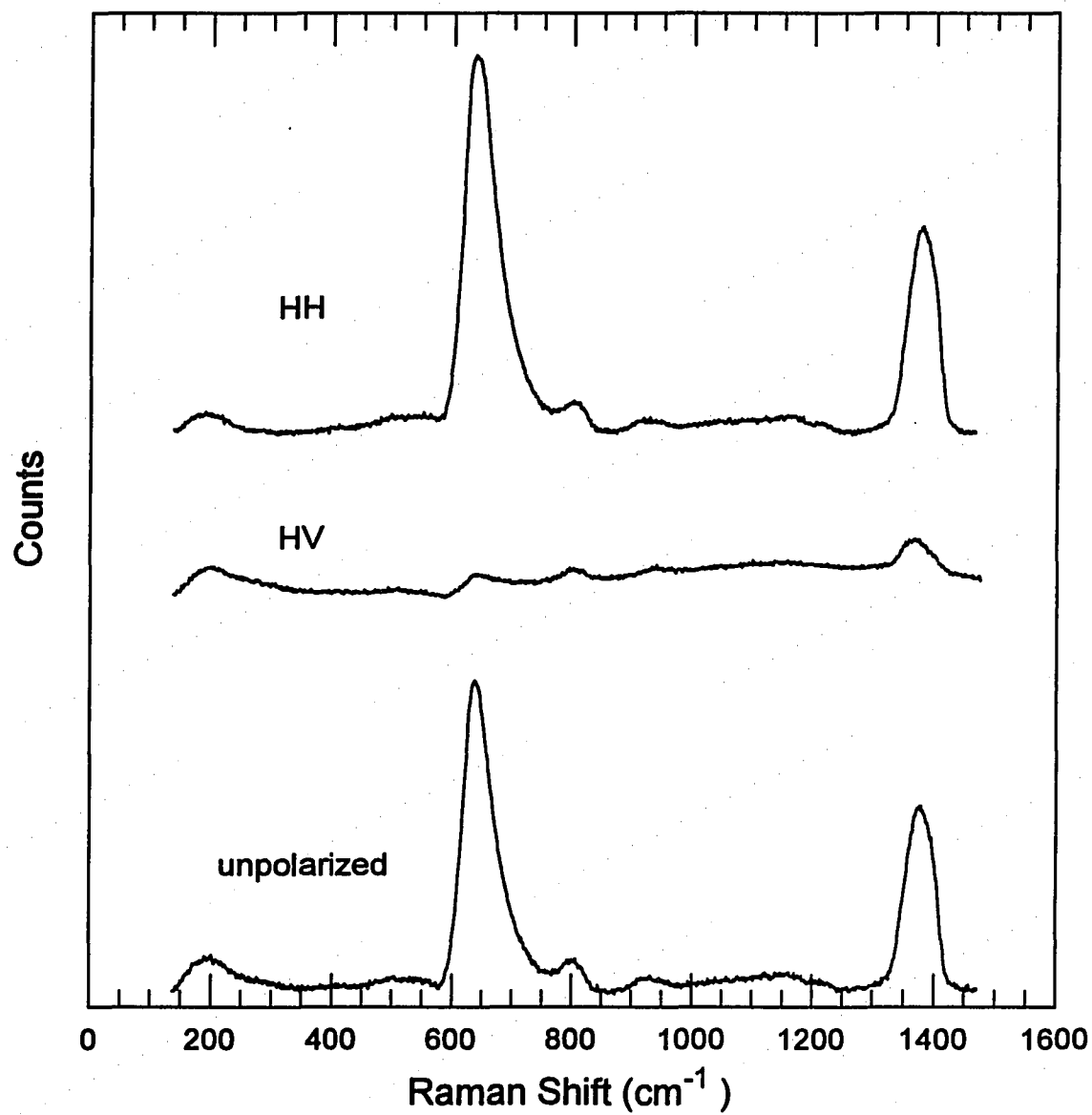


Figure C.20 The unpolarized, HV polarized, and HH polarized Raman spectrum of 0.05 Li_2O + 0.95 P_2O_5 glass.

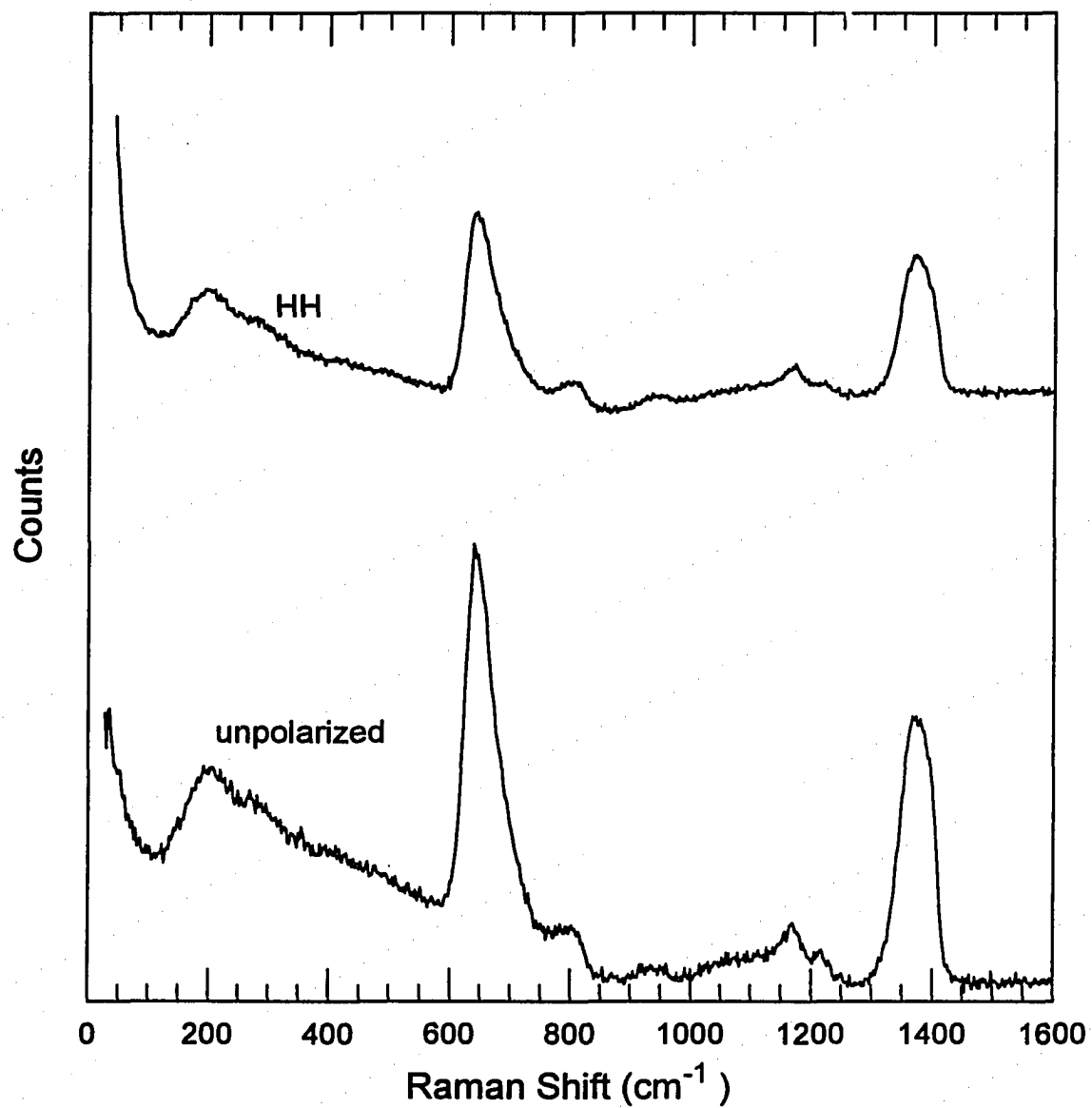


Figure C.21 The unpolarize, and HH polarized Raman spectrum of 0.10 Li₂O + 0.90 P₂O₅ glass.

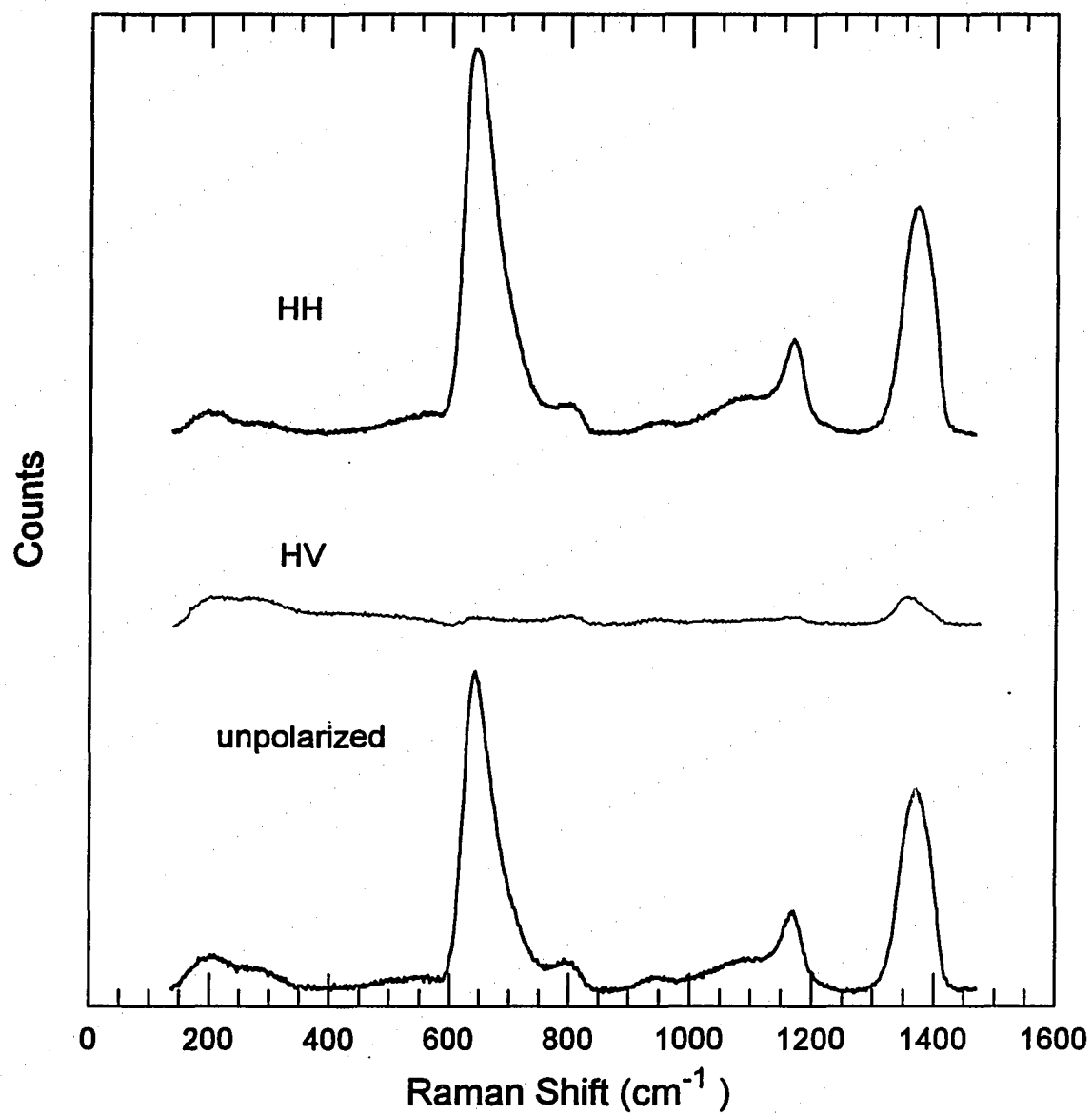


Figure C.22 The unpolarize, and HH polarized Raman spectrum of 0.15 Li₂O + 0.85 P₂O₅ glass.

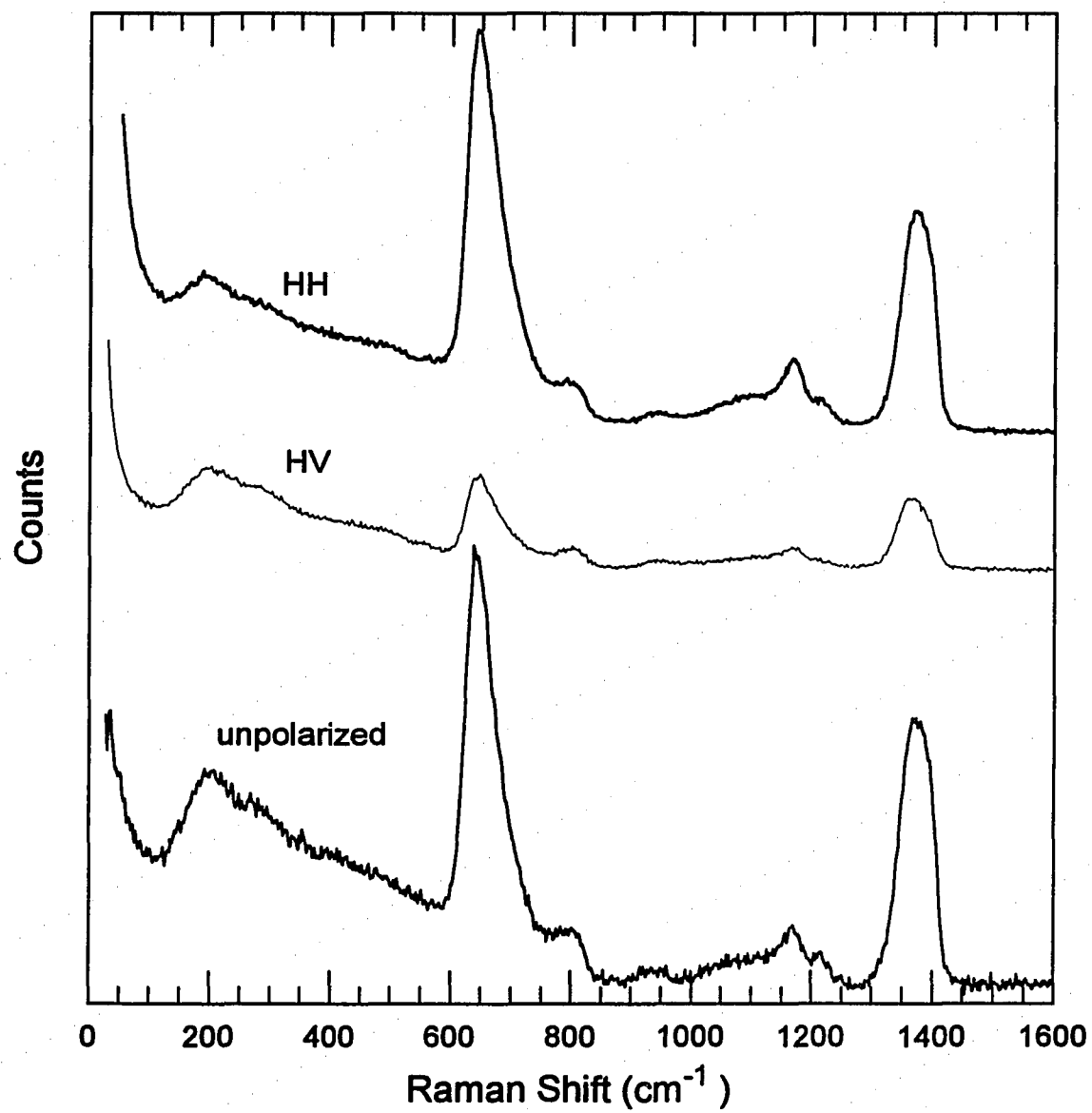


Figure C.23 The unpolarize, and HH polarized Raman spectrum of 0.20 Li₂O + 0.80 P₂O₅ glass.

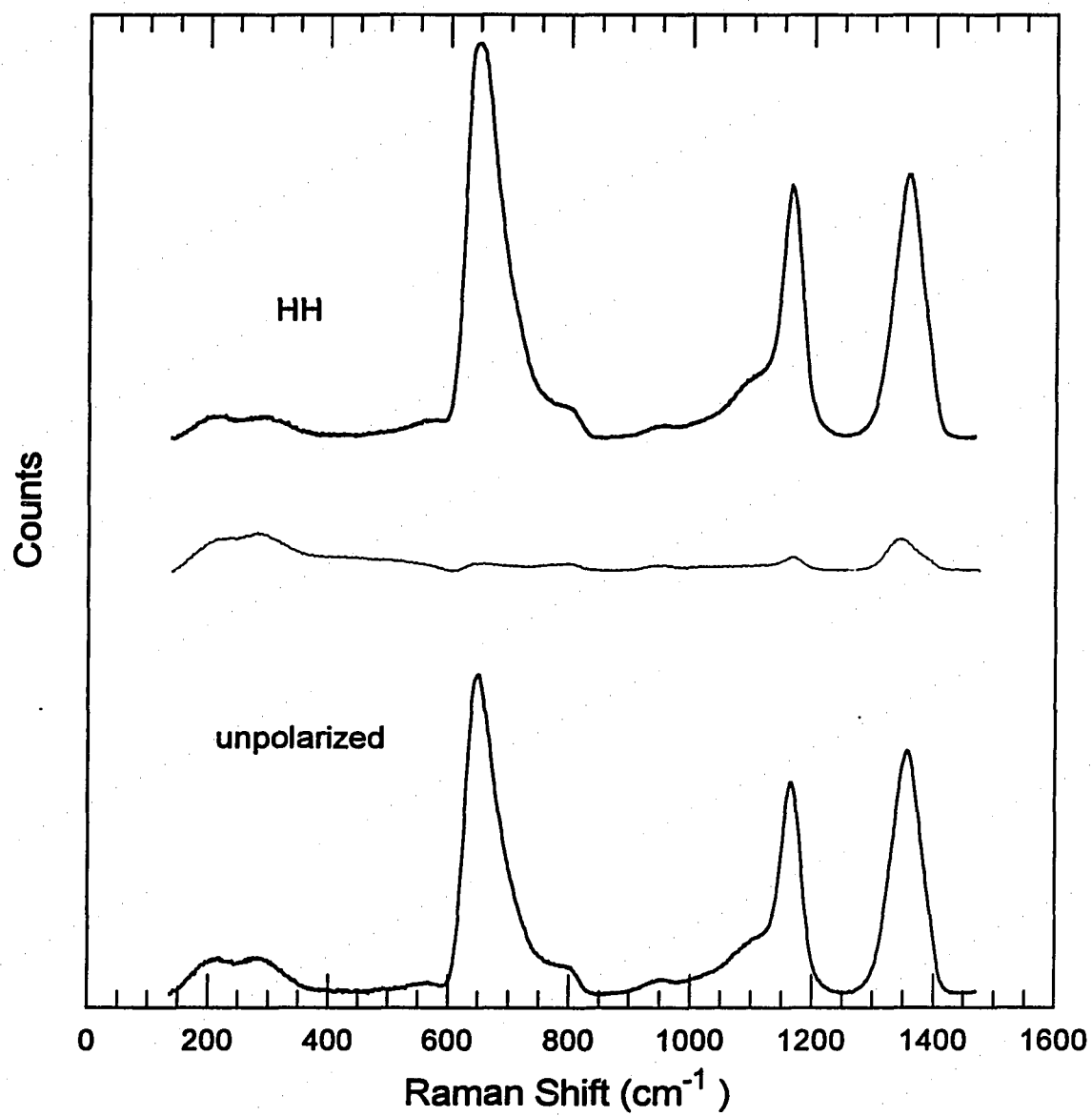


Figure C.24 The unpolarize, and HH polarized Raman spectrum of 0.25 Li₂O + 0.75 P₂O₅ glass.

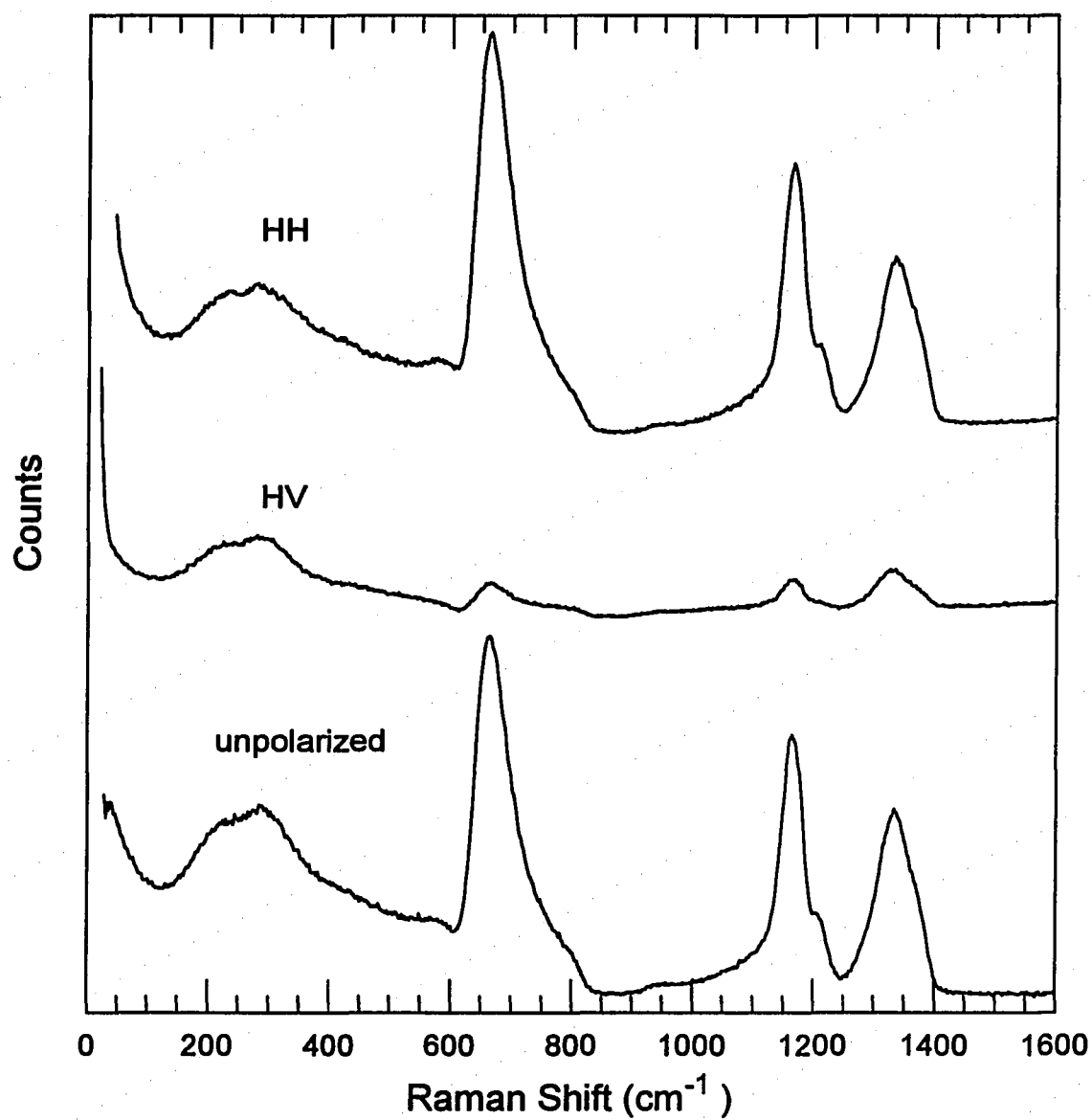


Figure C.25 The unpolarize, and HH polarized Raman spectrum of 0.30 Li₂O + 0.70 P₂O₅ glass.

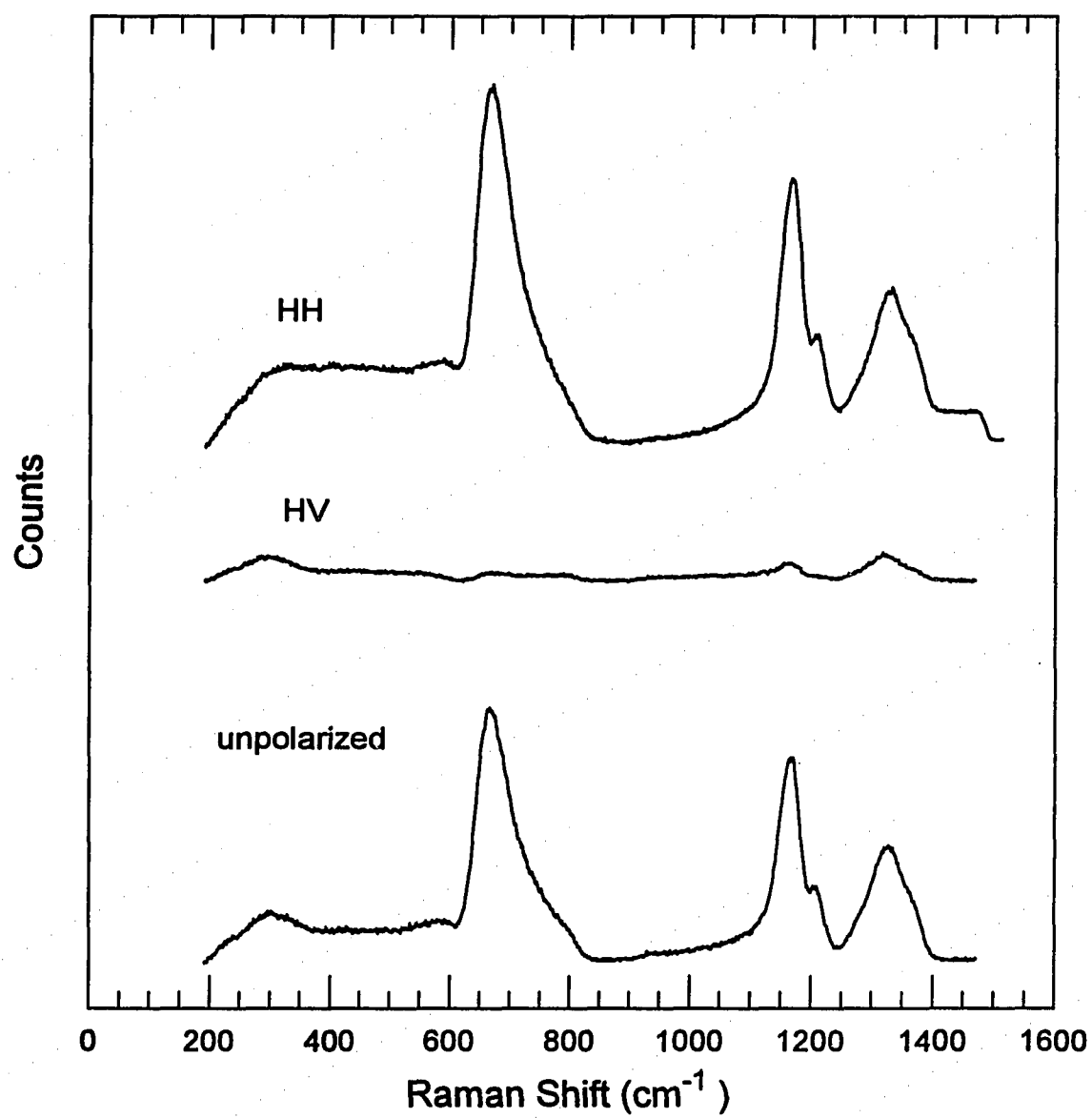


Figure C.26 The unpolarized, and HH polarized Raman spectrum of 0.35 Li₂O + 0.65 P₂O₅ glass.

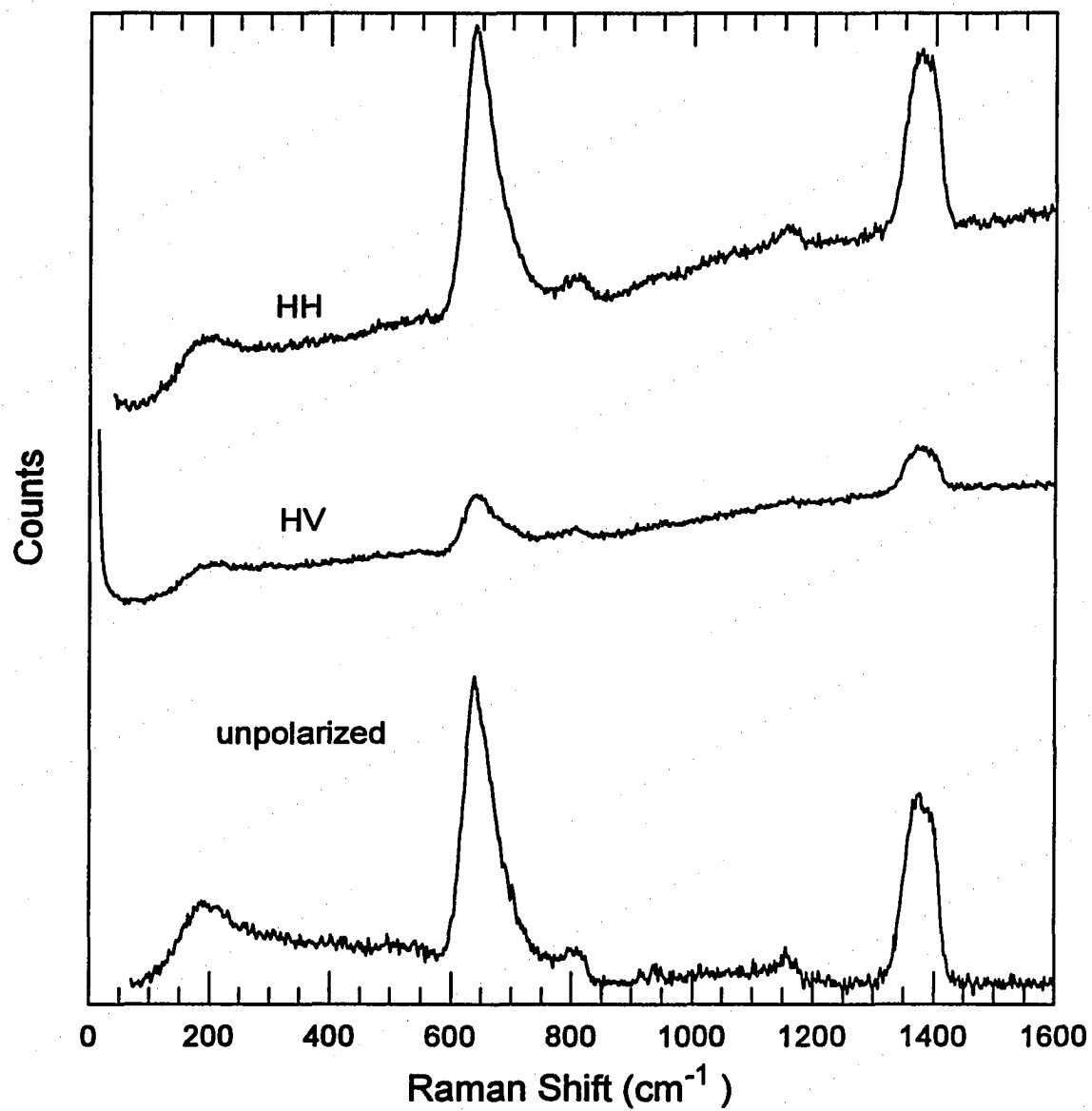


Figure C.27 The unpolarized, and HH polarized Raman spectrum of 0.05 Na₂O + 0.95 P₂O₅ glass.

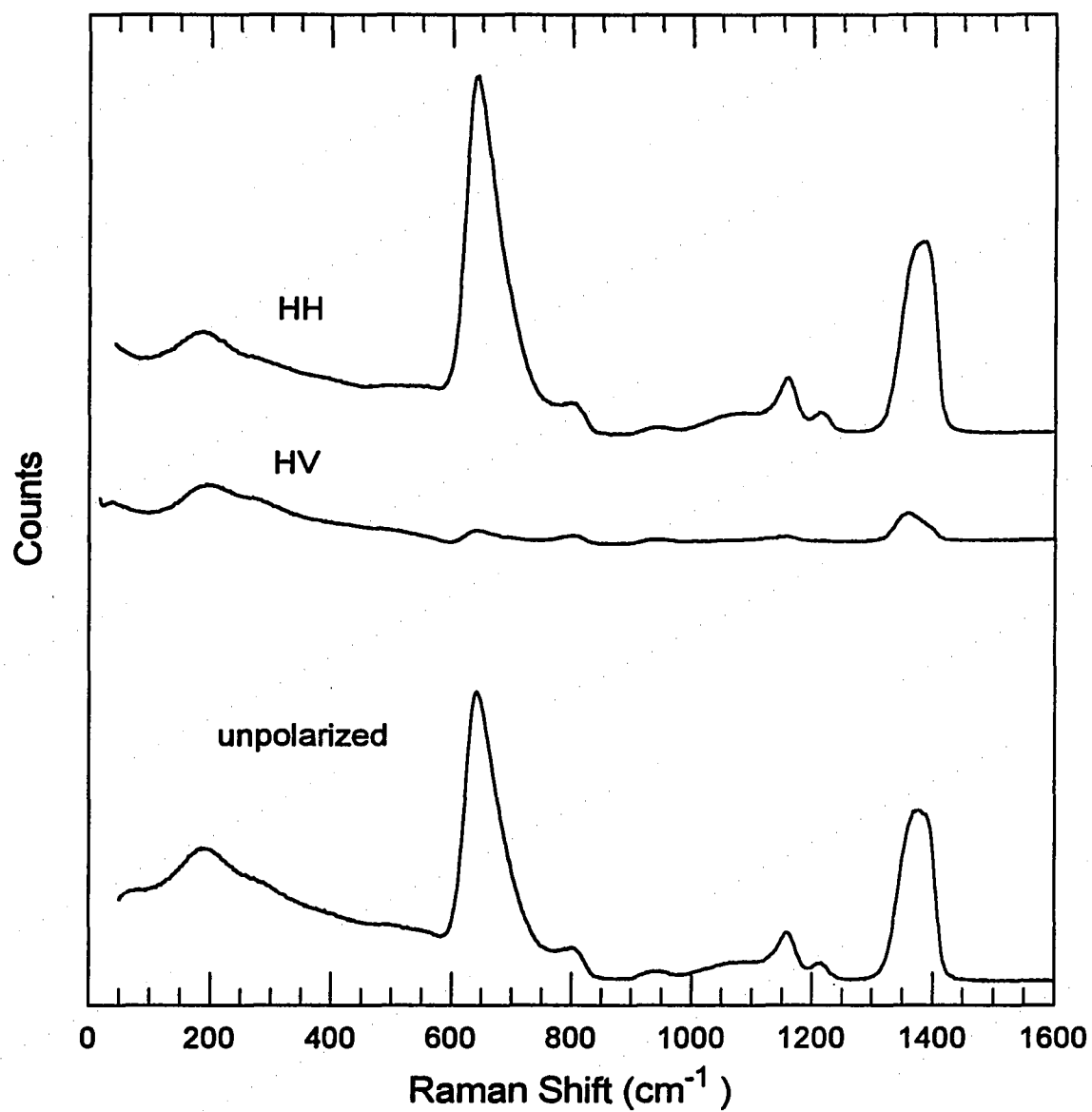


Figure C.28 The unpolarized, and HH polarized Raman spectrum of 0.10 Na₂O + 0.90 P₂O₅ glass.

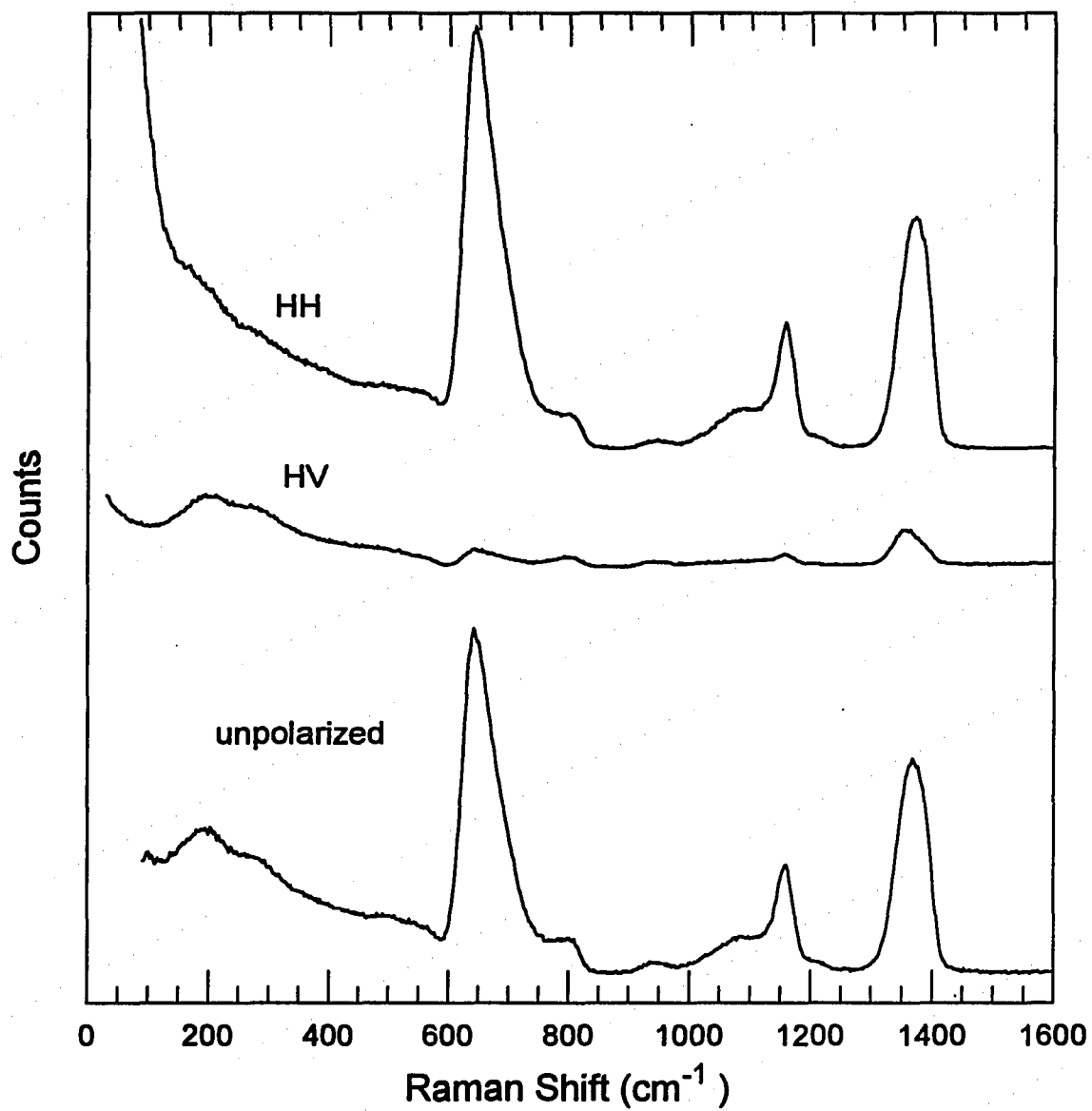


Figure C.29 The unpolarized, and HH polarized Raman spectrum of 0.15 Na₂O + 0.85 P₂O₅ glass.

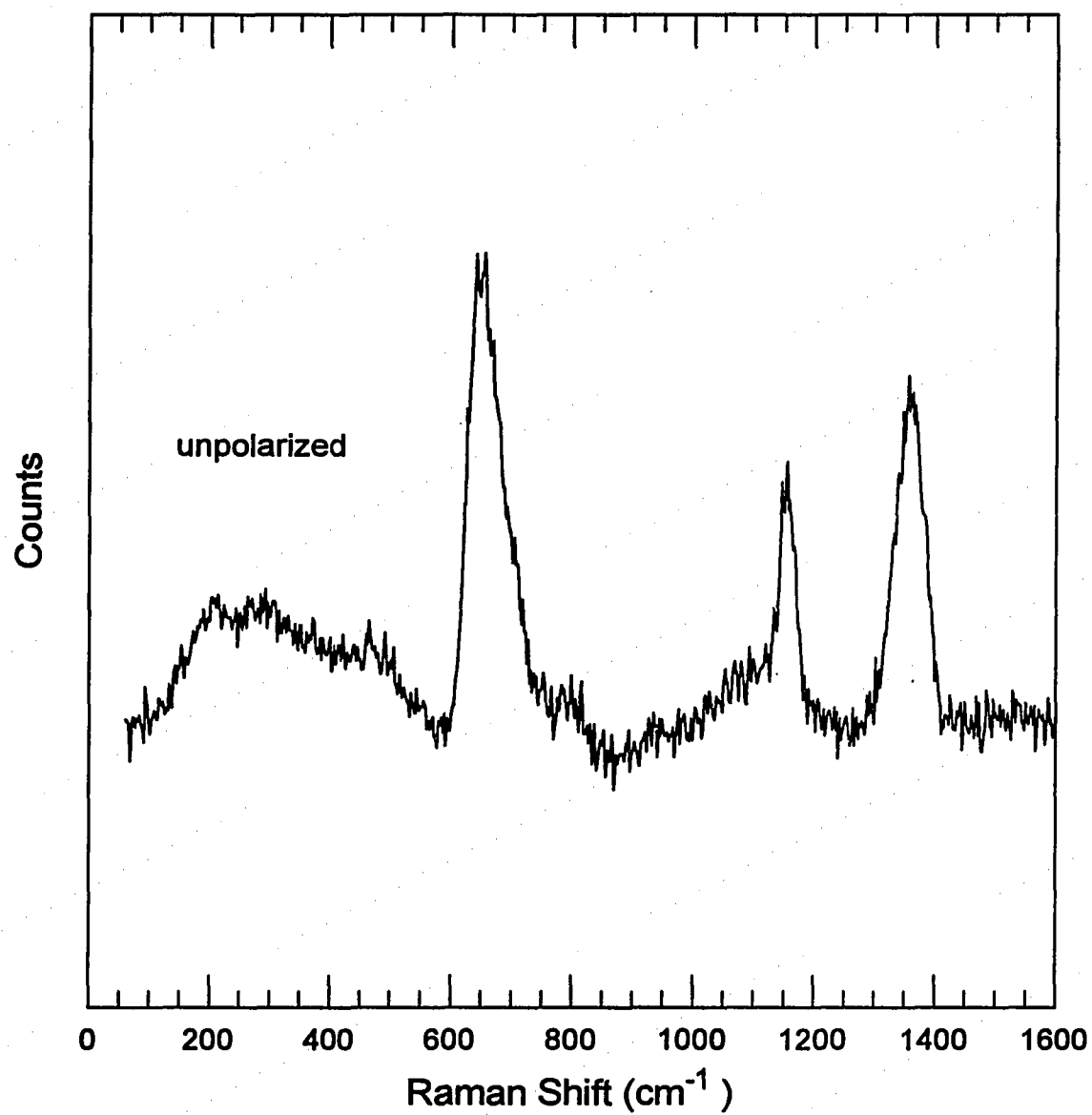


Figure C.30 The unpolarized Raman spectrum of 0.20 Na₂O + 0.80 P₂O₅ glass.

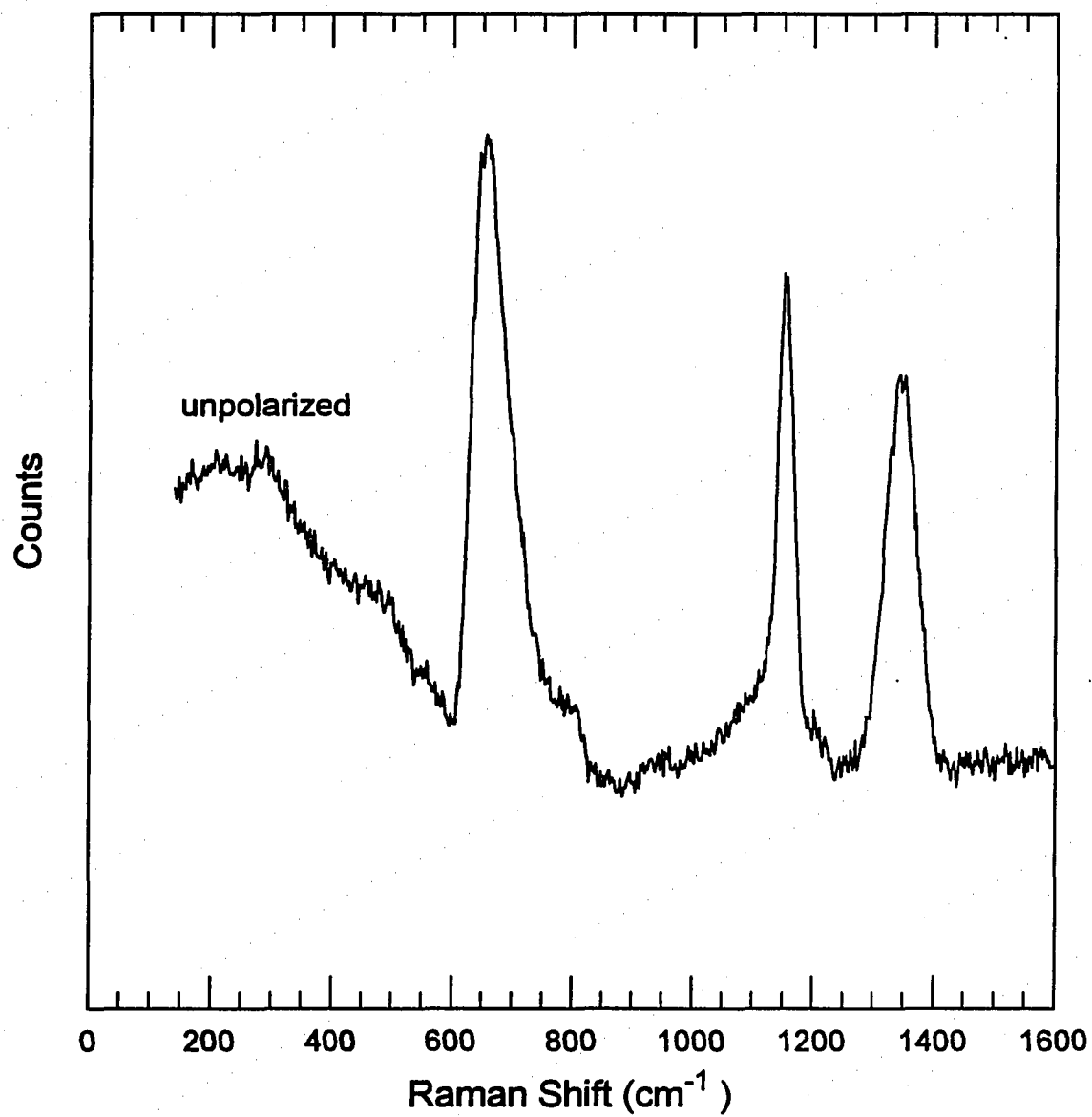


Figure C.31 The unpolarized Raman spectrum of 0.25 Na₂O + 0.75 P₂O₅ glass.

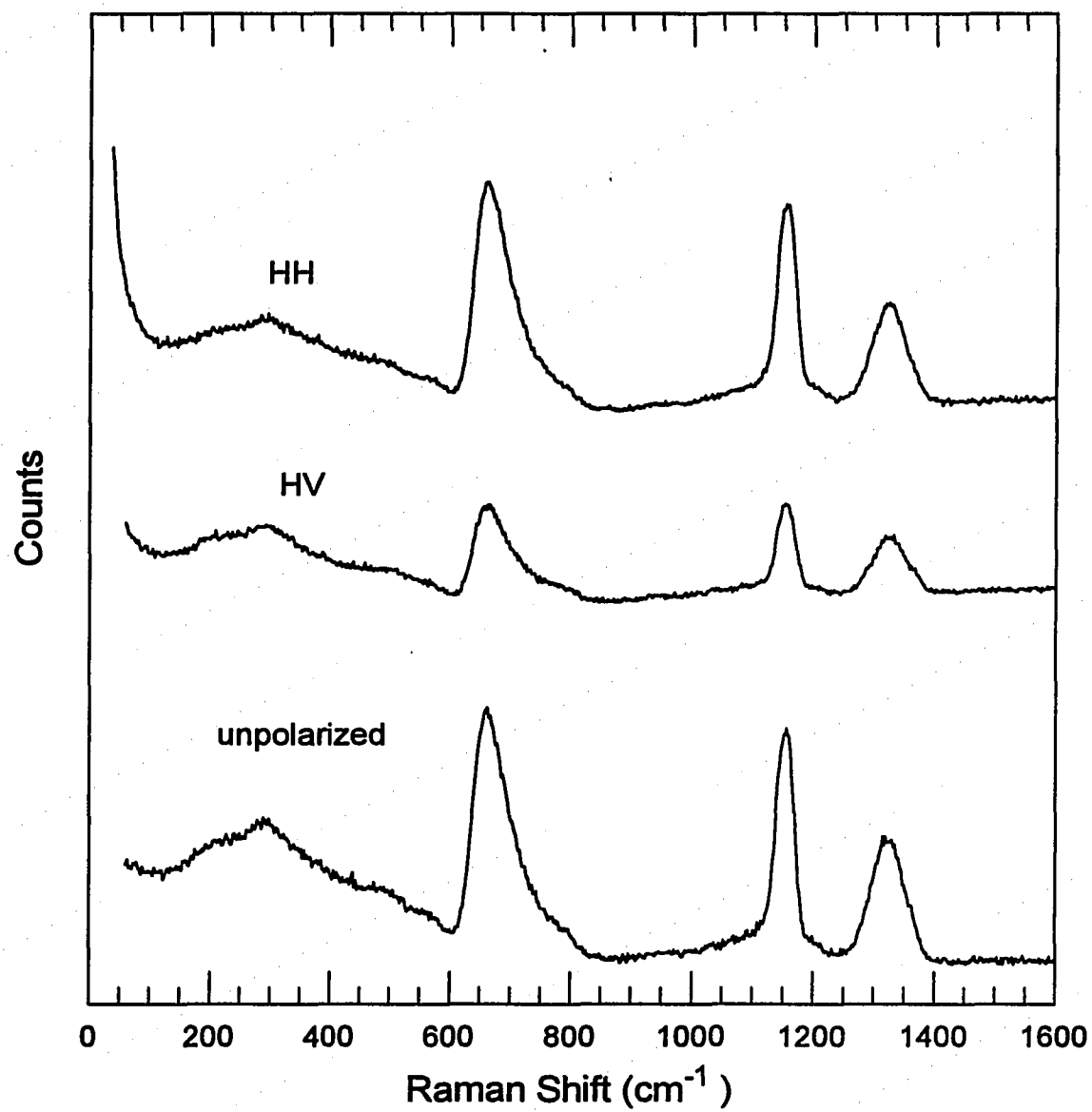


Figure C.32 The unpolarized Raman spectrum of 0.30 Na₂O + 0.70 P₂O₅ glass.

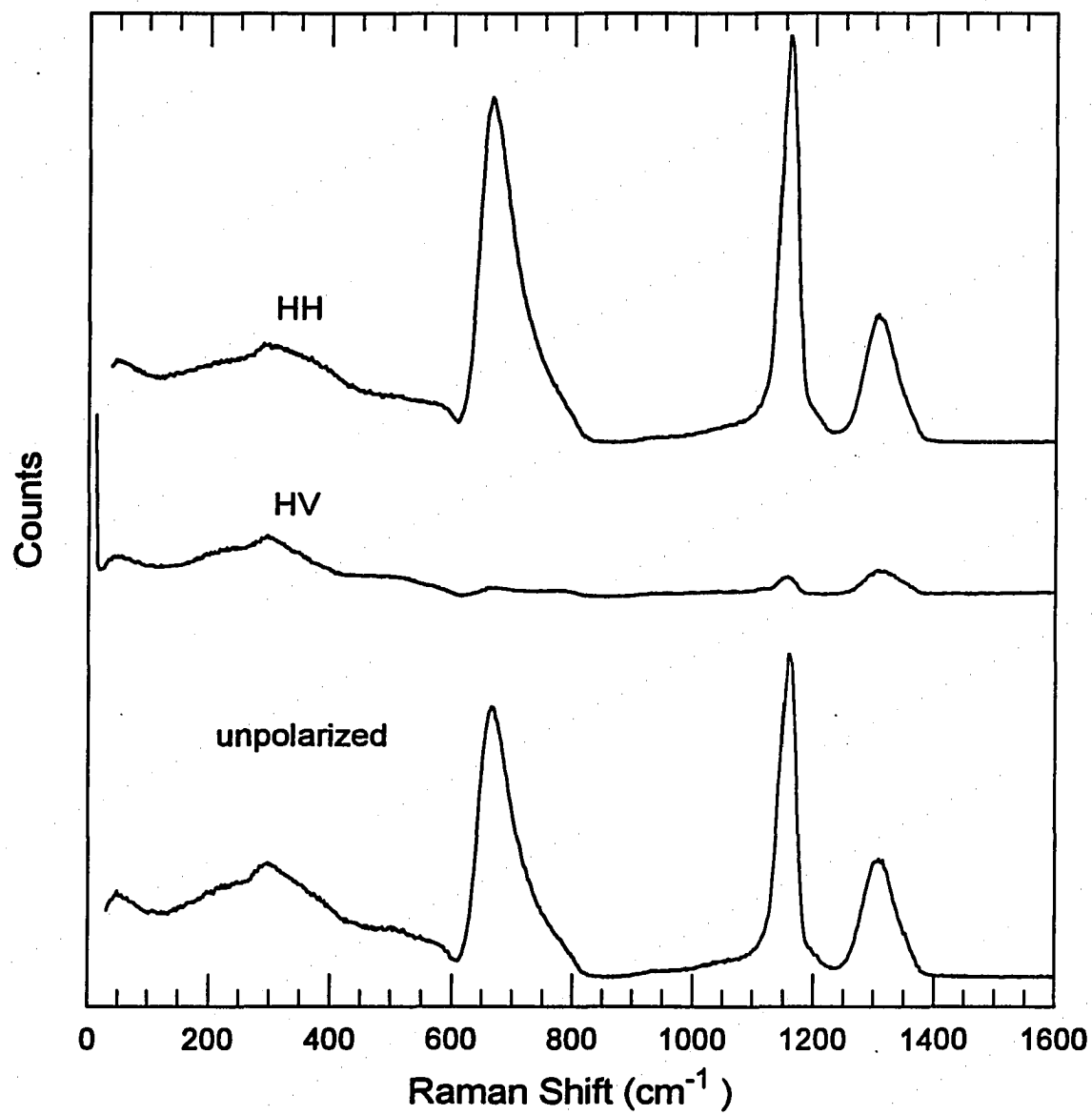


Figure C.33 The unpolarized Raman spectrum of 0.35 Na₂O + 0.65 P₂O₅ glass.

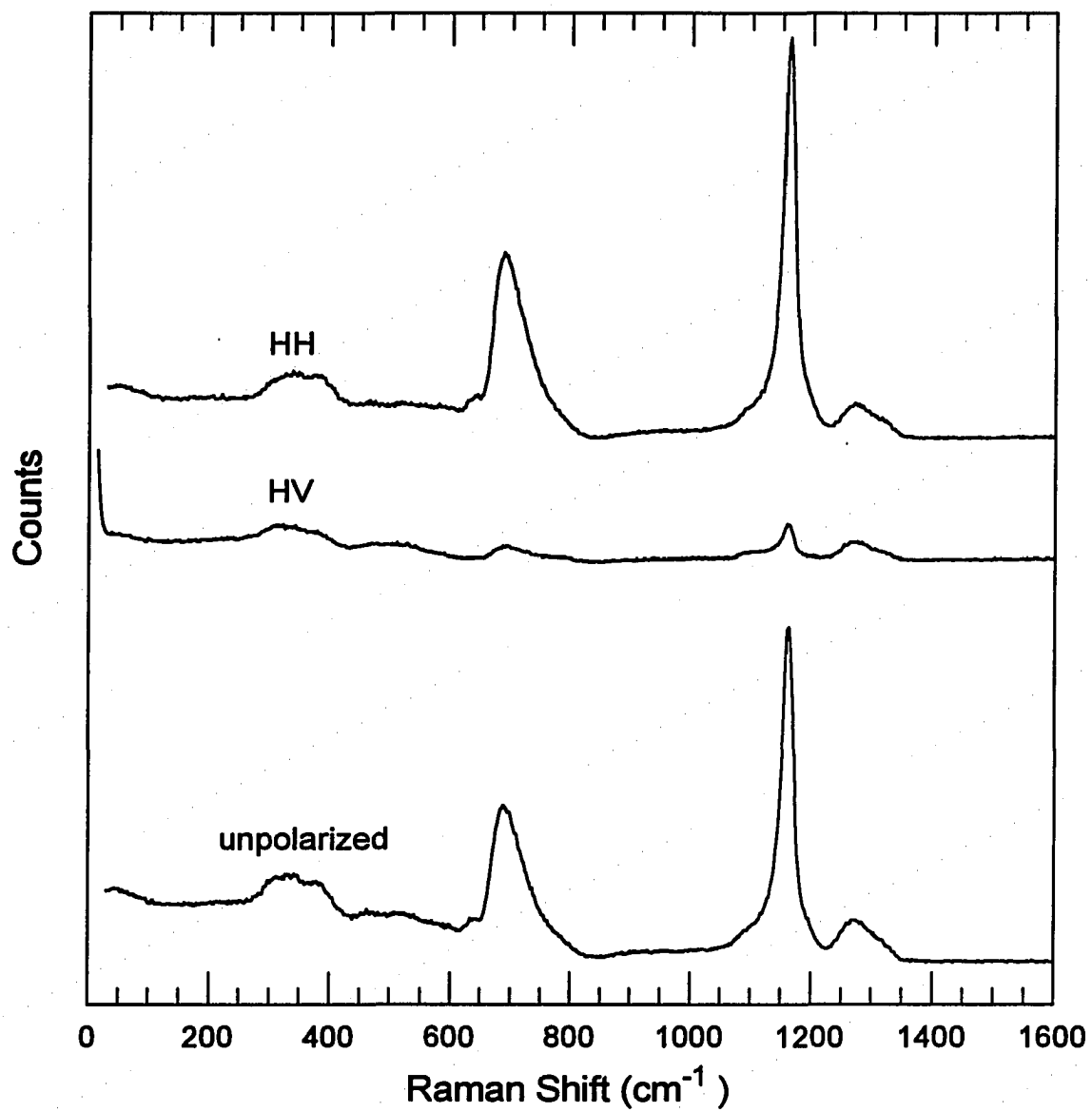


Figure C.34 The unpolarized Raman spectrum of 0.45 Na₂O + 0.55 P₂O₅ glass.

**APPENDIX D: THE ^{31}P MAS-NMR SPECTRUM OF ALKALI
ULTRA-PHOSPHATE GLASSES**

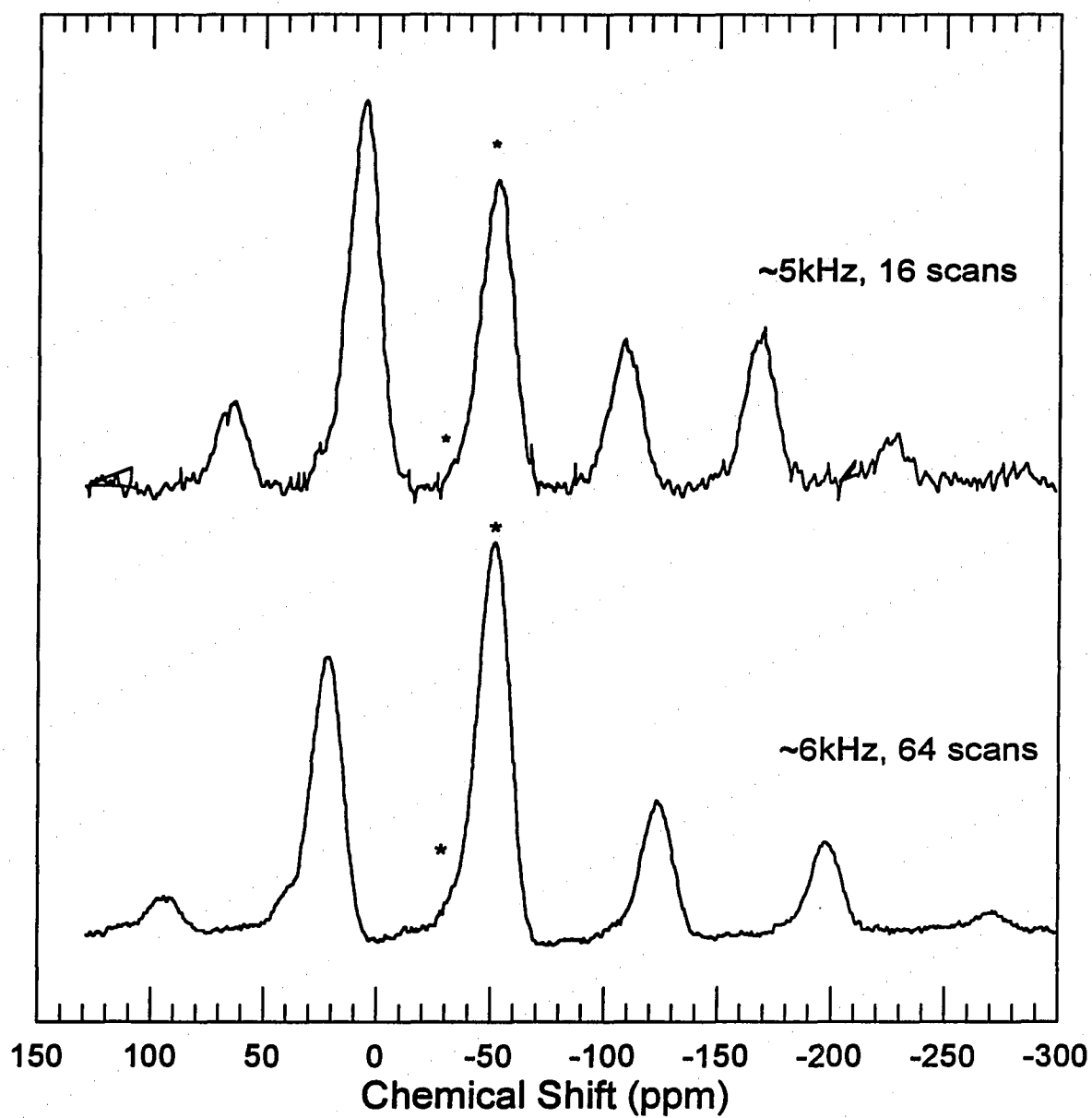


Figure D.35 The ^{31}P MAS-NMR spectrum of the 0.05 Li_2O + 0.95 P_2O_5 glass composition. The spectrum were obtained at two different spinning speeds to identify spinning sidebands. Isotropic chemical shifts are marked with asterisks (*), while the remaining peaks are spinning sidebands..

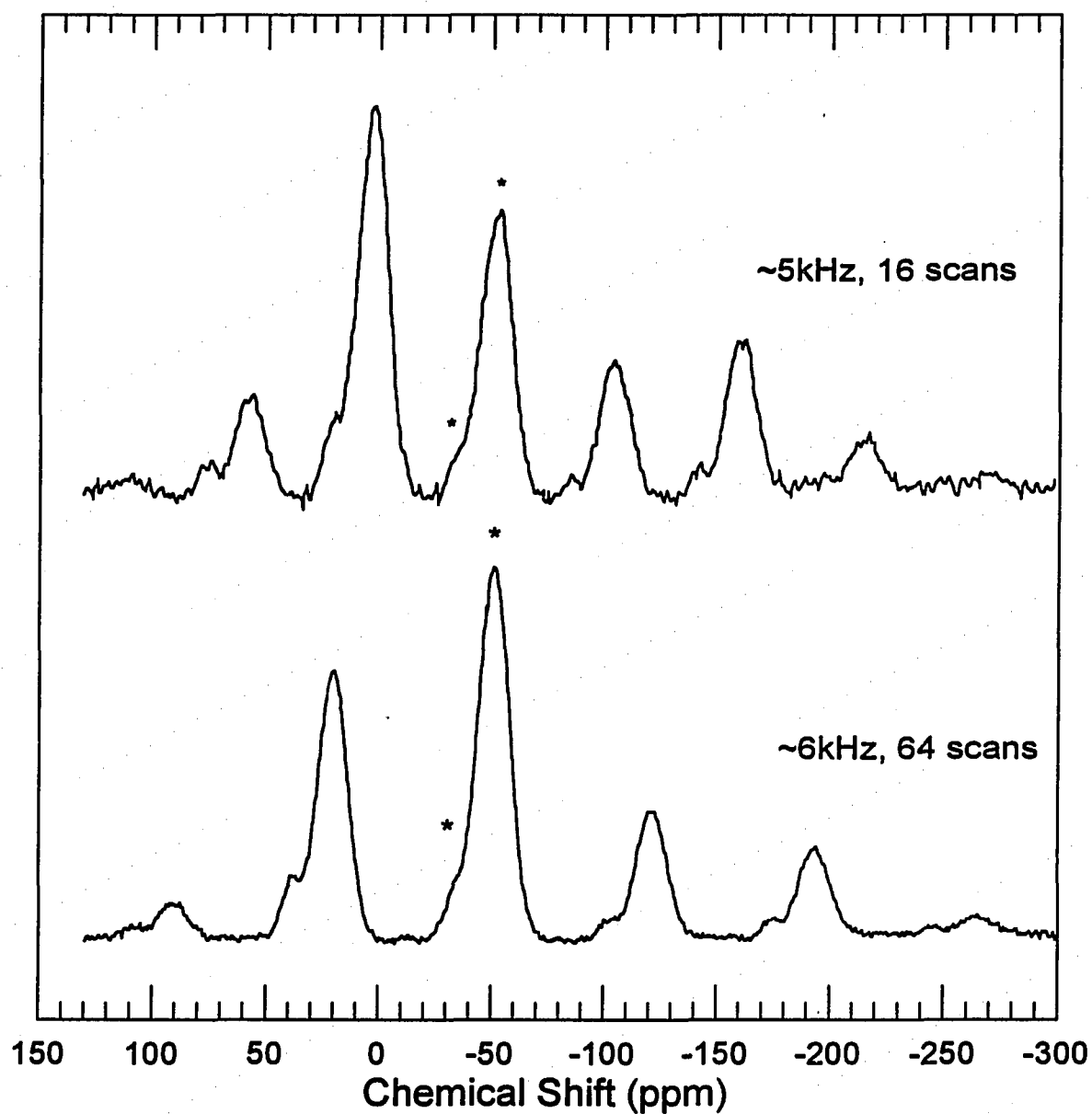


Figure D.36 The ^{31}P MAS-NMR spectrum of the $0.10 \text{ Li}_2\text{O} + 0.90 \text{ P}_2\text{O}_5$ glass composition. The spectrum were obtained at two different spinning speeds to identify spinning sidebands. Isotropic chemical shifts are marked with asterisks (*), while the remaining peaks are spinning sidebands..

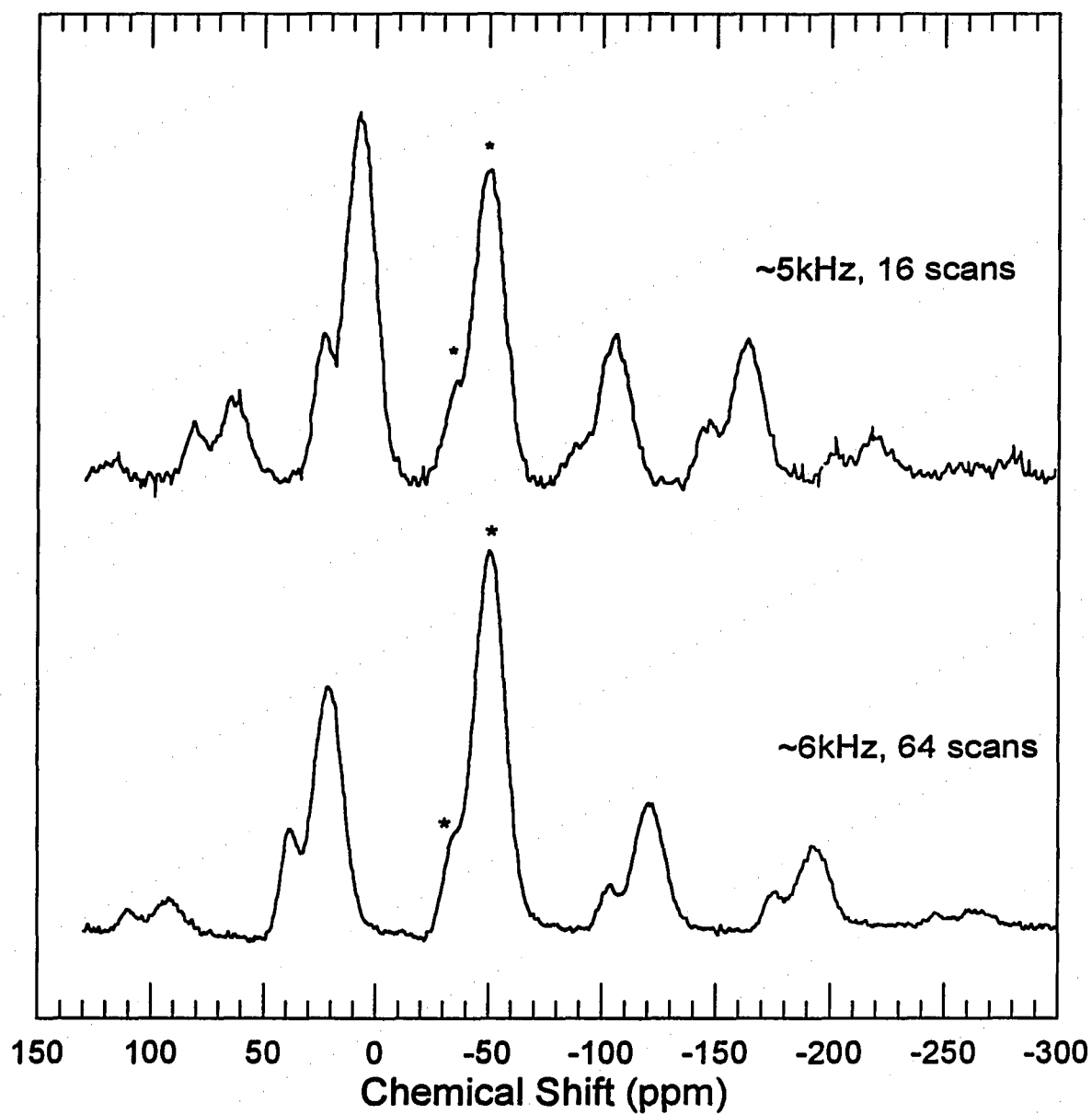


Figure D.37 The ^{31}P MAS-NMR spectrum of the $0.15 \text{ Li}_2\text{O} + 0.85 \text{ P}_2\text{O}_5$ glass composition. The spectrum were obtained at two different spinning speeds to identify spinning sidebands. Isotropic chemical shifts are marked with asterisks (*), while the remaining peaks are spinning sidebands..

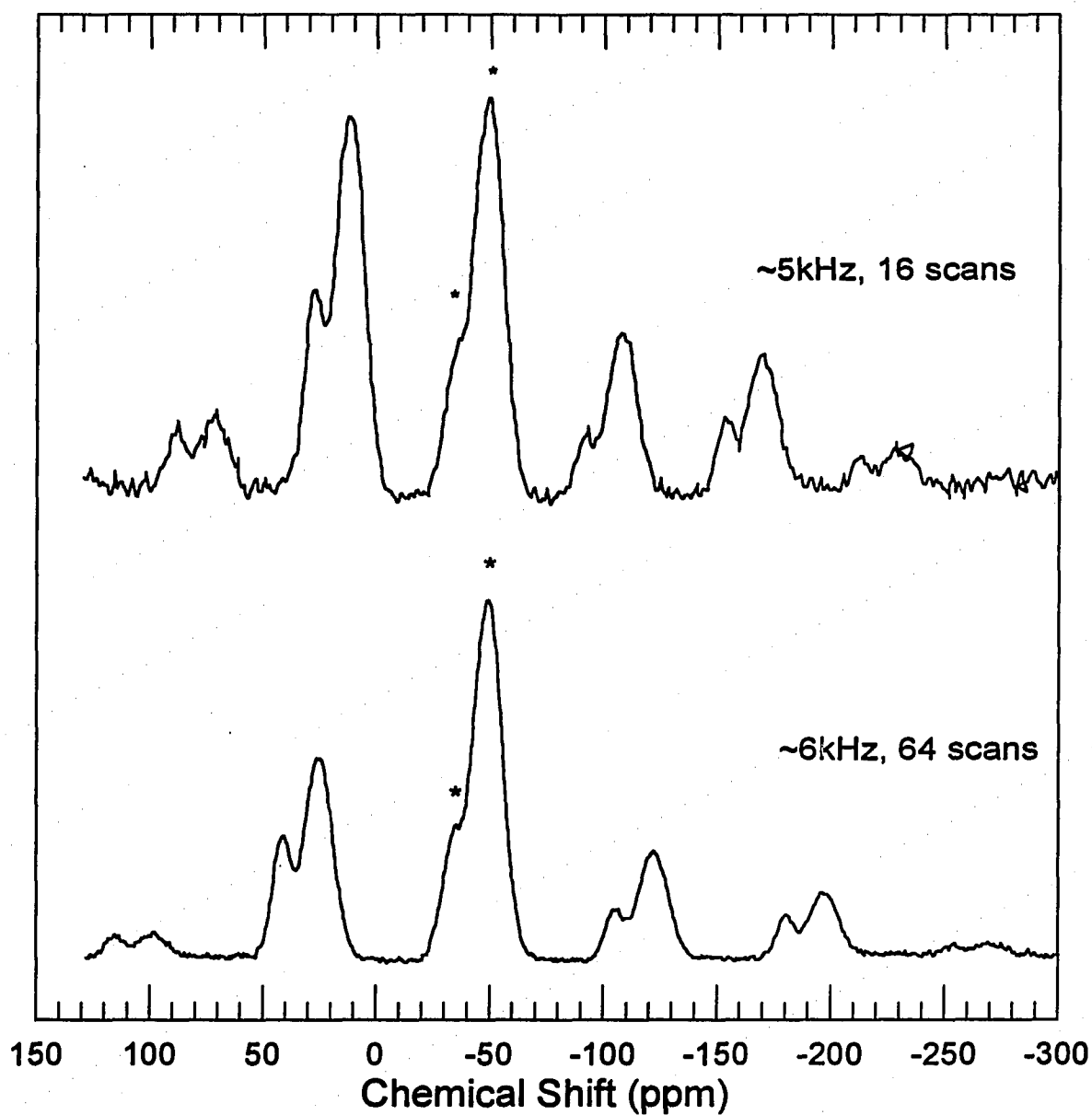


Figure D.38 The ^{31}P MAS-NMR spectrum of the $0.20 \text{ Li}_2\text{O} + 0.80 \text{ P}_2\text{O}_5$ glass composition. The spectrum were obtained at two different spinning speeds to identify spinning sidebands. Isotropic chemical shifts are marked with asterisks (*), while the remaining peaks are spinning sidebands.

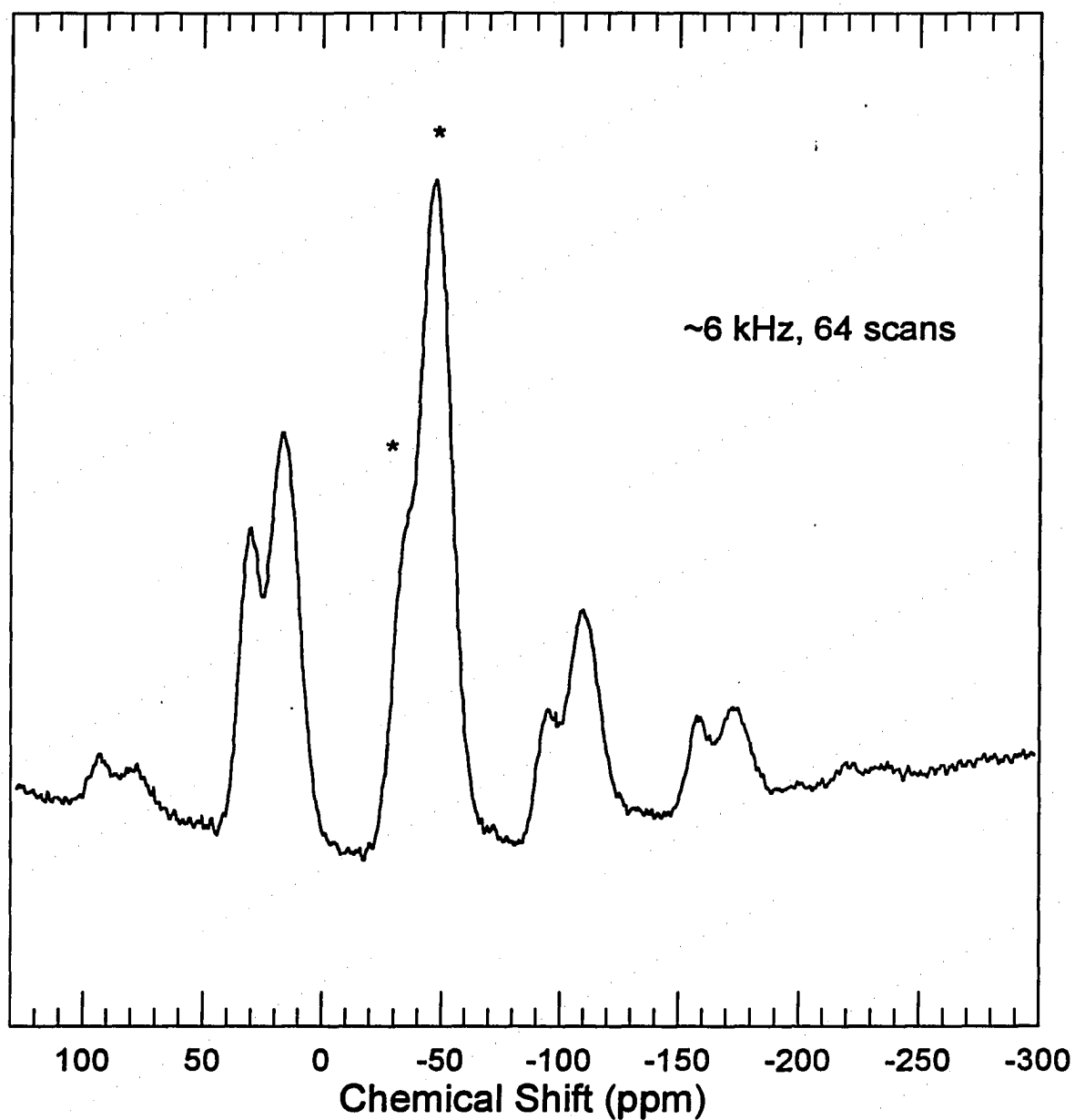


Figure D.39 The ^{31}P MAS-NMR spectrum of the 0.25 Li_2O + 0.75 P_2O_5 glass composition. Isotropic chemical shifts are marked with asterisks (*), while the remaining peaks are spinning sidebands.

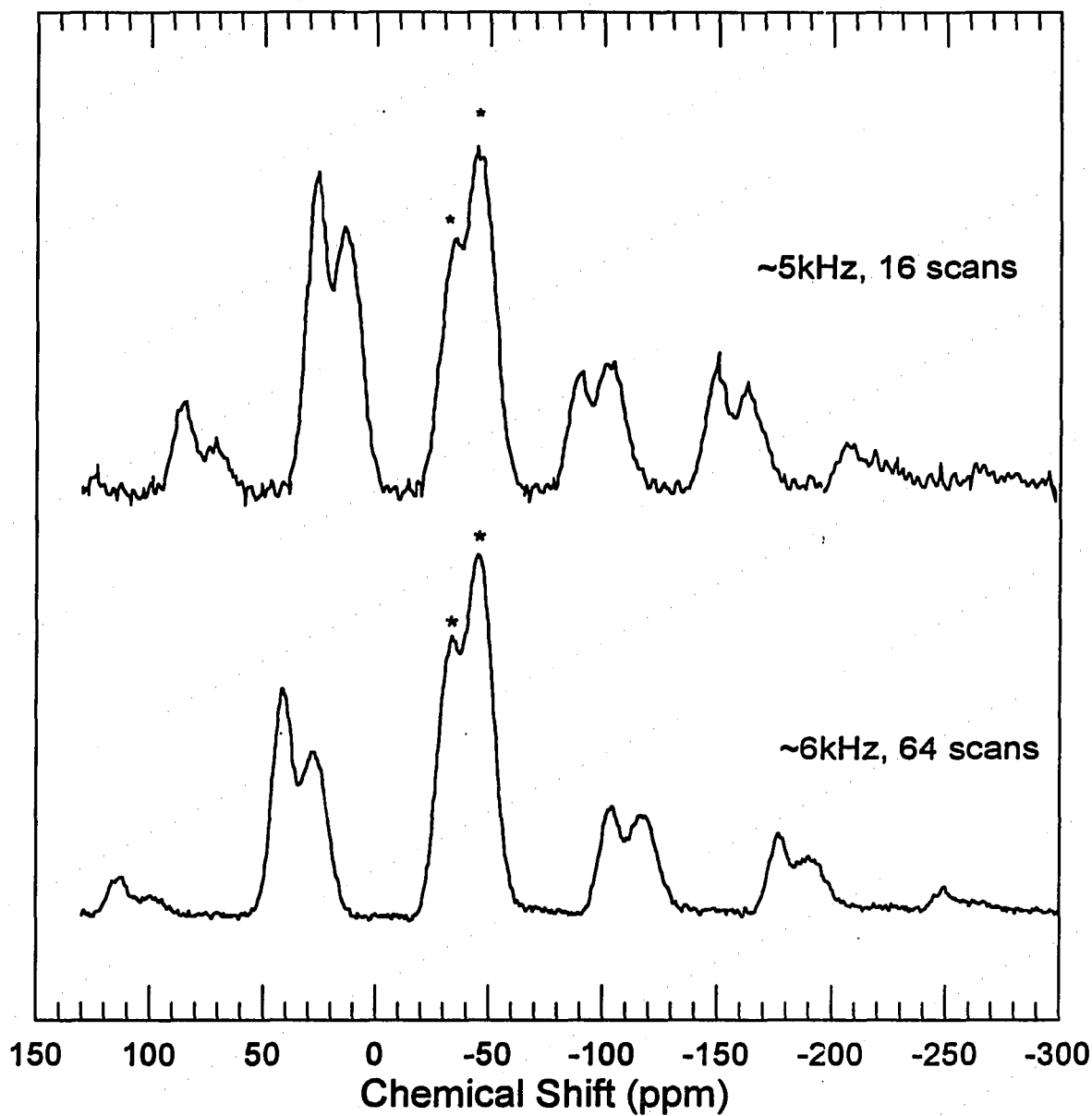


Figure D.40 The ^{31}P MAS-NMR spectrum of the $0.30 \text{ Li}_2\text{O} + 0.70 \text{ P}_2\text{O}_5$ glass composition. The spectrum were obtained at two different spinning speeds to identify spinning sidebands. Isotropic chemical shifts are marked with asterisks (*), while the remaining peaks are spinning sidebands.

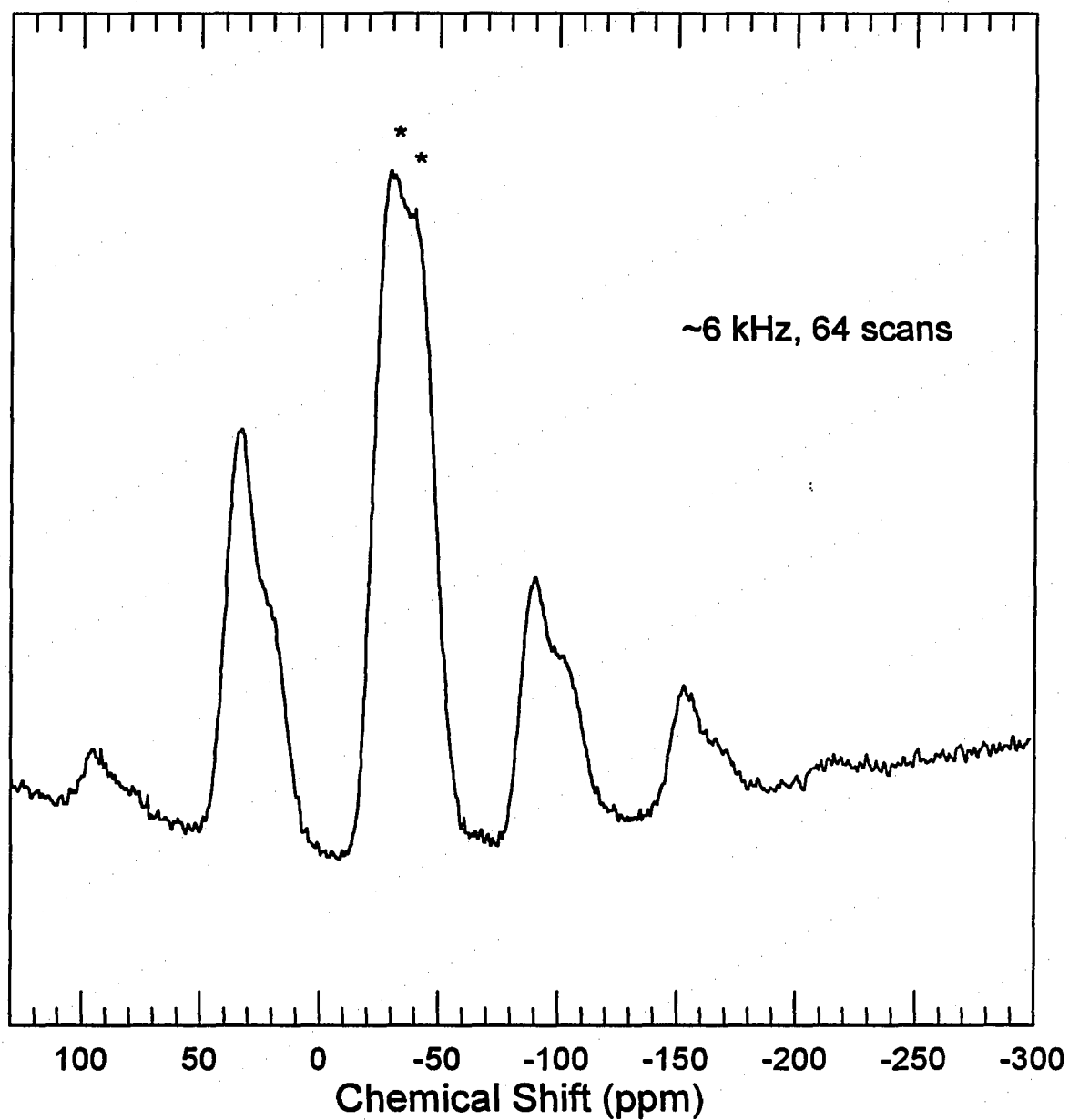


Figure D.41 The ^{31}P MAS-NMR spectrum of the $0.35 \text{ Li}_2\text{O} + 0.65 \text{ P}_2\text{O}_5$ glass composition. Isotropic chemical shifts are marked with asterisks (*), while the remaining peaks are spinning sidebands.

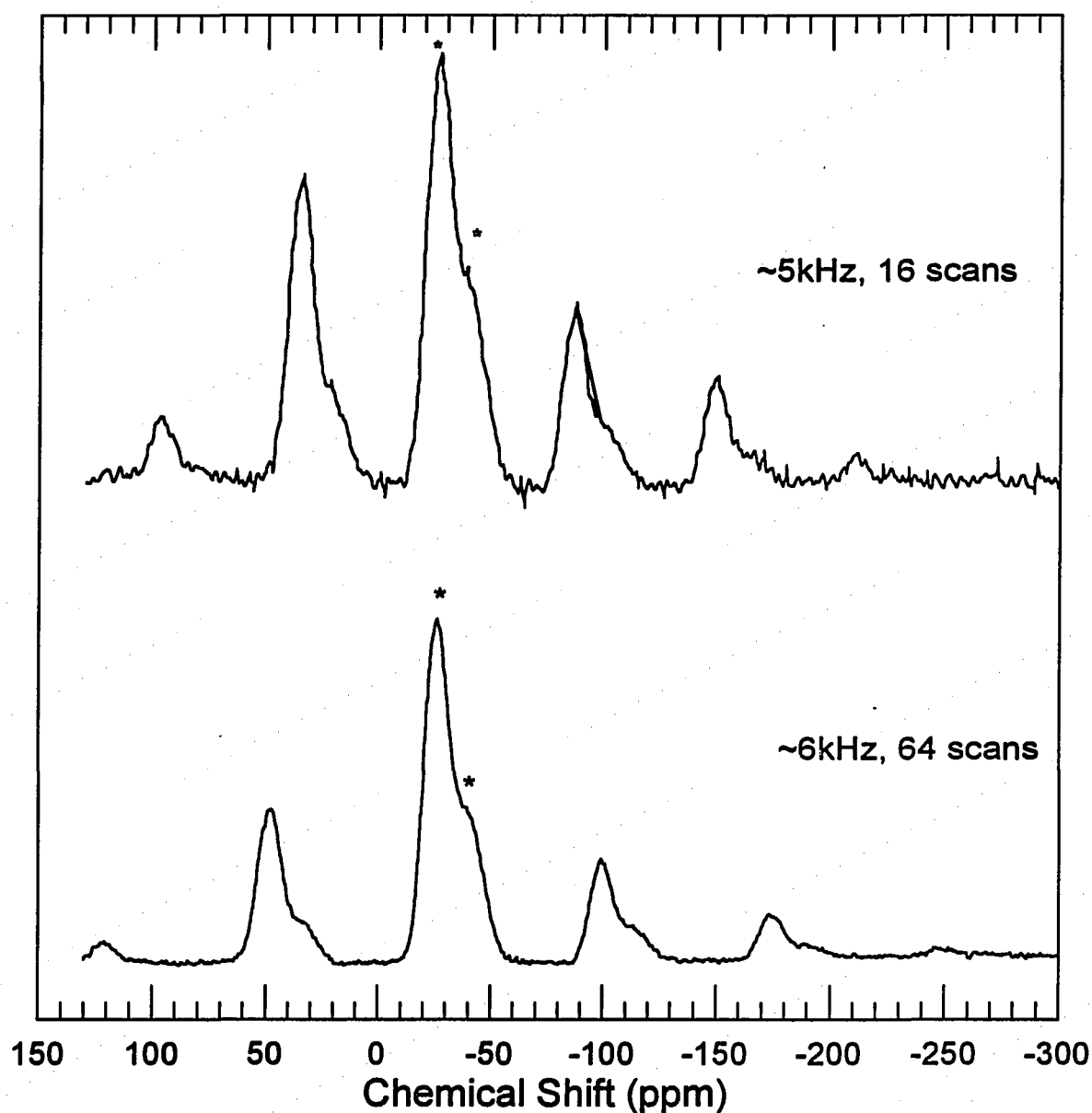


Figure D.42 The ^{31}P MAS-NMR spectrum of the $0.40 \text{ Li}_2\text{O} + 0.60 \text{ P}_2\text{O}_5$ glass composition. The spectrum were obtained at two different spinning speeds to identify spinning sidebands. Isotropic chemical shifts are marked with asterisks (*), while the remaining peaks are spinning sidebands.

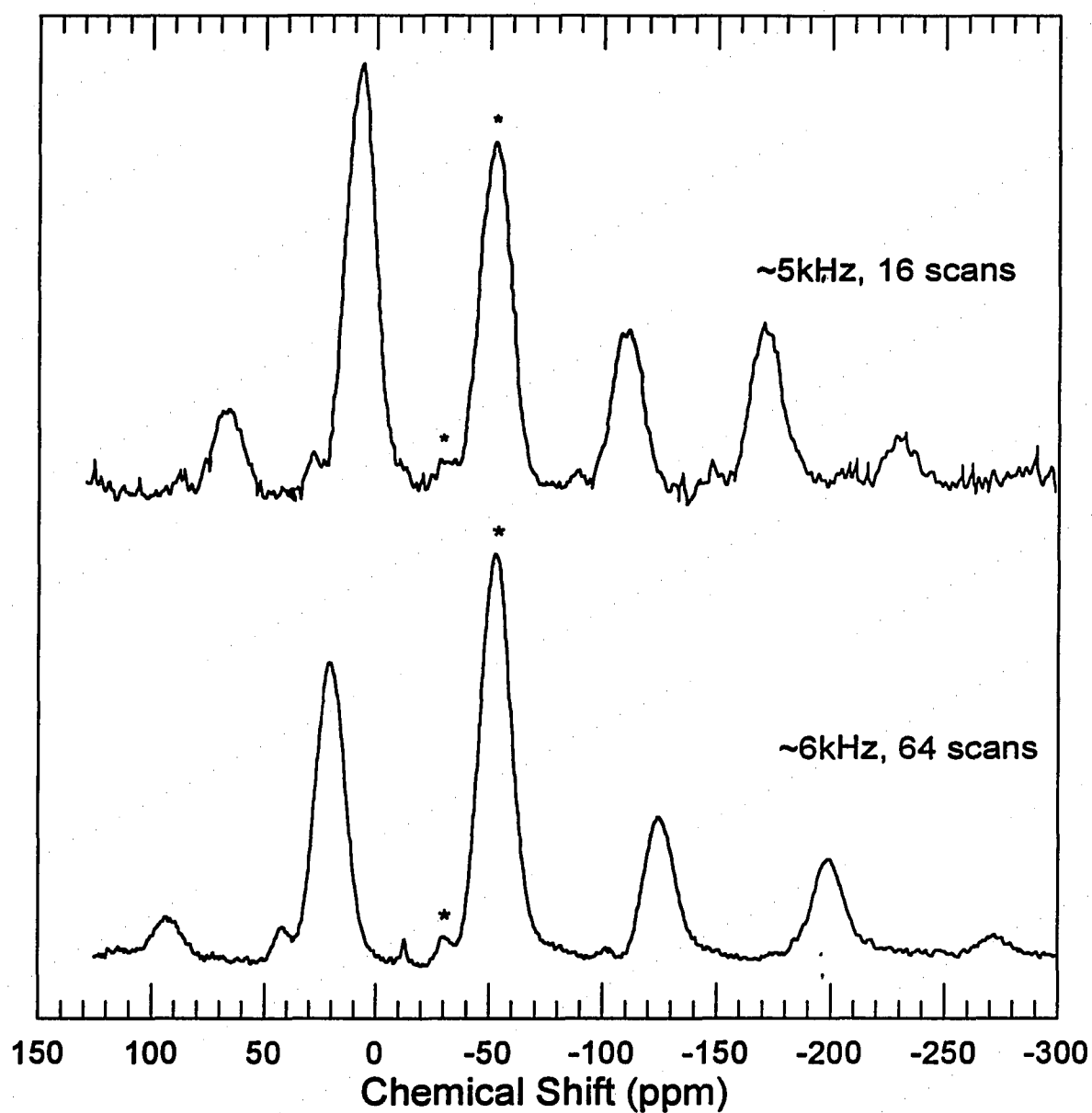


Figure D.43 The ^{31}P MAS-NMR spectrum of the $0.05 \text{ Na}_2\text{O} + 0.95 \text{ P}_2\text{O}_5$ glass composition. The spectrum were obtained at two different spinning speeds to identify spinning sidebands. Isotropic chemical shifts are marked with asterisks (*), while the remaining peaks are spinning sidebands

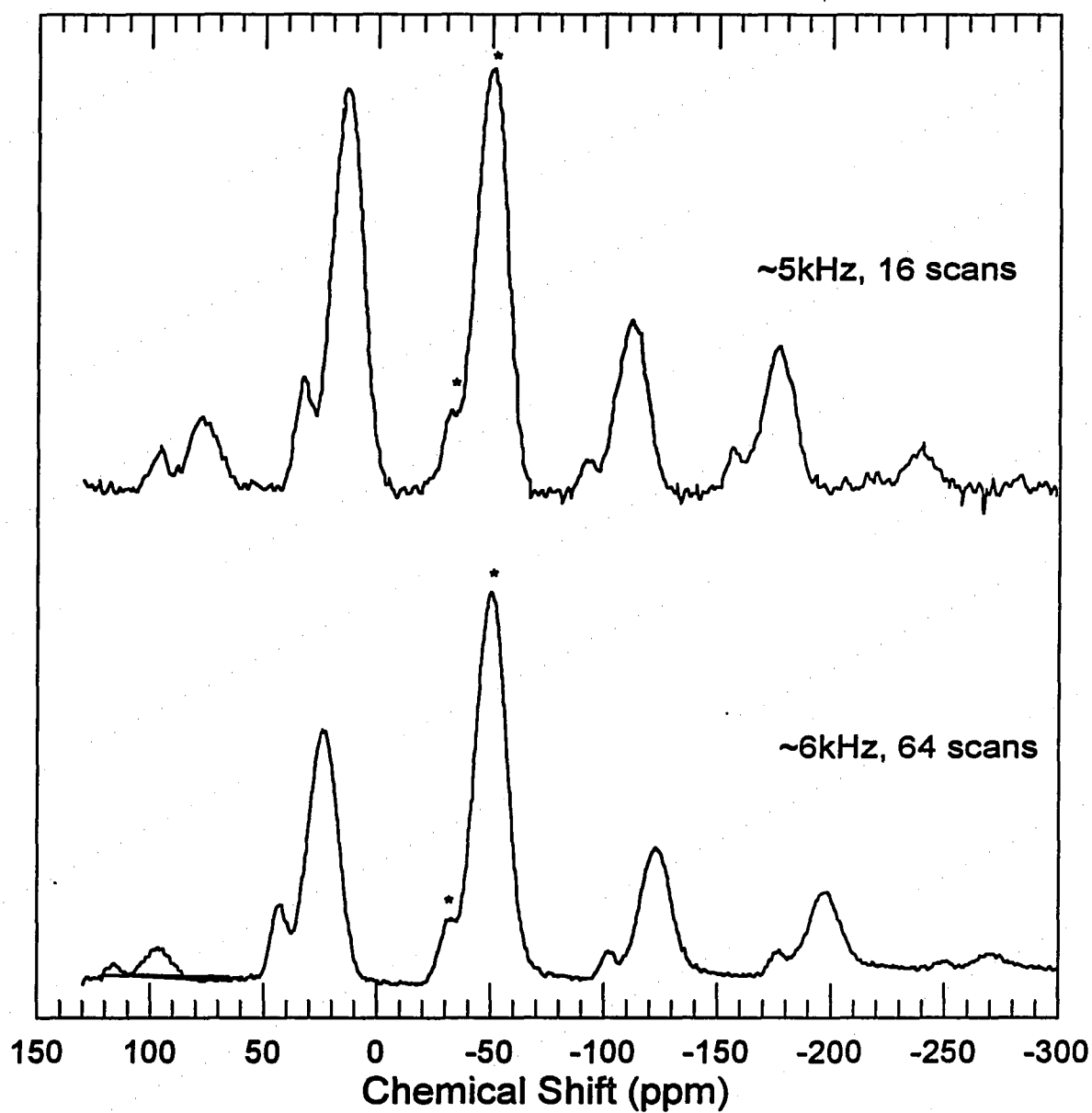


Figure D.44 The ^{31}P MAS-NMR spectrum of the 0.10 Na_2O + 0.90 P_2O_5 glass composition. The spectrum were obtained at two different spinning speeds to identify spinning sidebands. Isotropic chemical shifts are marked with asterisks (*), while the remaining peaks are spinning sidebands.

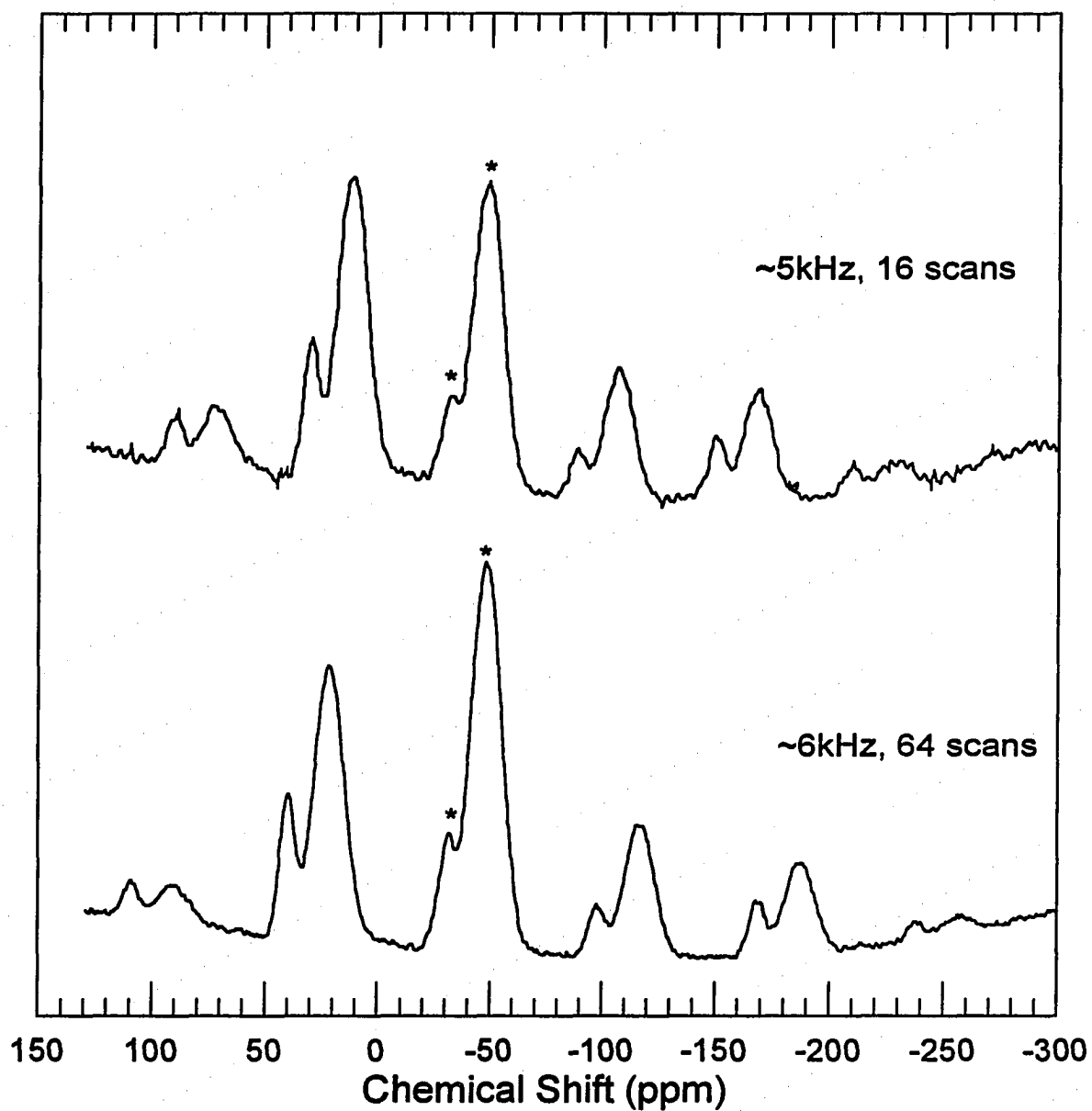


Figure D.45 The ^{31}P MAS-NMR spectrum of the $0.15 \text{ Na}_2\text{O} + 0.85 \text{ P}_2\text{O}_5$ glass composition. The spectrum were obtained at two different spinning speeds to identify spinning sidebands. Isotropic chemical shifts are marked with asterisks (*), while the remaining peaks are spinning sidebands

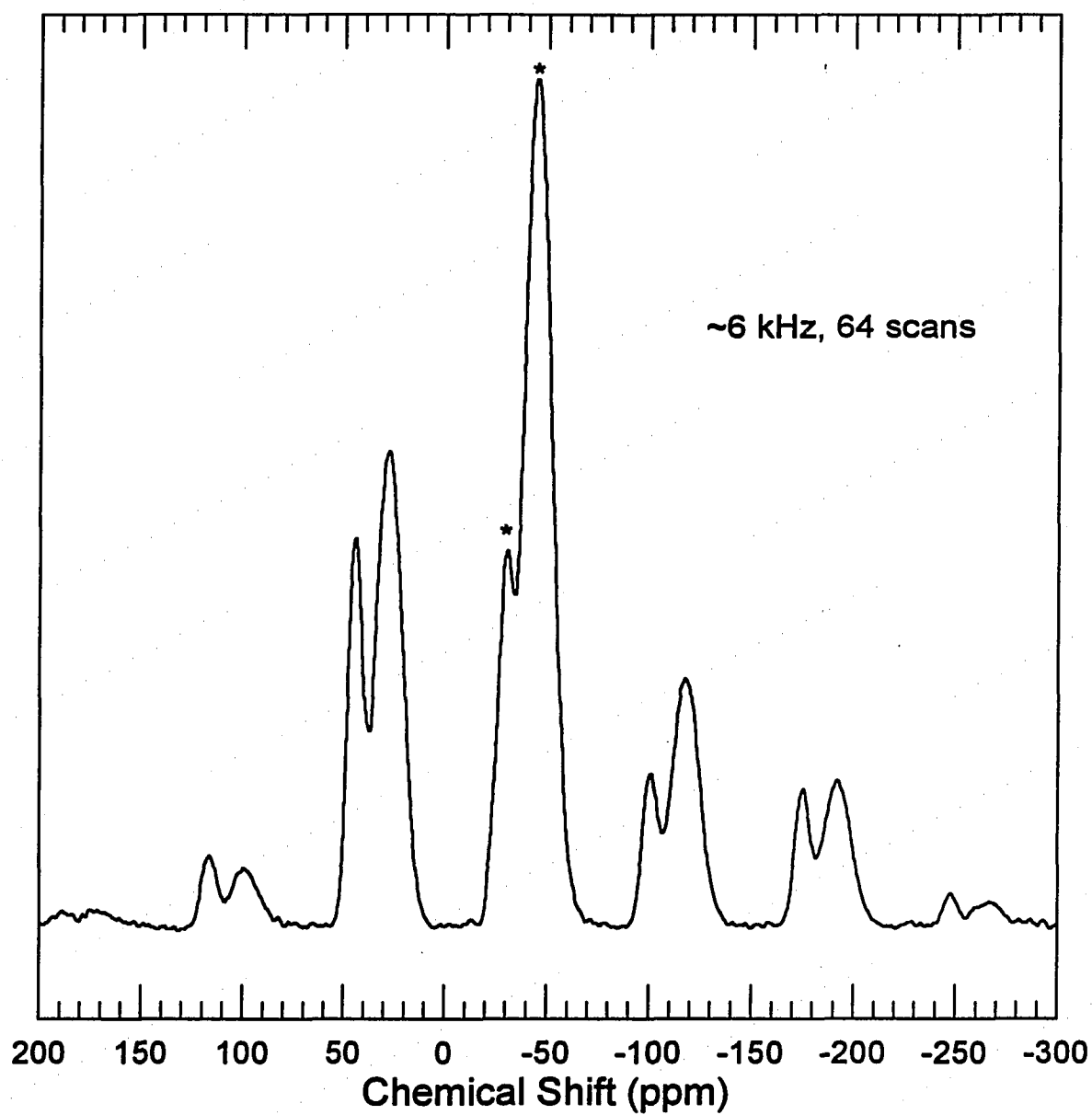


Figure D.46 The ^{31}P MAS-NMR spectrum of the 0.20 Na_2O + 0.80 P_2O_5 glass composition. Isotropic chemical shifts are marked with asterisks (*), while the remaining peaks are spinning sidebands

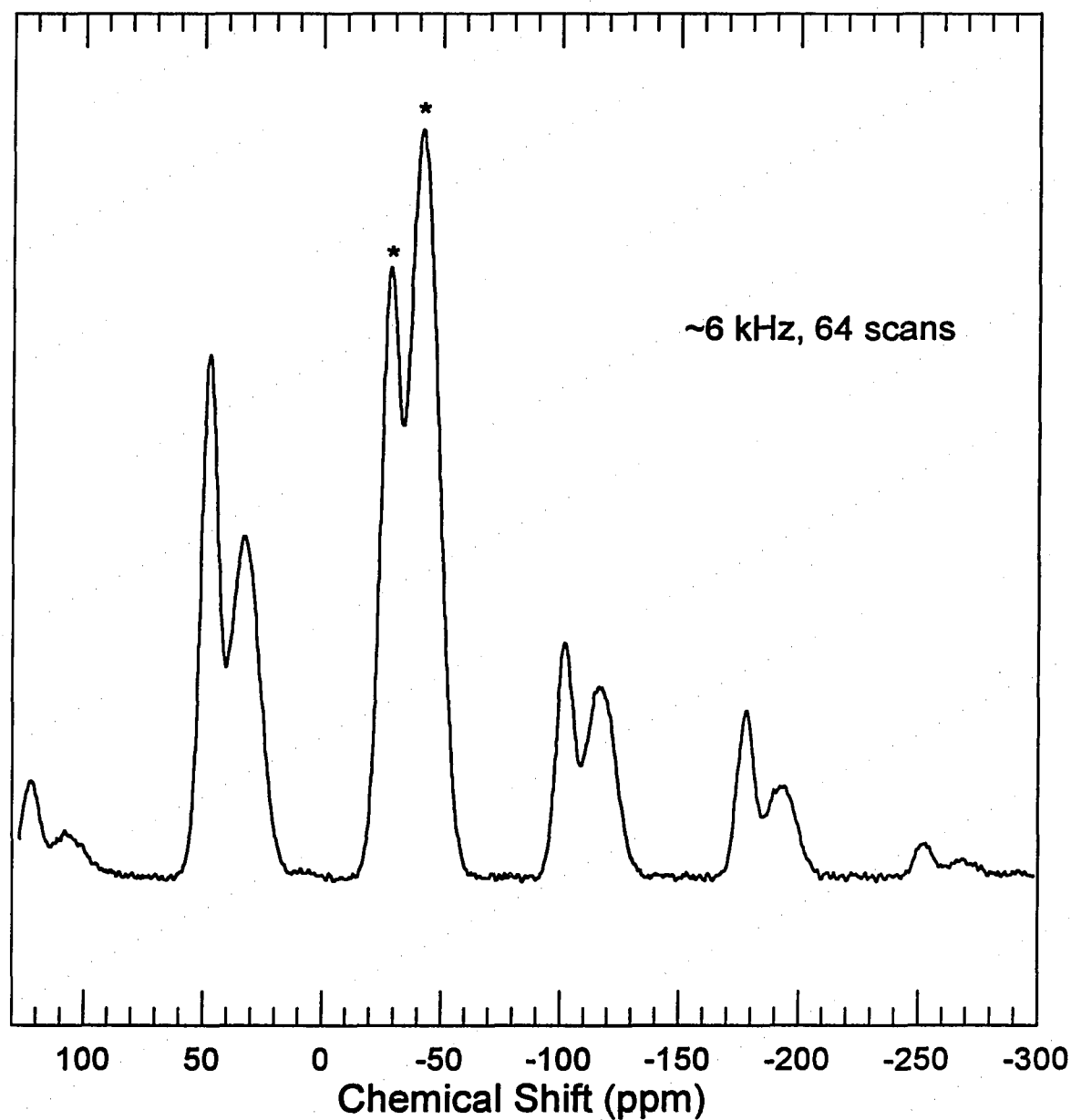


Figure D.47 The ^{31}P MAS-NMR spectrum of the $0.25 \text{ Na}_2\text{O} + 0.75 \text{ P}_2\text{O}_5$ glass composition. Isotropic chemical shifts are marked with asterisks (*), while the remaining peaks are spinning sidebands.

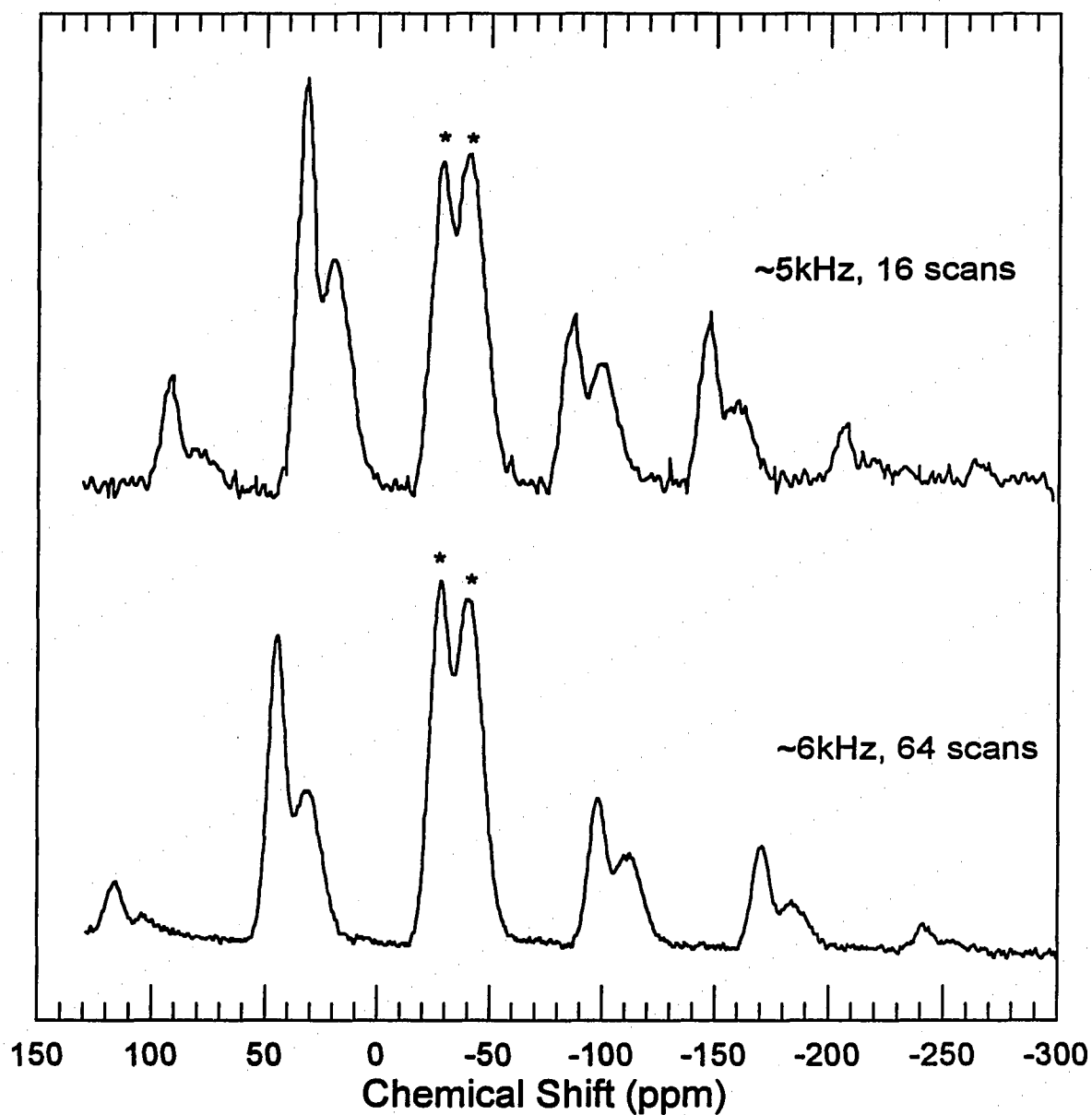


Figure D.48 The ^{31}P MAS-NMR spectrum of the 0.30 Na_2O + 0.70 P_2O_5 glass composition. The spectrum were obtained at two different spinning speeds to identify spinning sidebands. Isotropic chemical shifts are marked with asterisks (*), while the remaining peaks are spinning sidebands

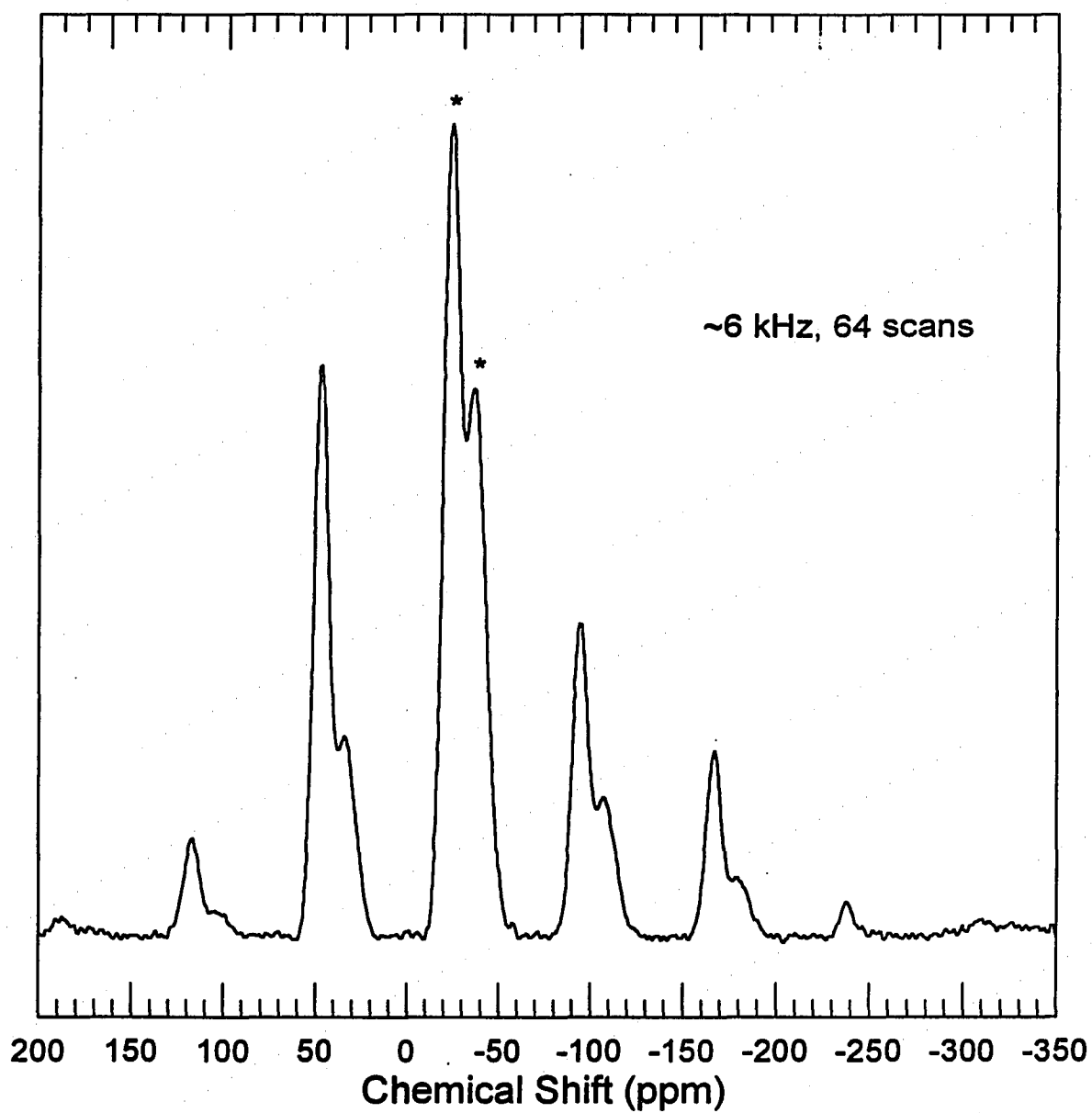


Figure D.49 The ^{31}P MAS-NMR spectrum of the $0.35 \text{ Na}_2\text{O} + 0.65 \text{ P}_2\text{O}_5$ glass composition. Isotropic chemical shifts are marked with asterisks (*), while the remaining peaks are spinning sidebands

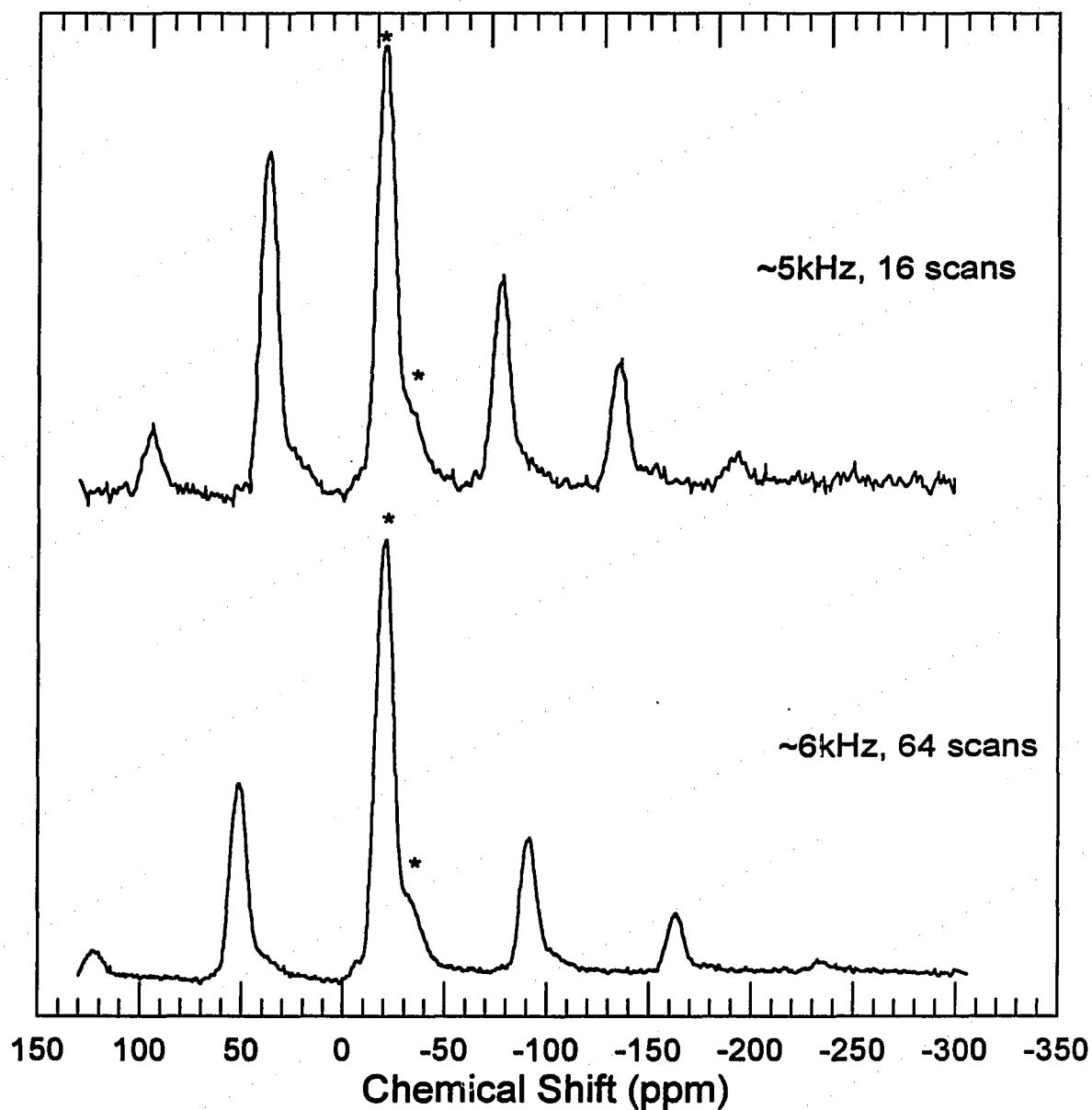


Figure D.50 The ^{31}P MAS-NMR spectrum of the $0.45 \text{ Na}_2\text{O} + 0.55 \text{ P}_2\text{O}_5$ glass composition. The spectrum were obtained at two different spinning speeds to identify spinning sidebands. Isotropic chemical shifts are marked with asterisks (*), while the remaining peaks are spinning sidebands

APPENDIX E: COMPUTER PROGRAM "TN"

```

CHARACTER*60 TITLE,TITLE1
CHARACTER*15 INFILE,OUTFILE
REAL LNTAU, LNTAU1
DIMENSION TF(600),TAU(600),E(600),TRED(600),TR(600),CP(600)
DIMENSION TIME(600),P(800),A(3,5),AC(3,5),X(200),B(3),Z(200)
DIMENSION Y(200), BV(3), BMIN(3), BMAX(3), FV(3), DV(3)
DIMENSION HD(20), T(600), T1(200), TRH(600), S(600)

```

```

LOGICAL QUES

```

```

EXTERNAL FUNC

```

```

COMMON TF,TAU,E,TRED,TR,TIME,PR,H,T,QC,DT
COMMON TIMEA,QH,TANEAL,AA,TSTART,S,T1

```

```

5  PRINT *, 'ENTER THE NAME OF THE DATA INPUT FILE'
   READ '(A)', INFILE
   OPEN (UNIT=10, FILE=INFILE, STATUS='OLD',ACCESS='SEQUENTIAL',
+    FORM='FORMATTED',ERR=5)
2  PRINT *, 'ENTER THE NAME OF THE DESIRED OUTPUT FILE'
   READ '(A)', OUTFILE
   OPEN (UNIT=3, FILE=OUTFILE, STATUS='NEW',ERR=2)

```

```

READ (10,1111) TITLE
READ (10,1111) TITLE1

```

```

1111  FORMAT (A)

```

```

READ (10,*)
READ (10,*) TIMEA,TANEAL,QH,QC,TSTART,AA,B(1),BETA,XX,DT
READ (10,*)
READ (10,*)

```

```

COUNT=1

```

```

1  READ (10,*,END=3) Y(COUNT)
   COUNT=COUNT+1
   GO TO 1

```

```

3  NN=COUNT-1

```

```

PRINT '(1X,A)', TITLE
PRINT '(1X,A)', TITLE1

```

```
PRINT 1234, COUNT
PRINT 2221, TIMEA
PRINT 3333, TANEAL
PRINT 2222, QH
PRINT 2223, QC
PRINT 2224, TSTART
PRINT 2225, AA
PRINT 2226, B(1)
PRINT 2227, BETA
PRINT 2228, XX
```

```
1231 FORMAT (1X,A)
1232 FORMAT (1X,'DATA FILE =',A)
1234 FORMAT (//,1X,'NUMBER OF POINTS =',F5.0)
2221 FORMAT (1X,'ANNEAL TIME =',F7.2)
2222 FORMAT (1X,'HEATING RATE =',F5.2)
2223 FORMAT (1X,'COOLING RATE =',F5.2)
2224 FORMAT (1X,'STARTING TEMPERATURE =',F7.2)
2225 FORMAT (1X,'ACTIVATION ENTHALPY =',F7.2)
2226 FORMAT (1X,'ESTIMATE OF PRE-EXPONENTIAL =',F7.2)
2227 FORMAT (1X,'ESTIMATE OF BETA =',F7.2)
2228 FORMAT (1X,'ESTIMATE OF X =',F7.2,/)
3333 FORMAT (1X,'ANNEAL TEMPERATURE =',F7.2)
```

NO=3

```
WRITE(NO, 1231), TITLE
WRITE(NO, 1231), TITLE1
WRITE(NO, 1232), INFILE
WRITE(NO, 1234), COUNT
WRITE(NO, 2221), TIMEA
WRITE(NO, 3333), TANEAL
WRITE(NO, 2222), QH
WRITE(NO, 2223), QC
WRITE(NO, 2224), TSTART
WRITE(NO, 2225), AA
WRITE(NO, 2226), B(1)
WRITE(NO, 2227), BETA
WRITE(NO, 2228), XX
```

```
BMIN(1) = B(1) - 15
BMAX(1) = B(1) + 15
```



```

KK = 3
BMIN(2) = 0.001
BMAX(2) = 1.0
BMIN(3) = 0.001
BMAX(3) = 1.0
B(2) = BETA
B(3) = XX

```

```
CALL MARTEK (KK, NN, B, BMIN, BMAX, Y, PH, Z, NO, FUNC)
```

```

6001 FORMAT (/, 5X, 40A)
11  WRITE (NO, 20)
20  FORMAT (5X, 'VALUES OF THE SEARCHED PARAMETERS ARE:')
    WRITE (NO, 21) B(1), AA, B(2), B(3)
21  FORMAT (//, 5X, 'A = ', F7.3, 2X, 'DH = ', F6.3, 2X, 'X = ', F8.4, 2X,
    * 'BETA = ', F8.4)
    WRITE (NO, 5001) PH
5001 FORMAT (/, 5X, 'RESIDUAL = ', E15.8)
    WRITE (NO, 22)
22  FORMAT (//, 5X, 'PREDICTED CURVE VALUES')
    WRITE (NO, 23)
23  FORMAT (/, 4X, 'T(I)', 10X, 'CP EXPERIMENTAL', 7X,
    * 'CP PREDICTED', 5X, 'FICTIVE TEMP')
    WRITE (NO, 24) (T1(I), Y(I), Z(I), TF(NN-I+1), I = 1, NN)
24  FORMAT (3X, F8.2, 5X, E16.7, 5X, E16.7, 5X, F8.2)
25  FORMAT (1X, F6.4)
26  FORMAT (1X, F8.4)

```

```
CALL GRAPH(TITLE, TITLE1, QC, QH, TSTART, DT, NN, B, T1, Y, Z)
```

```

STOP
END

```

```
SUBROUTINE GRAPH(TITLE, TITLE1, QC, QH, TSTART, DT, NN, B, T1, Y, Z)
```

```

REAL XDRA(200,1), YDRA(200,2), Y(200), Z(200), T1(200), B(3)
REAL MIN, MAX

```

```

C
C OPEN GKS, OPEN WORKSTATION OF TYPE 1, ACTIVATE WORKSTATION
C
CALL OPNGKS

```

```

C
C LOAD DATA INTO 3-D MATRIX
C
  DO 25 J=1,200
    YDRA(J,1)=1
    YDRA(J,2)=1
    XDRA(J,1)=TSTART+NN*DT
25  CONTINUE
  DO 27 G=1,NN
    XDRA(G,1)=T1(G)
    YDRA(G,1)=Y(G)
    YDRA(G,2)=Z(G)

27  CONTINUE
C
C SET UP X-AXIS LABELS
C
  CALL AGSETC ('LABEL/NAME.','B')
  CALL AGSETI ('LINE/NUMBER.',-100)
  CALL AGSETC ('LINE/TEXT.','TEMPERATURE(K)$')
C
C X-AXIS BOUNDARIES
C
  MIN=TSTART
  MAX=TSTART+NN*DT
  CALL AGSETF ('X/MINIMUM.',MIN)
  CALL AGSETF ('X/MAXIMUM.',MAX)
C
C Y-AXIS LABELS
C
  CALL AGSETC ('LABEL/NAME.','L')
  CALL AGSETI ('LINE/NUMBER.',100)
  CALL AGSETC ('LINE/TEXT.','NORMALIZED HEAT CAPACITY$')

C
C DRAW THE BACKGROUND
C
  CALL EZMXY (XDRA,YDRA,200,2,200,TITLE)
C
C DEACTIVATE AND CLOSE WORKSTATION, CLOSE GKS.
C
  CALL CLSGKS

```

```
RETURN
END
```

```
SUBROUTINE MARTEK (KK, NN, B, BMIN, BMAX, Y, PH, Z, NO, FUNC)
```

```
DIMENSION P(800), A(3,5), AC(3,5), X(200), B(3), Z(200), Y(200)
DIMENSION BV(3), BMIN(3), BMAX(3), FV(3), DV(3)
```

```
EXTERNAL FUNC
```

```
FNU = 0.
FLA = 0.
TAU = 0.
EPS = 0.
PHMIN = 0.
I = 0
KD = KK
DO 100 J = 1, KK
  FV(J) = 0.
  BV(J) = 1.0
100 CONTINUE
```

```
ICON = KK
ITER = 0
```

```
WRITE (NO, 015)
015 FORMAT (10X, 'MARQUARDT REGRESSION ALGORITHM')
```

```
200 CALL BSOLVE (KK, B, NN, Z, Y, PH, FNU, FLA, TAU,
  * EPS, PHMIN, I, ICON, FV, DV, BV, BMIN, BMAX, P,
  * FUNC, DERIV, KD, A, AC, GAMM)
```

```
NO=3
ITER = ITER + 1
PRINT *, ITER
WRITE (NO,001) ICON, PH, ITER, B(1), B(3), B(2)
001 FORMAT (/, 'ICON=', I3, 2X, 'PH =', E11.4, 2X, 'ITER.NO.=',
  * I3, 2X, 'A =', F6.2, 2X, 'BETA =', F6.3, 2X, 'X =', F6.3)
```

```

      IF (ICON) 10, 300, 200
10   IF (ICON + 1) 20, 60, 200
20   IF (ICON + 2) 30, 70, 200
30   IF (ICON + 3) 40, 80, 200
40   IF (ICON + 4) 50, 90, 200
50   GO TO 95
60   CONTINUE

      WRITE (NO, 004)
004  FORMAT (//, 2X, 'NO FUNCTION IMPROVEMENT POSSIBLE')
      GO TO 300
70   WRITE (NO, 005)
005  FORMAT (//, 2X, 'MORE UNKNOWN THAN FUNCTIONS')
      GO TO 300
80   WRITE (NO, 006)
006  FORMAT (//, 2X, 'TOTAL VARIABLES ARE ZERO')
      GO TO 300
90   WRITE (NO, 007)
007  FORMAT (//, 2X, 'CORRECTIONS SATISFY CONVERGENCE REQUIREMENTS
      * BUT LAMBDA FACTOR IS STILL LARGE')

      GO TO 300
95   WRITE(NO, 008)
008  FORMAT (//, 2X, 'THIS IS NOT POSSIBLE')
300  CONTINUE
      WRITE (NO, 002)
002  FORMAT (//, 2X, 'VALUES OF PARAMETERS')
      DO 400 J = 1, KK
      WRITE (NO, 003) J, B(J)
003  FORMAT (/, 2X, 2HB(, I2, 4H) = , E16.8)

400  CONTINUE

1000 RETURN

```

END

SUBROUTINE BSOLVE (KK, B, NN, Z, Y, PH, FNU, FLA, TAU,
 * EPS, PHMIN, I, ICON, FV, DV, BV, BMIN, BMAX, P,
 * FUNC, DERIV, KD, A, AC, GAMM)

DIMENSION P(800), A(3,5), AC(3,5), X(200), B(3), Z(200),
 * Y(200)

DIMENSION BV(3), BMIN(3), BMAX(3), FV(3), DV(3)

EXTERNAL FUNC, DERIV

K = KK

N = NN

KP1 = K + 1

KP2 = K + 2

KBI1 = K * N

KBI2 = KBI1 + K

KZI = KBI2 + K

IF (FNU 0.LE. 0.) FNU = 10.

IF (FLA 0.LE. 0.) FLA = 0.01

IF (TAU 0.LE. 0.) TAU = 0.001

IF (EPS 0.LE. 0.) EPS = 0.00002

IF (PHMIN 0.LE. 0.) PHMIN = 0.

120 KE = 0

130 DO 160 I1 = 1, K

160 IF(BV(I1) 0.NE. 0) KE = KE + 1

IF(KE 0.GT. 0.) GO TO 170

162 ICON = -3

163 GO TO 2120

170 IF (N 0.GE. KE) GO TO 500

180 ICON = -2

190 GO TO 2120

500 I1 = 1

530 IF (I 0.GT. 0) GO TO 1530

550 DO 560 J1 = 1, K

J2 = KBI1 + J1

P(J2) = B(J1)

J3 = KBI2 + J1

560 P(J3) = ABS (B(J1)) + 1.E-2

GO TO 1030

590 IF (PHMIN 0.GT. PH 0.AND. I 0.GT. 1) GO TO 625

DO 620 J1 = 1, K

N1 = (J1 - 1) * N

IF (BV(J1)) 601, 620, 605

601 CALL DERIV (K, B, N, Z, P(N1+1), FV, DV, J1, JTEST)

IF (JTEST 0.NE. (-1)) GO TO 620

BV(J1) = 1.0

605 DO 606 J2 = 1, K

J3 = KBI1 + J2

606 P(J3) = B(J2)

J3 = KBI1 + J1

J4 = KBI2 + J1

DEN = 0.001 * AMAX1 (P(J4), ABS (P(J3)))

IF (P(J3) + DEN 0.LE. BMAX(J1)) GO TO 55

P(J3) = P(J3) - DEN

DEN = -DEN

GO TO 56

55 P(J3) = P(J3) + DEN

56 CALL FUNC (K, P(KBI1+1), N, P(N1+1), FV)

DO 610 J2 = 1, N

JB = J2 + N1

610 P(JB) = (P(JB) - Z(J2)) / DEN

620 CONTINUE

625 DO 725 J1 = 1, K

N1 = (J1 - 1) * N

A(J1, KP1) = 0.0

IF (BV(J1)) 630, 692, 630

630 DO 640 J2 = 1, N

N2 = N1 + J2

640 A(J1, KP1) = A(J1, KP1) + P(N2) * (Y(J2) - Z(J2))

650 DO 680 J2 = 1, K

660 A(J1, J2) = 0.0

665 N2 = (J2 - 1) * N

670 DO 680 J3 = 1, N

672 N3 = N1 + J3

674 N4 = N2 + J3

680 A(J1, J2) = A(J1, J2) + P(N3) * P(N4)

IF (A(J1, J1) 0.GT. 1.0E-20) GO TO 725

692 DO 694 J2 = 1, KP1

694 A(J1, J2) = 0.0

695 A(J1, J1) = 1.0

725 CONTINUE

```

GN = 0.0
DO 729 J1 = 1, K
729 GN = GN + A(J1,KP1) * A(J1,KP1)
DO 726 J1 = 1, K
726 A(J1,KP2) = SQRT (A(J1,J1))
DO 727 J1 = 1, K
A(J1,KP1) = A(J1,KP1) / A(J1,KP2)
DO 727 J2 = 1, K
727 A(J1,J2) = A(J1,J2) / (A(J1,KP2) * A(J2,KP2))
730 FL = FLA / FNU
GO TO 810
800 FL = FNU * FL
810 DO 840 J1 = 1, K
820 DO 830 J2 = 1, KP1
830 AC(J1,J2) = A(J1,J2)
840 AC(J1,J1) = AC(J1,J1) + FL
DO 930 L1 = 1, K
L2 = L1 + 1
DO 910 L3 = L2, KP1
IF (AC(L1,L1)) 890, 900, 890
890 AC(L1,L3) = AC(L1,L3) / AC(L1,L1)
GO TO 910
900 AC(L1,L3) = 1.0E+30

910 CONTINUE

918 DO 930 L3 = 1, K
IF(L1-L3) 920, 930, 920
920 DO 925 L4 = L2, KP1
925 AC(L3,L4) = AC(L3,L4) - AC(L1,L4) * AC(L3,L1)

930 CONTINUE

DN = 0.0
DG = 0.0
DO 1028 J1 = 1, K
AC(J1,KP2) = AC(J1,KP1) / A(J1,KP2)
J2 = KBI1 + J1
P(J2) = AMAX1 (BMIN(J1), AMIN1 (BMAX(J1), B(J1) + AC(J1,KP2)))
DG = DG + AC(J1,KP2) * A(J1,KP1) * A(J1,KP2)
DN = DN + AC(J1,KP2) * AC(J1,KP2)
1028 AC(J1,KP2) = P(J2) - B(J1)
COSG = DG / SQRT(DN*GN)

```

```

      JGAM = 0
      IF(COSG) 1100, 1110, 1110
1100  JGAM = 2
      COSG = -COSG

1110  CONTINUE

      COSG = AMIN1(COSG, 1.0)
      GAMM = ARCOS (COSG) * 180.0 / 3.14159265
      IF (JGAM 0.GT. 0.0) GAMM = 180.0 - GAMM
1030  CALL FUNC (K, P(KBI+1), N, P(KZI+1), FV)
1500  PHI = 0.0
      DO 1520 J1 = 1, N
      J2 = KZI + J1
1520  PHI = PHI + (P(J2) - Y(J1)) ** 2

2500  IF (PHI 0.LT. 1.0E-10) GO TO 3000
      IF (I 0.GT. 0) GO TO 1540
1521  ICON = K
      GO TO 2110
1540  IF (PHI 0.GE. PH) GO TO 1530
1200  ICON = 0
      DO 1220 J1 = 1, K
      J2 = KBI + J1
1220  IF (ABS (AC(J1,KP2)) / (TAU + ABS (P(J2)))) 0.GT. EPS)
      * ICON = ICON + 1
      IF (ICON 0.EQ. 0) GO TO 1400
      IF (FL 0.GT. 1.0 0.AND. GAMM 0.GT. 90.0 ) ICON = -1
      GO TO 2105
1400  IF (FL 0.GT. 1.0 0.AND. GAMM 0.LE. 45.0) ICON = -4
      GO TO 2105
1530  IF (I1 - 2) 1531, 1531, 2310
1531  I1 = I1 + 1
      GO TO (530, 590, 800), I1
2310  IF (FL 0.LT. 1.0E08) GO TO 800
1320  ICON = -1
2105  FLA = FL

      DO 2091 J2 = 1, K
      J3 = KBI + J2
2091  B(J2) = P(J3)
2110  DO 2050 J2 = 1, N

```



```

      J3 = KZI + J2
2050  Z(J2) = P(J3)
      PH = PHI
      I = I + 1
2120  RETURN
3000  ICON = 0
      GO TO 2105

```

```

END

```

```

SUBROUTINE FUNC (KK, B, NN, Z, FV)

```

```

REAL LNTAU1, LNTAU, TRC

```

```

REAL TF(600), TAU(600), E(600), TRED(600), TR(600), CP(600)
REAL TIME(600), B(3), Z(200), FV(3), S(600), T1(200), TRH(600), T(600)

```

```

COMMON TF, TAU, E, TRED, TR, TIME, PR, H, T, QC, DT
COMMON TIMEA, QH, TANEAL, AA, TSTART, S, T1

```

```

LNTAU1=0.
TRC=DT*60./QC
H = AA * 1000/1.987
R = INT (10.0 * LOG10 (TIMEA))
IIR = NN + R
15  TO = TSTART + NN*DT
    K = 0
    NANEAL = (TO - TANEAL)/DT
    MANEAL = NANEAL + R
    TM = TIMEA ** (1 / R)
    T(1) = TO - DT
C   LNTAU = B(1) + B(2) * H / (TO - DT) + (1.0 - B(2)) * H / TO
    IF (LNTAU1 + 70.0) 20, 20, 30
20  E(1) = 0.0
    TAU(1) = 1.0E-30
    TIME(1) = TRC
    GO TO 40
30  TAU(1) = EXP (LNTAU1)
    E(1) = EXP (-((TRC / TAU(1)) ** B(3)))
40  TF(1) = T(1) + E(1)
    CP(1) = TO - TF(1)
    DO 45 I = 1, (IIR + 1)
45  S(I) = DT

```

```

DO 290 I = 2, (IIR * 2)
  TRH(I) = S(I) * 60.0 / QH
  IF (I - (IIR + 1)) 50, 60, 60
50  IF (I - NANEAL) 51, 51, 53
51  T(I) = T(I-1) - S(I)
    GO TO 70
53  IF (I - MANEAL) 55, 55, 51
55  T(I) = T(I-1)
    GO TO 70
60  T(I) = T(I-1) + S(I)
70  ARG = B(2) * H / T(I) + (1.0 - B(2)) * H / TF(I-1)
    TAULN = B(1) + ARG
    IF (TAULN + 70) 80, 80, 90
80  TAU(I) = 1.0E-29
    GO TO 115
90  IF(TAULN - 70) 110, 100, 100
100 TAU(I) = 1.0E+20
    GO TO 115
110 TAU(I) = EXP(TAULN)
115 IF (I - IIR) 120, 120, 140
120 IF (I - NANEAL) 130, 130, 160
130 TRED(I) = TRC / TAU(I)
    TIME(I) = TIME(I-1) + TRC
    GO TO 170
140 TRED(I) = TRH(I) / TAU(I)
    TIME(I) = TIME(I-1) + TRH(I)
    GO TO 170
160 IF (I - MANEAL) 161, 161, 130
161 TMM = TM ** (I - NANEAL)
    IF (I 0.EQ. (NANEAL + 1)) GO TO 165
    TM1 = TMM * (1.0 - 1.0 / TM)
    GO TO 167
165 TM1 = TM
167 TRED(I) = TM1 / TAU(I)
    TIME(I) = TIME(NANEAL) + TMM
170 TR(I) = TRED(I)
180 DO 190 J = 1, (I-1)
190 TR(I-J) = TR(I-J+1) + TRED(I-J)
    DO 200 J = 2, I
200 E(J) = S(J) * EXP(-((TR(J))**B(3)))
210 SUM = 0.0
212 IF (I - IIR) 213, 213, 250
213 IF (I - NANEAL) 220, 220, 214

```

```

214 IF (I - MANEAL) 217, 217, 242
217 DO 218 J = 1, NANEAL

218 SUM = SUM + E(J)
    GO TO 235
220 DO 230 J = 1, I
230 SUM = SUM + E(J)
235 TF(I) = T(I) + SUM
240 CP(I) = (TF(I-1) - TF(I))
    GO TO 280
242 DO 243 J = 1, NANEAL
243 SUM = SUM + E(J)
    DO 244 J = (MANEAL+1), I
244 SUM = SUM + E(J)
    GO TO 235
250 DO 252 J = 1, NANEAL
252 SUM = SUM + E(J)
    DO 254 J = (MANEAL+1), IIR
254 SUM = SUM + E(J)
    DO 256 J = (IIR+1), I
256 SUM = SUM - E(J)
275 TF(I) = T(I) + SUM
    CP(I) = (TF(I) - TF(I-1)) / S(I)
    IF (CP(I) - 1.01) 278, 278, 276
276 S(I+1) = DT / CP(I)
    GO TO 280
278 S(I+1) = DT
280 CONTINUE
290 L=1
    DO 2800 I=IIR+1,2*IIR
        TEST=ABS((T(I)-T(IIR+1))/DT)
        NTEST=INT(TEST)
        IF(NTEST.EQ.TEST) GO TO 2600
        TEMPI=NTEST*DT+T(IIR+1)+DT
        DO 2300 J=1,100
            JJ=J
            IF(T(I+J).GE.TEMPI) GO TO 2400
2300 CONTINUE
2400 IF(JJ.NE.1) GO TO 2800
        IF(TEMPI.EQ.T1(L-1)) GO TO 2800
        T1(L)=TEMPI
        Z(L)=CP(I)+(CP(I+1)-CP(I))*(TEMPI-T(I))/(T(I+1)-T(I))
        L=L+1

```

```

      GO TO 2700
2600  Z(L)=CP(I)
      T1(L)=T(I)
      L=L+1
2700  IF (L.GT.NN)GO TO 2900
2800  CONTINUE
2900  RETURN
      END

```

```

FUNCTION ARCOS (Z)
X = Z
KEY = 0
IF (X 0.LT. -1.0) X = -1.0
IF (X 0.GT. 1.0) X = 1.0
IF (X 0.GE. -1.0 0.AND. X 0.LT. 0.0) KEY = 1
IF (X 0.LT. 0.0) X = ABS (X)
IF (X 0.EQ. 0.0) GO TO 10
ARCOS = ATAN (SQRT (1.0 - X * X) / X)
IF (KEY 0.EQ. 1) ARCOS = 3.1415926 - ARCOS
GO TO 999
10  ARCOS = 1.5707963
999  RETURN
      END

```

```

SUBROUTINE DERIV (K, B, N, Z, PN1, FV, DV, J1, JTEST)

```

```

      RETURN
      END

```